



# Modélisation, caractérisation et exploitation des milieux réverbérants

Florian Monsef

## ► To cite this version:

Florian Monsef. Modélisation, caractérisation et exploitation des milieux réverbérants. Electromagnetism. Université Paris XI Paris-Sud, 2019. tel-04552730

HAL Id: tel-04552730

<https://hal.science/tel-04552730>

Submitted on 19 Apr 2024

**HAL** is a multi-disciplinary open access archive for the deposit and dissemination of scientific research documents, whether they are published or not. The documents may come from teaching and research institutions in France or abroad, or from public or private research centers.

L'archive ouverte pluridisciplinaire **HAL**, est destinée au dépôt et à la diffusion de documents scientifiques de niveau recherche, publiés ou non, émanant des établissements d'enseignement et de recherche français ou étrangers, des laboratoires publics ou privés.

NNT : 2016SACLcxx

HABILITATION À DIRIGER DES RECHERCHES  
de  
l'Université PARIS-SACLAY  
Laboratoire Geeps

(Univ. Paris-Sud, CNRS, CentraleSupélec, UPMC Sorbonne Université)

**Modélisation, caractérisation et exploitation des milieux réverbérants**

ÉCOLE DOCTORALE N° : 575  
Physique et Ingénierie : Électrons, Photons, Sciences du vivant (EOBE)

Spécialité : Electromagnétisme

Par

**Florian MONSEF**

Habilitation à diriger les Recherches

**Habilitation présentée et soutenue à Gif-sur-Yvette, le 17 juin 2019**

**Composition du Jury :**

Rapporteurs :

Julien De Rosny Directeur de Recherche CNRS, Institut Langevin, ESPCI  
Philippe Besnier Directeur de Recherche CNRS, IETR INSA Rennes  
Elodie Richalot Professeur des Universités, Univ. Paris-Est Marne-la-vallée

Examinateurs :

Marc Lambert Chargé de Recherche CNRS, Geeps, Univ. Paris-Sud, CentraleSupélec  
Fouzia Boukour Directrice de Recherche IFSTTAR, Villeneuve d'Ascq  
Franco Moglie Professeur à l'Université delle Marche, Ancona (Italie)  
Cyril Decroze Maître de Conférences à l'Université de Limoges (XLIM)



---

## Table des matières

---

<b>1 Curriculum Vitae</b>	<b>1</b>
I Formation universitaire . . . . .	1
II Parcours Professionnel . . . . .	1
III Domaines de Compétences . . . . .	1
III.1 Compatibilité Electromagnétique (CEM) . . . . .	2
III.2 Acoustique des Chambres . . . . .	2
III.3 Retournement Temporel (RT) . . . . .	2
IV Activités d'enseignement . . . . .	2
V Activités d'encadrement . . . . .	3
V.1 Stagiaires encadrés . . . . .	4
Stagiaires encadrés/co-encadrés . . . . .	4
V.2 Doctorants encadrés . . . . .	4
VI Collaborations . . . . .	4
<b>2 Physique des Chambres Réverbérantes</b>	<b>5</b>
I Régime surmodé ou régime diffus . . . . .	6
II Régime non surmodé . . . . .	8
II.1 Ergodicité . . . . .	8
II.2 Approche modale . . . . .	11
III Du Régime sous-modé au régime sur-modé . . . . .	19
IV Conclusion et perspectives . . . . .	22
Références . . . . .	22
<b>3 Retournement Temporel</b>	<b>65</b>
I Retournement Temporel classique . . . . .	65
II Métrique utile : le contraste en énergie et le contraste pic . . . . .	68
III Contributions au RT classique . . . . .	69
III.1 Influence du nombre de sources . . . . .	69
III.2 RT pour la synthèse de front d'ondes : la <i>TREC</i> . . . . .	73
IV Conclusion et perspectives . . . . .	80
Références . . . . .	80
<b>4 Mesure d'antenne en milieu échogène</b>	<b>109</b>
I Modélisation du problème dans le cas monoécho . . . . .	109
II Pertinence du modèle proposé . . . . .	111
II.1 Hypothèse de Champ lointain . . . . .	111
II.2 Diffraction de l'antenne . . . . .	113

## *Table des matières*

II.3	Plaque de dimension finie . . . . .	115
III	Inversion du problème . . . . .	117
III.1	Nombre de conditionnement dans l'approche classique . . . . .	117
III.2	Approche par Régresseurs . . . . .	119
IV	Configurations multi-échos . . . . .	124
IV.1	Structures Diédrales . . . . .	125
IV.2	Cas des plaques parallèles . . . . .	125
V	Conclusion et perspectives . . . . .	126
	Références . . . . .	126
<b>5</b>	<b>Liste de mes publications</b>	<b>127</b>
I	Articles dans des revues internationales à comité de lecture . . . . .	127
II	Articles dans des conférences internationales à comité de lecture avec actes . . . . .	128
III	Brevets . . . . .	129

---

## Table des figures

---

2.1 Chambre réverbérante à brassage de modes de CentraleSupelec. Le pale en mouvement modifie les conditions limites et permet de « brasser le champ » au sein de l'enceinte. . . . .	6
2.2 Taux de réjection d'hypothèse de gaussianité d'une distribution à $N$ échantillons corrélés. Le niveau de corrélation (type lag-1) est représenté en abscisse, le taux de réjection est donné par l'axe des ordonnées. Les tests d'hypothèse suivants ont été étudiés : Liliefors, Anderson-Darling (AD), Kolmogorov-Smirnov (KS) ainsi que le $\chi^2$ . . . . .	8
2.3 Chambre réverbérante acoustique du LNE (Trappes). Les plaques suspendues sont des diffuseurs servant à casser tout degré de symétrie afin d'assurer une chaoticité du milieu ; les microphones suspendus servent quant à eux à échantillonner le champ. Au centre une tige rotative qui sert à échantillonner le champ ; le mouvement de cette tige a un effet de brassage du champ. . . . .	9
2.4 (a) Illustration du recouvrement modal (bas à gauche) où chaque mode est représenté. Réponse spectrale résultante (gauche haut). (b) Réponse expérimentale montrant la complexité effective de la superposition modale. $B_e$ est la bande effective à considérer incluant le nombre utile de modes. . . . .	12
2.5 Valeur moyenne (trait gras) et limites des intervalles de confiance de $\hat{\zeta}_P^2$ fonction du nombre moyen $M_M$ de modes recouverts pour différentes valeurs de $N_{sp}$ positions indépendantes de brasseur (reportées sur le graphe). Les limites supérieures et inférieures de l'intervalle de confiance sont au-dessus et en-dessous du trait gras respectivement. . . . .	13
2.6 Densité de probabilité de Wigner (trait gras plein), de Poisson (tirets), des plus proches voisins ( $NN$ ) (trait plein fin) et triangulaire (traits en pointillés). . . . .	15
2.7 Variabilité estimée $\hat{\zeta}_W^2$ (axe y gauche) de la densité d'énergie électrique, fonction du nombre $M_M$ de modes dans le cas où la chambre est vide (a) et chargée (b). Les déviations relatives à la valeur asymptotique de $1/3$ sont reportées (axe des ordonnées de droite). Les résultats expérimentaux (symboles gris), ceux de simulation MC (points noirs) et les résultats analytiques sont reportés (trait plein). Les barres d'incertitude verticales traduisent un intervalle de confiance de 95% et les barres horizontales rendent compte de la dispersion que le paramètre $M_M$ autour de sa valeur moyenne. . . . .	16
2.8 (a) Temps de réverbération estimés lorsque la chambre est vide (cercles) et chargée (carrés) (gauche). (b) Estimation du nombre de modes recouverts dans une bande modale dans les cas respectifs où la chambre réverbérante est vide (cercles) et chargée (carrés) (droite). . . . .	17
2.9 . . . . .	17

## Table des figures

2.10 Variabilités de la valeur quadratique du champ de pression obtenues expérimentalement (trait fin), analytiquement via la relation (2.10) pour $K = 2.7$ et $K = 3$ (trait plein gras et trait en tirets-pointillés respectivement). Les résultats par simulation MC (points noirs) y sont reportés avec les barres d'incertitude associées pour le cas d'une chambre vide (figure gauche) et d'une chambre chargée (figure de droite). Le modèle de Weaver (trait en tirets) y est reporté ainsi que le modèle de Davy/Lyon (traits pointillés) qui suppose pour ce dernier un espacement entre fréquences propres régi par une loi de Poisson. . . . .	18
2.11 Illustration du recouvrement modal dans le cas où les réponses en fréquences sont des Lorentziennes (traits gras) et dans le cas où les réponses en fréquence sont des portes en fréquence (traits fins). Si la bande modale à -3dB est notée $B_M$ , on montre que une bande $\pi B_M$ des fonction portes mène à une variabilité identique . . . . .	19
2.12 Estimation du nombre $M_M$ de modes se recouvrant dans une bande modale en fonction de la fréquence pour une chambre réverbérante vide de $13m^3$ ; le modèle de Weyl y est reporté également (trait plein) . . . . .	20
2.13 Evolution du paramètre de forme $b$ de la distribution de Weibull en fonction du nombre $M_M$ de modes se recouvrant. On propose également une expression de la courbe de tendance afin d'avoir une relation explicite entre les deux paramètres. . . . .	21
2.14 Evolution du paramètre de forme $b$ estimé en fonction de la fréquence (gauche) et du nombre $M_M$ (droite). L'estimation s'est faite sur la base de 1500 échantillons. Les symboles gris ont été obtenus expérimentalement, la courbe en trait plein découle de la relation obtenue Fig. 2.13 couplée à l'estimation du nombre $M_M$ en fonction de la fréquence. Les barres d'incertitude ont été obtenues par simulation Monte Carlo. . . . .	21
 3.1 Phase d'émission et d'enregistrement des signaux par les MRT (gauche) et réémission par réinjection des signaux dans les MRT (droit) dans le protocole du RT classique (d'après <i>Tourin (ESPCI)</i> ). . . . .	66
3.2 Relevés expérimentaux de $ S_{21} ^2$ en quatre points de la CR pour une position de brasseur fixe. On constate que les moments statistiques ont des valeurs proches pour ces quatre positions. . . . .	67
3.3 La fonction de transfert (haut) est pondérée par une gaussienne. On obtient le signal focalisé pour un template du type impulsion gaussienne. Le bruit du signal focalisé est extrait et représenté sur le graphe du bas. . . . .	68
3.4 Setup expérimental : (a) une des 12 antennes papillons, montées sur les parois de la chambre réverbérante, avec un espaceur de 3 cm en polystyrène ; (b) La sonde électro-optique Enprobe's EFS105, équipée d'une tête de mesure de 6.6 mm de large. . . . .	70
3.5 Apport incrémental à l'ajout d'un MRT sachant $N_A$ MRT déjà présents, en considérant un niveau moyen de cohérence $\bar{\mu}_r$ (en pourcentage sur chaque ligne).	71
3.6 Correlation moyenne estimée entre différentes fonction de transfert (trait plein) ; régression au sens des moindres carrés est superposée (pointillés). . . . .	71
3.7 Exemple de milieu indoor dans lequel les performances du RT ont été étudiées (gauche) avec les dimensions et positionement(s) des émetteurs/récepteur (droite). On constate des trajets directs ( <i>LOS</i> ) et des parcours multi-trajets ( <i>NLOS</i> ). . . . .	72

3.8	Réponses impulsionnelles des différents milieux étudiés : en-dehors de la chambre (en haut à gauche), dans un couloir (en haut ) droite), dans la chambre réverbérante (en bas à gauche) et dans le hall illustré Fig. 3.7. . . . .	72
3.9	Illustration du SNR obtenu par RT avec une fréquence de 5 GHz : rapport des deux pics considérés (écho et impulsion utile). . . . .	73
3.10	SNR obtenus (gauche) dans les différents milieux <i>indoor</i> étudiés et le gain qu'apporte le RT (droite) par rapport une transmission classique. . . . .	73
3.11	L'arche constituant le coeur de la TREC consiste en un échantillonneur spatial du champ suivant les coordonnées polaires $\theta$ et $\varphi$ (a) - Un zoom met en évidence le système de courroie utilisé ainsi que le chariot accueillant la sonde électro-optique (b). . . . .	74
3.12	Topographies 3D (gauche) et coupe 2D (droite) obtenues avec la TREC . . . . .	75
3.13	Topographie de champ visé où la concentration de l'onde est confinée spatialement et localement plane. . . . .	76
3.14	Pour une largeur $W=5$ et un angle $\Theta = 30^\circ$ , on illustre les fonctions propres résultantes avec les valeurs propres $\lambda_n$ correspondantes. . . . .	77
3.15	Topographies des fonctions Slepian pour $W = 5$ et un angle $\Theta = 20^\circ$ . . . . .	77
3.16	Topographie de champ obtenue en incluant 4 Slepians . . . . .	78
3.17	Evolution du rapport des parties cohérentes et fluctuantes en fonction du degré de perturbation illustré par le coefficient $(1 - \rho^2)$ . Les résultats expérimentaux sont représentés par les symboles pour trois statistiques différentes de chambre ; les modèles théoriques sont représentés par les courbes en tirets. . . . .	79
3.18	Evolution relative du contraste en fonction du niveau de perturbation de la chambre, et ce, pour trois statistiques différentes. . . . .	79
4.1	Antennes utilisés pour l'analyse du concept proposé : (a) dimensions des AST (b) Coefficients de réflexion $S_{11}$ correspondants et bandes de fonctionnement. .	110
4.2	Principe de la mesure exploitant les échos. (a) La sonde est placée à une distance $r_0$ de l'AST et l'écho parcourt une distance $r_1$ . (b) Schéma équivalent utilisant le principe des images mettant en évidence la mesure de deux points du diagramme en une mesure. . . . .	111
4.3	Erreur $\epsilon_{FF}$ en module (dB) pour le cas TM (isotrope) - (a) cas du dipole (b) cas de l'antenne biconique . . . . .	112
4.4	Evolution des erreurs sur le module (a) $\epsilon_{\parallel E_z \parallel}$ et la phase (b) $\epsilon_{\angle E_z}$ , pour le cas TM isotrope. . . . .	113
4.5	Erreur obtenue en espace libre [dB] sachant l'hypothèse de champ lointain - cas TE : (a) $\epsilon(E_x)_{HWD}$ (b) $\epsilon(E_y)_{HWD}$ (c) $\epsilon(E_x)_{biconique}$ (d) $\epsilon(E_y)_{biconique}$ . . . . .	114
4.6	Cartographie de l'erreur liée au champ diffracté par l'antenne sous test en mode TM ; plaque en $x_p = 10\lambda_0$ : (a) $\epsilon_0^d$ , (dipôle) (b) $\epsilon_1^d$ (dipôle) (c) $\epsilon_0^d$ (biconique) (d) $\epsilon_1^d$ (biconique). . . . .	116
4.7	Configuration considérée sachant une plaque de dimension finie afin d'en évaluer l'effet de diffraction par les bords. . . . .	117

## Table des figures

4.8	Erreur obtenue sur le diagramme de rayonnement de l'antenne dipôle en fonction de la position de la sonde et impact des champs diffractés par les bords et les angles de coin. La plaque est tronquée en $h_y = [-5\lambda_0, 10\lambda_0]$ et $h_z = \pm 5\lambda_0$ et positionnée en $x_p = 10\lambda_0$ (a) erreur sur l'amplitude de la partie directe (TM), UFBW = 4% (b) erreur sur l'amplitude UFBW = 4% (c) TE LOS amplitude error, basic model (d) TE image amplitude error, basic model. . . . .	118
4.9	Bords de la plaque arrondis afin de réduire la diffraction par les arêtes de la plaque. . . . .	119
4.10	Exemple de réduction du problème de diffraction par les bords en utilisant des bords recourbés. La partie plate de la plaque a les dimensions suivantes : $h_y = [-5\lambda_0, 10\lambda_0]$ and $h_z = \pm 5\lambda_0$ . $x_p = 10\lambda_0$ . HWD. (a) Erreur sur l'amplitude de la partie LOS (TM, UFBW = 4%) (b) Amplitude de l'erreur de la partie image (TM, UFBW = 4%) (c) Amplitude de l'erreur de la partie LOS (TE) avec le modèle de base (d) erreur sur la partie image (TE) avec le modèle de base. . . . .	120
4.11	Relation entre le facteur de projection $\rho$ et le nombre de conditionnement $\kappa(\mathbf{G}_{TM})$ . Mise en évidence des positions optimales montrant l'intérêt des hyperboles optimales (tirets) et des cercles de conditionnement (trait plein). La plaque se situe en $x_p = 10\lambda_0$ et une bande relative $\Delta f_b$ de 4% est utilisée : (a) $\kappa(\mathbf{G}_{TM})$ ; (b) $\Delta f_b = 20\%$ , $\kappa(\mathbf{G}_{TM})$ ; (c) $\kappa(\mathbf{G}_{TE})$ ; (d) $\kappa(\mathbf{G}_{TE})$ avec diversité fréquentielle (bande de 4%). . . . .	121
4.12	Fonctions <i>RBF</i> définies sur un intervalle angulaire de $180^\circ$ , $N_r = 5$ , $s = 36^\circ$ . . . . .	122
4.13	Illustration de l'inversion par régression dans le cas du dipole (cas TE) avec 10 points de mesure (soit 20 angles) $(x, y) = (-9\lambda_0 : 2\lambda_0 : 9\lambda_0, 5\lambda_0)$ , $d = 10\lambda_0$ . Bruitage des données avec bruit blanc (SNR = 20dB). $\Delta f = 4\%$ : (a) RBF regression, $N_r = 90$ , $s = 1^\circ$ , (b) RBF regression, $N_r = 10$ , $s = 36^\circ$ , (c) RBF regression, $N_r = 3$ , $s = 36^\circ$ , (d) RBF regression, $N_r = 5$ , $s = 36^\circ$ . . . . .	123
4.14	Extension du cas simple plaque aux configurations permettant du multi-échos ; (a) Configuration diédrale d'angle $\phi_{in}$ (b) Configuration diédrale, avec $\phi_{in} = 90^\circ$ .	124

# CHAPITRE 1

---

## Curriculum Vitae

---

### I Formation universitaire

- 1999-2002 **Thèse de doctorat**, Institut d'Electronique Fondamentale, Université Paris-Sud  
Spécialité : Electronique
- 1998-1999 **D.E.A** en Electronique et Conception de Circuits Intégrés. Option micro-ondes.
- 1995-1998 Ecole Normale Supérieure de Cachan - Intégration en 3ème année.  
Agrégation en Ingénierie Electrique (option : électronique).

### II Parcours Professionnel

- 1999-2002 Maître de Conférences au département de Mesures Physiques à l'IUT d'Orsay,  
Université Paris-Sud
- 2002-2009 Professeur Agrégé à l'IUT de Ville d'Avray au Département de Génie Electrique  
Rang : 1er.
- 1995-1998 Ecole Normale Supérieure de Cachan - Intégration en 3ème année.  
Agrégation en Ingénierie Electrique (option : électronique).

### III Domaines de Compétences

Depuis mon doctorat, j'ai pu développé des compétences en matière d'enseignement, de développement et de recherche. Les compétences en enseignement ont pu se faire grâce à un poste en tant qu'enseignant à plein temps au niveau IUT mais également avec des publics de techniciens et ingénieurs venus de l'industrie en formation continue. Au niveau de ces enseignements, des compétences techniques ont été mises en oeuvre et développées dans le cadre de mise en place de travaux pratiques et de projets.

Au niveau de la recherche, mon poste MCF m'a amené à une conversion thématique passant de la physique des semiconducteurs à l'électromagnétisme dans le domaine des microondes dans des cavités chaotiques à taille humaine, appelées *Chambres Réverberantes à Brassage de Modes (CRBM)*. Ces dispositifs sont essentiellement utilisés dans les domaines de la compatibilité électromagnétique.

L'investissement dans ces thématiques m'a conduit également en début de poste vers l'acoustique où des problématiques analogues existent. En outre, la technique de retournement tem-

## 1 Curriculum Vitae

porel (RT) appliquée au cas des milieux complexes a permis de développer de nouvelles perspectives métrologiques pour les mesures en *CRBM*.

La dernière thématique abordée dans le cadre d'une thèse a porté sur la mesure de diagramme de rayonnement d'antenne. Cette thématique est en semi-rupture avec les autres thématiques. Les recherches dans le cadre de cette thèse ont débouché également sur un dépôt de brevet et m'a permis d'appréhender de plus près les difficultés expérimentales liées à une « bonne » mesure d'antenne.

La liste qui suit donne une vision d'ensemble des thématiques abordées dans le domaine de la recherche et constituent le noyau central de mes compétences de chercheur.

### III.1 Compatibilité Electromagnétique (CEM)

Une partie de mes travaux ont porté sur la pertinence de certains postulats ou directives présentes dans les standards liés aux *CRBM*. Cela a permis de se familiariser avec les techniques propres à la CEM dans ce type d'environnement d'essais standardisés. Une fois les attentes de la communauté connues, une de mes motivations principales a porté sur une meilleure compréhension de la physique des *CRBM* dans un but d'affinage métrologique. Les compétences actuelles portent sur la capacité à prévoir les intervalles de confiance pour les mesures de puissance rayonnée.

### III.2 Acoustique des Chambres

Une autre partie de mes travaux a porté sur les problématiques abordées dans le cadre de chambre réverbérante acoustique. Une collaboration avec le *Laboratoire National d'Essais (LNE)* a permis de se familiariser avec un environnement standard et les protocoles de mesure dans ce domaine. L'immersion dans ce domaine permet de s'ouvrir à d'autres approches autour de problématiques analogues et permet un partage inter communautés. L'intérêt pour les travaux d'acoustique a permis un éclairage sur l'utilité d'introduire un niveau de chaoticité dans les chambres réverbérantes.

### III.3 Retournement Temporel (RT)

Familiarisation avec le RT classique développé en acoustique et prise en main du concept de RT généralisé développé au laboratoire. Cette technique est une façon de faire de la synthèse de front d'onde dans un environnement naturellement peu propice à ce type de synthèse. Une étude amont sur de la viabilité de cette technique pour de la mesure d'antenne et pour la génération d'impulsions de puissance en chambre réverbérante a été menée à travers des thèses de doctorat.

Au-delà de ces applications, le RT généralisé permet d'élargir la précision des mesures pour la CEM. Cet aspect mérite de plus amples investigations en cours.

## IV Activités d'enseignement

Mes activités d'enseignement ont essentiellement eu lieu au Département Mesures Physiques de l'IUT d'Orsay.

Dès mon recrutement, j'ai eu l'opportunité de monter un module portant sur la conversion photovoltaïque. Ce module a été chronophage car aucune expérience personnelle et locale n'était présente. Cela a consisté à mettre en place des procédures expérimentales de caractérisation de panneaux solaires d'une part et d'étudier le couplage de tels dispositifs avec un convertisseur de puissance de type hacheur. Il s'agit d'un module de 30h effectué en semestre 4 classique et en semestre décalé.

J'ai eu également la charge du module d'électronique d'instrumentation. Ma contribution dans le cadre de ce module a consisté à introduire des séances de travaux pratiques dédiées à la mesure et la mise en évidence du bruit thermique. J'ai eu également la responsabilité de modules d'automatique et de micro-contrôleur au début de mon poste. Certains sujets ont été remaniés. Il s'agit de modules de 30h effectué en semestre 3 et 4 ainsi qu'en semestres décalés.

Mon expérience d'enseignement s'est élargie aux écoles d'ingénieurs telles que l'Ecole Supérieure d'Electricité (aujourd'hui CentraleSupelec) et l'Ecole Supérieure de Physique et Chimie Industriels (ESPCI) de Paris.

Les périodes importantes jalonnant cette expérience d'enseignement sont résumées ci-dessous :

Période	Nombre d'heures	Statut
2009-2017	200h	Maître de Conférences IUT d'Orsay (Dpt Mesures Physiques), Université Paris-Sud. Domaines : automatique, électronique d'instrumentation et conversion photovoltaïque.
2002-2009	500h	Professeur Agrégé à l'IUT de Ville d'Avray au Département de Génie Electrique (électronique analogique, numérique et programmation).
1999-2002	64h	Moniteur à l'Université Paris-Sud en électronique

## V Activités d'encadrement

Dès mon arrivée à CentraleSupelec, j'ai été amené à participer à l'encadrement d'Houmam Moussa en profitant de l'immersion dans son sujet sur le RT pour démarrer ma conversion thématique. Mon introduction à l'encadrement de ce doctorant a eu lieu en 2009. Mon intégration s'est faite en rejoignant les thématiques développées par Andrea Cozza. Ces thématiques portent sur la physique des chambres réverbérantes et le retournement temporel (RT).

La deuxième année j'ai été amené à encadrer des stagiaires niveau Master ou équivalent. L'encadrement de doctorants a débuté avec le travail de Philippe Méton qui s'est déroulé officiellement avec la collaboration du CEA de Gramat. Cet encadrement s'est poursuivi avec le travail d'Henri Vallon en collaboration avec Thalès. Enfin, la thèse de Mouad Djedidi a été la dernière thèse encadrée.

Ci-dessous la liste des stagiaires et doctorants encadrés :

## V.1 Stagiaires encadrés

- 2012 Rana SALEH et Zareh DEMIRDJIAN, Université Libanaise, stage de fin d'études de 4 mois. Travail sur le retournement temporel.  
Yann GIBONI, DUT de l'IUT de Cachan : échantillonneur linéaire du champ électrique.
- 2013 Djamila ABERKANE - Etudiante du Master CAT (Univ. Paris-Sud) - sujet : déconvolution des réponses en fréquence d'une CRBM pour en extraire la statistique des fréquences propres et des poids modaux
- 2014 Aloïs DUFOUR, Stagiaire de Licence/Magistère de Physique Fondamentale. Etude de l'effet d'absorption de métamatériaux en CRBM.

## V.2 Doctorants encadrés

Année	Taux Encadrement	Sujet et doctorant	Chapitre
2011-2015	50 %	Philippe METON, sujet : Étude et développement d'un concept de caractérisation rapide d'antennes basé sur le principe du retournement temporel en chambre réverbérante.	3
2012-2016	40%	Henri VALLON - Sujet : Focalisation d'impulsions forte puissance en utilisant le Retournement Temporel. Thèse CIFRE (Thalès Defense).	3
2013-2016	80%	Mouad DJEDIDI, sujet : Mesure de diagramme de rayonnement en milieu échogène l'effet d'absorption de métamatériaux en CRBM.	4

## VI Collaborations

Collaborateur	Pays	Thématique
Laboratoire National d'Essais (Garches)	France	Chambre réverbérante acoustique
Ramiro Serra (Université Eindhoven)	Pays-Bas	Test d'hypothèse en chambre réverbérante
Franco Moglie (Université d'Ancona)	Italie	Simulation chambre réverbérante
Thalès Defense	France	Mesures en chambre réverbérante en aluminium et financement thèse
CEA Gramat	France	Financement thèse

# CHAPITRE 2

---

## Physique des Chambres Réverbérantes

---

Les chambres réverbérantes à brassage de modes (CRBM) sont des dispositifs utilisés dans l'industrie, automobile et aéronautique notamment, pour des mesures de puissance rayonnée et des tests de susceptibilité électromagnétique ; ce type d'applications s'inscrit dans les thématiques de la communauté de la Compatibilité Electromagnétique (CEM). La notion de brassage de modes est liée à l'utilisation d'un brasseur qui correspond à une pale métallique (rotative en général). Le rôle du brasseur est de générer un ensemble de scénarios de tests en modifiant les conditions limites.

Les CRBM sont des cavités microondes dont le volume peut aller de moins d'un mètre cube à quelques centaines de mètres cube. Un cliché de ce type de dispositifs est donné Fig. 2.1. Une CRBM est classée dans la catégorie des systèmes dits complexes car la prédiction du champ électromagnétique (EM) en leur sein y est délicate dans la pratique. En effet la position du brasseur ainsi que l'objet (forme, matière,...) sous test vont modifier et fixer la topographie finale du champ EM. Dans la pratique une centaine de positions de brasseurs sont utilisées typiquement. Ainsi, si l'on désire déterminer les topographies de champ par une approche déterministe l'utilisation de logiciels de simulation numérique est indispensable. La simulation de tels systèmes peut être néanmoins coûteux en temps de calcul.

Dans le cadre des travaux développés depuis 2009 le recours à la simulation pour des CRBM a fait l'objet de collaboration avec des numéritiens de l'université d'Ancona (Italie) dans le cadre de la thèse de Philippe Méton (cf. Chap. 3). Dans le reste des cas, une approche statistique du champ au sein de la CRBM a été privilégiée. Les avantages d'une approche statistique permet de prédire le niveau moyen du champ au sein de la CRBM sans se préoccuper des détails des divers éléments présents à l'intérieur de la chambre. La contrepartie est d'accepter un degré d'incertitude (intervalle de confiance) du niveau de champ en un point par rapport au niveau moyen prédit.

L'approche statistique a été initialement appliquée à un régime asymptotique pour lequel le nombre de modes excités dans la cavité est tel que le champ peut être vu en première approximation comme Gaussien. Nous présenterons notre contribution quant aux questions pendantes dans le cadre de ce régime et les questions soulevées par rapport aux approches existantes. Certaines références à l'acoustique y seront présentées dans la mesure où deux contributions ont été faites dans ce domaine. Dans un second temps nous abordons le degré d'homogénéité de la densité d'énergie et/ou de puissance au sein de la cavité.

## I Régime surmodé ou régime diffus

En utilisant une approche modale, le champ peut être décomposé en une superposition de modes. Il est d'usage en CEM de travailler principalement en régime harmonique, i.e., en appliquant une excitation sinusoïdale. Suivant la fréquence de travail, un ensemble plus ou moins important de modes seront excités, et ce, en vertu de la densité modale établie par Weyl (WEYL 1912). Cette dernière varie avec le cube de la fréquence pour une cavité 3D et est deux fois moins importante dans le cas d'un champ de pression acoustique.

Dans une approche statistique, le champ est une somme de vecteurs aléatoires. Chacun de ces vecteurs correspond à un mode donné en un point considéré. Les excitations de ces modes sont fonction de la position de l'émetteur et du récepteur ainsi que de leur polarisation. Si le nombre d'éléments « significatifs<sup>1</sup> » composant cette somme est suffisamment élevé, les parties réelles et imaginaires du champ, sur une composante cartésienne, pourront être vues comme des variables gaussiennes en vertu du théorème de la limite centrale. Si chaque mode est décomposé comme une somme d'ondes planes, alors le champ est classiquement représenté par une somme infinie d'ondes planes (HILL 1998). Cette représentation en acoustique est bien antérieure puisqu'elle était déjà proposé par Morse et Bolt dans les années 1940 (MORSE et BOLT 1944). Nous verrons un peu plus loin notre proposition, en rupture avec le modèle classique, de considérer un nombre fini d'ondes planes pour décrire le champ.



FIGURE 2.1 – Chambre réverbérante à brassage de modes de CentraleSupélec. Le pale en mouvement modifie les conditions limites et permet de « brasser le champ » au sein de l'enceinte.

En électromagnétisme, on parle de champ gaussien, bien que la quantité concernée soit la partie réelle/imaginaire d'une composante cartésienne du champ. En acoustique en revanche, la grandeur d'intérêt correspond directement au champ de pression qui est une grandeur scalaire ;

1. Nous verrons dans la section II.2 de ce que l'on entend par « significatifs »

dans ce cas le champ de pression peut être effectivement vu comme gaussien. Les acousticiens parlent depuis les années 1950 de régime *diffus* (COOK, WATERHOUSE et al. 1955) ; la communauté CEM parle de régime *surmodé*.

Ainsi le modèle du champ gaussien reste une approximation asymptotique. Dans la pratique, une trentaine de termes suffisent à adopter une approximation gaussienne ; ce nombre peut être vu à la baisse suivant la densité de probabilité des poids d'excitation. Lorsque ce régime est atteint à une fréquence donnée, la gaussianité du champ est, en première approximation<sup>2</sup>, assurée pour toutes les fréquences supérieures à celle-ci. Dans le domaine de l'acoustique cette fréquence est appelée fréquence de Schroëder - elle correspond à une excitation de trois modes dans la bande modale moyenne à  $-3\text{ dB}$  (SCHROEDER et K. KUTTRUFF 1962).

La contribution dans la recherche liée aux CRBM en régime diffus a porté sur l'utilisation d'outils statistiques permettant de vérifier la gaussianité du champ. Plus précisément, nous avons étudié la nécessité d'avoir des échantillons indépendants dans l'utilisation de tests d'adéquation.

Pour situer l'intérêt de cette étude, il convient de rappeler les deux points suivants. Premièrement, dans l'utilisation des CRBM, il est d'usage de rassembler les valeurs du champ (ou d'une de ses composantes) obtenues sur l'ensemble des positions du brasseur. Deuxièmement, il est de coutume de vérifier les performances du brasseur en estimant le niveau de corrélation entre chaque position du brasseur ; plus le niveau de corrélation est bas, plus le brasseur est vu comme performant dans sa capacité à générer des nouvelles topographies de champ. En-deçà d'un certain niveau de corrélation, il est accepté<sup>3</sup> de voir les échantillons comme décorrélés (et donc indépendants dans le cas gaussien). .

Il est souvent stipulé que les tests d'adéquation doivent être utilisés sur la base d'échantillons indépendants. Si cette règle s'avère vraie, cela poserait deux inconvénients quant à leur utilisation. D'une part, nous ne pourrions pas toujours être sûrs que lesdits échantillons sont vraiment indépendants (sachant l'incertitude liée à l'estimateur de corrélation) ; et d'autre part, cela pousserait à décimer les échantillons à disposition, augmentant la barre d'incertitude quant à l'issue du test d'adéquation. Dans le cas d'un test type  $\chi^2$  par exemple, il ne nous était pas intuitif que les échantillons doivent être indépendants sachant que le prérequis est que seules les observations, elles, soient indépendantes. Après quelques recherches, il nous est apparu qu'aucune preuve n'existe quant à la nécessité de satisfaire cette condition dans l'hypothèse nulle d'un test d'adéquation.

En collaboration avec Ramiro Serra de l'Université d'Eindoven (Pays-Bas), nous avons donc étudié (MONSEF, SERRA et al. 2015) l'influence de la corrélation sur l'issue des tests d'adéquation suivants : le  $\chi^2$ , le test de Kolmogorov-Smirnov (KS), le test de Liliefors et le test de d'Anderson-Darling (AD). L'étude a fait ressortir que les tests d'adéquation type Lilliefors, AD et  $\chi^2$  sont insensibles à la corrélation entre échantillons jusqu'à des valeurs de 90% ! Le test KS est quant à lui très sensible à la corrélation. Pour les détails des travaux nous renvoyons à la Ref. (MONSEF, SERRA et al. 2015) donné en annexe. Toutefois, il est remarquable de constater la différence de comportement entre les tests KS et Lilliefors. En effet, le test de Lilliefors est un test KS qui prend en compte la moyenne et la variance de l'échantillon car ce test a été introduit dans le cas où le test d'adéquation s'adresse à un ensemble de données dont la moyenne et l'écart-type ne sont pas connus a priori. Le résultat principal est donné Fig. 2.2.

---

2. la densité modale n'est pas strictement monotone et des zones de déplétion modale peuvent exister comme clairement expliqué dans (COZZA 2012).

3. d'après la norme IEC 61000-4-21 (*Reverberation Chamber Test Methods* 2011) associée à l'utilisation des CRBM

Pour ce faire, on a généré entre 50 et 500 échantillons gaussiens. Un niveau de corrélation  $\rho$  a été considéré entre deux échantillons successifs. On a alors procédé à l'exécution des tests d'hypothèse cités ci-avant (5000 fois pour chaque cas), et ce, avec un ensemble de 50 et 100 échantillons. Le taux de réjection de l'hypothèse nulle (hypothèse que les échantillons sont bien gaussiens) est reporté sur l'axe des ordonnées ; le niveau de corrélation est reporté en abscisse. On observe la particularité du test KS quant à sa sensibilité au niveau de corrélation. Outre le fait que ce résultat est intéressant à étudier, dans le cas d'une statistique connue, le test KS pourrait être détourné de sa fonction principale, et être utilisé comme détecteur de corrélation. Cette éventualité est laissée en perspective.

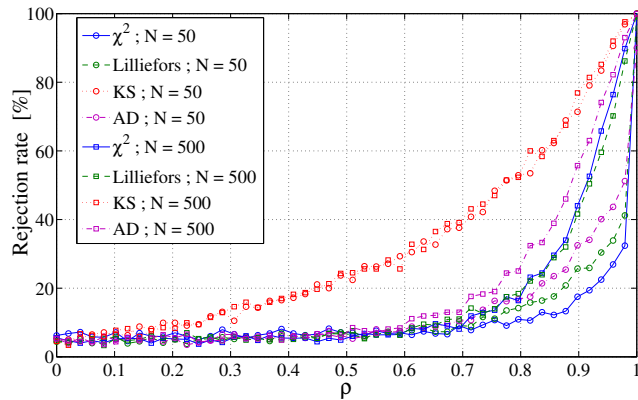


FIGURE 2.2 – Taux de réjection d'hypothèse de gaussianité d'une distribution à  $N$  échantillons corrélés. Le niveau de corrélation (type lag-1) est représenté en abscisse, le taux de réjection est donné par l'axe des ordonnées. Les tests d'hypothèse suivants ont été étudiés : Lilliefors, Anderson-Darling (AD), Kolmogorov-Smirnov (KS) ainsi que le  $\chi^2$ .

## II Régime non surmodé

Le cas du régime surmodé reste une approximation. L'utilisation des chambres s'étend à des régimes où le nombre de modes significatifs n'est pas nécessairement suffisant pour justifier d'une approximation de régime diffus. Un de mes premiers travaux réalisés dans l'hypothèse d'un régime non diffus a porté sur l'étude de la propriété d'ergodicité que l'on retrouve souvent adoptée de manière implicite (en acoustique notamment) sans vraiment de référence permettant de justifier de son domaine de validité. Comme nous le verrons, nos travaux sont basés sur une décomposition du champ de pression en une somme finie d'ondes planes indépendantes. Les autres travaux présentés dans un deuxième temps portant sur l'hypothèse de régime non diffus considèrent quant à eux une décomposition modale.

### II.1 Ergodicité

L'étude des chambres réverbérantes en acoustique est bien antérieure à celles de l'électromagnétisme pour des raisons métrologiques évidentes. Les premières mesures en acoustique ont consisté à relever le temps de réverbération d'une salle ... à l'oreille<sup>4</sup> !

4. Sabine WC. The American Architect 1900

A notre connaissance, les premiers travaux traitant de l'utilisation du brasseur en acoustique remontent aux années 1950 (BALACHANDRAN 1959), mais son utilisation s'est rapidement faite très rare, au profit d'utilisation de chambres réverbérantes de formes chaotiques dans lesquelles l'approche statistique est spatiale, i.e., une statistique basée sur un échantillonnage spatial du champ. On expose Fig. 2.3 l'intérieur d'une chambre réverbérante acoustique, en l'occurrence celle du LNE (Trappes), où l'on peut voir des diffuseurs (plaques gondolés) et des micro suspendus servant à échantillonner le champ de pression. Au centre, une tige rotative munie d'un micro a pour but d'échantillonner de manière dynamique le champ - sachant la taille de la tige, le mouvement rotatif a en fait un effet de brassage sur le champ. En d'autres termes, l'étude de la statistique du champ de pression est spatiale et non sur un ensemble de réalisations (i.e., et non sur un ensemble de positions du brasseur). Il est commun en acoustique de considérer que les statistiques obtenues en prenant un jeu d'échantillons spatiaux et un jeu d'échantillons extraits d'un ensemble de chambres réverbérantes (un échantillon par chambre) convergent : on parle de principe d'ergodicité. Ce principe est bien connu dans l'étude du bruit thermique par exemple où l'on considère que la statistique obtenue via l'ensemble des valeurs d'une mesure unique sur un ensemble de résistances convergera vers la statistique de l'ensemble des valeurs obtenues dans le temps sur une seule résistance. Le but des travaux entrepris a été de fixer un



FIGURE 2.3 – Chambre réverbérante acoustique du LNE (Trappes). Les plaques suspendues sont des diffuseurs servant à casser tout degré de symétrie afin d'assurer une chaoticité du milieu ; les microphones suspendus servent quant à eux à échantillonner le champ. Au centre une tige rotative qui sert à échantillonner le champ ; le mouvement de cette tige a un effet de brassage du champ.

cadre de validité de cette hypothèse. Si dans le domaine des signaux aléatoires cette hypothèse est souvent tacite, c'est entre autre parce que le nombre d'échantillons indépendants dans le temps peut être relativement important ; dans le cas des chambres réverbérantes le nombre d'échantillons spatiaux indépendants étant fini, un impact sur la précision des estimateurs peut être limitant. Pour ce faire, le champ de pression (scalaire) considéré, noté  $p$ , a été exprimé en une somme finie d'ondes planes pour rendre compte de la possibilité de modéliser un régime

## 2 Physique des Chambres Réverbérantes

non surmodé. Celui-ci a été considéré à une pulsation  $\omega$ . A notre connaissance, le lien entre le nombre d'ondes planes et le degré de diffusivité du champ n'a pas été établie à l'heure actuelle. De nombreuses questions autour de ce modèle peuvent être intéressantes à approfondir.

Pour mener l'étude, nous avons cherché à analyser la convergence de l'estimateur de moyenne spatiale vers la moyenne d'ensemble vraie. La grandeur utile dans l'étude est l'erreur relative, notée  $\epsilon$ , et définie telle que (MONSEF et COZZA 2011),

$$\epsilon = \frac{\hat{\mu}_{p_\omega^2} - \mu_{p_\omega^2}}{\mu_{p_\omega^2}}, \quad (2.1)$$

où  $\hat{\mu}_{p_\omega^2}$  est la moyenne spatiale estimée et  $\mu_{p_\omega^2}$  la moyenne d'ensemble vraie. Afin d'évaluer la précision de l'estimateur spatial, les deux premiers moments de l'erreur ont été dérivés.

Il apparaît que l'estimateur est non biaisé, i.e., la moyenne de l'erreur est nulle. Sa variance en revanche a l'expression suivante (MONSEF et COZZA 2011),

$$\sigma_\epsilon^2 = \left[ \frac{N-1}{N} G_\Omega(\mathbf{a}) + \frac{1}{N} \right] (\nu_4 - \nu_2^2), \quad (2.2)$$

où  $\nu_n$  est l'espérance d'ordre  $n$  des poids des ondes planes,  $G_\Omega(\mathbf{a})$  une intégrale faisant intervenir le lieu géométrique  $\mathbf{a}$  inscrit dans un domaine  $\Omega$  sur lequel les échantillons spatiaux sont considérés et  $N$  correspond au nombre d'ondes planes composant le champ de pression. La densité de probabilité des poids des ondes planes est souvent considérée comme suivant une loi normale. Deux cas sont dès lors intéressants à considérer.

Le premier cas est celui du régime diffus pour lequel  $N \mapsto \infty$ . La variance suit alors l'évolution de  $G_\Omega(\mathbf{a})$ . Il est alors intéressant de constater que suivant la dimensionnalité du domaine d'échantillonnage (1D, 2D ou 3D), la vitesse de convergence de l'estimateur différera dans des rapports qui ne suivent pas le rapport des dimensionnalités, et ce, en raison de la corrélation spatiale. Pour des échantillons régulièrement espacés, on obtient les décroissances suivantes :

$$G_\Omega(\mathbf{a}) \simeq \begin{cases} 0.5/(a/\lambda) \text{ dans le cas 1D} \\ 0.2133/(a/\lambda)^{1.8} \text{ dans le cas 2D} \\ 0.0740(a/\lambda)^{-2} \text{ dans le cas 3D} \end{cases} \quad (2.3)$$

où  $\lambda$  correspond à la longueur d'onde.

Le deuxième cas est celui d'un régime non diffus pour lequel on aurait un échantillonnage tel que  $G_\Omega(\mathbf{a}) \ll 1/N$ . On constate alors que la variance de l'estimateur spatial présenterait une borne basse en  $1/N$  liée au degré de mélange du milieu. Ce résultat met en évidence que même si le nombre d'échantillons spatiaux étaient infinis et indépendants, une incertitude plafond existerait au niveau de l'estimateur. On constate que la précision de l'estimateur est conditionnée par le nombre d'ondes planes. Ce résultat est purement théorique et nécessiterait de pouvoir être validé en pratique. La distinction entre les deux termes de la variance de l'estimateur ne s'annonce pas aisée expérimentalement. De plus, pour ce faire, il serait utile d'éclaircir le sens de  $N$ . Or le nombre  $N$  d'ondes planes n'est en réalité pas facile à évaluer à l'heure actuelle et il sera intéressant de voir s'il peut être relié au nombre de degré de liberté du champ. Cette notion de degré de liberté a été étudiée uniquement dans le cadre d'une approche modale (cf. Sec. II.2). Pour un détail des résultats on renvoie à l'article joint en annexe.

Intuitivement le concept d'ergodicité nécessite un niveau de complexité suffisant. Si cette condition est nécessaire, elle n'est pas suffisante. On voit en effet clairement apparaître dans (2.2) le rôle de la corrélation spatiale comme facteur limitant.

## II.2 Approche modale

Dans le domaine de la CEM, la description du champ EM dans une CRBM par une approche modale a été proposée dans un rapport de Lehman (1993) (LEHMAN May 1993). La formalisation du rôle du recouvrement modal et son importance dans la statistique du champ au sein d'une CRBM n'a été publiée qu'en 2011 par Andrea Cozza (COZZA 2011). Pour une meilleure compréhension des explications qui suivront, le champ électrique est exprimée de la manière suivante (COZZA 2011),

$$\mathbf{E}(\mathbf{r}, f) = \sum_{i=1}^{\infty} \alpha_i \psi_i(f) \mathbf{e}_i(\mathbf{r}), \quad (2.4)$$

où  $\mathbf{e}_i$  est le vecteur propre du  $i$ ème mode qui n'a aucune forme spécifique supposée ;  $\alpha_i$  est le poids modal, i.e., la constante de couplage entre le  $i$ ème mode propre et la source tel que :  $\alpha_i = \langle \mathbf{J}_s(\mathbf{r}), \mathbf{e}_i(\mathbf{r}) \rangle_{\Omega_s}$ , où  $\langle \cdot \rangle_{\Omega_s}$  correspond au produit scalaire appliqué au domaine ( $\Omega_s$ ) de la source. Ainsi, si la polarisation de la source, i.e., la polarisation du vecteur  $\mathbf{J}_s$ , est normale au vecteur  $\mathbf{e}_i(\mathbf{r})$ , le mode ne pourra être excité. La fonction  $\psi_i$  est la réponse en fréquence du  $i$ ème mode. Dans le cadre de milieu à « faibles pertes » cette fonction est approximée à une Lorentzienne.

L'analyse se limitant en un point  $\mathbf{r}$ , la factorisation modale des modes peut être introduites, telle que,

$$\mathbf{e}_i(\mathbf{r}) = e_i(\mathbf{r}) \hat{\xi}_i(\mathbf{r}), \quad (2.5)$$

où  $\hat{\xi}_i(\mathbf{r})$  est un vecteur de polarisation supposé uniformément réparti sur  $4\pi$  stéradians.

Nous ré-exprimons alors le champ tel que

$$\mathbf{E}(\mathbf{r}, f) = \sum_{i=1}^{\infty} \tilde{\gamma}_i \psi_i(f) \hat{\xi}_i(\mathbf{r}), \quad (2.6)$$

où les grandeurs complexes  $\tilde{\gamma}_i$  sont considérés comme des poids modaux équivalents, dont la partie réelle et imaginaire suivent respectivement une loi normale. Cette hypothèse n'a aucune justification physique et constitue une étude intéressante en soi. En acoustique, les modèles classiques ne fusionnent pas les poids modaux ; les poids modaux côté source et côté récepteur sont considérés comme Gaussiens et indépendants (sous réserve que la source et le récepteur sont suffisamment loin l'un de l'autre). La justification d'une loi normale est donnée par (MCDONALD et KAUFMAN 1988). En électromagnétisme, la grosse différence tient au produit scalaire entre la source et les modes propres. Comme nous allons le voir, le recouvrement entre modes est un des aspects les plus importants dans la statistique du champ ; nous expliciterons la grandeur utilisée pour quantifier ce que l'on entend par « statistique du champ ».

### Recouvrement modal

Une illustration du recouvrement entre modes (ou recouvrement modal) présent dans (2.6) est donné Fig. 2.4. Du fait des réponses de type Lorentzienne, on y constate que le nombre de modes qui se recouvrent est en toute rigueur infini!! Ainsi le degré de surmodage ou de diffusivité du champ dans une chambre nécessite intuitivement de définir une bande arbitraire, notée ici  $B_e$  sur la Fig. 2.4. Cette bande est centrée sur la fréquence de travail à laquelle la chambre est excitée.

En acoustique des salles, l'effet du recouvrement modal a été approfondi par Schroeder (SCHROEDER et K. KUTTRUFF 1962) qui considérait comme bande  $B_e$  la bande à  $-3\text{ dB}$

## 2 Physique des Chambres Réverbérantes

de la réponse d'un mode. En toute rigueur, chaque mode a des pertes différentes car celles-ci découlent directement de la topographie et de la polarisation (dans le cas EM). Toutefois, dans une approche statistique, les modes ne sont, par définition, pas explicités de manière déterministe ; on en est alors réduit à considérer des pertes moyennes identiques pour des modes « proches ». En électromagnétisme, on quantifie habituellement les pertes par le coefficient de qualité. Celui-ci est alors le facteur de qualité dit *composite* de la chambre ; en acoustique il est plutôt d'usage de considérer un coefficient d'amortissement (H. KUTTRUFF 2009) dont l'inverse donne (à un facteur près) une image du temps de réverbération.

La représentation donnée Fig. 2.4 pose alors la question de savoir jusqu'à quel  $n$ -ième mode il est nécessaire d'aller pour approcher la statistique du champ observée en pratique. Dit autrement, on s'est intéressé au nombre de bande modale  $B_M$  à inclure dans  $B_e$ . Cette question est traitée en détail dans (MONSEF 2012) jointe en annexe.

On y montre que la réponse n'est pas directe et que la bande  $B_e$  à considérer est fonction de la densité modale. Ainsi, à faible recouvrement modal, la bande  $B_e$  doit approcher presque 20 fois la bande modale ; ce facteur décroît avec l'augmentation de la densité modale. La justification à ce résultat est que plus le recouvrement modal est faible plus chaque mode aura une influence sur la statistique et il faudra donc aller chercher « loin » chaque mode pouvant avoir une contribution. A contrario, quand la densité modale augmente, le nombre de modes fixant la statistique est d'autant plus vite atteint et permet alors d'avoir un  $B_e$  plus étroit.

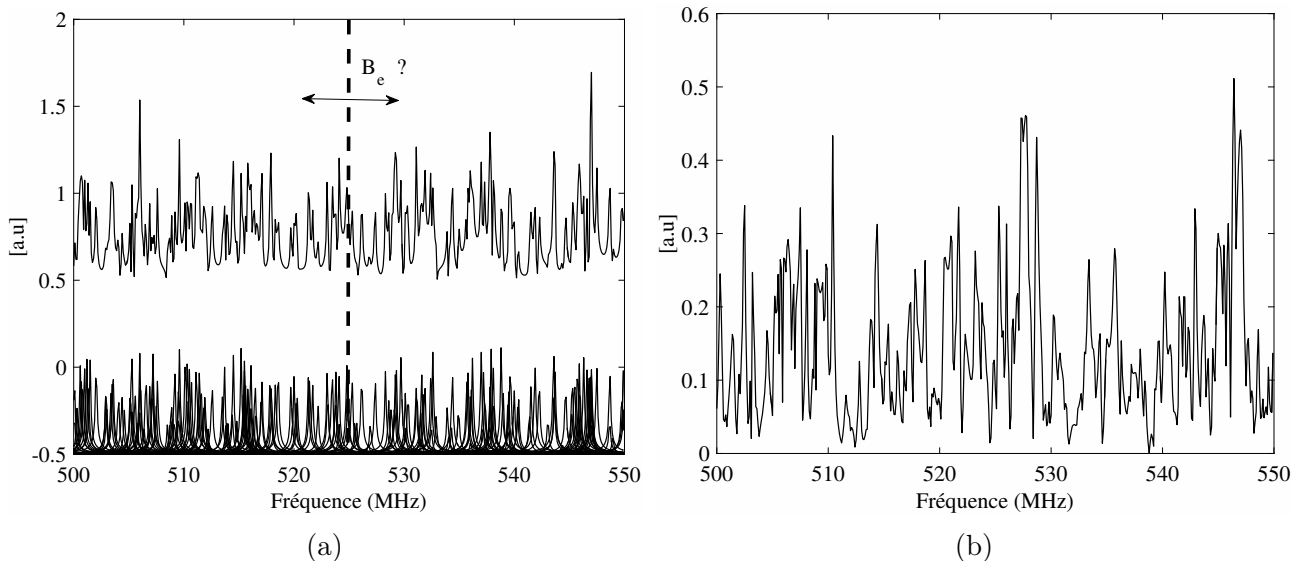


FIGURE 2.4 – (a) Illustration du recouvrement modal (bas à gauche) où chaque mode est présenté. Réponse spectrale résultante (gauche haut). (b) Réponse expérimentale montrant la complexité effective de la superposition modale.  $B_e$  est la bande effective à considérer incluant le nombre utile de modes.

### Variabilité de la puissance et statistique du champ

Il est question depuis le début de ce manuscrit de statistique du champ. Il convient de préciser ce que l'on entend par là. Dans le domaine de la CEM et de l'acoustique, la grandeur d'intérêt est le carré de la valeur efficace du champ ; en EM, il peut s'agir d'une composante cartésienne du champ. Pour ce dernier cas, la grandeur d'intérêt correspondrait à une image de la puissance

reçue par une (petite) antenne linéairement polarisée. Dans une chambre réverbérante, pour des mesures de puissance rayonnée ou de puissance absorbée, un des objectifs est d'avoir une variabilité la plus réduite possible concernant les grandeurs précitées ci-dessus. On se réfère à la variabilité spatiale (sur un tour de brasseur si brasseur il y a) afin de ne pas à avoir à se préoccuper de l'emplacement de l'objet sous test ; en d'autres termes, que la mesure puisse être indépendante de la position des objets considérés. On s'intéresse alors à la variabilité de la « puissance ». Ce choix est orienté par les normes de standardisation pour les mesures de puissance rayonnée. On pourrait s'intéresser à la variabilité de la densité d'énergie électrique (ou magnétique) comme dans (COZZA 2011). La notion de « statistique du champ » est donc un abus de langage, notamment en électromagnétisme, la grandeur étant vectorielle. La grandeur considérée est néanmoins intéressante à expliciter puisqu'en régime diffus par exemple, la variabilité de la densité d'énergie est trois fois inférieure à celle de la puissance !

Formellement, si  $P_r$  est la puissance reçue, la variabilité, notée  $\zeta_P^2$  sera définie telle que,

$$\zeta_P^2 = \frac{\mathbb{E}[P_r^2]}{\mathbb{E}^2[P_r]} - 1, \quad (2.7)$$

où  $\mathbb{E}[\cdot]$  désigne l'opérateur de moyenne d'ensemble.

On montre que  $\zeta_P^2$  est telle que (MONSEF et COZZA 2014),

$$\zeta_P^2 = 1 + \frac{8}{5\pi M_M}. \quad (2.8)$$

Ces travaux ont permis d'apporter des résultats à intérêt métrologique car ceux-ci précisent les intervalles de confiance à considérer lorsqu'une mesure est effectuée en CRBM. On montre Fig. 2.5 l'évolution des intervalles de confiance des variabilités estimées  $\zeta_P^2$  en fonction du nombre  $M_M$  de modes recouverts dans une bande modale  $B_M$  à -3 dB.

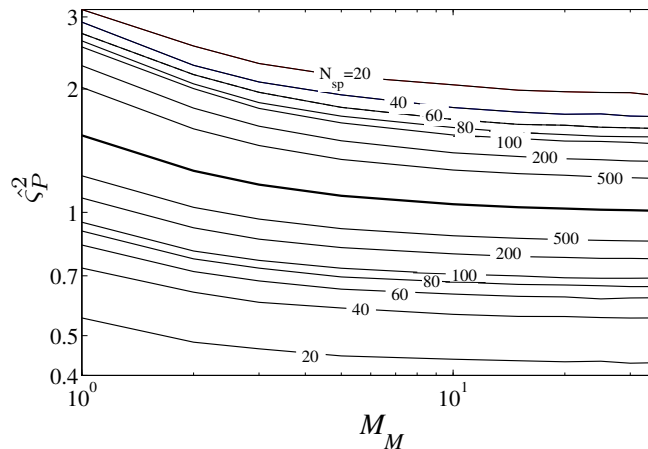


FIGURE 2.5 – Valeur moyenne (trait gras) et limites des intervalles de confiance de  $\zeta_P^2$  fonction du nombre moyen  $M_M$  de modes recouverts pour différentes valeurs de  $N_{sp}$  positions indépendantes de brasseur (reportées sur le graphe). Les limites supérieures et inférieures de l'intervalle de confiance sont au-dessus et en-dessous du trait gras respectivement.

De la même manière, pour une densité d'énergie  $W$ , nous aurions une variabilité, notée  $\zeta_W^2$ , telle que (MONSEF, COZZA, MONSEF et al. 2014),

$$\zeta_W^2 = \frac{1}{3} + \frac{2}{3\pi M_M}. \quad (2.9)$$

## 2 Physique des Chambres Réverbérantes

Le cas de l'acoustique a été également abordé en collaboration avec le Laboratoire National d'Essais. On a montré que la variabilité du carré de la valeur efficace du champ de pression  $p$  est tel que (MONSEF, COZZA, RODRIGUES et al. 2014) :

$$\varsigma_{p^2}^2 = 1 + \frac{K^2 - 2}{\pi M_M}, \quad (2.10)$$

où  $K$  est le kurtosis des poids modaux;  $K = 3$  si les poids modaux sont considérés comme gaussiens.

Ces résultats ont été dérivés sur la base d'une hypothèse d'indépendance entre fréquences propres. Cette hypothèse est importante à souligner car les statistiques d'espacement entre fréquences propres adjacentes a été un domaine de recherche important, notamment depuis l'émergence de la théorie des matrices aléatoires (MEHTA 2004).

### Espacement moyen entre fréquences propres

Pour les cavités non chaotiques (ou intégrables), présentant des symétries, la densité de probabilité de l'espacement entre fréquences propres correspond à une loi de Poisson (LYON 1969) dont l'expression est,

$$p(x) = \exp(-x) \quad (2.11)$$

et dont la représentation est rappelée Fig. 2.6 (traits en tirets). En revanche, quand la cavité est chaotique, la densité de probabilité correspond à une loi de Wigner<sup>5</sup> dont l'expression est la suivante,

$$p(x) = \frac{\pi x}{2} \exp\left(-\frac{\pi x^2}{4}\right) \quad (2.12)$$

et dont la loi est représentée Fig. 2.6 (trait gras plein).

La différence majeure réside dans l'espacement moyen des modes adjacents. La densité de Poisson met en évidence que dans les cavités non chaotiques la dégénérescence des fréquences propres est très probable, i.e., des fréquences propres peuvent être confondues. Dans le cas de la distribution de Wigner en revanche, on constate que la dégénérescence ne peut avoir lieu. La pente à l'origine témoigne de ce que l'on appelle l'effet de *répulsion* entre fréquences propres. Cette propriété permet une meilleure distribution (spectrale) des réponses en fréquence et réduit les risques de forte déplétion modale (COZZA 2012). C'est la raison pour laquelle les acousticiens ont opté pour des chambres réverbérantes à forme chaotique. En CEM, bien que les chambres réverbérantes soient, vue de l'extérieur, comme parallépipédiques, l'insertion du brasseur, d'une antenne et d'un objet sous test permet de rompre les symétries et d'avoir un degré de chaoticité au sein de la chambre.

Le travail le plus complet à notre connaissance sur l'effet des distributions de l'espacement moyen entre fréquences propres sur la variabilité est celui de Lyon (1969) en acoustique (LYON 1969). Ce travail est digne d'être une référence y compris pour la communauté des CRBM en CEM. L'auteur avait connaissance de la loi de Wigner mais a opté pour la loi dite *des plus proches voisins* (*Nearest Neighbour (NN)* en anglais) dont l'expression est la suivante,

$$p(x) = 2\pi \cdot x \exp(-x\sqrt{2\pi}) \quad (2.13)$$

---

5. qui correspond à une loi de Rayleigh de paramètre  $2/\pi$

et dont une représentation est donnée Fig. 2.6 (trait plein fin). Lyon utilise des résultats publiés douze ans avant en physique nucléaire. Ces résultats, proposés par *Guverich et Pevsner* (GUREVICH et PEVSNER 1957) proposaient un modèle de statistique mettant en évidence l'effet de répulsion. Lyon cherchait à voir l'effet de la répulsion sur la statistique du champ en chambre réverbérante. Il a donc utilisé cette densité de probabilité ; en utilisant (2.13), on peut parvenir à une expression littérale de la variabilité ; ce qui n'est pas possible avec la loi de Wigner donnée en (2.12).

Bien que la répulsion soit surestimée, l'auteur a su, de manière intéressante, analyser l'effet de cet effet sur les variabilités. Il a montré que la répulsion du modèle *NN* avait un impact (3dB) sur la variabilité par rapport au cas de Poisson à fort recouvrement modal ; en revanche, l'effet de la répulsion est négligeable à faible recouvrement modal [p.560 Ref. (LYON 1969)]. Le modèle de Wigner étant reconnu comme décrivant le plus correctement les systèmes chao-

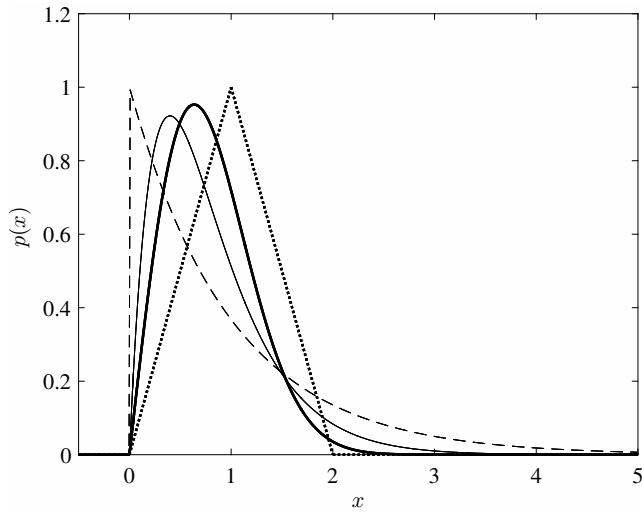


FIGURE 2.6 – Densité de probabilité de Wigner (trait gras plein), de Poisson (tirets), des plus proches voisins (*NN*) (trait plein fin) et triangulaire (traits en pointillés).

tiques de l'Ensemble Orthogonal Gaussien (système à réversibilité temporelle), une publication (R. WEAVER 1989) de Richard Weaver a eu pour but de combler ce manque. Une analyse détaillée (MONSEF, COZZA, RODRIGUES et al. 2014) de ses travaux nous a amené à remettre en question les résultats proposés, considérant que l'approximation utilisée était trop grossière. Comme expliqué dans la section II de l'article joint en annexe, le modèle proposé revient à un modèle de Poisson avec absence de dégénérescence. Nous avons proposé un modèle où les fréquences propres sont considérées comme indépendantes, uniformément réparties dans des *slots* de largeur  $1/m$  ( $f_w$ ) où  $m$  ( $f_w$ ) est la densité modale à la fréquence  $f_w$ . Celà revient à considérer une densité de probabilité triangulaire pour l'espacement moyen entre fréquences propres (cf Fig. 2.6 (traits pointillés)). L'intérêt est d'avoir l'effet de répulsion proche de celle de Wigner (pente à l'origine) avec un modèle simple. Pour le calcul des variabilités associées, nous utilisons un principe d'équivalence entre moyenne d'ensemble et moyenne fréquentielle. Pour le détail de la dérivation nous renvoyons respectivement aux références (MONSEF, COZZA, MONSEF et al. 2014) et (MONSEF, COZZA, RODRIGUES et al. 2014) joints en annexe pour l'électromagnétisme et l'acoustique. Il est à noter que le domaine de validité de cette équivalence repose l'hypothèse classique de pertes identiques pour l'ensemble des modes excités à une fréquence donnée.

Il est à noter que notre remise en cause des travaux de Weaver a remis également en cause un article d'un autre auteur J.L-Davy (J. DAVY 1981). Notre publication nous a valu les foudres

## 2 Physique des Chambres Réverbérantes

de ces deux auteurs dans un commentaire publié en 2015 (J. L. DAVY et R. L. WEAVER 2015).

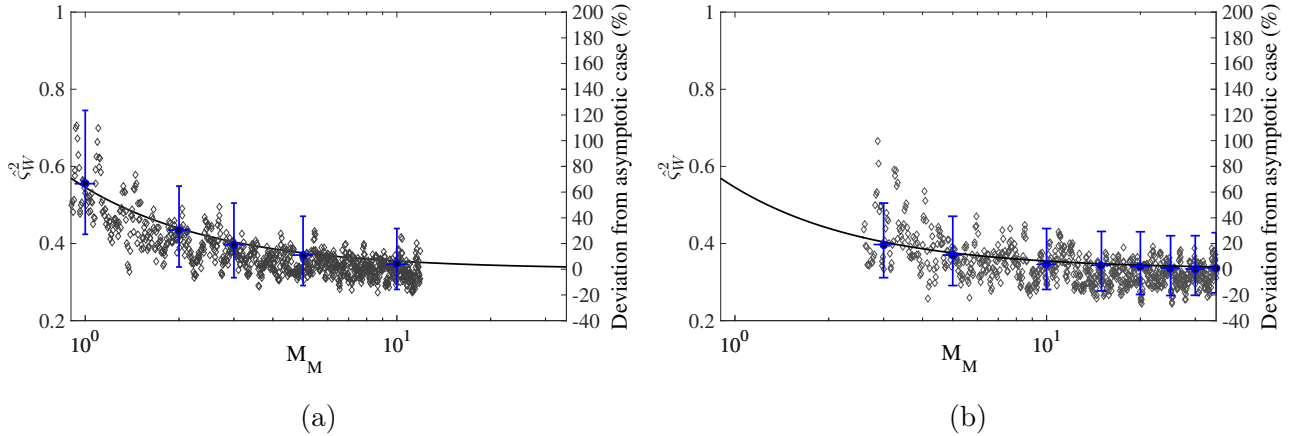


FIGURE 2.7 – Variabilité estimée  $\hat{\zeta}_W^2$  (axe y gauche) de la densité d'énergie électrique, fonction du nombre  $M_M$  de modes dans le cas où la chambre est vide (a) et chargée (b). Les déviations relatives à la valeur asymptotique de  $1/3$  sont reportées (axe des ordonnées de droite). Les résultats expérimentaux (symboles gris), ceux de simulation MC (points noirs) et les résultats analytiques sont reportés (trait plein). Les barres d'incertitude verticales traduisent un intervalle de confiance de 95% et les barres horizontales rendent compte de la dispersion que le paramètre  $M_M$  autour de sa valeur moyenne.

### Variabilités du champ

La validation de l'approche a été basée sur une comparaison avec des résultats expérimentaux. Pour le cas électromagnétique, la CRBM de  $13 \text{ m}^3$  (CentraleSupélec) a été utilisée dans deux scénarios : vide et chargée de mousse absorbante. Le deuxième scénario vise à insérer des pertes modifiant ainsi le recouvrement modal. Les résultats expérimentaux (symboles) sont reportés Fig. 2.7. On observe un bon accord avec le résultat analytique rappelé en (2.9). Le modèle modal a également été simulé par simulation Monte Carlo (MC). Le but étant d'une part, de vérifier la consistence des résultats, et d'autre part, de pouvoir évaluer les intervalles de confiance. On constate que ces derniers sont également en bon accord avec les résultats expérimentaux.

Une approche analogue a été entreprise avec une chambre réverbérante acoustique vide et chargée de quelques absorbants. Pour ce faire, nous avons ouvert une collaboration avec le Laboratoire National d'Essais (LNE) basé à Trappes. Les temps de réverbération, classiquement notés  $T_{60}$ , ont été évalués par bandes de tiers d'octave et les résultats sont reportés Fig. 2.8a dans les cas respectifs d'une chambre vide (cercles) et d'une chambre chargée (carrés).

En utilisant l'approximation de la densité modale donnée par la formule de Weyl, nous avons pu estimer le nombre  $M_M$  de modes qui se recouvrent dans une bande modale ; les résultats sont reportés Fig. 2.8b dans les cas respectifs d'une chambre vide (cercles) et chargée (carrés). On y remarque que l'effet des pertes est particulièrement observable à basse fréquence. Comme expliqué précédemment, il est d'usage en acoustique de procéder à un échantillonnage spatial pour estimer la variabilité de la valeur efficace du champ de pression. Toutefois, la méthode d'échantillonnage spatial dans la chambre réverbérante consiste à faire tournoyer un microphone

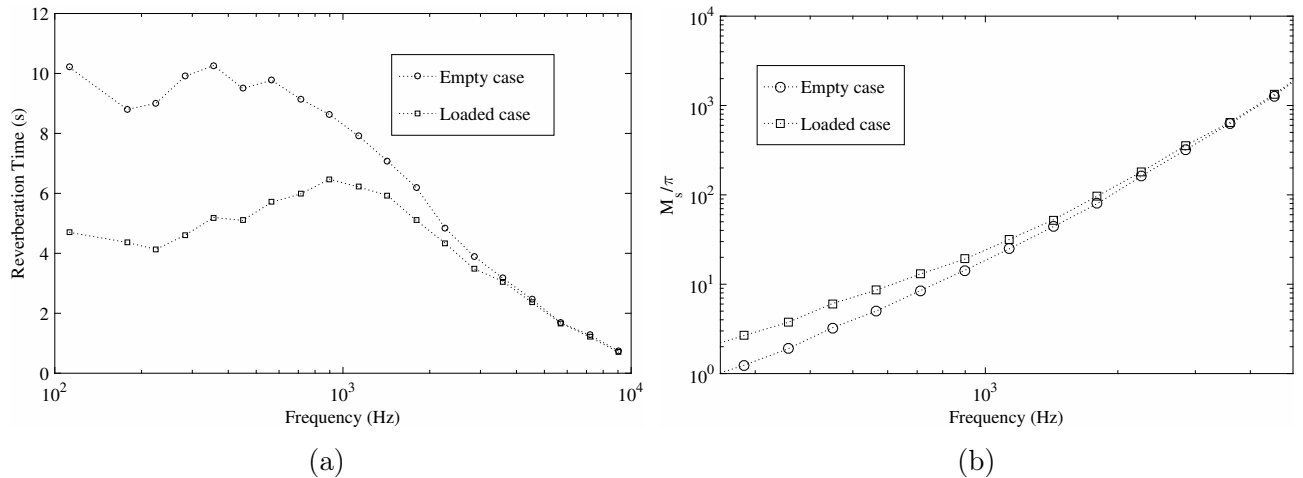


FIGURE 2.8 – (a) Temps de réverbération estimés lorsque la chambre est vide (cercles) et chargée (carrés) (gauche). (b) Estimation du nombre de modes recouverts dans une bande modale dans les cas respectifs où la chambre réverbérante est vide (cercles) et chargée (carrés) (droite).

FIGURE 2.9

au bout d'une perche de 1,5 m de long et de diamètre proche du centimètre. Après analyse, cette technique est en fait perturbative au sens d'un brasseur. Pour cette raison nous avons estimer la statistique en utilisant des points fixes dans la chambre. La dispersion a alors été réduite en utilisant un moyennage fréquentiel<sup>6</sup>.

### Nombre effectif de modes

Les recherches se sont poursuivies autour de la compréhension et de l'élaboration de modèles statistiques du champ pour en estimer la variabilité. Ces travaux ont été motivés par le constat suivant. En toute rigueur, quelque soit la fréquence de travail, le nombre de modes excités est mathématiquement infini et rien ne permet de définir clairement la notion de « modes significatifs » sans introduire une bande de fréquence arbitraire ! Le problème est que, suivant la bande choisie, la *significativité* d'un mode change !

Nous avons donc cherché à définir un modèle dans lequel nous n'aurions pas à relier ce que l'on entend par « mode significatif » au choix arbitraire d'une bande donnée. Pour ce faire, nous avons tout simplement créé un modèle dans lequel nous ne subissons pas les queues des Lorentziennes qui mènent à un recouvrement modal rigoureusement infini.

Le critère choisi est donc de créer un modèle équivalent dans lequel la réponse en fréquence des modes est une porte en fréquence. Pour que le modèle soit équivalent au modèle physique, il doit mener à une variabilité identique à celles présentées dans les parties précédentes. De la satisfaction de ce critère découle la largeur de bande  $\pi \cdot B_M$  à assurer pour les réponses « portes ». Nous avons donc à considérer un scénario où le recouvrement modal est comme montré Fig. 2.11. Cette bande est appelée *bande statistique*.

6. La plus large bande modale a été estimée autour de 0.5 Hz sur une bande [250 Hz : 1 kHz]. Une décimation par pas de 2 Hz a alors été appliquée.

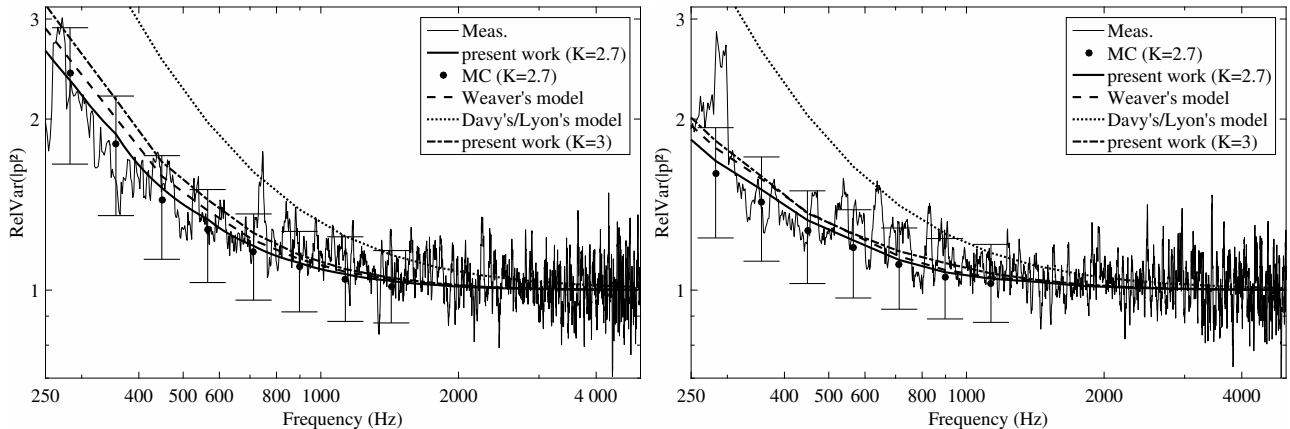


FIGURE 2.10 – Variabilités de la valeur quadratique du champ de pression obtenues expérimentalement (trait fin), analytiquement via la relation (2.10) pour  $K = 2.7$  et  $K = 3$  (trait plein gras et trait en tirets-pointillés respectivement). Les résultats par simulation MC (points noirs) y sont reportés avec les barres d'incertitude associées pour le cas d'une chambre vide (figure gauche) et d'une chambre chargée (figure de droite). Le modèle de Weaver (trait en tirets) y est reporté ainsi que le modèle de Davy/Lyon (traits pointillés) qui suppose pour ce dernier un espacement entre fréquences propres régi par une loi de Poisson.

Il en découle alors que le nombre significatifs de modes est  $\pi$  fois le nombre recouverts dans une bande modale. Une question émerge alors quant à la signification de ces modes.

Si chaque mode en un point de l'espace est une variable aléatoire, exprimer le champ<sup>7</sup> comme une somme de modes revient, d'un point de vue statistique, à considérer une somme de variables aléatoires ... pondérées par la réponse en fréquence des modes. Via le modèle équivalent, il apparaît que la pondération est du tout ou rien. Ce modèle équivalent revient donc à voir le champ comme une somme de variables aléatoires (VA) indépendantes et identiquement distribuées (iid). Le nombre  $\pi M_M$  de modes fictifs n'est autre que le nombre de VA iid ; en d'autres termes, et par analogie avec une distribution de type  $\chi^2$ ,  $\pi M_M$  est le nombre de degré de liberté du champ intervenant dans la variabilité de ce dernier au sein de la chambre réverbérante.

### Approche statistique : critère minimum de pertinence de l'approche

Comme nous l'avons vu, l'approche statistique est assez commode dans les environnements complexes tels que les chambres réverbérantes. L'utilisation idéale d'une chambre est en régime diffus ou surmodé sachant que ce régime permet une dispersion minimale quant aux performances moyennes attendues.

Dans les normes existantes, il est néanmoins possible et prévu d'utiliser les chambres dans des régimes non diffus. Dans ces cas là, de plus grandes barres d'incertitude sont attendues. Une question est alors de savoir jusqu'à quelle fréquence minimale est-on susceptible d'utiliser une chambre. La fréquence est alors connue sous l'acronyme de LUF pour *Lowest Useable Frequency* (Fréquence d'utilisation Minimale). La définition actuelle de la LUF n'est pas basée sur un critère en lien avec la physique de la chambre.

Sans rentrer dans le débat de la définition de la LUF, le concept de degré de liberté, introduit plus haut, nous permet de proposer une borne basse et un critère pour lesquelles l'approche

7. en fait la puissance, la densité d'énergie ou le carré de la valeur *rms* du champ de pression ;-)

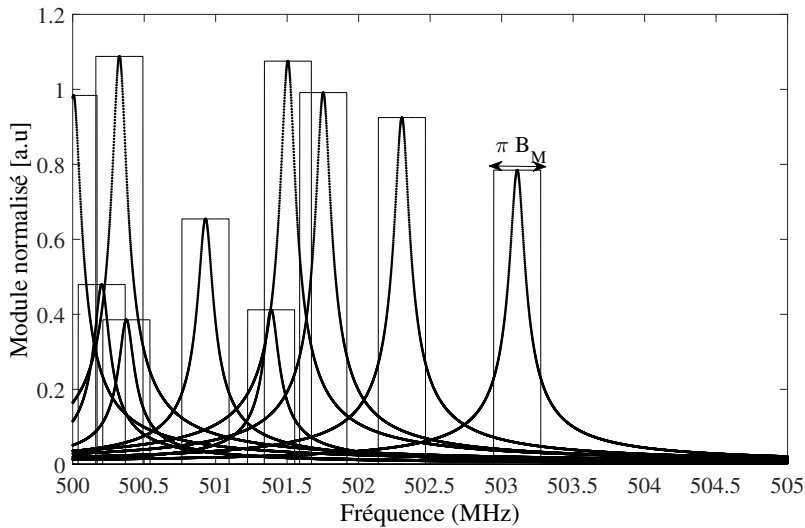


FIGURE 2.11 – Illustration du recouvrement modal dans le cas où les réponses en fréquences sont des Lorentziennes (traits gras) et dans le cas où les réponses en fréquence sont des portes en fréquence (traits fins). Si la bande modale à -3dB est notée  $B_M$ , on montre que une bande  $\pi B_M$  des fonction portes mène à une variabilité identique .

statistique peut faire sens. Comme présenté dans (MONSEF et COZZA 2015a) donné en annexe, le critère qui nous a paru le plus intuitif est d'avoir un seul degré de liberté au minimum, et ce, afin de pouvoir considérer au moins un terme dans la décomposition modale liée au modèle équivalent introduit plus haut. L'avantage de cette borne est son adaptation au degré de pertes présent dans la chambre. Ainsi, dans le cas d'une chambre avec un objet à faible perte, ou au contraire, une chambre chargée par un objet dissipatif, la fréquence associée à un degré unique de liberté différera. Un pire cas pourra être associé au cas d'une chambre vide. Le lien avec la LUU dépendra des barres d'incertitude acceptée pour la variabilité. Ceci n'est pas explicité dans les normes actuelles (*Reverberation Chamber Test Methods* 2011). Dans le contexte des chambres, on rappelle que c'est la statistique du champ maximum qui intéresse la communauté de la CEM ; l'étude du maximum du champ avec une approche modale n'est pas aisée et n'a pas été développée à notre connaissance. En revanche, un des aspects intéressant la communauté est de pouvoir proposer un modèle qui puisse décrire le cas d'une chambre réverbérante du cas sous-modé jusqu'au régime asymptotique.

### III Du Régime sous-modé au régime sur-modé

Une des questions pendantes est de pouvoir proposer un modèle statistique d'une des grandeurs d'intérêt et de le relier à la physique de la chambre ; la contrainte étant de pouvoir décrire n'importe quel régime de fonctionnement avec un tel modèle. Une approche statistique basé sur la distribution de Weibull, sans lien avec la physique de la chambre, a été proposé par Bunting (BUNTING 2002) ; le but étant de pouvoir utiliser une loi de distribution de la puissance mesurée par une antenne pour n'importe quel régime de fonctionnement de la chambre. Cette distribution, notée ici  $f_X(x)$ , a l'expression suivante,

$$f_X(x) = abx^{b-1} \exp(-ax^b), \quad (2.14)$$

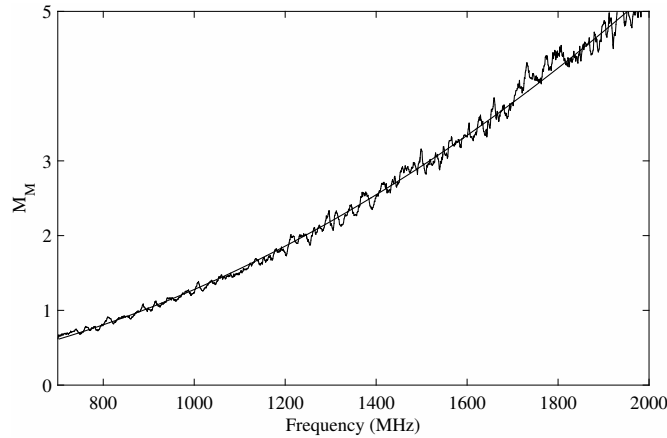


FIGURE 2.12 – Estimation du nombre  $M_M$  de modes se recouvrant dans une bande modale en fonction de la fréquence pour une chambre réverbérante vide de  $13m^3$ ; le modèle de Weyl y est reporté également (trait plein)

où  $a$  et  $b$  sont respectivement les paramètres d'échelle et de forme de la distribution. Dans le cas d'un régime surmodé, le champ étant Gaussien, la puissance suit une loi exponentielle, i.e.,  $a = b = 1$ .

Comme on l'a vu précédemment, un des paramètres physiques, pour ne pas dire le seul, mesurant le degré de « surmodage » de la chambre est le nombre de modes significatifs découlant du recouvrement modal; sans perte de généralité, le nombre  $M_M$  de modes se recouvrant dans la bande modale moyenne peut également être considérée sachant un facteur  $\pi$  constant entre les deux grandeurs. Notre proposition a donc été de relier l'approche modale à la distribution de Weibull afin d'exprimer son paramètre de forme en fonction du nombre  $M_M$  de modes.

L'approche proposée a consisté en une identification des variabilités obtenues par le modèle de Weibull et l'approche modale. Comme montré dans (MONSEF et COZZA 2015b), cela revient à étudier l'égalité suivante,

$$\frac{\text{Var}[P]}{\text{E}^2[P]} = 1 + \frac{8}{5\pi M_M} = \frac{\Gamma(1 + \frac{2}{b})}{\Gamma^2(1 + \frac{1}{b})} - 1, \quad (2.15)$$

où  $\Gamma(\cdot)$  est la fonction d'Euler.

Comme on peut le constater, une expression reliant le paramètre de forme  $b$  au nombre  $M_M$  de modes ne peut être explicitée. Par résolution numérique, on obtient l'évolution donnée Fig. 2.13; on propose dans la figure une courbe de tendance reliant le paramètre statistique au paramètre physique.

Pour valider cette relation, on a procédé à des estimations du paramètre  $b$  par le biais de relevés expérimentaux. Ces mesures ont consisté à faire des mesures sur une bande [700 MHz : 3 GHz] avec 1000 points en fréquence pour chaque composante cartésienne du champ; l'opération a été effectuée pour 100 positions de brasseur. On a alors regroupé les échantillons par 5 dans l'espace des fréquences. L'estimation a ainsi été effectuée sur la base de 1500 échantillons pour les 200 fréquences considérées.

Par l'estimation de la variabilité, on a pu remonter au nombre  $M_M$  de modes qui se recouvrent dans une bande modale. On reporte les résultats Fig. 2.12. On peut constater que la chambre est sous-modée au sens de Schroëder pour des fréquences inférieures à 1.5 GHz approximativement. On a établi une courbe de tendance (trait plein) afin de pouvoir établir dans un second temps une comparaison avec les valeurs estimées de  $b$ .

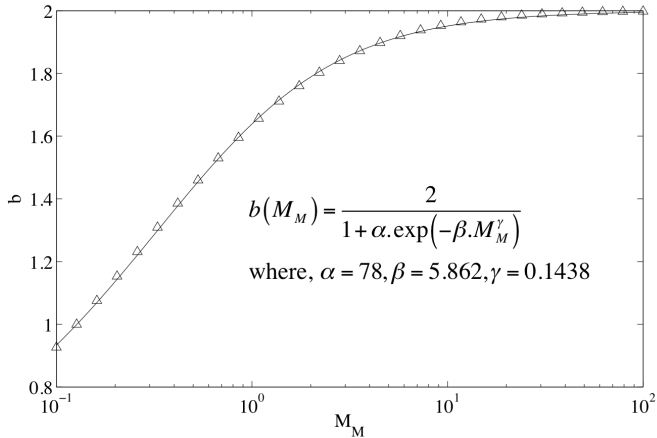


FIGURE 2.13 – Evolution du paramètre de forme  $b$  de la distribution de Weibull en fonction du nombre  $M_M$  de modes se recouvrant. On propose également une expression de la courbe de tendance afin d'avoir une relation explicite entre les deux paramètres.

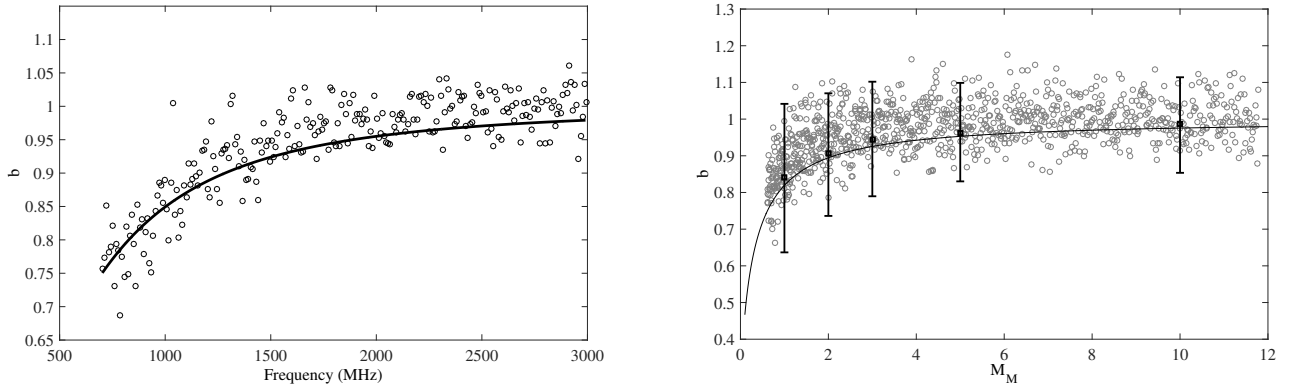


FIGURE 2.14 – Evolution du paramètre de forme  $b$  estimé en fonction de la fréquence (gauche) et du nombre  $M_M$  (droite). L'estimation s'est faite sur la base de 1500 échantillons. Les symboles gris ont été obtenus expérimentalement, la courbe en trait plein découle de la relation obtenue Fig. 2.13 couplée à l'estimation du nombre  $M_M$  en fonction de la fréquence. Les barres d'incertitude ont été obtenues par simulation Monte Carlo.

A l'aide des données expérimentales, nous avons également estimé les fonctions de distribution de la puissance, et par ce biais, nous avons pu estimer les facteurs de forme  $b$  de la loi de Weibull. On peut voir les ordres de grandeur à l'aide de la Fig. 2.14. Comme attendu une convergence vers la valeur unité est observée avec l'augmentation de la fréquence. A l'aide de la courbe de tendance  $M_M(f)$  obtenue via la Fig. 2.12, nous avons déduit la courbe en trait plein de la Fig. 2.14 gauche. Une comparaison avec l'évolution de  $b(M_M)$  est également présentée Fig. 2.14 (droite). Afin de savoir si la dispersion des points expérimentaux (cercles gris) était à imputer à l'incertitude statistique, nous avons procédé à une simulation du modèle modal en un point. Nous obtenons des barres d'incertitude en bon accord avec la dispersion observée expérimentalement, confirmant que cette dispersion est liée à la nature aléatoire du champ EM au sein de la chambre.

## IV Conclusion et perspectives

En conclusion, la plupart des travaux ont porté sur la statistique de la moyenne du champ au carré au sein d'une chambre réverbérante. Les travaux menés sur cette thématique ont permis de mieux estimer les intervalles de confiance en fonction du degré de surmodage d'une chambre. Une des contributions jugée comme intéressante concerne la possibilité d'associer un nombre de degrés de liberté suivant la statistique du champ au sein de l'enceinte.

Une des perspectives, déjà entamée par ailleurs, porte sur l'extension et l'exploitation de ces résultats au domaine des télécommunications. Les chambres réverbérantes étant vues comme des émulateurs de canaux, les résultats obtenus permettent d'étendre l'utilisation de ces dernières à de nouveaux types de *fading*.

Toutefois, un des défis sur la thématique des chambres réverbérantes porte sur la statistique des maxima de champ. Dans les tests de susceptibilité électromagnétique ce sont les maxima qui intéressent la communauté et dans des conditions de surmodage intermédiaire, la statistique de ces maxima n'est pas aisée à trouver.

Cette étude est laissée en perspective. Pour y parvenir, une des étapes porterait sur l'étude de la statistique des poids modaux. A défaut de pouvoir statuer sur ce point, la gaussianité de ces poids est considérée jusque lors mais rien n'indique que ce modèle soit le bon. Un travail en ce sens a été entamé. Avec le modèle modal équivalent proposé il serait intéressant de voir si la statistique des maxima serait alors vérifiée expérimentalement.

Un autre point laissé en perspective concerne la décomposition du champ en ondes planes avec notamment l'étude d'une corrélation potentielle entre un nombre fini d'ondes planes qu'inclurait le modèle et le recouvrement modal.

## Références

- BALACHANDRAN, C. (1959). « Random sound field in reverberation chambers ». *J. Acoust. Soc. Am* 31, p. 1319 (cf. p. 9).
- BUNTING, C. F. (2002). « Statistical characterization and the simulation of a reverberation chamber using finite-element techniques ». *IEEE Trans. Electromagn. Compat.* 44.1, p. 214-221 (cf. p. 19).
- COOK, R. K., R. WATERHOUSE, R. BERENDT, S. EDELMAN et M. THOMPSON JR (1955). « Measurement of correlation coefficients in reverberant sound fields ». *J. Acoust. Soc. Am.* 27.6, p. 1072-1077 (cf. p. 7).
- COZZA, A. (2012). « Probability Distributions of Local Modal-Density Fluctuations in an Electromagnetic Cavity ». *IEEE Trans. Electromagn. Compat.* 54.5, p. 954-967 (cf. p. 7, 14).
- COZZA, A. (2011). « The role of losses in the definition of the overmoded condition for reverberation chambers and their statistics ». *IEEE Trans. Electromagn. Compat.* 53.2, p. 296-307 (cf. p. 11, 13).
- DAVY, J. (1981). « The relative variance of the transmission function of a reverberation room ». *J. Sound Vib.* 77.4, p. 455-479. ISSN : 0022-460X (cf. p. 15).
- DAVY, J. L. et R. L. WEAVER (2015). « Comment on “Relative variance of the mean squared pressure in multimode media : Rehabilitating former approaches”[J. Acoust. Soc. Am. 136, 2621–2629 (2014)] ». *J. Acoust. Soc. Am.* 137.3, p. 1598-1601 (cf. p. 16).
- GUREVICH, I. et M. PEVSNER (1957). « Repulsion of nuclear levels ». *Nuclear Physics* 2.5, p. 575-581 (cf. p. 15).

- HILL, D. (1998). « Plane-wave integral representation for fields in reverberation chambers ». *IEEE Trans. Electromagn. Compat.* 40, p. 209-217 (cf. p. 6).
- KUTTRUFF, H. (2009). « Room acoustics ». 5th. Oxon : Spon Press. Chap. 3 (cf. p. 12).
- LEHMAN, T. H. (May 1993). « A Statistical Theory of Electromagnetic Fields in Complex Cavities ». *Interaction Notes, USAF Phillips Laboratory Note* 494 (cf. p. 11).
- LYON, R. (1969). « Statistical analysis of power injection and response in structures and rooms ». *J. Acoust. Soc. Am.* 45, p. 545 (cf. p. 14, 15).
- MCDONALD, S. et A. KAUFMAN (1988). « Wave chaos in the stadium : statistical properties of short-wave solutions of the Helmholtz equation ». *Phys. Rev. A* 37.8, p. 3067 (cf. p. 11).
- MEHTA, M. L. (2004). *Random Matrices*. Sous la dir. d'E. INC. Third. T. 142. Amsterdam, Oxford, San Diego, London : Academic Press (cf. p. 14).
- MONSEF, F. (2012). « Why a Reverberation Chamber Works at Low Modal Overlap ». *IEEE Trans. Electromagn. Compat.* 54.6, p. 1314-1317 (cf. p. 12).
- MONSEF, F., A. COZZA, F. MONSEF et A. COZZA (2014). « Average number of significant modes excited in a mode-stirred reverberation chamber ». *IEEE Trans. Electromagn. Compat.* 56.2, p. 259-265 (cf. p. 13, 15).
- MONSEF, F. et A. COZZA (2011). « Limitations of the equivalence between spatial and ensemble estimators in the case of a single-tone excitation ». *J. Acoust. Soc. Am.* 130, p. 1943 (cf. p. 10).
- MONSEF, F. et A. COZZA (2014). « Variability and confidence intervals of the power measured in a reverberation chamber ». *IEEE Trans. Electromagn. Compat.* 56.5, p. 1238-1241 (cf. p. 13).
- MONSEF, F. et A. COZZA (2015a). « A Possible Minimum Relevance Requirement for a Statistical Approach in a Reverberation Chamber ». *IEEE Trans. Electromagn. Compat.* 57.6, p. 1728-1731 (cf. p. 19).
- MONSEF, F. et A. COZZA (2015b). « Predicting Power Distribution Inside a Reverberation Chamber ». *URSI-RASC Conference Proceedings*. IEEE (cf. p. 20).
- MONSEF, F., A. COZZA, D. RODRIGUES, P. CELLARD et J.-N. DUROCHER (2014). « Relative variance of the mean-squared pressure in multimode media : Rehabilitating former approaches ». *J. Acoust. Soc. Am.* 136.5, p. 2621-2629 (cf. p. 14, 15).
- MONSEF, F., R. SERRA et A. COZZA (2015). « Goodness-of-Fit Tests in Reverberation Chambers : Is Sample Independence Necessary ? » *IEEE Trans. Electromagn. Compat.* 57.6, p. 1748-1751 (cf. p. 7).
- MORSE, P. M. et R. H. BOLT (1944). « Sound waves in rooms ». *Rev. Mod. Phys.* 16.2, p. 69 (cf. p. 6).
- Reverberation Chamber Test Methods* (2011). International Electrotechnical Commission (IEC), Std. 61 000-4-21 (cf. p. 7, 19).
- SCHROEDER, M. R. et K. KUTTRUFF (1962). « On frequency response curves in rooms. Comparison of experimental, theoretical, and Monte Carlo results for the average frequency spacing between maxima ». *J. Acoust. Soc. Am.* 34.1, p. 76-80 (cf. p. 7, 11).
- WEAVER, R. (1989). « On the ensemble variance of reverberation room transmission functions, the effect of spectral rigidity ». *J. Sound Vib.* 130.3, p. 487-491. ISSN : 0022-460X (cf. p. 15).
- WEYL, H. (1912). « Das asymptotische Verteilungsgesetz der Eigenwerte linearer partieller Differentialgleichungen (mit einer Anwendung auf die Theorie der Hohlraumstrahlung)(Asymptotic distribution of the partial differential equations eigenvalues (with an application to black body theory)) ». *Mathematische Annalen* 71.4, p. 441-479. ISSN : 0025-5831 (cf. p. 6).

# Limitations of the equivalence between spatial and ensemble estimators in the case of a single-tone excitation

Florian Monsef<sup>a)</sup> and Andrea Cozza

Département de Recherche en Électromagnétisme, L2S, UMR8506  
Univ Paris-Sud, SUPELEC, CNRS  
3 rue Joliot Curie - 91190 Gif-sur-Yvette, France

(Dated: August 14, 2011)

The ensemble-average value of the mean-square pressure is often assessed by using the spatial-average technique, underlying an equivalence principle between spatial and ensemble estimators. Using the ideal-diffuse-field model, the accuracy of the spatial-average method has been studied theoretically forty years ago in the case of a single-tone excitation. This study is revisited in the present work on the basis of a more realistic description of the sound field accounting for a finite number of plane waves. The analysis of the spatial-average estimator is based on the study of its convergence rate. Using experimental data from practical examples, it is shown that the classical expression underestimates the estimator uncertainty even for frequencies greater than Schroeder's frequency, and that the number of plane waves may act as lower bound on the spatial-average estimator accuracy. The comparison of the convergence rate with an ensemble-estimator shows that the two statistics cannot be regarded as equivalent in a general case.

PACS numbers: 43.55.Cs, 43.55.Br, 43.55.Gx

## I. INTRODUCTION

In room acoustics, the interest of statistical approaches lies in the ability of predicting statistical properties of the sound field independently of the fine details of a specific configuration. Indeed, the configuration of a room and the position of the source impact on the modal topographies or equivalently on the directions and the amplitudes of the plane waves composing the sound field. If one considers an ensemble of rooms with approximately the same volume and the same reverberation time, one should recover the same estimated moments in accordance with the statistical model.

Statistical models have been developed for more than a half century. The most common one, called the ideal-diffuse-field model, is based on random wave theory<sup>1</sup>. The model considers, on the one hand, the reverberant part of the sound field, that is the sound field measured at some distance from the source and, on the other hand, that the modal overlap is sufficiently great. It has been shown that a minimum average overlap of three modes is needed<sup>2</sup>, from which ensues Schroeder's frequency. Other studies<sup>3-5</sup>, based on a modal approach, aimed at deriving models that could be applied to a more general class of systems, i.e., to configurations where a low modal overlap can be assumed.

In practice, the validation of any model depends on estimation techniques based on the use of samples from which estimates of the statistical moments (generally the first two moments) must be derived. The random samples can be obtained mainly by two different methods. The first method consists in sampling the sound pres-

sure in the central volume of a room<sup>4,6,7</sup>, for a given configuration of the sound-field topography. The estimation is based on a single realization of the sound-field topography. The estimation method using spatial samples will hereafter be referred to as the spatial-estimator method. The second method consists in using a single spatial sample for an ensemble of different sound-field topographies<sup>8,9</sup> that can be obtained electronically, by the use of a varying tone signal<sup>10</sup>, or mechanically, using a large rotating vane<sup>8,9</sup>. This latter is particularly well-suited for single-tone excitation which is the case of interest in the present study. Hereafter, this estimation method will be referred to as an ensemble-estimator method.

Using the squared value of the sound pressure related to each samples set, two estimations of the mean-square pressure can then be computed. Although never demonstrated, to the best of our knowledge, the estimates resulting from the spatial- and ensemble-average estimators are often regarded as equivalent. This equivalence principle implies a similar asymptotic convergence rate of both estimators. The equivalence assumption is directly related to the mixing (and consequently ergodic) property of dynamical systems<sup>11</sup>. Using a classical wave theory approach, an analogous mixing property is found within the ideal-diffuse-field description<sup>12</sup>. This equivalence assumption has been widely used to optimize spatial-averaging techniques, studied in detail by Schroeder<sup>13,14</sup>, Lubman<sup>15-17</sup> and Waterhouse<sup>18</sup> forty years ago, to provide the effective number of discrete independent spatial samples for practical experiments. However, in the case of a single-tone excitation, these works are restricted to frequencies above Schroeder's frequency.

The aim of the present paper is to study theoretically, in the case of a harmonic excitation and considering only the reverberant part of the sound pressure, whether the spatial- and ensemble-average estimators can be regarded

---

<sup>a)</sup>[florian.monsef@lss.supelec.fr](mailto:florian.monsef@lss.supelec.fr)

as equivalent. To this end, considering the mean-square pressure, expressions of the first two moments of the estimators are derived. The ensemble and spatial estimators are shown to be both unbiased but with different convergence rates. As a result, the confidence intervals related to both estimators cannot be regarded as identical.

To derive these results, a plane-wave model ensuing from a modal expansion is used to express the sound pressure. Recalling on the one hand that a mode can be expanded into a strictly finite number of plane waves<sup>19</sup>, and considering on the other hand a finite number of overlapping modes, the model used includes a discrete number of plane waves. Hence, this approach ensures a realistic description of the field and is presented in section II. Using this sound-field model, we establish in section III a general expression of the spatial-average estimator variance. The accuracy of the estimation is assessed on the basis of its convergence rate, and it is shown to present a lower bound directly related to the number of plane waves composing the sound pressure. In section IV we relate the number of plane waves to the room parameters, providing a predictive model applied to practical-room examples. We show that the lower bound of the convergence rate has a significant impact on the accuracy of the estimated value even for frequencies above Schroeder's frequency.

## II. HARMONIC SOUND FIELD MODEL

### A. From modal theory to discrete plane-wave expansion

In any enclosure with reflective boundaries (room, theater, reverberation chamber,...), a sound pressure induced by a source signal is made up of standing waves related to the normal modes that form a complete set of orthogonal functions<sup>19</sup>. Accordingly, a harmonic sound field can be expressed as a sum of  $M$  dominant overlapping modes at a given frequency. Considering a harmonic excitation, the sound pressure will be expressed in the frequency domain. The resulting complex pressure  $p_\omega(\mathbf{r})$  can then be stated as

$$p_\omega(\mathbf{r}) = \sum_{m=1}^M \alpha_m p_m(\mathbf{r}) \psi_m(f), \quad (1)$$

where  $p_m(\mathbf{r})$ ,  $\alpha_m$  and  $\psi_m(f)$  correspond to the modal topography, the modal weight and the frequency response of the  $m^{th}$ -mode, respectively.

As it will be presented thereafter, the spatial-average estimator consists basically in computing a spatial integral in which the modal topographies are needed. The computation is achievable if explicit expressions of the modes are available which is only the case in very specific configurations. This points out a serious limitation of the modal expansion in (1) as a way to study the accuracy of the spatial-average estimator.

Nevertheless, in the case of a standard room, a mode can be expanded into a finite number of plane waves. Consequently, for a finite modal overlap, the sound field can be rigorously expressed by means of a finite number

of plane waves. To the best of our knowledge, this is the first analysis in room acoustics introducing such a model, allowing a more realistic description of the sound field. Indeed, it has been known for a long time that the infinite number of plane waves assumed in the ideal diffuse model is an unrealistic concept<sup>20</sup> and is not physically justified. In practical terms, the finite number of plane waves accounts for the finite number of possible paths (as illustrated in Ref.10), or periodic orbits<sup>21</sup>, inducing cavity resonances and stationary waves. The resulting complex pressure  $p_\omega(\mathbf{r})$  expressed in (1) can then be restated as

$$p_\omega(\mathbf{r}) = \sum_{p=1}^N \gamma_p e^{-j k_0 \hat{k}_p \cdot \mathbf{r}}, \quad (2)$$

where  $N$  is the number of plane waves,  $\mathbf{r}$  is the position at which the pressure is sampled and  $k_0 = \omega/c$  is the propagation constant for the homogeneous medium filling the cavity, with  $\omega$  the angular frequency of the harmonic excitation signal and  $c$  the sound speed. The  $p^{th}$ -plane wave propagates along the direction  $\hat{k}_p$ , with a complex amplitude  $\gamma_p$ .

We want to stress that the plane-wave model introduced in (2) should be regarded as a modal approach expressed in the Fourier basis. In other words, using (1) or (2) is totally equivalent. The main advantage of (2) over (1) however, is that the exponential term provides an explicit spatial dependence well suited to the study in section III of the spatial estimator. This will allow thereafter a rigorous derivation of the statistical moments of the spatial estimator.

### B. Ensemble statistics

In practice, the plane-wave sets of parameters  $\{\hat{k}\} = \{\hat{k}_1, \dots, \hat{k}_N\}$  and  $\{\gamma\} = \{\gamma_1, \dots, \gamma_N\}$  cannot be measured, the only observable being the pressure. As commonly done in statistical mechanics and in the modeling of complex systems, the use of (2) allows studying sound field statistics in a simple way, as soon as the two plane-wave sets of parameters  $\{\hat{k}\}$  and  $\{\gamma\}$  are treated as random variables.

Hence, to make the derivation of our approach simpler, we adopt the following assumptions on  $\{\hat{k}\}$  and  $\{\gamma\}$

1. the two sets will be assumed to be independent
2. for each set, variables identified by different indexes  $p$  in (2) will be regarded as independent and identically distributed (iid).

Although the expression of the sound pressure in (2) holds in a general case, i.e., for the sound field near the source and at some distance from the source, the hypotheses made on the sets  $\{\hat{k}\}$  and  $\{\gamma\}$  implies physically a certain degree of diffusion of the sound field. Accordingly, the model that will be established in the present study is meaningful only for the reverberant part of the field with a certain degree of diffusion.

The mean-square pressure being the quantity of interest, we use (2) to express the square of the pressure as follows

$$p_\omega^2(\mathbf{r}) = \sum_{p=1}^N |\gamma_p|^2 + \sum_{i \neq j}^N \gamma_i \gamma_j^* e^{-jk_0(\hat{k}_i - \hat{k}_j) \cdot \mathbf{r}}, \quad (3)$$

where \* stands for the complex conjugate.

In order to derive the statistical properties of (3), we start by expressing its ensemble-average value  $\mu_{p_\omega^2}(\mathbf{r})$  defined as

$$\begin{aligned} \mu_{p_\omega^2}(\mathbf{r}) &= \mathbb{E}[p_\omega^2(\mathbf{r})] \\ &= \sum_{p=1}^N \mathbb{E}[|\gamma_p|^2] + \sum_{i \neq j}^N \mathbb{E}[\gamma_i \gamma_j^*] \mathbb{E}[e^{-jk_0(\hat{k}_i - \hat{k}_j) \cdot \mathbf{r}}], \end{aligned} \quad (4)$$

where  $\mathbb{E}[\cdot]$  stands for the ensemble-average operator. It is noteworthy that we have taken advantage of the independence assumption between the sets  $\{\gamma\}$  and  $\{\hat{k}\}$  to split the ensemble operator in the last term in (4).

One of the properties sought in room acoustics applications, e.g., power measurements, is the statistical uniformity of the sound field. In other words,  $\mu_{p_\omega^2}$  is expected to be independent of the position  $\mathbf{r}$ . One way to justify this property in some previous work<sup>14</sup>, is to consider  $\{\gamma\}$  as a set of zero mean complex random variables, such as

$$\mathbb{E}[\gamma_i^* \gamma_j] = \mathbb{E}[\gamma_i^*] \mathbb{E}[\gamma_j] = 0 \quad \forall i \neq j. \quad (5)$$

In fact, this assumption is not necessary, as long as the sampling position is in a region where the ensemble of the plane waves cover uniformly angles of arrival over  $4\pi$  steradian. It is worth noting that this property holds even for a finite number of plane waves. Assuming the  $\{\hat{k}\}$  to be iid leads to have the ensemble-average value of the complex exponential term in (4) to be equal to zero. Therefore,

$$\begin{aligned} \mu_{p_\omega^2}(\mathbf{r}) &= \sum_{p=1}^N \mathbb{E}[|\gamma_p|^2] \\ &= N \mathbb{E}[|\gamma_p|^2]. \end{aligned} \quad (6)$$

### III. SPATIAL ESTIMATOR

In order to characterize in detail the properties of this estimation method, we make use, for convenience, of a continuous spatial average which provides the following estimated value  $\hat{\mu}_{p_\omega^2}$

$$\hat{\mu}_{p_\omega^2} = \frac{1}{M_\Omega} \int_{\Omega} p_\omega^2(\mathbf{r}) d\mathbf{r} = \langle p_\omega^2(\mathbf{r}) \rangle_{\Omega}, \quad (7)$$

where  $\langle \cdot \rangle_{\Omega}$  stands for the space averaging operator as taken over the sample region  $\Omega$ .

In order to derive a more explicit expression of the spatial-average estimation, we substitute (3) into (7).

Accordingly,

$$\begin{aligned} \hat{\mu}_{p_\omega^2} &= \frac{1}{M_\Omega} \sum_{i=1}^N \sum_{j=1}^N \gamma_i \gamma_j^* \int_{\Omega} e^{-jk_0(\hat{k}_i - \hat{k}_j) \cdot \mathbf{r}} d\mathbf{r} \\ &= \sum_{i=1}^N \sum_{j=1}^N \gamma_i \gamma_j^* \langle e^{-jk_0(\hat{k}_i - \hat{k}_j) \cdot \mathbf{r}} \rangle_{\Omega}. \end{aligned} \quad (8)$$

Organizing the set of the plane-wave weights  $\{\gamma\}$  into the  $\boldsymbol{\gamma}$  column vector yields the following quadratic form

$$\hat{\mu}_{p_\omega^2} = \boldsymbol{\gamma}^H \mathbf{P} \boldsymbol{\gamma}, \quad (9)$$

where  $H$  stands for the Hermitian operator and  $\mathbf{P}$  is a matrix with elements  $P_{ij}$  defined as

$$P_{ij} = \langle e^{-jk_0(\hat{k}_i - \hat{k}_j) \cdot \mathbf{r}} \rangle_{\Omega}. \quad (10)$$

In the case of a 3D cartesian sampling volume, the elements of  $\mathbf{P}$  can be expressed as,

$$P_{ij} = \frac{1}{M_\Omega} \int_{\Omega} e^{-jk_0(\hat{k}_i - \hat{k}_j) \cdot (x\hat{n}_1 + y\hat{n}_2 + z\hat{n}_3)} dx dy dz, \quad (11)$$

where  $\hat{n}_1$ ,  $\hat{n}_2$  and  $\hat{n}_3$  are the Cartesian unit vectors related to the  $x$ ,  $y$  and  $z$  components, respectively. If we consider a square parallelepiped whose sides are referred to as  $a_1$ ,  $a_2$ ,  $a_3$ , respectively, and if the origin is taken at the middle of the sampling volume  $\Omega$ , we can easily restate (11) as

$$P_{ij} = \prod_{v=1}^3 \text{sinc}\left(\pi \frac{a_v}{\lambda} (\hat{k}_i - \hat{k}_j) \cdot \hat{n}_v\right), \quad (12)$$

where  $\text{sinc}(\cdot)$  is the sine cardinal function,  $\lambda$  is the wavelength in the filling medium. We note that the elements of matrix  $\mathbf{P}$  are a function of the random variables  $\hat{k}_i - \hat{k}_j$ .

Beyond the mathematical convenience provided by the concise form of (9), the matrix  $\mathbf{P}$  is of particular interest in understanding the influence of the non-diagonal terms of  $\mathbf{P}$  on the estimator accuracy. To illustrate our statement, suppose that  $\mathbf{P}$  reduces to the identity matrix  $\mathbb{I}$ . A perfect estimator is obtained since  $\hat{\mu}_{p_\omega^2}$  converges to the ensemble average given in (6). The scenario ensuring this convergence is however unrealistic since corresponding to an infinite sampling volume as illustrated by relation (12). Indeed, if  $a_v$  tends to infinity the cross-terms  $P_{ij}$  tend to zero.

In practice however, the sampling volume being finite, non-diagonal terms of  $\mathbf{P}$  will appear, i.e.,  $\mathbf{P} \neq \mathbb{I}$ , inducing inevitably estimation errors. In other words, the analysis of the spatial-estimator accuracy lays on the analysis of the eigenvalues of  $\mathbf{P}$ .

In order to study the accuracy of the estimate  $\hat{\mu}_{p_\omega^2}$ , we need to compute the moments of the spatial estimator with respect to ensemble statistics.

#### A. Statistics of the error induced by a spatial estimator

The accuracy of the spatial estimator lies in the ability of the corresponding estimate to provide the true ensemble-average value. Accordingly, the quantity

$$\epsilon = \frac{\hat{\mu}_{p_\omega^2} - \mu_{p_\omega^2}}{\mu_{p_\omega^2}} \quad (13)$$

provides a measure of the relative error of the spatial-average value with respect to the ensemble-average value. In order to assess the accuracy of the spatial estimator the two statistical moments of (13) must be studied. The first moment, i.e., the mean value, informs on the asymptotic convergence of the spatial estimator towards the ensemble-mean value, i.e., informs on the biased or unbiased nature of the estimator. The second moment, i.e., the variance, is crucial since it assesses the confidence interval of the estimated value, i.e., indicates the accuracy of the estimate. Before proceeding, we express the relative error  $\epsilon$  in a different form for a more convenient mathematical derivation. We start by expressing (13) in a more explicit form. Using (6) and (9) yields

$$\begin{aligned} \epsilon &= \frac{\hat{\mu}_{p_\omega^2}}{\mu_{p_\omega^2}} - 1 \\ &= \frac{\boldsymbol{\gamma}^H \mathbf{P} \boldsymbol{\gamma}}{N E[|\gamma_p|^2]} - 1. \end{aligned} \quad (14)$$

It is convenient to introduce the random vector

$$\mathbf{v} = \frac{\boldsymbol{\gamma}}{\sqrt{E[|\gamma_p|^2]}}, \quad (15)$$

which is made up of iid normalized random variables, i.e.,  $E[|v_i|^2] = 1, \forall i \in [1, N]$ .

That allows recasting (14) in a simpler form

$$\epsilon = \frac{1}{N} \mathbf{v}^H \mathbf{P} \mathbf{v} - 1. \quad (16)$$

As explained in the previous subsection, a convenient way of analyzing the accuracy of the spatial estimator is to introduce the eigenvalues of  $\mathbf{P}$  using the following change of basis

$$\mathbf{P} = \mathbf{X} \boldsymbol{\Lambda} \mathbf{X}^{-1}, \quad (17)$$

where  $\boldsymbol{\Lambda}$  is a diagonal matrix composed of the eigenvalues  $\lambda_i$  of  $\mathbf{P}$ . Consequently,

$$\epsilon = \frac{1}{N} \mathbf{w}^H \boldsymbol{\Lambda} \mathbf{w} - 1, \quad (18)$$

where  $\mathbf{w} = \mathbf{X}^{-1} \mathbf{v}$  is the vector of the plane-wave weights in the new basis.  $\mathbf{X}$  being a unitary matrix, the probability density function of the random variables  $v_i$  and  $w_i$  is the same. Moreover, by computing the covariance matrix of the set  $\{w\}$ , it can easily be shown that the statistical properties assumed for the  $v_i$  random variables are conserved for the  $w_i$ .

## B. Mean of the error

The statistical description of the relative error deals with a multivariate statistics analysis. To perform such

analysis we need to consider a joint probability density function  $p(\{v\}, \{\hat{k}\})$ . Recalling the independence assumptions between the two sets of random parameters  $\{v\}$  and  $\{\hat{k}\}$ , the joint probability function can be factored into the following way

$$p(\{v\}, \{\hat{k}\}) = p_v(\{v\}) p_{\hat{k}}(\{\hat{k}\}), \quad (19)$$

where  $p_v(\{v\})$  and  $p_{\hat{k}}(\{\hat{k}\})$  are the marginal probability density function of the random sets  $\{v\}$  and  $\{\hat{k}\}$ , respectively.

Hereafter, we will adopt the notation  $E_v[\epsilon]$  related to the conditional average of the random function  $\epsilon$  conditioned by the random set  $\{v\}$ , defined as

$$E_v[\epsilon] = \int \epsilon(\{v\}, \{\hat{k}\}) p_{\hat{k}}(\{\hat{k}\}) d\{\hat{k}\}. \quad (20)$$

The ensemble average  $\mu_\epsilon$  of the error can then be derived using nested conditional averages applied to the two sets of concern in (18) as follows

$$\mu_\epsilon = E[\epsilon] = E_k[E_w[\epsilon]]. \quad (21)$$

From expressing the average at the inner level, it follows that

$$\begin{aligned} E_w[\epsilon] &= \frac{1}{N} E_w[\mathbf{w}^H \boldsymbol{\Lambda} \mathbf{w}] - 1 \\ &= \frac{1}{N} \sum_{i=1}^N \lambda_i E[|w_i|^2] - 1. \end{aligned} \quad (22)$$

Reminding that  $\mathbf{X}$  is a unitary matrix yields

$$E[|w_i|^2] = E[|v_i|^2] = 1 \quad \forall i \in [1, N]. \quad (23)$$

Consequently,

$$E_w[\epsilon] = \frac{1}{N} \sum_{i=1}^N \lambda_i - 1. \quad (24)$$

The sum over the  $\lambda_i$  is equal to  $\text{Tr}(\mathbf{P})$ , the trace of  $\mathbf{P}$ . Besides, the main diagonal of  $\mathbf{P}$  being made of ones, it follows that

$$\text{Tr}(\mathbf{P}) = \sum_{i=1}^N \lambda_i = N, \quad (25)$$

which implies in a clear way that

$$E[\epsilon] = 0. \quad (26)$$

We can see that the estimator  $\hat{\mu}_{p_\omega^2}$  is still unbiased for a finite number of plane waves, provided that these latter are sufficiently stirred to justify of a statistical approach that assumes the independence between the sets of random variables. The unbiased nature of the spatial estimator provides a necessary but not sufficient condition to consider spatial-averaging and ensemble-averaging measures as mean-ergodic processes<sup>22</sup>. Indeed, one needs to study the variance of the error to assert the equivalence properties in a more general frame.

### C. Variance of the error

The mean of the error being null according to (26), the variance  $\sigma_\epsilon^2$  of the error reduces to  $E[\epsilon^2]$ . Adopting much the same approach as previously, the variance can be expressed using nested conditional averages as

$$\sigma_\epsilon^2 = E_{\mathbf{k}} [E_w [\epsilon^2]]. \quad (27)$$

From (18) we express  $\epsilon^2$  as follows

$$\begin{aligned} \epsilon^2 &= \left( \frac{1}{N} \mathbf{w}^H \boldsymbol{\Lambda} \mathbf{w} - 1 \right)^2 \\ &= \left( \frac{1}{N} \sum_{i=1}^N \lambda_i |w_i|^2 \right)^2 + 1 - \frac{2}{N} \sum_{i=1}^N \lambda_i |w_i|^2. \end{aligned} \quad (28)$$

At the inner level of (27) the conditional average on the  $\{w\}$  set can be developed as

$$\begin{aligned} E_w [\epsilon^2] &= E_w \left[ \left( \frac{1}{N} \sum_{i=1}^N \lambda_i |w_i|^2 \right)^2 \right] + 1 \\ &\quad - \frac{2}{N} \sum_{i=1}^N \lambda_i E_w [|w_i|^2]. \end{aligned} \quad (29)$$

Recalling that the components  $w_i$  are normalized random variables, the use of (25) yields the simpler form

$$E_w [\epsilon^2] = \frac{1}{N^2} E_w \left[ \left( \sum_{i=1}^N \lambda_i |w_i|^2 \right)^2 \right] - 1. \quad (30)$$

To obtain a more explicit expression, we expand the term between square brackets as

$$\left( \sum_{i=1}^N \lambda_i |w_i|^2 \right)^2 = \sum_{i=1}^N \lambda_i^2 |w_i|^4 + \sum_{i \neq j} \lambda_i \lambda_j |w_i|^2 |w_j|^2. \quad (31)$$

This allows recasting (30) as

$$E_w [\epsilon^2] = \frac{1}{N^2} \left( \nu_4 \sum_{i=1}^N \lambda_i^2 + \nu_2^2 \sum_{i \neq j} \lambda_i \lambda_j \right) - 1, \quad (32)$$

where the  $\nu_n$  terms are the following conditional moments defined as,

$$\nu_n = E_w [|w_i|^n] = E [|w_i|^n]. \quad (33)$$

In order to make (32) more tractable, we use algebraic properties stating that

$$\sum_{i=1}^N \lambda_i^2 = \text{Tr} (\mathbf{P}^T \mathbf{P}) = \|\mathbf{P}\|_F^2 = \sum_{i=1}^N \sum_{j=1}^N P_{ij}^2, \quad (34)$$

where  $\|\mathbf{P}\|_F$  stands for the Frobenius norm of matrix  $\mathbf{P}$ . Taking the square of (25)

$$(\text{Tr}(\mathbf{P}))^2 = \sum_{i=1}^N \lambda_i^2 + \sum_{i \neq j} \lambda_i \lambda_j = N^2, \quad (35)$$

and using (34), we can show that

$$\sum_{i \neq j} \lambda_i \lambda_j = N^2 - \|\mathbf{P}\|_F^2. \quad (36)$$

Whence,

$$E_w [\epsilon^2] = \frac{\|\mathbf{P}\|_F^2}{N^2} (\nu_4 - \nu_2^2). \quad (37)$$

In order to express the variance of the error, we still need to compute the conditional average on the  $\{\hat{k}\}$  set, leading to

$$\begin{aligned} \sigma_\epsilon^2 &= E_{\mathbf{k}} \left[ \frac{\|\mathbf{P}\|_F^2}{N^2} (\nu_4 - \nu_2^2) \right] \\ &= \frac{1}{N^2} (\nu_4 - \nu_2^2) E_{\mathbf{k}} [\|\mathbf{P}\|_F^2]. \end{aligned} \quad (38)$$

We can note that the conditional moment on  $\{\hat{k}\}$  only applies on the square Frobenius norm since this latter is the only term in (37) depending on the plane-wave directions. Reminding the structure of  $\mathbf{P}$ , we can restate (34) as

$$\|\mathbf{P}\|_F^2 = \sum_{i,j} P_{ij}^2 = N + \sum_{i \neq j} P_{ij}^2 \quad (39)$$

The non-diagonal elements  $P_{ij}$ , denoted by a function  $\Phi(\hat{k}_i - \hat{k}_j)$ , inherit the iid property from the  $\{\hat{k}\}$  random set. Accordingly, we can expand the conditional average  $E_{\mathbf{k}} [\|\mathbf{P}\|_F^2]$  as

$$E_{\mathbf{k}} [\|\mathbf{P}\|_F^2] = N + N(N-1)E_{\mathbf{k}} [\Phi^2(\hat{k}_i - \hat{k}_j)]. \quad (40)$$

Finally, the variance of the error can be expressed as

$$\sigma_\epsilon^2 = \left[ \frac{N-1}{N} G_\Omega(\mathbf{a}) + \frac{1}{N} \right] (\nu_4 - \nu_2^2) \quad (41)$$

with,

$$G_\Omega(\mathbf{a}) = \iint_{\Omega} \Phi^2(\hat{k}_i - \hat{k}_j) p_{\hat{\mathbf{k}}}(\hat{k}_i) p_{\hat{\mathbf{k}}}(\hat{k}_j) d\hat{k}_i d\hat{k}_j, \quad (42)$$

which is the only term depending on the dimensions of  $\Omega$ , where  $\mathbf{a}$  is a vector gathering the sampling-area dimensions  $a_v$  used in (12). Using a Monte-Carlo method and assuming a uniform angular distribution, the evolution of  $G_\Omega$  is plotted in Fig.1, where a line of length  $a$  (dashed line), a square of side  $a$  (dotted line) and a cube of side  $a$  (solid line) have been considered, respectively.

As shown in Appendix A, the term  $\nu_4 - \nu_2^2$  in (41) is the relative-ensemble variance  $\sigma_{r,p^2}^2$  of the mean-square pressure, defined as,

$$\sigma_{r,p^2}^2 = E \left[ \frac{(p_\omega^2(\mathbf{r}) - \mu_{p_\omega^2}(\mathbf{r}))^2}{\mu_{p_\omega^2}^2(\mathbf{r})} \right]. \quad (43)$$

If no spatial averaging is performed, then  $G_\Omega(\mathbf{0}) = 1$ . It follows that the variance  $\sigma_\epsilon^2$  of the relative error reduces logically to  $\sigma_{r,p^2}^2$ , i.e., to the relative variance of

the mean-square pressure in a single point. The relative-ensemble variance has been widely studied in the literature using wave theory<sup>7,23</sup> and modal theory<sup>3–5</sup> models and will not be analyzed in detail herein. All these models have been validated experimentally, and show that the relative-ensemble variance  $\sigma_{r,p^2}^2$  is inversely proportional to the number of overlapping modes  $M_s$  and tends to one for an ideal diffuse field, i.e., for an infinite number of plane waves.

Concerning spatial averaging, the modal models of Davy<sup>4</sup> and Weaver<sup>5</sup> included the influence of multiple independent receivers, i.e., of independent spatial samples, in the overall relative variance. Accordingly, if we consider a single fixed source and  $N_R$  independent receivers, the mean estimated value  $\hat{\mu}_{p_\omega^2}$  of  $p_\omega^2(\mathbf{r})$  can be deduced using an arithmetic mean, i.e., a discrete version of (7), as

$$\hat{\mu}_{p_\omega^2} = \frac{1}{N_R} \sum_{i=1}^{N_R} p_{\omega,i}^2, \quad (44)$$

which is the traditional mean-estimator. Using modal models<sup>4,5</sup>, it follows that

$$\sigma_\epsilon^2 = \frac{1}{N_R} \sigma_{r,p^2}^2, \quad (45)$$

where  $1/N_R$  is referred to as the convergence rate. Within the modal approach, it appears that the more (independent) receivers we take the more accurate the estimated mean value will be. This of course unrealistic because a spatial correlation exists; but as explained in section II modal models cannot include easily the effect of spatial field distribution into the moments of spatial-average estimates.

Using the plane-wave model presented herein, (41) can interestingly be restated as follows

$$\sigma_\epsilon^2 = G(\mathbf{a}, N) \sigma_{r,p^2}^2, \quad (46)$$

where  $G(\mathbf{a}, N)$  is the convergence rate of the spatial estimator expressed as

$$G(\mathbf{a}, N) = \frac{N-1}{N} G_\Omega(\mathbf{a}) + G_{PW}(N), \quad (47)$$

with  $G_{PW}(N) = 1/N$ .

Note that on a single point, i.e., for  $\mathbf{a} = \mathbf{0}$  the convergence rate  $G(\mathbf{0}, N) = 1$  as expected, independently of the number  $N$  of plane waves.

It turns out that the convergence rate of the spatial estimator obtained in (47) is conditioned by two terms. The first term, as expected, is related to the influence of the sampling term  $G_\Omega(\mathbf{a})$  whose inverse corresponds to an equivalent number of independent samples. The number of plane waves has very little influence on the first term of (47). On the contrary, the second term depends only on the number of plane waves.

The influence of the number of plane waves in the spatial-averaging convergence rate has never been predicted to the best of our knowledge by any study.

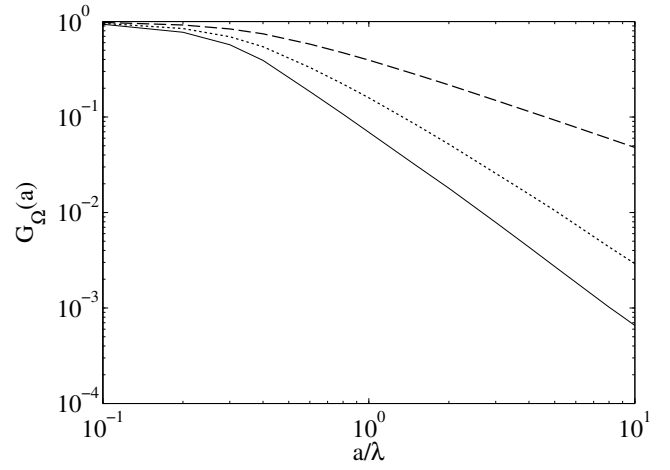


FIG. 1. Evolution of the spatial term  $G_\Omega(\mathbf{a})$  in (42). 1D, 2D and 3D sampling domains have been considered, related to a line stretch of length  $a$  (dashed line), to a square (dotted line) and a cube of side  $a$  (solid line), respectively.

The study of the accuracy of the spatial-average estimator consists then in analyzing the convergence rate given in (47) which can be simplified as,

$$G(\mathbf{a}, N) \simeq G_\Omega(\mathbf{a}) + G_{PW}(N), \quad (48)$$

since the term  $(N-1)/N$  can be reasonably neglected.

Accordingly, to study which of the two terms dominates in the overall estimator variance, the knowledge of  $\sigma_{r,p^2}^2$  is not needed since this latter is common. Consequently, we shall focus our analysis in the next section, on a comparison of the two terms of (48).

## IV. ACCURACY OF THE SPATIAL ESTIMATOR

### A. Existence of a lower bound

We are interested in comparing the two terms in (48) in order to see if the contribution of the plane waves may be significant in some cases. This is of relevant importance because the presence of the  $1/N$  term in the variance expression acts as a lower bound in the spatial-average estimator accuracy. Indeed, the number of plane waves is related to the room configuration, but is independent of the sampling area  $\Omega$ . Consequently, if the sampling area is larger, the  $G_\Omega$  term will decrease, as seen in Fig. 1, but leaving the  $1/N$  term unchanged. In practical terms, raising the sampling area will not diminish continuously the degree of uncertainty deduced from the spatial-average-estimator variance.

To stress the significative risk of this limitation, we study in the next subsection practical room cases for which an assessment of the two contributing terms, i.e., of  $G_{PW}$  and  $G_\Omega$ , is performed.

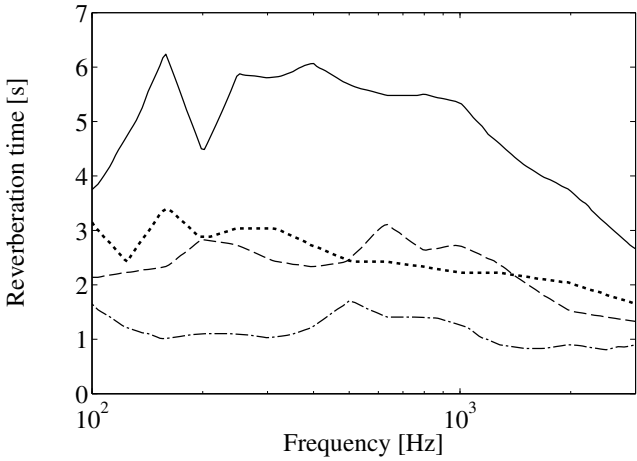


FIG. 2. Reverberation times from Ref.7. Four configurations have been considered : a large room (solid line), a large damped room (dotted line), a small room lightly damped (dashed line) and a small damped room (dashed-dotted line).

### B. Influence of room parameters

In order to assess quantitatively the role of  $G_{PW}$ , we consider real room configurations. We use the experimental data presented in Ref. 7 for the case of a small room ( $40 \text{ m}^3$ ) and a large reverberation room ( $245 \text{ m}^3$ ) with large fixed diffusers. Both rooms are essentially rectangular. For the small room, lightly damped and damped cases are considered. The corresponding Schroeder's frequencies are 500 Hz and 330 Hz, respectively<sup>7</sup>. For the large room very little damping and large damping cases have been considered. The corresponding Schroeder's frequency are of 310 Hz and 200 Hz, respectively<sup>7</sup>. The measurements of the reverberation time  $T_{60}$  were performed on a frequency range [100 Hz : 3.2 kHz] and is shown in Fig. 2.

The configuration of a room has a direct impact on the modal topographies but also on the frequency response and consequently on the number of plane waves composing the sound field. In order to fruitfully use the experimental room parameters we need to establish a way to relate them to the number of plane waves in the following way. At a frequency  $f$ , we may consider  $\beta$  plane waves per resonant mode. In order to assess the number  $M$  of modes that are found within the average resonant -3dB bandwidth  $B_M$ , we use the simplest form of Weyl's approximation<sup>24</sup> of the modal density. The number of plane waves involved in the sound field can then be approximated as

$$N = \beta \cdot M = \beta n(f)B_M \simeq \beta \frac{4\pi V f^2}{c^3} B_M, \quad (49)$$

where  $n(f)$  is the modal density (in modes per Hertz),  $V$  is the volume of the room and  $c$  the sound speed. Recalling that the reverberation time  $T_{60}$  is related to the average bandwidth of a mode  $B_M$ , such as  $B_M = 6.91/\pi \cdot T_{60}$  yields the following expression of the plane-

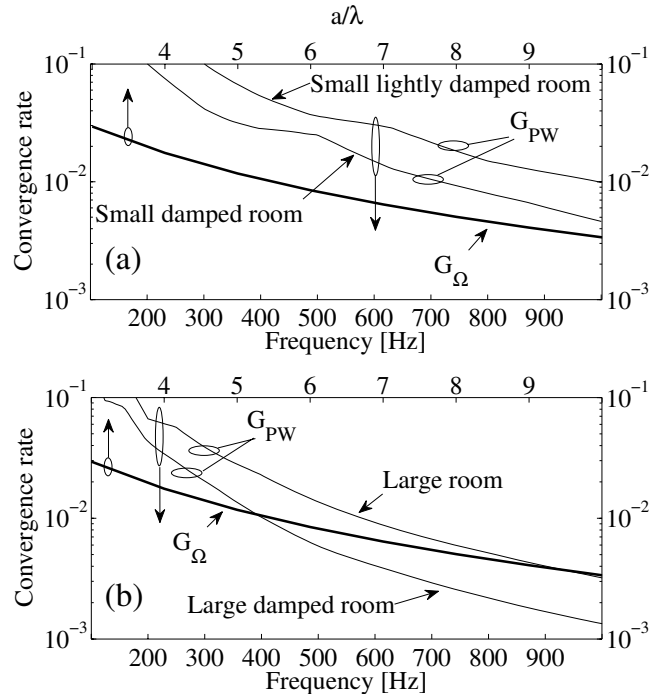


FIG. 3. Comparison of the lower bound  $G_{PW}$  as a function of frequency (lower x-axis) (with ten plane waves per mode) with the 2D-square spatial term  $G_\Omega$  as a function of  $a/\lambda$  (upper x-axis) for (a) the small room configurations and (b) the large room configurations of Ref. 7. A value of 3.3 m was considered for the parameter  $a$ .

wave term in (48)

$$G_{PW} = \frac{c^3 T_{60}}{27.64 \beta V f^2}, \quad (50)$$

providing a relation allowing to assess the lower-bound term using the room reverberation time  $T_{60}$  and the room volume  $V$ . For the four room configurations, Fig.3 shows the evolution of  $G_{PW}$  as a function of frequency (lower x-axis), and the evolution of the spatial  $G_\Omega$  term as a function of  $a/\lambda$  in the 2D case for  $3 < a/\lambda < 10$  (upper x-axis) where a value of 3.3 meters has been assumed for the parameter  $a$ . As already said, the number of plane waves per mode is hard to estimate. The rooms being essentially rectangular we can expect approximately eight plane waves per mode. In order to consider an upper bound we use a value of ten plane waves per mode. We stress that this value being used for all the modes on average, the  $G_{PW}$  term may not be regarded as overvalued.

For the case of the small room Fig.3a shows that the plane-wave term dominates even for frequencies above Schroeder's frequency, whereas for the large room cases described in Fig.3b, the two terms are of the same order of magnitude. These results can be regarded as a further proof to the well-known fact that the acoustics of small rooms are in a way more complicated than those of large ones. In the present case, it is an illustration that, at a given frequency, the smaller the room the worse the accuracy of the spatial estimate will be; not only because of the relative-ensemble variance as commonly known, but

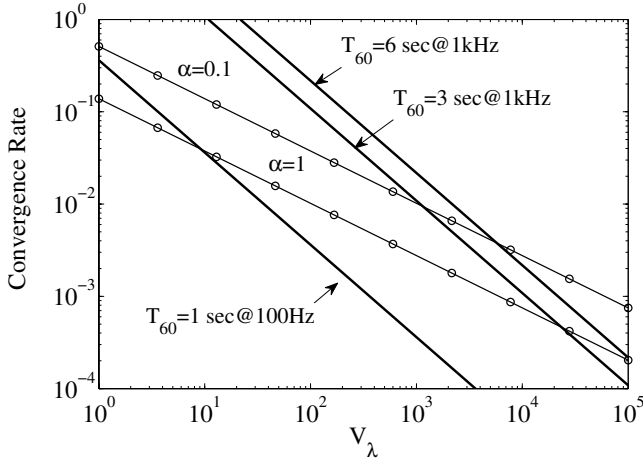


FIG. 4.  $G_{PW}$  (bold line) and  $G_\Omega$  (solid line with circles) as a function of the acoustical volume  $V_\lambda$  of a room.  $G_\Omega$  is related to the 2D-section of the sampling volume for which two cases are considered : the sampling volume fits the entire room volume ( $\alpha = 1$ ) and only 10% of the room volume is used in the second case ( $\alpha = 0.1$ ). For  $G_{PW}$ , frequencies below and above Schroeder's frequencies have been chosen (100Hz and 1kHz, respectively) and three values of reverberation times given in Fig. 2 were used, namely the minimum value of 1 s, the maximum value of about 6 s and an in-between value of 3 s.

also due to the spatial-averaging effect assessed herein. In both cases of Fig. 3, the finite number of plane waves has an influence on the overall convergence rate not only for frequencies near Schroeder's limit, as intuitively expectable, but in fact for a frequency range whose upper limit would be approximately ten times Schroeder's frequency.

At this stage a comparison between  $G_{PW}$  and  $G_\Omega(\alpha)$  has not been performed on the basis of a common parameter. To this end, we consider that the 3D-sampling zone, referred to as  $\Omega_{3D}$ , is a portion  $\alpha$  of the room volume  $V$ , such as  $\Omega_{3D} = \alpha V$ . In order to include the influence of the frequency (or equivalently the wavelength  $\lambda$ ) at which the measurement is performed, we introduce the acoustical sampling volume defined as  $\Omega_\lambda^{3D} = \Omega_{3D}/\lambda^3$ . Equivalently, we define the acoustical volume of the room defined as  $V_\lambda = V/\lambda^3$ , yielding

$$G_{PW} = \frac{T_{60} f}{27.64 \beta V_\lambda}. \quad (51)$$

The computation of  $G_\Omega$  requires the dimensions of the rooms. These latter being not known, we consider the following geometrical ratios 3 : 4 : 5, related to the width  $a_1$ , the height  $a_2$  and the length  $a_3$  of the sampling volume, respectively. These ratios account for the absence in practice of degenerate eigenfrequencies.

For the sake of plotting clarity, we restrict the analysis to the  $a_2 a_3$  section, referred to as  $\Omega_{2D}$ , of the sampling volume  $\Omega_{3D}$ . To compute the resulting  $G_\Omega$  term, two cases of  $\Omega_{3D}$  are considered : the case for which the sampling volume fits the total room volume, i.e., for  $\alpha = 1$ , and the case for which the sampling volume repre-

sents 10% of the room volume, i.e., for  $\alpha = 0.1$ . Accordingly, Fig. 4 shows the resulting 2D- $G_\Omega$  term for  $\alpha = 1$  and  $\alpha = 0.1$ , and the plane-wave term. For this latter, frequencies below and above Schroeder's frequency were considered, 100 Hz and 1 kHz, respectively, and three values of reverberation times were chosen on the basis of the experimental data provided by Fig. 2. The selected values correspond to the minimum of 1 s, to the maximum of about 6 s and to an in-between value of 3 s well suited to the large damped room and small lightly damped room cases.

We can see in Fig. 4 that at a fixed frequency (1kHz in the present case), the decrease of the reverberation time induces a lower convergence rate as stated by (51). If the frequency  $f$  varies, so does the acoustical volume since this latter is a function proportional to the cube of  $f$ . If we refer to the large and small rooms cases, taken at 1 kHz, respective acoustical volumes of 6000 and 991 are found. Using Fig. 4 for  $\alpha = 0.1$ , we find that  $G_{PW} = G_\Omega = 10^{-2}$  for the small room; for the large room,  $G_{PW} = 2 \cdot 10^{-3}$  and  $G_\Omega = 3.5 \cdot 10^{-3}$ . This illustrates the influence of the plane-wave term, since it contributes, for the small room case, to 50% of the overall convergence rate.

TABLE I. For sampling volumes corresponding to 10% ( $\alpha = 0.1$ ) and 100% ( $\alpha = 1$ ) of the small- and large-room volumes, respectively, relative margin of errors  $m_{r,\epsilon}$  and the corresponding 2D sampling areas  $\Omega_{2D}$  are reported. The number  $N_{eq}$  of equivalent independent spatial samples is also reported for  $\alpha = 0.1$ , assumed as a more realistic case.

Configuration	$m_{r,\epsilon}$	$\Omega_{2D}$	$N_{eq}$
small room	$\alpha = 1$	20%	31m <sup>2</sup>
	$\alpha = 0.1$	28%	6.8m <sup>2</sup>
large room	$\alpha = 1$	10%	105m <sup>2</sup>
	$\alpha = 0.1$	15%	22m <sup>2</sup>

In practice, the spatial-average estimate expressed in (7) can be regarded as a random Gaussian variable whose relative standard deviation  $\sigma_\epsilon$  conditions the confidence interval, i.e., the accuracy of the estimator. We define the *margin of error*  $m_\epsilon$  value as the half-width of the confidence interval. If we consider that 95% of the cases fall into this latter, the margin of error is approximately  $m_\epsilon = 2\sigma_\epsilon$ .

Our concern dealing with the comparison of the two terms of (48), the estimator efficiency can be described by the following relative margin of error  $m_{r,\epsilon} = m_\epsilon / \sigma_{r,p^2} = 2\sqrt{G_\Omega + G_{PW}}$ , plotted in Fig. 5 as a function of the acoustical volume of the room, for the 1D (triangles), 2D (circles) and 3D (squares) cases. For the plane-wave term a reverberation time of 3 s at 1 kHz has been used. We consider the cases for  $\alpha = 1$  (solid line) and  $\alpha = 0.1$  (dashed line) in order to assess the influence of the sampling area on the uncertainty range related to the spatial estimator efficiency.

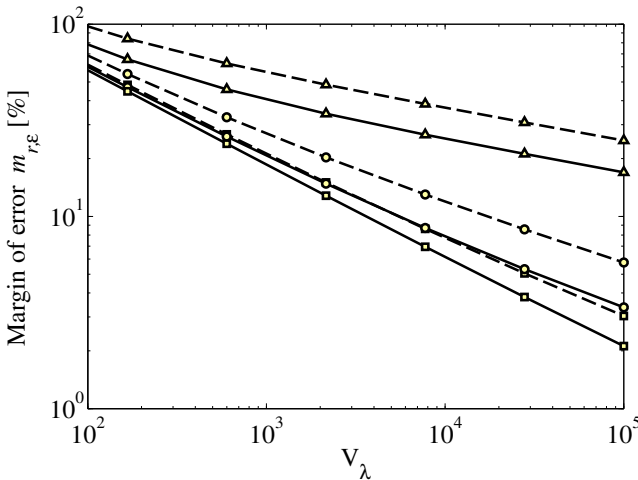


FIG. 5. The relative margin of error related to (48) for a 95% confidence interval and a reverberation time of about 3 s at 1 kHz. Sampling volumes in 1D (triangles), 2D (circles) and 3D (squares) are considered. The case for which the sampling volume  $\Omega$  fits the entire room volume ( $\alpha=1$ ) is plotted in solid line - the case for which the sampling volume is 10% of the room volume is plotted in dashed line.

If we refer to the practical cases described previously for which  $G_{PW} = G_\Omega = 10^{-2}$  for the small room and  $G_{PW} = 2 \cdot 10^{-3}$  and  $G_\Omega = 3.5 \cdot 10^{-3}$  for the large room, we find the respective relative margins of error of 20% and 10% for  $\alpha = 1$ , and 28% and 15% for  $\alpha = 0.1$ .

Regarding the  $G_\Omega$  term as an inverse number  $N_{eq}$  of equivalent independent discrete spatial samples, 100 and 250 equivalent samples are found for the small and large room, respectively, for  $\alpha = 0.1$ . All these values are summed up in Tab. I where the equivalent sampling 2D-areas  $\Omega_{2D}$  have also been reported providing the order of magnitude of the surface related to the relative margins of error previously mentioned.

Interestingly, if the  $\alpha = 0.1$  case of the spatial estimator were replaced by an ensemble estimator (using a rotating vane or moving the source and receiver positions as in Ref.7) based on  $N_s$  independent samples, we would need, on the basis of the same margins of error, i.e., 28% and 15%, 51 and 177 samples for the small and large room, respectively. For the small room case, to compensate the plane-wave term  $G_{PW}$ , a spatial-averaging process needs twice more independent samples than an ensemble estimator. It is worth stressing that in the case of an ensemble estimator, each realization corresponds to the case of  $G(\mathbf{0}, N) = 1$ , i.e., the number of plane waves has no influence.

The method presented herein can be then extended in a general way to any configuration. It provides a practical theoretical tool for predictions and estimation procedures applied to the mean-square pressure in room acoustics.

In the general model derived in section III, we did not make any assumption on the degree of diffusion of the field unlike the works dedicated to spatial averaging in the literature<sup>13,15–18</sup>. Indeed, these latter have been carried out within the frame of the ideal diffuse field hypothesis.

To the best of our knowledge, no other studies have been presented in a more general case. Accordingly, it is interesting to analyze how the general expression, given in (46), becomes in the particular case of an ideal diffuse field.

### C. The ideal diffuse field case

#### 1. Relative variance expression

In the case of an ideal diffuse field, i.e., for an infinite number of plane waves, using (47), we can show that the convergence rate  $G(\mathbf{a}, N)$  reduces to  $G_\Omega(\mathbf{a})$ . The relative-error variance of the spatial estimator given in (46) can then be expressed as

$$\lim_{N \rightarrow \infty} \sigma_\epsilon^2 = G_\Omega(\mathbf{a}) \sigma_{r,p^2}^2. \quad (52)$$

The relative-ensemble variance of the mean square pressure  $\sigma_{r,p^2}^2$  can be analyzed in a straightforward way. Indeed, the complex plane-waves weights  $\{w\}$  in the new basis result from an infinite sum of the  $\{\gamma\}$  random variables. Accordingly, using the central limit theorem, we can state that the real and imaginary parts of the set  $\{w\}$  follow a normal distribution. Consequently, the elements  $|w_i|^2$  follow a chi-square distribution with two degrees of freedom whose moments are such that

$$\frac{E[|w_i|^4]}{E[|w_i|^2]^2} = \frac{\nu_4}{\nu_2^2} = 2. \quad (53)$$

Hence, recalling that  $E[|w_i|^2] = 1$ , the relative variance  $\sigma_{r,p^2}^2$  reduces to unity as commonly accepted for the ideal diffuse field case.

We can then express (52) in the following simpler form

$$\lim_{N \rightarrow \infty} \sigma_\epsilon^2 = G_\Omega(\mathbf{a}), \quad (54)$$

which is the expression given by Schroeder<sup>13</sup>. In Schroeder's work<sup>13</sup> a Gaussian assumption is made on the  $\{\gamma\}$  set distribution. Note that, in the model derived in section III such assumption is not necessary to recover the expression of the error variance in the case of an ideal diffuse field.

#### 2. Estimators equivalence

In order to analyze if a spatial- and ensemble-average estimators are equivalent, one needs to compare their convergence rates.

To this end, we introduce the ensemble-mean-estimated value of the mean-square pressure  $\bar{\mu}_{p_\omega^2}$  defined as,

$$\bar{\mu}_{p_\omega^2} = \frac{1}{M_r} \sum_{i=1}^{M_r} p_{\omega,i}^2, \quad (55)$$

where  $p_{\omega,i}^2$  is the mean-square pressure corresponding to the  $i$ -th realization of the ensemble statistics and  $M_r$  is

the number of independent realizations. A realization can either be a position of a rotating vane or a pair of source/receiver positions. If the total number  $M_r$  of realizations are independent,  $\bar{\mu}_{p_\omega^2}$  is a random variable whose centered and normalized form, as done in (13), follows a normal distribution of zero mean and of variance  $\sigma_{r,p^2}^2/M_r$ .

The spatial-average (centered and normalized) estimate  $\epsilon$  follows also a normal distribution with a zero mean. However, the variance and/or convergence rate is not identical in all the spatial-sampling configurations as shown in Fig. 1. Indeed, we observe different slopes preventing a general equivalence principle between spatial-and ensemble-average estimates as the confidence interval is not identical. Accordingly, the claim in Ref.17 that the spatial-average estimator provides the "true estimate" is not correct in a strict sense although the 1D/2D/3D-spatial-variances  $G_\Omega$  tend asymptotically to zero.

In order to carry on a more accurate comparison of the convergence rates of  $\hat{\mu}_{p_\omega^2}$  and  $\bar{\mu}_{p_\omega^2}$ , we focus on the different slopes of  $G_\Omega$  for the 1D, 2D and 3D cases which turn to be 0.5, 0.4 and 0.26 per octave, respectively. For the 1D case, the slope is in accordance with the asymptotic expansion of the expression of Ref.13. For the 2D-square and 3D-cube cases no analytical expressions being available, we have estimated the following asymptotic expressions

$$G_\Omega(a) \simeq \begin{cases} 0.5/(a/\lambda) & \text{in the 1D case} \\ 0.2133/(a/\lambda)^{1.8} & \text{in the 2D case} \\ 0.0740(a/\lambda)^{-2} & \text{in the 3D case} \end{cases} \quad (56)$$

valid for  $a/\lambda > 2$ .

These expressions, derived for the first time for the 2D and 3D cases to the best of our knowledge, allow to see the impact of the dimensionality of  $\Omega$  on  $G_\Omega$  slopes.

The difference of slopes, linked to the difference of exponent power value in the asymptotic expressions of  $G_\Omega$ , is induced by the spatial correlation of the field in the room. The correlation effects on the spatial variance have already been studied in the cases of a line, a circle and a disk sampling areas<sup>15-17</sup>. For the mean-square pressure, the spatial autocorrelation function  $R(k_0\Delta r)$  was shown to be<sup>17,25</sup>,

$$R(k_0\Delta r) = \left( \frac{\sin(k_0\Delta r)}{k_0\Delta r} \right)^2, \quad (57)$$

where  $\Delta r$  is the distance between two points.

Using (57), a zero correlation is found for distances of  $\lambda/2$ , or entire multiples. On the basis of this property, the ensuing idea of using a discrete, rather than a continuous, spatial-average estimator has been studied by Waterhouse<sup>18</sup> who was interested in studying the different possible arrangements in 1D, 2D and 3D to have uncorrelated discrete samples. It can be shown that the 1D equivalent discrete averaging estimator, i.e., sampling along a line on positions apart from  $\lambda/2$  (or multiples), is the only case for which uncorrelated samples can be obtained. Indeed, in the 2D and 3D cases no geometrical configuration can provide a zero correlation between

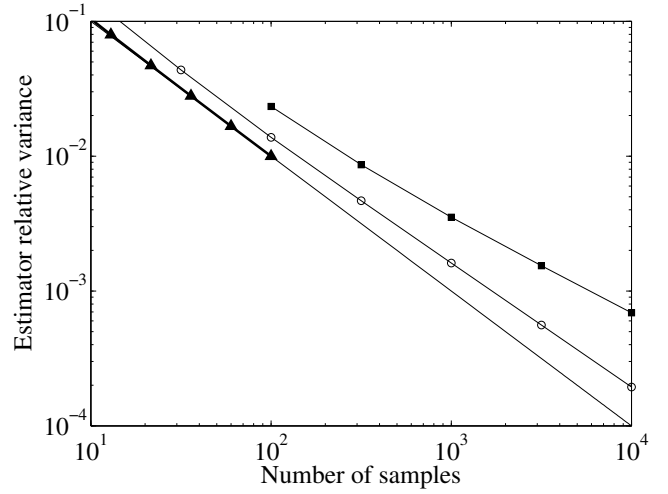


FIG. 6. Variance of the spatial-average estimator in the 1D (triangles), 2D (circles) and 3D (squares) cases with respect to the ensemble-mean estimator (solid line with no markers), as a function of the discrete number of samples.

each pair of points. Consequently, in the 1D case, doubling the number of (independent) samples, i.e. doubling  $a/\lambda$ , will reduce the estimator variance  $\sigma_\epsilon^2$  of a factor 2, confirming the slope obtained in the 1D case in Fig.1.

To compare  $G_\Omega$  with the convergence rate  $1/M_r$  of the ensemble estimator, we need to use a discrete spatial-average estimator in order to have the number samples as a common parameter.

It has been shown<sup>18</sup> that the relative-error variance of the discrete spatial-average estimator can be fairly approximated by  $G_\Omega$ , as long as the geometric parameter  $a$  is greater than  $3/2 \lambda$ . Accordingly, assuming a sufficient number of samples allows using (56) to describe properly the asymptotic convergence rate of the discrete spatial-average estimator. In order to compare the convergence rates of the two estimators, we need to introduce a number of spatial samples whose arrangement will impact inevitably on the accuracy of the spatial-average estimate.

We choose a regular arrangement of the samples separated by a distance  $\lambda/2$ . This arrangement allows, on the one hand, to have samples easily placed and on the other hand, to have a zero-correlation in many cases. If  $N_s$  is the number of samples in the 1D case ensuing from the regular arrangement,  $N_s^2$  and  $N_s^3$  will be the samples obtained in the 2D-square and 3D-cube cases, respectively. Moreover, if a length  $a$  is assumed for the 1D case, the integer part of  $1 + a/(\lambda/2)$  correspond to the number of samples. Equivalently, for a sufficient value of  $a$ , we have approximately  $2a/\lambda$  samples along a line or along the side of a square and a cube of length  $a$ . Consequently, using the asymptotic approximations of  $G_\Omega$  we can compute the following asymptotic convergence rates

$$G_\Omega(N_s) \propto \begin{cases} N_s^{-1} & \text{in the 1D case} \\ N_s^{-0.9} & \text{in the 2D case} \\ N_s^{-0.666} & \text{in the 3D case} \end{cases} \quad (58)$$

Using the results of  $G_\Omega$  shown in Fig.1, we plot in Fig.6 the variance of the relative error of both estimators as a function of the number of samples.

The 1D case and the ensemble estimator being based on independent samples, they converge with the same rate. Whereas, the 2D and 3D cases are affected by spatial correlation. Consequently, their convergence rates are lower. Accordingly, for the scenarios where the ideal diffuse field model can be assumed as reliable, the often-invoked equivalence assumption between spatial-average (in the 2D and 3D cases) and ensemble-average estimators does not hold.

## V. CONCLUSION

The present study showed that the spatial- and ensemble-average estimators cannot be regarded as equivalent, since their convergence rates differ. The results were obtained using a wave-theory approach based on a finite number of plane waves; the plane-wave model is equivalent to a modal expansion, while allowing to explicitly express the spatial dependence of the sound-field distribution, well-suited to the study of the spatial estimator.

For an infinite number of plane waves the spatial-averaging estimates coincide with the results presented forty years ago using an ideal-diffuse field model. In the general case, the present work points out theoretically that the number of plane waves induce a limitation of the spatial-estimator accuracy, emphasizing the uselessness of over-sampling. This effect has never been predicted to the best of our knowledge. On the basis of practical cases, the results show that this effect impacts the convergence rate for frequencies about ten times Schroeder's frequency.

Although the model is physically justified and theoretically reliable, it would be interesting to establish this limitation on the basis of experimental measurements. These studies would provide an experimental evidence of the maximum accuracy that can be expected.

## APPENDIX A: IDENTIFICATION OF THE VARIANCE

In order to identify the relative-ensemble variance  $\sigma_{r,p^2}^2$  of the mean-square pressure defined as,

$$\sigma_{r,p^2}^2 = E \left[ \left( \frac{p_\omega^2(\mathbf{r}) - \mu_{p_\omega^2}(\mathbf{r})}{\mu_{p_\omega^2}(\mathbf{r})} \right)^2 \right] = E [\epsilon^2], \quad (\text{A1})$$

we must consider the error expression in (13) in a single point. The matrix  $\mathbf{P}$  is then made of ones. Consequently, the matrix being of unitary rank, we have only a single non-zero eigenvalue  $\lambda_1$  such as,

$$\lambda_1 = N. \quad (\text{A2})$$

Accordingly, (32) can be expressed with the following simpler form,

$$E_w [\epsilon^2] = \nu_4 - 1. \quad (\text{A3})$$

Recalling that  $\nu_2^2 = 1$ , the final variance is obtained computing the conditional average on the  $\{\hat{k}\}$  set. However,  $\nu_4$  is independent of the  $\{\hat{k}\}$  set, finally yielding

$$\sigma_{r,p^2}^2 = \nu_4 - \nu_2^2. \quad (\text{A4})$$

- <sup>1</sup> M. Schroeder, "Statistical parameters of the frequency response curves of large rooms", *J. Audio Eng. Soc* **35**, 299–305 (1987).
- <sup>2</sup> M. Schroeder and K. Kuttruff, "On frequency response curves in rooms. comparison of experimental, theoretical, and monte carlo results for the average frequency spacing between maxima", *J. Acoust. Soc. America* **34**, 76 (1962).
- <sup>3</sup> R. Lyon, "Statistical analysis of power injection and response in structures and rooms", *J. Acoust. Soc. America* **45**, 545 (1969).
- <sup>4</sup> J. Davy, "The relative variance of the transmission function of a reverberation room", *Journal of Sound and Vibration* **77**, 455–479 (1981).
- <sup>5</sup> R. Weaver, "On the ensemble variance of reverberation room transmission functions, the effect of spectral rigidity", *Journal of Sound and Vibration* **130**, 487–491 (1989).
- <sup>6</sup> R. Waterhouse, "Statistical properties of reverberant soundfields", *J. Acoust. Soc. America* **35**, 1894 (1963).
- <sup>7</sup> F. Jacobsen and A. Molares, "The ensemble variance of pure-tone measurements in reverberation rooms", *J. Acoust. Soc. America* **127**, 233 (2010).
- <sup>8</sup> C. Balachandran, "Random sound field in reverberation chambers", *J. Acoust. Soc. America* **31**, 1319 (1959).
- <sup>9</sup> F. Jacobsen and T. Roisin, "The coherence of reverberant sound fields", *J. Acoust. Soc. America* **108**, 204 (2000).
- <sup>10</sup> H. Kuttruff, *Room acoustics*, chapter 3, 86–88 and 76, 5th edition (Spon Press, Oxon) (2009).
- <sup>11</sup> W. Joyce, "Sabine's reverberation time and ergodic auditoriums", *J. Acoust. Soc. America* **58**, 643 (1975).
- <sup>12</sup> M. Witting, *Modelling of diffuse sound field excitations and dynamic response analysis of lightweight structures*, chapter 2, 10 (Herbert Utz Verlag, München) (1999).
- <sup>13</sup> M. Schroeder, "Spatial averaging in a diffuse sound field and the equivalent number of independent measurements", *J. Acoust. Soc. America* **46**, 534 (1969).
- <sup>14</sup> M. Schroeder, "Effect of frequency and space averaging on the transmission responses of multimode media", *J. Acoust. Soc. America* **46**, 277 (1969).
- <sup>15</sup> D. Lubman, "Spatial averaging in a diffuse sound field", *J. Acoust. Soc. America* **46**, 532 (1969).
- <sup>16</sup> D. Lubman, "Spatial averaging in sound-power measurements", *J. Acoust. Soc. America* **45**, 337 (1969).
- <sup>17</sup> D. Lubman, R. Waterhouse, and C. Chien, "Effectiveness of continuous spatial averaging in a diffuse sound field", *J. Acoust. Soc. America* **53**, 650 (1973).
- <sup>18</sup> R. Waterhouse and D. Lubman, "Discrete versus continuous space averaging in a reverberant sound field", *J. Acoust. Soc. America* **48**, 1 (1970).
- <sup>19</sup> P. M. Morse and K. U. Ingard, *Theoretical Acoustics*, chapter 9, 556–558 (McGraw-Hill, Inc., New York) (1968).
- <sup>20</sup> R. Lyon, "Needed: a new definition of diffusion", *J. Acoust. Soc. America* **56**, 1300 (1974).
- <sup>21</sup> P. Chinnery and V. Humphrey, "Experimental visualization of acoustic resonances within a stadium-shaped cavity", *Physical Review E* **53**, 272 (1996).
- <sup>22</sup> A. Papoulis, *Probability, random variables, and stochastic processes*, chapter 9, 245–247, 2nd edition (McGraw-Hill, Inc., New York) (1984).
- <sup>23</sup> F. Jacobsen and A. Molares, "Sound power emitted by a

- pure-tone source in a reverberation room”, J. Acoust. Soc. America **126**, 676 (2009).
- <sup>24</sup> H. Weyl, “Das asymptotische Verteilungsgesetz der Eigenwerte linearer partieller Differentialgleichungen (mit einer Anwendung auf die Theorie der Hohlraumstrahlung)(Asymptotic distribution of the partial differential equations eigenvalues (with an application to black body theory))”, Mathematische Annalen **71**, 441–479 (1912).
- <sup>25</sup> W. Chu, “Note on the independent sampling of mean-square pressure in reverberant sound fields”, J. Acoust. Soc. America **72**, 196–199 (1982).

# Goodness-Of-Fit tests in Reverberation Chambers : Is Sample Independence Necessary?

Florian Monsef\*, Ramiro Serra†, Andrea Cozza\*

\*GeePs UMR 8507, Univ Paris-Sud, CentraleSupelec, CNRS, UPMC, Gif-sur-Yvette, France,

E-mail: florian.monsef@geeps.centralesupelec.fr

†Eindhoven University of Technology, Eindhoven, The Netherlands.

**Abstract**—Goodness-of-fit (GoF) tests are interesting tools to test the overmodedness of the field inside a reverberation chamber (RC). In the definition of GoF tests independent and identically-distributed samples are required. In the present paper we focus on the effect of partial data correlation on GOF tests. We analyze the sensitivity of the most common GOF tests used in electromagnetic compatibility. The results presented herein are based on numerical and experimental data. We show that most of GOF tests are insensitive to correlations up to rather high values depending on the type of GOF test chosen. Implications for practical applications are discussed.

**Index Terms**—Autocorrelation Coefficient, Data Independence, Random Fields, Reverberation Chambers, Statistical Electromagnetism.

## I. INTRODUCTION

Statistical dispersion of field-related quantities in a reverberation chamber (RC) is conditioned by the degree of homogeneity of the field inside the chamber. Ideally, the excitation of a minimum number of modes [1] allows the field to approximatively follow a Gaussian law.

It is common to quantify stirrer efficiency by assessing the number of stirrer steps for which the field can be regarded as reasonably uncorrelated between two contiguous steps [2]. The question of how to estimate this number of positions has been the topic of many papers [3]–[6] and will not be considered here. If the case of the standards are considered, a large number of samples is used in order to obtain a more accurate estimate of the autocorrelation coefficient, from which a decimation factor can then be deduced. This decimation factor allows reducing the number of stirrer positions to the one that ideally corresponds to independent test configurations within the RC, avoiding redundant test results and ultimately saving time.

In order to check the Gaussian fit of the field, goodness-of-fit (GOF) tests can be used as explained in [2]. To the best of our knowledge, it is not clear if the set of data to use must be the decimated one, i.e., the set made up of uncorrelated data, or the complete set of data which provides more samples, even though partially correlated. It is indeed commonly thought that GoF need independent samples to be applied. In practice, samples being correlated, the condition of using independent samples is cut short and one may wonder about the possible use of correlated (and whence dependent) data.

The present work aims to give some insight into this question. To that end, we will recall in Section II the most common

GOF tests used in the context of RCs, while Section III will analyze GOF outcomes according to the autocorrelation model used to generate correlated data. Section III-C will also focus on GOF results but in the case of measured data. Finally, a tentative interpretation of the results will be proposed in Sec. IV.

Our findings show to what extent different GOF tests usually implemented within the EMC community are sensitive to data autocorrelation.

## II. GOODNESS-OF-FIT TESTS

In order to determine if a set of samples belong to a given probability distribution, GOF tests can be used as a statistical decision tool. These tests can be performed, e.g., with the real and/or imaginary parts of the electric field in order to check if these follow a Gaussian law. But these tests can also be applied to field modulus samples in order to check whether these follow a Rayleigh distribution. In both cases, a *null hypothesis*, referred to as  $H_0$ , is formulated and tested.

There are several existing GOF tests, and, with the same set of data, the outcome can differ from one GOF test to another. This is due to the fact that each GOF is based on a different metric. The question raised herein is not to know which GOF is the more adequate to RC applications but rather to use the most popular ones and to analyze their sensitivity to correlated data. Although not exhaustive, the most commonly encountered ones are the following:

- the  $\chi^2$  test [7],
- The Lilliefors (L) test [8],
- the Kolmogorov-Smirnov (KS) test [9],
- the Anderson-Darling (AD) test [5], [10].

The  $\chi^2$  test determines whether there is a significant difference between the theoretical frequencies of occurrence and the observed frequencies. It tells if the inevitable difference between the expected and observed values is due to stochastic dispersion in the sample, or if it there is a significant underlying difference. The Lilliefors and KS tests both estimate the maximum distance between the empirical cumulative distribution function (*cdf*) and the expected one. The distance is compared to a critical value, often referred to as  $D_{KS}$ , in order to decide whether the sample data belong to the expected distribution. The Lilliefors test uses sample moments unlike KS for which the moments of the expected distribution need to be specified *a priori*. The AD test integrates a weighted

difference between the sample *cdf* and the expected one. The weighted function is such that the test focuses more on the tails of the distribution than in other tests.

In what follows, these GOF tests will be performed on synthetic data generated numerically and on data obtained experimentally.

### III. SENSITIVITY OF GOF ON SYNTHESIZED DATA

In this section we will present an approach where the first lag correlation coefficient is controlled in order to analyze if the outcomes of GOF tests are somewhat related to the degree of correlation.

#### A. Correlation Models

The idea is to generate correlated data to emulate, on average, what one could obtain by using a stirrer in practice. We are interested in generating two different correlation models. This allows us to see if the sensitivity is only linked to the lag-1 correlation, referred to as  $\rho_l$ , or if the correlation model itself has an impact on GOF outcomes.

We consider a set  $x_i$  whose samples follow a standardized normal law. For such a case, let us recall that the lag-1 coefficient is such that  $\rho_l = E[x_i x_{i-1}]$ , where  $E[\cdot]$  is the ensemble average operator.

The first model is a first-order autoregressive (AR(1)) [11] model based on the following recursive equation:

$$\begin{aligned} x_1 &= \eta_1, \\ x_i &= \rho x_{i-1} + \eta_i \sqrt{1 - \rho^2}, \end{aligned} \quad (1)$$

where the random variable  $\eta$  is standardized, i.e.,  $\eta \sim \mathcal{N}(0, 1)$ . For such an AR(1) model, we report in Fig. 1 the autocorrelation function obtained (by using 5000 samples) for  $\rho = 0.3$  and  $\rho = 0.7$ , respectively.

It is clear that  $\rho_l$  corresponds to  $\rho$ .

The second model considered herein is an AR(2) model for the correlation that may exist between a field value obtained at a given position and those obtained at the two preceding positions. The recursive equation reads in that case,

$$x_i = \rho x_{i-1} + \rho' x_{i-2} + \gamma \eta_i. \quad (2)$$

Note that (2) can be regarded as a dynamic system that may be unstable<sup>1</sup> if  $\{\rho, \rho'\}$  are not properly chosen. As in (1), the coefficient weighting  $\eta_i$ , here  $\gamma$ , is set to ensure  $x_i$  to be standardized such that  $\gamma = \sqrt{1 - (\rho + \rho')^2}$ . This condition also provides a restriction on the possible values of  $\rho$  and  $\rho'$  since  $(\rho + \rho')^2$  must be less than 1. The (somewhat arbitrary) choice made to fulfill the constraints on  $\rho$  and  $\rho'$  is such that  $\rho' = 0.25 \rho$ . Although not intuitive, for an AR(2) model,  $\rho_l$  is a function of  $\rho$  and  $\rho'$  such that  $\rho_l = \rho/(1 - \rho')$ , i.e., is larger than for an AR(1) model for a given  $\rho$  and  $\rho' \neq 0$ . In what follows, the number of data per set will be referred to as  $N$ .

#### B. Results

By considering a AR(1) model and by using (1), we generated data used as input to the GOF tests. The simulation

<sup>1</sup>if the poles modulus is larger than 1.

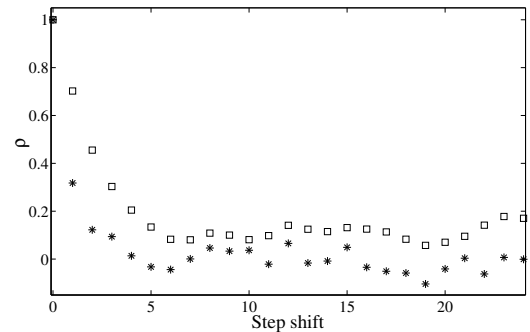


Fig. 1. Autocorrelation function obtained by using the model given by (1) for  $\rho = 0.3$  (asterisks) and  $\rho = 0.7$  (squares), respectively.

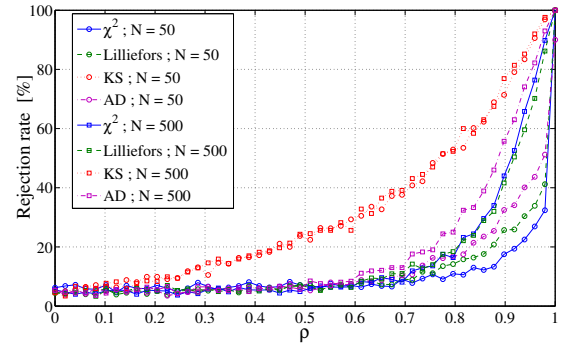


Fig. 2. Rejection rates ( $\alpha = 5\%$ ), obtained with an AR(1) model, for different sample sizes and GOF tests as a function of data autocorrelation.

study is carried out by generating sets of  $x_i$  with  $N = 50$  and  $N = 500$  and for 50 values of  $\rho$  uniformly distributed over [0:1]. To reduce statistical uncertainties, each realization was repeated a thousand times.

Fig. 2 summarizes the percentage of rejected null hypotheses of normality for different GOF tests under study and different sample sizes, for a significance level  $\alpha = 5\%$  (p-value). We stress the fact that these rejection rates are solely coming from data correlation, since the tested data sets come from a normal parent distribution, as described by the process in (1).

It can be seen that the KS test shows a higher sensitivity to data autocorrelation than other GOF tests. It seems also more robust against different sample sizes. From these results, it appears that KS test could be suggested as a way of identifying residual autocorrelation on data, even for low values of  $\rho$ .

In order to highlight the case of the KS test sensitivity, critical values are plotted in Fig. 3 for a varying number of independent realizations<sup>2</sup> and different correlation levels. We can see that  $D_{KS}$  values are shifted upwards as the correlation rises. For  $\rho < 0.5$ , we notice that  $D_{KS}$  is almost insensitive to the degree of correlation, i.e., is almost similar to the *iid* case.

Another interesting way to tackle this analysis is to wonder which correlation level corresponds to an average p-value of 5%, the average being performed over sets of p-values taken from tests repeated a thousand times. Fig. 4 shows the results

<sup>2</sup>that correspond to stirrer states ideally independent in practice.

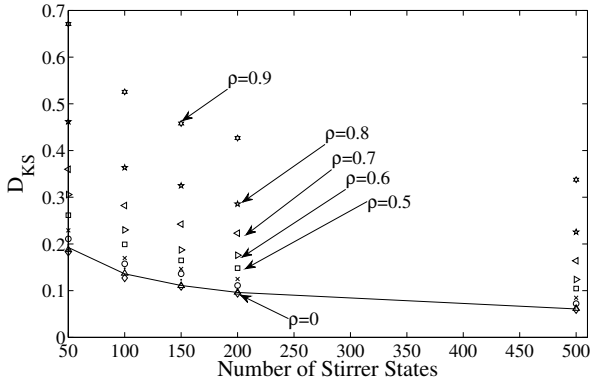


Fig. 3. The KS threshold obtained for different correlation levels as a function of the number of stirrer states. The threshold obtained for the classic (uncorrelated) case (solid line) is shown as well as the thresholds obtained for values of  $\rho$  reported in the figure and running from 0 to 0.9.

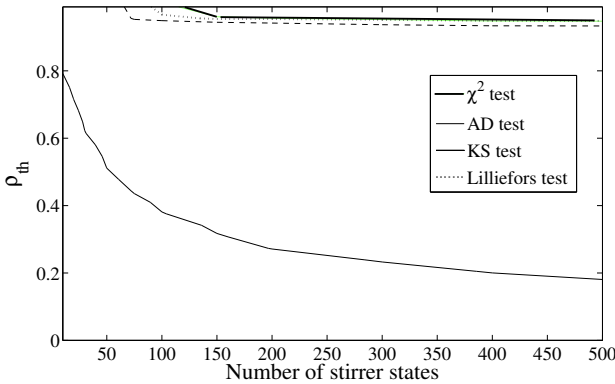


Fig. 4. Correlation threshold leading to an average empirical p-value of 5% as a function of the number of stirrer states.

obtained for the different GOF tests (see legend). We observe that the correlation level for non-KS tests is quite high and almost independent of the number of stirrer states.

Now, let us analyze the rejection rate obtained when using an AR(2) model. Fig. 5 shows the corresponding results. It can be seen that non-KS tests (dashed line, dashed-dotted line and green line) are still insensitive to correlation, whereas the KS rejection rate increases faster (solid line) than what was obtained with an AR(1) model (dotted line). In a way, the AR(2) provides a higher average correlation level<sup>2</sup> which could explain the difference of slopes in the rejection-rate curves obtained for the two AR models considered here.

### C. Experimental Setup and Measurements

We will check now if the sensitivity of the GOF tests studied herein is also observed when experimental data are used.

Measurements were performed in the RC facility of the Eindhoven University of Technology. The chamber is  $4 \times 5 \times 2.85$  (h) m with a lowest useable frequency of 200 MHz, according to the criteria in [2]. A signal generator, a RF power

<sup>2</sup>as for the lag-1 case, for a given  $\rho$ , the lag-2 coefficient is larger for the case of an AR(2) model than for an AR(1) model; it equals  $\rho' + \rho^2/(1 - \rho')$  for the former and only  $\rho^2$  for the latter.

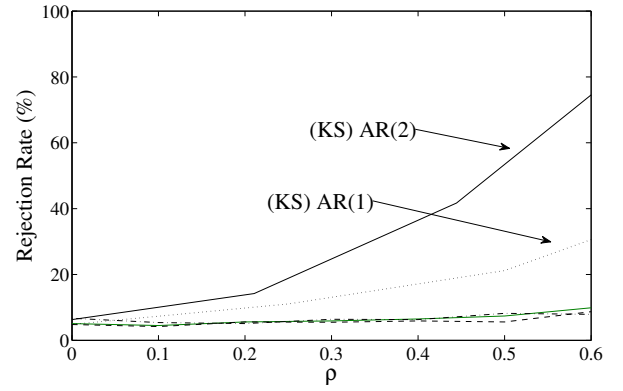


Fig. 5. Rejection rates obtained with an AR(2) model for  $N = 500$ .  $\chi^2$  (dashed line) AD (dashed dotted line) and Lilliefors (Green) do not seem to be sensitive to correlation, unlike the KS test, for which the AR(1) result has been reported for comparison.

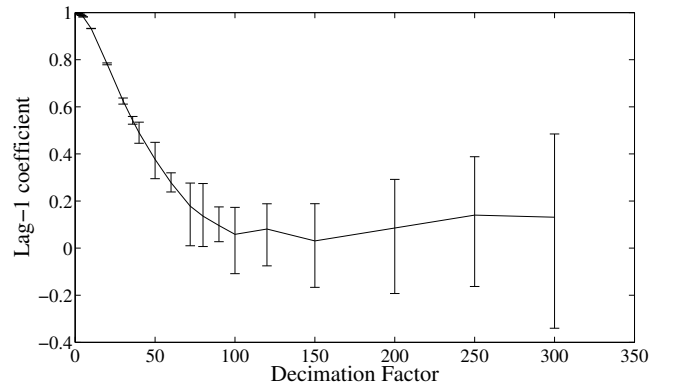


Fig. 6. Average lag-1 autocorrelation coefficient of measured data inside an RC at 1GHz, for different levels of sample decimation (different sample size). Vertical bars stand for 95% confidence intervals.

amplifier and a log-periodic antenna (80 MHz - 1 GHz) were used in order to inject electromagnetic energy into the RC at a fixed frequency of 1 GHz. The three cartesian components of the electric field magnitude were measured by an electric field probe located inside the working volume for a total of 3600 stirrer positions (one field sample every  $0.1^\circ$ ). As is well known, ideally each field component is expected to follow a Rayleigh distribution. By taking such small stirrer step angles, we intend to generate highly correlated data that are also reasonably Rayleigh distributed as well.

The procedure is to start with the complete set of 3600 samples, estimate  $\rho_l$  and apply the different GOF tests. Subsequently, we will decimate the set, in order to get a lower  $\rho_l$  (as well as a lower number of samples) and again apply the different GOF tests. We perform this process with increasing decimation until reaching a set of 12 samples. Fig. 6 shows the estimated  $\rho_l$  by using the three field components as a function of the sample size. As expected, the degree of correlation lowers as the decimation factor increases.

Three different GOF tests were applied to the increasingly decimated data: the  $\chi^2$ , the KS, and the AD tests. The Lilliefors test could be applied to test against a Rayleigh

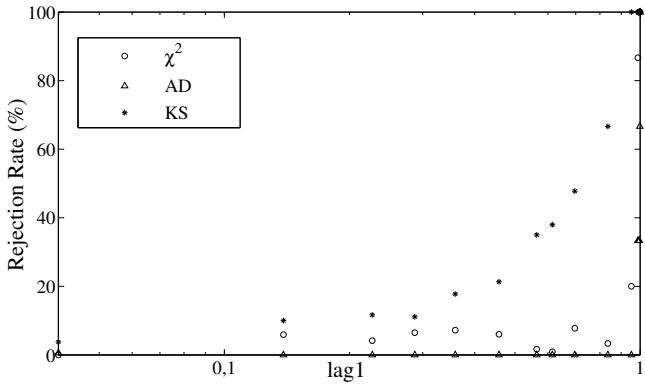


Fig. 7. Rejection rates ( $\alpha = 5\%$ ) for different GOF tests (see legend) as a function of lag-1 autocorrelation for measured data.

distribution but tables needed for that specific case are not available. Fig. 7 highlights the rejection rates as a function of lag-1 correlation for the measured (and decimated) sets of data. Similar conclusions as from the simulation study can be drawn: GOF tests other than the KS appear insensitive to data autocorrelation, even for relatively high values of  $\rho_l$ , whereas KS tests seem to be as sensitive as what was observed with numerical results.

#### IV. DISCUSSION

To understand the pertinence of the results presented in the previous sections, it is worth recalling that the main effect of correlation is to reduce the range value spanned by the successive data samples, by introducing a direct dependence, roughly said, a sort of drag or inertia.

This has an impact on the number of bins that need to be set for the  $\chi^2$  test. As long as the correlation allows the data to span a sufficiently wide range of values to balance the frequencies in the different classes according to Cochran's criterion, the  $\chi^2$  test remains operational. When the correlation becomes too strong, the values spread collapses to a narrow value interval that makes possible only the definition of a single bin. And then the test fails.

The same idea can be transposed to the AD test where the empirical *cdf* fails to be representative of the whole real distribution; only a small portion of the *cdf* becomes accessible and the comparison to a reference distribution becomes no longer possible.

Concerning the KS test, the outcome is conditioned by Kolmogorov statistics. This statistics are sometimes called the Brownian bridge that assumes a random Brownian motion. Variations are due to trajectories, assumed to be independent. This independence is not the same concept required for independent data samples, as repeatedly used throughout the present work. However, a causality seems to exist. The correlation has an impact on the KS critical value, but to the best of our knowledge, there is no simple relation between the proper  $D_{KS}$  value and  $\rho_l$ . From the results presented in the previous section, the typical critical value  $1.36/\sqrt{N}$  (solid line in Fig. 3) seems too be low when correlation intervenes, such that  $H_0$  is often rejected.

Finally, the Lilliefors test seems to be more robust by using sample moments than the KS test, but it is not easy to be more specific on the reasons that make it more robust.

#### V. CONCLUSIONS

Uncorrelated data were shown not to be necessary when performing  $\chi^2$ , Anderson-Darling, or Lilliefors GOF tests. It seems that these tests fail when a correlation of about 90% is reached. However, the Kolmogorov-Smirnov test was shown to be very sensitive to correlation. These results were obtained by using synthetic data and experimental data. The rejection rate obtained highlighted the same clear trends.

As stated in standards, GOF evaluates the mismatch between the measured and the theoretical (ideal) distribution functions of field or power density. As highlighted in the present work, an RC user can perform some of these GOF tests without caring about the possible correlation that may exist between samples. In other terms, if the test is well chosen, there is no need to decimate the data to have an insight on the overmodedness of the chamber.

As a perspective, the KS GOF test could be thought as a way to detect correlation in scenarios where the data distribution is known in advance.

#### REFERENCES

- [1] F. Monsef, "Why a Reverberation Chamber Works at Low Modal Overlap," *IEEE Transactions on Electromagnetic Compatibility*, vol. 54, no. 6, pp. 1314–1317, 2012.
- [2] *Reverberation chamber test methods*, International Electrotechnical Commission (IEC), Std. 61 000-4-21, 2011.
- [3] F. Moglie and V. Primiani, "Analysis of the independent positions of reverberation chamber stirrers as a function of their operating conditions," *IEEE Transactions on Electromagnetic Compatibility*, vol. 53, pp. 288–295, 2011.
- [4] S. Pfennig and H. Krauthausen, "A general method for determining the number of independent stirrer positions in reverberation chambers," in *Electromagnetic Compatibility (EMC EUROPE), 2012 International Symposium on*. IEEE, 2012, pp. 1–6.
- [5] C. Lemoine, P. Besnier, and M. Drissi, "Estimating the effective sample size to select independent measurements in a reverberation chamber," *IEEE Transactions on Electromagnetic Compatibility*, vol. 50, no. 2, pp. 227–236, 2008.
- [6] O. Lundén and M. Backstrom, "Stirrer Efficiency in FOA Reverberation Chambers. Evaluation of Correlation Coefficients and chi-squared tests," in *IEEE International Symposium on Electromagnetic Compatibility*, vol. 1. IEEE, 2000, pp. 11–16.
- [7] J. Kostas and B. Boverte, "Statistical Model for a Mode-Stirred Chamber," *IEEE Transactions on Electromagnetic Compatibility*, vol. 33, no. 4, pp. 366–370, 1991.
- [8] F. Monsef and A. Cozza, "Goodness-of-fit tests in radiated susceptibility tests," in *Workshop on Aerospace EMC, 2012 Proceedings ESA*. IEEE, 2012, pp. 1–5.
- [9] P. Corona, G. Ferrara, and M. Migliaccio, "Reverberating chambers as sources of stochastic electromagnetic fields," *IEEE Transactions on Electromagnetic Compatibility*, vol. 38, no. 3, pp. 348–356, 1996.
- [10] V. Mariani Primiani and F. Moglie, "Numerical simulation of reverberation chamber parameters affecting the received power statistics," *IEEE Transactions on Electromagnetic Compatibility*, vol. 54, no. 3, pp. 522–532, 2012.
- [11] C. Lemoine, P. Besnier, and M. Drissi, "Using autoregressive models to estimate the number of independent samples available with stirrer rotation in reverberation chamber," in *Electromagnetic Compatibility, 2007. EMC Zurich 2007. 18th International Zurich Symposium on*. IEEE, 2007, pp. 469–472.

# Why a Reverberation Chamber Works at Low Modal Overlap

Florian Monsef, *Member, IEEE*

**Abstract**—The physical parameter well adapted to assess the degree of overmodedness of a reverberation chamber (RC) is the number  $M_M$  of modes overlapping in a mode bandwidth. The lowest usable frequency of an RC often corresponds to a low modal overlap of one or two modes. Notwithstanding, in spite of this poor number of modes the RC still works. We show, using Monte Carlo simulation, that the number of modes must, in fact, not be restrained to  $M_M$  and that the number of modes contributing to the field statistics can be, even at low modal overlap, somewhat larger than expected.

**Index Terms**—Cavity resonators, electromagnetic compatibility (EMC), modal analysis, parametric statistics, reverberation chamber (RC).

## I. INTRODUCTION

IN RECENT years, there has been a considerable interest in understanding the physics of reverberation chambers (RC) used for electromagnetic (EM) test methods [1]. Due to the complexity of the system, a statistical approach is often adopted [2]–[5] and considers the EM field as a superposition of normal modes [6] or, alternatively, as a superposition of plane waves [7]. The former allows for a more physical description, whereas the latter can be regarded as a proper first-approximation model only if the RC is well overmoded. For this regime, the commonly accepted statistical distribution of the electric energy follows a chi-squared distribution with 6 degrees of freedom (DOF). This distribution is asymptotic and assumes an infinite number of modes to be uniformly excited at working frequency in a continuous wave mode.

In reality, the frequency response of each mode corresponds to a Lorentzian whose influence becomes negligible beyond a certain bandwidth. Accordingly, as shown in Fig. 1, one may look for the effective bandwidth  $B_e$  that includes the dominant modes.

Intuitively, the  $-3$ -dB bandwidth of a mode, referred to as  $B_M$ , can be thought of as being the right frequency bandwidth into which the dominant modes fall. This intuition may probably ensue from the analogy that one may make, consciously or unconsciously, with filtering theory, where the  $-3$ -dB bandwidth is regarded as the frequency band beyond which the attenuation is often regarded as sufficient.

Moreover,  $B_M$  is an easy assessable quantity in the context of an RC, and the modal overlap, or degree of overmodedness,

Manuscript received September 7, 2012; accepted September 13, 2012. Date of publication October 25, 2012; date of current version December 14, 2012.

The author is with the Laboratoire des Signaux et Systèmes, Département de Recherche en Electromagnétisme, UMR 8506 Univ Paris-Sud, SUPELEC, CNRS 91190 Gif-sur-Yvette, France (e-mail: florian.monsef@lss.supelec.fr).

Color versions of one or more of the figures in this paper are available online at <http://ieeexplore.ieee.org>.

Digital Object Identifier 10.1109/TEMC.2012.2222028

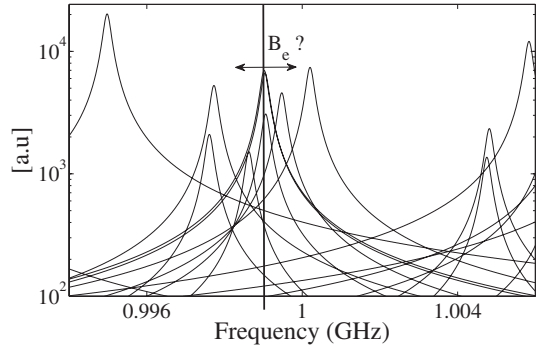


Fig. 1. Illustration of the modal overlap.  $B_e$  is the effective frequency extension to assess, centered around a working frequency (vertical solid line).

conveniently refers to the number of modes found within this bandwidth.

The aim of this short paper is to check whether this notion of *modal overlap* suffices to provide the right order of magnitude on the number of effective modes contributing to the field statistics.

The determination of such a number obviously cannot be controlled by experimental means, making us resort to numerical methods with which the number of modes can easily and arbitrarily be set.

In the first part of this paper, the field model adopted will be presented. The second step consists in validating the numerical approach by checking that the statistical moments fit those obtained experimentally. This validation allows to proceed to a parametric analysis aimed at finding the number of excited modes.

## II. FIELD MODEL

To model the physics in an RC, a modal approach is used, as in [4]. The electric field  $\mathbf{E}$  at a position  $\mathbf{r}$  and at a frequency  $f$  can be approximated as follows:

$$\mathbf{E}(\mathbf{r}, f) \simeq \sum_{i=1}^{M_e} \alpha_i \psi_i(f) \mathbf{e}_i(\mathbf{r}), \quad (1)$$

where  $M_e$  is the number of modes included in  $B_e$ ,  $\mathbf{e}_i$  is the eigenvector of the  $i$ th mode that is assumed not to have a specific form,  $\psi_i$  is the frequency response of the  $i$ th mode, and  $\alpha_i$  is the modal weight, i.e., the coupling constant of the source to the  $i$ th eigenmode.

Limiting our analysis to a generic position  $\mathbf{r}$ , the following factorization for the modal topographies can be used

$$\mathbf{e}_i(\mathbf{r}) = e_i(\mathbf{r}) \hat{\xi}_i(\mathbf{r}), \quad (2)$$

where  $\hat{\xi}_i(\mathbf{r})$  is a unitary polarization vector assumed to be uniformly distributed over  $4\pi$  sr.

Accordingly, (1) can be recast as

$$\mathbf{E}(\mathbf{r}, f) \simeq \sum_{i=1}^{M_e} \tilde{\gamma}_i \psi_i(f) \hat{\xi}_i(\mathbf{r}), \quad (3)$$

where the complex quantities  $\tilde{\gamma}_i$  are regarded as equivalent modal weights, whose real and imaginary parts follow a Normal law, respectively. As stated in [4], the law assumption is not constraining; a uniform law would not greatly change the final results.

It is worth recalling that the number of modes intervening in (1) reads

$$M_e = \int_{f-B_e/2}^{f+B_e/2} m(\phi) d\phi, \quad (4)$$

where  $m(f)$  is the modal density in  $\text{Hz}^{-1}$ . A usual approximation of this latter reads

$$m(f) \simeq \frac{8\pi V f^2}{c^3}, \quad (5)$$

where  $V$  and  $c$  are the volume of the RC and the speed of light, respectively. It is worth stressing that the modal density is, in a strict way, a fluctuating quantity whose mean is given by (5).

### III. NUMERICAL MODEL VALIDATION

The first step before proceeding to a parametric study consists in validating the numerical model based on Monte Carlo (MC) simulations. The effective bandwidth (see Fig. 1) is chosen such as  $B_e = k_M B_M$  where  $k_M$  is referred to as the relative bandwidth extension and is set to 51. We will see in the next section that this value is large enough, ensuring all dominant modes take part in the field statistics. The validation criterion is based on a comparison between the relative variance  $\zeta_W^2$  obtained by numerical simulations and the one obtained experimentally.

#### A. Experimental Setup

The experimental measurements are similar to those used in [4], where both empty and loaded (hybrid absorber made up of four pyramids about 30 cm high, standing in the center of the RC) cases are considered. As a brief recall, the setup takes place in a 13.3-m<sup>3</sup> RC equipped with a 100-step mechanical stirrer blade of 50 cm wide; its lowest usable frequency (LUF) being around 550 MHz. The relative variance is studied over the frequency range of 0.7–3 GHz. The measured quality factors, as a function of frequency, allow to compute the modal bandwidth often regarded as the correlation bandwidth in frequency stirring techniques [6].

For the empty and loaded scenarios, the maximum modal bandwidths are 150 and 375 kHz, respectively. On the frequency range of interest, 1000 linearly spaced frequency bins are used, inducing a 2.3-MHz frequency space between each point. This frequency space is much larger than the maximum value of the modal bandwidths previously mentioned, allowing to consider each measured point as uncorrelated between one another. The uncertainty can then be further minimized by applying a moving average over five contiguous points, followed by a decimation whose factor equals 5 accordingly. It is worth recalling that

modal bandwidths and the modal density are two parameters that can considerably fluctuate. The moving average followed by the decimation aim at extracting the mean trend, in accordance with the model used herein.

In practice, the modal bandwidth  $B_M$  is related to the composite quality factor  $Q$  [8] of the chamber and the working frequency  $f$ , such as  $B_M = f/Q$ .

To compute the number of modes  $M_M$ , we would normally need to use (4) where  $B_M$  would replace  $B_e$ . However, the relative bandwidth  $B_M/f_i$  being of the order of 0.07%, the integral can be reduced, and  $M_M$  reads

$$M_M = m(f)B_M. \quad (6)$$

#### B. MC Simulation Setup

In order to lead this study, we need to vary the number of overlapping modes by modifying the modal density. As stated by (5), two parameters can be changed for this purpose: the frequency  $f$  (like in the experimental approach) or the volume  $V$  of the RC. The former requires us to know how the quality factor varies with frequency. Although this could be done using the quality factor values given in [4], it is more convenient to adopt the latter way, i.e., to vary the volume of the RC at fixed working frequency and fixed quality factor; this also has the main advantage of coping with a single modal bandwidth  $B_M$  set arbitrarily herein to 1MHz; the volume  $V$  will be chosen to obtain the desired modal overlap  $M_M$ , and  $B_e$  has been set large enough (to 51) to include the dominant modes.

Each MC simulation consisted in generating 20 times 50 000 independent random realizations of the electric field described by (3). The resulting estimated variance is averaged over the 20 values.

The statistical distributions of the different quantities are those assumed in [4] as they have been validated experimentally. Accordingly, the real and imaginary parts of the equivalent modal weights were assumed to follow a Normal law. A uniform distribution was assumed for both the polarization of the modes, over  $4\pi$  sr, and the resonance frequencies spread around the working frequency; the uniform distribution of the resonance frequencies is justified by the fact that the maximum frequency extension corresponds to a relative bandwidth of only 1.5%.

#### C. Results

In the experimental case, quality factors being known, the number of overlapping modes in the -3 dB modal bandwidth can easily be computed, using (6). The resulting relative variances as a function of  $M_M$  are shown in Fig. 2 for the empty (solid gray line) and loaded (dashed blue line) cases, respectively.

For the frequency range used, the number  $M_M$  runs from 1 to 13 and from 2.5–35 for the empty and loaded cases, respectively. This explains that the main part of the curve in the empty scenario is rather on the left part of the plot. The ratio of 2.5 found between the minimum values of  $M_M$ , for the empty and loaded

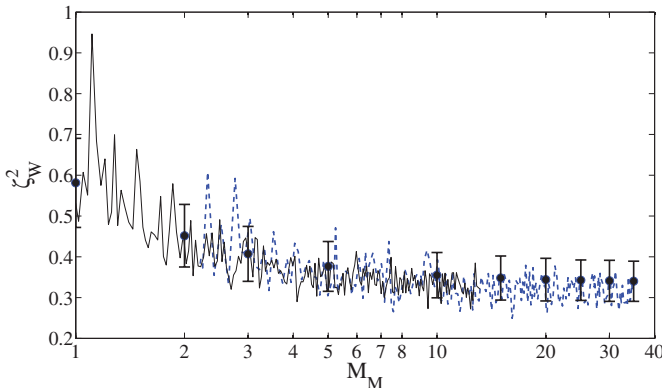


Fig. 2. Relative variance of the electric energy density obtained by MC simulations (full black circles) with the corresponding (vertical) uncertainty bars, and experimentally for the empty (solid gray line) and loaded (blue dashed line) scenario.

cases, is directly linked to the ratio between the maximum value of  $B_M$  obtained for these scenarios.

The results obtained by MC simulations have also been reported in Fig. 2 (full circles) for  $M_M = 1, 2, 3, 5, 10, 15, 20, 25, 30$ , and 35.

It is worth recalling that when experimental variances are deduced from sets made up of 100 samples, an unavoidable uncertainty has to be taken into account. To estimate the latter, MC simulations were used again; this merely consisted in computing 5000 times an estimated relative variance obtained over sets composed of 100 realizations—the standard deviation, referred to as  $\sigma_s$ , was then derived from the estimated-values ensemble. Recalling the five-points average process performed on the experimental data, the resulting standard deviation reads  $\sigma_s/\sqrt{5}$ . The estimated variance being normally distributed, and considering the possible fluctuations on a 95% confidence interval, uncertainty bars of twice the resulting standard deviation are reported in Fig. 2 (vertical bars) accordingly.

We can observe a very good agreement between the results obtained numerically and those obtained experimentally. At large modal overlap, i.e., for  $M_M = 30$  and 35, the relative variance  $\zeta_W^2$  obtained by MC simulation tends to the asymptotic value of  $1/3$  predicted by the central-limit theorem.

#### IV. EFFECTIVE BANDWIDTH AND NUMBER OF CONTRIBUTING MODES

The aim of this section is to assess more finely the effective bandwidth  $B_e$  that has to be considered, if one wants to determine the proper number of excited modes. It is worth recalling that although the number of modes has to be regarded over an infinite frequency range, they do not all contribute in the same manner to the field statistics.

The analysis is based on a parametric study which consists in varying the relative frequency extension  $k_M$ , or equivalently, the effective bandwidth  $B_e$ , and this, for different values of  $M_M$ .

In order to present the different cases on a single plot, we have normalized the relative variance  $\zeta_W^2$  to its convergence value, i.e., to the value reported in Fig. 2; this quantity, referred to as

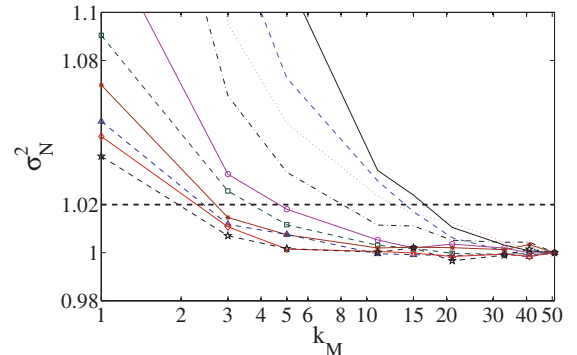


Fig. 3. Normalized relative variance for different values of  $M_M$  as a function of  $k_M$ , the frequency extension. The values of  $M_M$  reported are 1 (solid line), 2 (blue dashed line), 3 (red dotted line), 5 (dashed-dotted line), 10 (magenta solid line with circles), 15 (green dashed line with squares), 20 (brown solid line with asterisks), 25 (blue dashed line with triangles), 30 (red solid line with diamonds), and 35 (dashed line with crosses). The horizontal bold dashed line stands for an accepted error of 2% on the relative variance  $\zeta_W^2$ .

$\zeta_W^2$  is shown in Fig. 3 for  $M_M = 1$  (solid line), 2 (blue dashed line), 3 (red dotted line), 5 (dashed-dotted line), 10 (magenta solid line with circles), 15 (green dashed line with squares), 20 (brown solid line with asterisks), 25 (blue dashed line with triangles), 30 (red solid line with diamonds), and 35 (dashed line with crosses); all these are plotted as a function of  $k_M$  varying from 1 to 51.

For  $M_M = 1$ , the difference between the values of  $\zeta_W^2$  obtained at  $k_M = 41$  and  $k_M = 51$  corresponds to a shift of 0.086%. This shift can clearly be considered as negligible, and the value obtained at  $k_M = 51$  can therefore be regarded as a proper reference. It is noteworthy that the case of  $M_M = 1$  has been chosen because it corresponds, as observed in Fig. 3, to the worst case, i.e., to the case that has the slowest convergence rate.

The effective bandwidth  $B_e$  can now be determined, but is related, in any case, to an arbitrarily chosen criterion. In this study, we determine the effective bandwidth such that the number  $M_e$  of modes included in it, contribute at a 98% level to the field uniformity. In other terms,  $B_e$  is chosen with an accepted error of 2% on the relative variance  $\zeta_W^2$ . This error level of 2% is reported (dashed-bold horizontal line) in Fig. 3.

The intersections obtained between each curve and the 2% threshold line provide the minimum value of  $k_M$ , i.e., the number of modal bandwidths  $B_M$  that have to be considered.

Fig. 4 shows the resulting necessary frequency extension to consider as a function of the number  $M_M$ . The plot shows, quite clearly, that at low modal overlap, the modal bandwidth is not sufficient to properly assess the number of modes taking part to the field statistics. Indeed, for a modal overlap of 1, we can see that more than  $16B_M$  have to be considered, confirming that  $B_M$  must not be regarded as a filter and must not be restricted to its -3-dB bandwidth.

The resulting number of contributing modes can easily be computed by combining (4) and (6), such as

$$M_e = k_M M_M \quad (7)$$

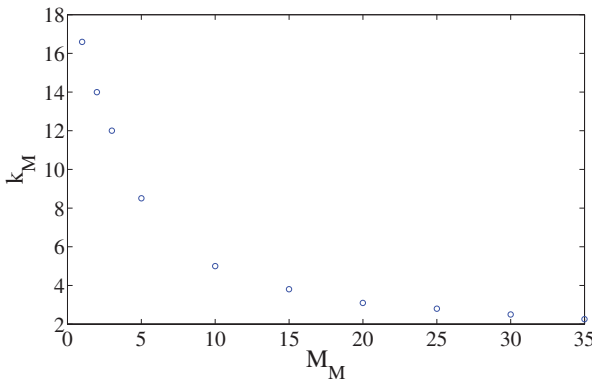


Fig. 4. Minimum value of  $k_M$  to consider for an accepted error of 2% on the relative variance  $\zeta_W^2$ . This value corresponds to the number of modal bandwidth  $B_M$  that includes the modes contributing to 98% of the relative variance  $\zeta_W^2$ .

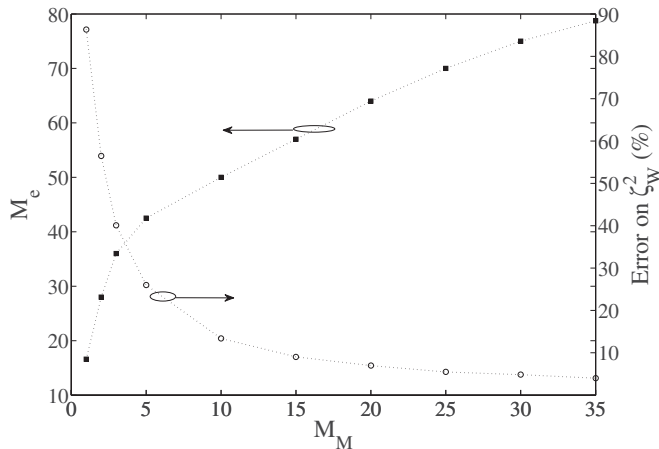


Fig. 5. Number of modes included in the effective bandwidth  $B_e$  using (7) (left y-axis). Error made on the relative variance  $\zeta_W^2$  if the modal bandwidth  $B_M$  is regarded as the right frequency range to use to assess the number of contributing modes.

and the values are reported in Fig. 5 (left y-axis).

We can see that more than 16 modes contribute to 98% of the field uniformity level when a single mode overlaps the modal bandwidth  $B_M$ .

Although the modes excitation is obviously not uniform, the order of magnitude found for  $M_e$  highlights the fact that an acceptable field uniformity can be obtained in an RC.

In the case of our chamber,  $M_M = 1$  is obtained at 550 and 700 MHz for the loaded and empty cases, respectively, i.e., for frequencies approaching the LUF. In practice, this shows that the insertion of some losses into the RC can be quite beneficial to

enhance the field uniformity for wanted and unwanted emissions tests.

As shown in Fig. 4, at a higher modal overlap  $M_M = 35$ , the frequency extension tends to 2, i.e., the modal bandwidth  $B_M$  is still not the right bandwidth to consider to assess the number of contributing modes; according to Fig. 5, 35 modes would be considered instead of about 80. This corresponds to more than a factor 2. This factor must not, however, be misleading. Indeed, the quantity of interest is the field uniformity, i.e., the relative variance  $\zeta_W^2$ .

Accordingly, the pertinent error to look at is the error made on  $\zeta_W^2$  whose values are given in Fig. 3 for  $k_M = 1$ , and summarized in Fig. 5.

For  $M_M = 1$ , we observe an error of 86% that decreases when the modal overlap rises. We can see that considering  $B_M$  at high modal overlap can be more justified; an error of (only) 6% is found for  $M_M = 35$ .

## V. CONCLUSION

The numerical method presented herein offers a very flexible way to determine the number of modes contributing to the field statistics. It has been shown that for a single mode overlap, the number of contributing modes is more than 15 times larger, highlighting the reasons why an RC can be used at low modal overlap.

This study was extended to larger modal overlap cases, providing a quantitative assessment of the number of modes on a wider range.

## REFERENCES

- [1] *Reverberation chamber test methods*, Int. Electrotech. Commission (IEC), Standard 61 000-4-21, 2003.
- [2] L. Arnaut, "Statistics of the quality factor of a rectangular reverberation chamber," *IEEE Trans. Electromagn. Compat.*, vol. 45, no. 1, pp. 61–76, Feb. 2003.
- [3] M. Hoijer, "Maximum power available to stress onto the critical component in the equipment under test when performing a radiated susceptibility test in the reverberation chamber," *IEEE Trans. Electromagn. Compat.*, vol. 48, no. 2, pp. 372–384, May 2006.
- [4] A. Cozza, "The role of losses in the definition of the overmoded condition for reverberation chambers and their statistics," *IEEE Trans. Electromagn. Compat.*, vol. 53, no. 2, pp. 1–12, May 2011.
- [5] C. Lemoine, P. Besnier, and M. Drissi, "Investigation of reverberation chamber measurements through high-power goodness-of-fit tests," *IEEE Trans. Electromagn. Compat.*, vol. 49, no. 4, pp. 745–755, Nov. 2007.
- [6] T. Lehman, "A statistical theory of electromagnetic fields in complex cavities," *Interaction Notes*, vol. 494, 1993.
- [7] D. Hill, "Plane-wave integral representation for fields in reverberation chambers," *IEEE Trans. Electromagn. Compat.*, vol. 40, no. 3, pp. 209–217, Aug. 1998.
- [8] B. Liu, D. Chang, M. Ma, and U. S. N. B. of Standards, *Eigenmodes and the composite quality factor of a reverberating chamber*. Nat. Bureau of Standards, 1983.

# Relative variance of the mean-squared pressure in multimode media: former approaches rehabilitated

Florian Monsef, Andrea Cozza<sup>a)</sup>

Département de Recherche en Électromagnétisme, L2S, UMR8506  
Univ Paris-Sud, SUPELEC, CNRS  
3 rue Joliot Curie - 91190 Gif-sur-Yvette, France

Dominique Rodrigues, Patrick Cellard, Jean-Noel Durocher  
Laboratoire National de métrologie et d'Essais  
29, avenue Roger Hennequin - 78197 Trappes cedex

(Dated: August 19, 2014)

The commonly accepted model of the relative variance of transmission functions in room acoustics is the one derived by Weaver which aimed at including the effects of correlation between eigenfrequencies. An analytical expression of the relative variance was advantageously derived by means of an approximated correlation function. The relevance of the approximation used for modeling such correlation is questioned here. Weaver's model was motivated by the fact that earlier models derived by Davy and Lyon, based on independent eigenfrequencies assumptions, led to an overestimation with respect to relative variances found in practice. It is shown that this overestimation is due to an improper definition of the ensemble average applying to the eigenfrequencies that turns out to be at the origin of an inconsistency clearly proven in the present work. Another definition is used that settles the inconsistency and the relative variance values are found to be in good agreement with experimental data. These results rehabilitate former approaches that were based on independence assumptions between eigenfrequencies.

PACS numbers: 43.55.Cs, 43.55.Br, 43.55.Gx

## I. INTRODUCTION

Ensemble variances of the mean-squared pressure and of the sound power have been a topic of interest in room acoustics for more than half a century<sup>1–6</sup>. After the first approach formulated by Schroeder<sup>1,7</sup> valid under the diffuse-field regime assumption<sup>1</sup>, Lyon<sup>8</sup> widened the ability of describing the variability of sound-field related quantities for frequencies below Schroeder's frequency.

To that end, he made use of modal theory, which allowed him to introduce the effect of limited modal overlap in a more formal way. His work is, in our opinion, a work of reference where statistical analysis of input impedances and transmission functions have been studied for 2D and 3D structures. His analysis considered the case for which eigenfrequencies are independent, i.e., for which the spacing of adjacent eigenfrequencies follow a Poisson distribution; he also studied the case of a point source on a plate for which the spacing statistics follow a distribution, referred to as the nearest-neighbor (NN) distribution<sup>2</sup>, for which correlation between eigenfrequencies exist. This distribution was improperly regarded some time ago<sup>9</sup> as a correct model of the level-repulsion effect; for chaotic cavities, the Wigner distribution turns out to be the proper theoretical distribution to consider as stated by random-matrix theory(RMT) [see section 3.1 of Ref.10]. Moreover, it is accepted today that chaotic cavities are systems belonging to the Gaus-

sian Orthogonal Ensemble (GOE).

Relative-variance models were then extended by Davy<sup>2</sup> to cover the case when transmission functions are averaged over multiple (independent) source and receiver positions, and this, for both distributions. Concerning the NN distribution, Davy explained that Lyon's formula was not correct and proposed a corrected one<sup>2</sup>.

Some years later, Weaver<sup>4</sup> proposed another expression of the relative variance of transmission functions. His work was motivated, on the one hand, by the fact that Davy's formula led to an overestimation of relative variances observed in practice, and on the other hand, because the modal-correlation function for GOE systems is rather different from the one obtained by using the NN distribution assumed by Davy<sup>2</sup> and Lyon<sup>8</sup>. The good agreement found with experimental makes it the accepted model today in room acoustics community. The arguments given by Weaver are all the more justified that the Wigner distribution related to GOE systems was in good agreement with experimental results for mesoscopic systems such as microwave<sup>11</sup> and acoustics chaotic cavities<sup>12,13</sup>.

In fact, if one analyzes closely the correlation model used by Weaver<sup>4</sup>, it appears that a somewhat crude approximation of the GOE two-point correlation function is used. To highlight this point, we will recall in section II the different correlation models considered in the literature, and this, in order to provide a better understanding of the limits of Weaver's approximation.

Besides, it is worth recalling that Lyon showed (for a 2D case) [pp.560-561 of Ref.8] that the effect of level repulsion is not that relevant at low modal overlap when

---

<sup>a)</sup>[florian.monsef@lss.supelec.fr](mailto:florian.monsef@lss.supelec.fr)

the variances of input impedances are studied for instance. Because of the high interest for RMT during the two last decades, this finding has been somewhat forgotten apparently. Although based on the NN distribution, the effect of level repulsion highlighted by Lyon motivated the present work for the case of transmission functions. It is worth recalling that the effect of level repulsion shown by Lyon at high modal overlap was challenged by Davy [pp. 458 of Ref.2] but not the one at low modal overlap. This is why Lyon's result raised some doubts and questioning about the overestimation found when comparing the analytical variability expression of transmission functions found at low modal overlap with experimental results, when Poisson distribution is considered. These doubts are also supported by the fact that the relative variance of transmission functions derived under the Poisson assumption has recently led to an analytical expression that was found to be in good agreement for the case of microwave cavities<sup>14,15</sup>.

To highlight these points, the present paper aims at revisiting in section III the derivation of the relative variance of the mean-square pressure by assuming the eigenfrequencies as independent. As we will see, the result differs from Davy's and Lyon's expression. We will present in section IV the origin of the discrepancy and we will show that the revised expression is found to be in good agreement with the experimental results presented in section V.

## II. CORRELATION MODELS

We briefly recall in the present section the concepts needed to understand why, from a theoretical point of view, the claim made by Weaver in the first part of his article<sup>4</sup> is correct. First, we need to recall what is meant by correlation model. To that end, we refer to Lyon's work<sup>8</sup> who gave an interesting contribution on that issue and invite the reader to be aware of the aforementioned work.

We adapt Lyon's approach for the case of a "bilateral" eigenfrequencies spectrum regarded as a random process, referred to as  $x$ , and characterized by a correlation function, referred to as  $\Phi_x(\omega)$ . When the process  $x$  is composed of Dirac's train where each Dirac position is a random variable related to an eigenfrequency,  $\Phi_x(\omega)$  can be expressed as,

$$\Phi_x(\omega) = n_s (\delta(\omega) + S(|\omega|)), \quad (1)$$

where  $n_s$  is the modal density. Constant for a 2D cavity, the modal density can be regarded as locally constant for room cases when a single-tone excitation is considered, an assumption also used by Weaver<sup>4</sup>;  $S(\omega)$  is the probability density of finding two distinct eigenfrequencies spaced by  $\omega$ .

If eigenfrequencies are regarded as uncorrelated the function  $S(\omega) \equiv S_P(\omega)$  is such that [sec. V of Ref.8],

$$S_P(\omega) = n_s, \quad (2)$$

and the result for the Poisson case is obtained. The correlation in (2) states that the probability density is uniform

for any spacing - it means that we have the same probability density of finding two eigenfrequencies at the same frequency than at two different frequencies.

For the case of the NN distribution, the function  $S(\omega) \equiv S_{NN}(\omega)$  is such that [see Sec. V of Ref.8],

$$S_{NN}(\omega) = n_s (1 - \exp(-4n_s\omega)). \quad (3)$$

As explained by Weaver, for GOE systems the function  $S(\omega)$  to consider is the two-point correlation function, commonly referred to as  $R_2(\omega)$ , and expressed as,

$$S_{GOE}(\omega) = R_2(\omega) = n_s (1 - Y_2(\omega)), \quad (4)$$

where  $Y_2(\omega)$  is the cluster function whose expression is given by [pp.109 of [10],[4]<sup>1</sup>]

$$Y_2(\omega) = \left( \frac{\sin(\pi n_s \omega)}{\pi n_s \omega} \right)^2 + \left[ \frac{\pi}{2} \operatorname{sgn}(n_s \omega) - \operatorname{Si}(\pi n_s \omega) \right] \times \left[ \frac{\cos(\pi n_s \omega)}{\pi n_s \omega} - \frac{\sin(\pi n_s \omega)}{(\pi n_s \omega)^2} \right]. \quad (5)$$

It appears clearly that the correlation function is indeed different from the NN case. The important feature of this function is the repulsion effect found at low distance (see pp. 109 of Ref.10) such that the first-order approximation of the two-point correlation function  $R_2(\omega)$  reads,

$$S_{GOE}(\omega) = R_2(\omega) \simeq \frac{\pi n_s \omega}{4}, \text{ for } n_s \omega \ll 1, \quad (6)$$

that can be compared, by using (3), to the first-order approximation that one would have with the NN distribution,

$$S_{NN}(\omega) \simeq 4n_s \omega, \text{ for } n_s \omega \ll 1. \quad (7)$$

The slope in (6) is larger than for the GOE case, which means that the repulsion effect is weaker for the NN case.

Now, if we consider the approximation used by Weaver, the function  $S(\omega) \equiv S_W(\omega)$  is such that,

$$S_W(\omega) \simeq n_s (1 - \delta(n_s \omega)). \quad (8)$$

This approximation was presented as valid at high overlap, an argument that we do not consider appropriate for the following reasons. First, if we relate what is meant by high overlap to a diffuse-field regime, the order of magnitude of  $n_s$  varies from 3 to 10 according to Schroeder's criterion<sup>16</sup>. Second, the approximation could make sense for high distance values  $\omega$ , but it is in contradiction with the distance range over which the level-repulsion effect is to be expected, i.e., for low values of  $\omega$  as stated by Eq. 6 and Eq. 7.

Apart from these arguments, if one compares (8) to (2), both expressions are quite similar except that (8)

---

<sup>1</sup> Note however that the  $\pi$  term preceding the  $\operatorname{sgn}(\cdot)$  operator is missing in [4]

has a Dirac's distribution that does not allow one to find two eigenfrequencies at the same value. In other terms, expression (8) is the correlation function that one would obtain with a Poisson-like distribution that does not allow eigenfrequencies degeneracy, i.e., does not allow two eigenfrequencies to be equal.

It appears that the repulsion effect of GOE systems, as the one described by (6), cannot be invoked by using such approximated model.

This is probably the reason why Lyon chose the NN distribution that allowed him to derive an explicit analytical expression of  $\Phi_x$ . Although the repulsion effect assumed by Lyon is not quantitatively correct, his study on the repulsion effect is of interest and is summarized in Fig. 14 of his work that shows that the variance at low modal overlap of input impedances is not affected by the level repulsion.

Given that Weaver's model is close to a Poisson model and given the study of Lyon on the effect of the repulsion level, the overestimation found for the case of the relative variance of transmission functions in rooms found by assuming independent eigenfrequencies is quite surprising. This motivated to redo the derivation of such quantities in the next section.

### III. RELATIVE VARIANCE OF TRANSMISSION FUNCTIONS

#### A. Sound field

In order to derive the relative-variance expression with the ability to make some connections with Davy's (and Lyon's) works easier, we will start our derivation by adopting the notations used in Ref.2.

For a single-tone excitation, the sound pressure at working angular frequency  $\omega_w$ , is expressed<sup>2</sup> as follows,

$$p(\mathbf{x}, \omega_w) = \sum_m -i\omega \rho c^2 \frac{b_m p_m(\mathbf{x})}{\omega_w^2 - \omega_m^2 - 2i\omega_w \gamma_m}, \quad (9)$$

where  $\rho$  is the ambient density,  $c$  the sound velocity,  $p_m(\mathbf{x})$  is the  $m^{th}$  eigenmode function,  $\gamma_m$  is its related damping constant and  $b_m$  is the coupling coefficient of the volume velocity  $Q(\mathbf{r})$  on the  $m^{th}$  mode at the source location, expressed as,

$$b_m = \frac{1}{V} \int_{(V)} Q(\mathbf{r}) p_m(\mathbf{r}) d\mathbf{r}, \quad (10)$$

where  $V$  stands for the effective volume of the source that contributes to the excitation of the  $m^{th}$  mode.

Using the usual hypothesis stating that, on the one hand, damping is much smaller than  $\omega_w$  and, on the other hand, that the main contribution comes from  $\omega_m$  close to angular working frequency  $\omega_w$ , the sound pressure  $p(\mathbf{x}, \omega_w)$  can be approximated as follows [as in Eq. (A23),

Ref.2],

$$\begin{aligned} p(\mathbf{x}, \omega_w) &\simeq \frac{\rho c^2}{2V} \sum_m p_m(\mathbf{x}) p_m(\mathbf{y}) \\ &\times (h(\omega_w - \omega_m) - ig(\omega_w - \omega_m)), \end{aligned} \quad (11)$$

where,

$$\begin{aligned} h(\omega) &= \frac{\gamma}{\omega^2 + \gamma^2} \\ g(\omega) &= \frac{\omega}{\omega^2 + \gamma^2}. \end{aligned} \quad (12)$$

The rest of the derivation will differ from Davy's and Lyon's approach in the sense that the modal expansion will still be based on an infinite number of modes as required by modal theory.

For brevity, we group the frequency response in a single function, referred to as  $\psi(f)$ , linked to  $h(\omega)$  and  $g(\omega)$  such that,

$$\psi(\omega) = h(\omega) - ig(\omega). \quad (13)$$

Moreover we introduce equivalent modal weights defined as,

$$c_m(\mathbf{x}) = p_m(\mathbf{x}) b_m, \quad (14)$$

and regarded as centered random variables.

So, at working angular frequency  $\omega_w$  the sound pressure can then be restated in a more concise form as follows,

$$p(\mathbf{x}, \omega_w) \simeq A \sum_{m=1}^{\infty} c_m(\mathbf{x}) \psi(\omega_w - \omega_m), \quad (15)$$

where  $A = \rho c^2 / 2$ .

It is worth recalling that Davy worked separately with the functions  $U$  and  $W$  defined as,

$$\begin{aligned} U(\omega) &= \Re(p(\mathbf{x}, \omega_w) / A) \\ W(\omega) &= \Im(p(\mathbf{x}, \omega_w) / A), \end{aligned} \quad (16)$$

where  $\Re$  and  $\Im$  refers to the imaginary and real part of a complex function, respectively.

#### B. Relative variance derivation

Our aim is to derive the relative variance of the mean-squared pressure defined as,

$$\text{RelVar}(|p(\mathbf{x}, \omega_w)|^2) = \frac{\langle |p(\mathbf{x}, \omega_w)|^4 \rangle}{\langle |p(\mathbf{x}, \omega_w)|^2 \rangle^2} - 1. \quad (17)$$

---

<sup>2</sup> except that we directly deal here with the sound field and not the transmission function; this one required in former works an assumption of a point-like source which is not assumed herein.

In order to have more concise expressions we adopt the following notations for the rest of the derivation,

$$\begin{aligned} E_{|\psi|^2} &= \left\langle \sum_m |\psi(\omega_w - \omega_m)|^2 \right\rangle \\ E_{|\psi|^4} &= \left\langle \sum_m |\psi(\omega_w - \omega_m)|^4 \right\rangle \\ E_{|\psi|^2|\psi|^2} &= \left\langle \sum_{k \neq l} |\psi(\omega_w - \omega_k)|^2 |\psi(\omega_w - \omega_l)|^2 \right\rangle, \end{aligned} \quad (18)$$

and  $\mu_n = \langle |c_m|^n \rangle$ , where the brackets  $\langle \rangle$  stand for the average over an ensemble of rooms sharing the same characteristics; in practice the ensemble can be taken in a single room into which the source(s) and receiver(s) are displaced so as to modify the boundary conditions and sample spatially the sound field.

We need then to establish the ensemble average of  $\langle |p(\mathbf{x}, \omega)|^2 \rangle^2$  and  $\langle |p(\mathbf{x}, \omega)|^4 \rangle$ , respectively. For the former it is straightforward to show that,

$$\langle |p(\mathbf{x}, \omega_w)|^2 \rangle = \mu_2 E_{|\psi|^2}. \quad (19)$$

For the latter,  $|p(\mathbf{x}, \omega_w)|^4$  can be expressed as,

$$\begin{aligned} |p(\mathbf{x}, \omega_w)|^4 &= \sum_m |c_m|^4 |\psi(\omega_w - \omega_m)|^4 \\ &+ 2 \sum_{k \neq l} |c_k|^2 |c_l|^2 |\psi(\omega_w - \omega_k)|^2 |\psi(\omega_w - \omega_l)|^2 \\ &+ 2 \sum_m |c_m|^2 |\psi(\omega_w - \omega_m)|^2 \\ &\times \sum_{k \neq l} c_k c_l \psi(\omega_w - \omega_k) \psi^*(\omega_w - \omega_l) + A_{ijkl}, \end{aligned} \quad (20)$$

where  $A_{ijkl}$  is a sum over four indices with, at least, one of them different from the others.

Given the assumption of independence between the modal parameters and recalling that  $\{c_m\}$  sets are made up of centered random variables it follows that,

$$\langle |p(\mathbf{x}, \omega_w)|^4 \rangle = \mu_4 E_{|\psi|^4} + 2\mu_2^2 E_{|\psi|^2|\psi|^2} \quad (21)$$

The relative variance can be recast at this stage as follows,

$$\text{RelVar}(|p(\mathbf{x}, \omega_w)|^2) = \frac{\mu_4 E_{|\psi|^4}}{\mu_2^2 E_{|\psi|^2}^2} + 2 \frac{E_{|\psi|^2|\psi|^2}}{E_{|\psi|^2}^2} - 1. \quad (22)$$

The critical part deals with the computation of ensemble averages involving the power of  $\psi$ . To highlight this point let us start with the term  $E_{|\psi|^2} = \sum_m |\psi(\omega_w - \omega_m)|^2$  in (19) that corresponds, for a given realization, to the sum of the black dots shown in the upper plot in Fig. 1. Under the assumption of quasi identical  $\gamma$  of the most contributing modes, this sum is also obtained approximately by rearranging these dots on the frequency response of the closest mode to working

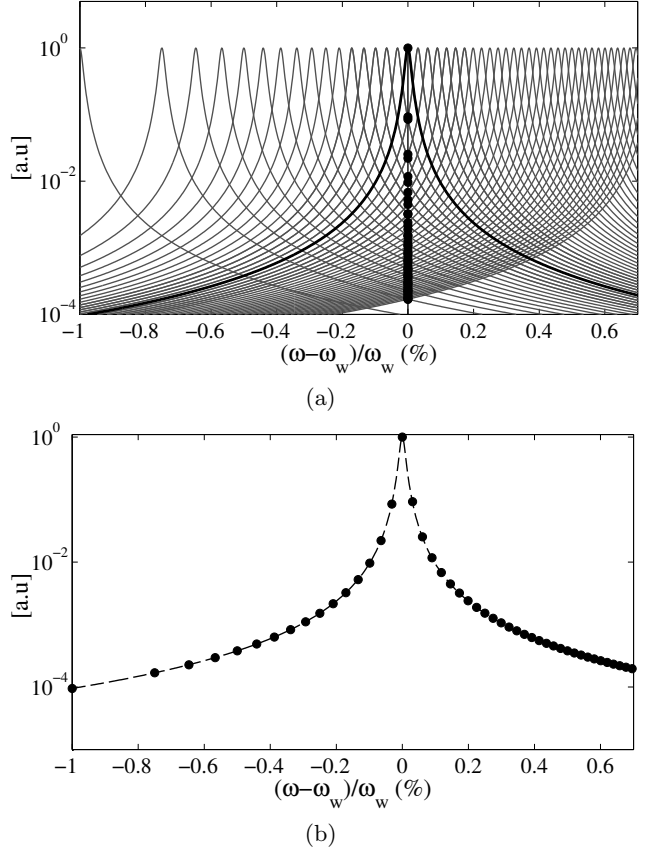


FIG. 1. The effect of modal overlap at a given angular frequency centered about the working angular frequency  $\omega_w$  (upper plot) transposed at the scale of the frequency response of a single mode (lower plot).

frequency, as shown by the lower plot in Fig. 1, so that,

$$\begin{aligned} E_{|\psi|^2} &\simeq \left\langle \int |\psi(\omega - \omega_w)|^2 \sum_m \delta(\omega - \omega_m) d\omega \right\rangle \\ &= \int \int p_{\omega_m}(\omega_m) |\psi(\omega - \omega_w)|^2 \delta(\omega - \omega_m) d\omega d\omega_m, \end{aligned} \quad (23)$$

where  $p_{\omega_m}(\omega_m)$  is the probability density function (*pdf*) of the  $\omega_m$ .

The first line of (23) shows how the density of eigenstates  $\sum_m \delta(\omega - \omega_m)$  gets involved in  $E_{|\psi|^2}$ . The second line allows computing  $E_{|\psi|^2}$  provided that the *pdf* of the  $\omega_m$  is known.

To clarify this point let us recall that the ensemble of realizations on which the brackets  $\langle \rangle$  apply, are the ensemble of pairs of positions source/receiver in a room. The displacement of the receiver (microphone) and above all of the source (given its larger size) in the room modifies the boundary conditions.

Modifications of these boundary conditions have a direct impact on modal topographies, but also on the eigenfrequencies. On an ensemble of realizations, it is reasonable to consider that the eigenfrequency of a given mode will vary on a bounded interval  $\Delta\omega(\omega)$  that can be fre-

quency dependent and that should, at least on average, be the eigenfrequencies mean spacing, i.e., the inverse of the modal density referred to as  $n$  whose first-order approximation for 3D structures is such that [pp.78, Ref.17],

$$n(\omega) \simeq \frac{V\omega^2}{2\pi^2 c^3}, \quad (24)$$

in modes/(rad/s).

If we consider that an eigenfrequency  $\omega_m$  is uniformly distributed over  $\Delta\omega$ , it follows that  $p_{\omega_m}(\omega_m) = n(\omega_m)$ .

Noting that the double integral in (23) can be simplified thanks to the delta function,  $E_{|\psi|^2}$  can be recast as,

$$\begin{aligned} E_{|\psi|^2} &\simeq \int \frac{1}{\Delta\omega(\omega)} |\psi(\omega - \omega_w)|^2 d\omega \\ &= \int n(\omega) |\psi(\omega - \omega_w)|^2 d\omega \end{aligned} \quad (25)$$

As already pointed out in Ref.8, this kind of integral does not have a convergence problem since the modal density for the rooms varies as the square of the frequency and  $|\psi|^2$  varies asymptotically as  $1/f^4$ . Given the sharpness of the resonances adopted within our low damping assumption with respect to the angular frequencies of interest, (25) can be further simplified by considering the modal density “sampled” at working frequency, such that,

$$E_{|\psi|^2} \simeq n(\omega_w) \int |\psi(\omega - \omega_w)|^2 d\omega = \frac{\pi n(\omega_w)}{\gamma}, \quad (26)$$

since  $\int |\psi(\omega - \omega_w)|^2 d\omega$  corresponds to  $h\#h(0) + g\#g(0) = \pi/\gamma$  where  $\#$  corresponds to the convolution operator in Davy's notations (see (A37) in Ref.2).

The same reasoning can be followed with  $E_{|\psi|^4}$  that reads,

$$E_{|\psi|^4} \simeq n(\omega_w) \int |\psi(\omega - \omega_w)|^4 d\omega = \frac{\pi n(\omega_w)}{2\gamma^3}, \quad (27)$$

since  $\int |\psi(\omega - \omega_w)|^4 d\omega$  corresponds to equation (A37), i.e.,  $(1/\gamma) \times \pi/2\gamma$ .

It is easy to show that the ratio  $E_{|\psi|^4}/E_{|\psi|^2}^2$  intervening in (22) is such that,

$$\frac{E_{|\psi|^4}}{E_{|\psi|^2}^2} = \frac{1}{2\pi n(\omega_w) \gamma} = \frac{1}{\pi M} = \frac{1}{M_s}, \quad (28)$$

where  $M_s$  refers to the number of modes overlapping in the statistical bandwidth of a mode, i.e., is  $\pi$  times the number  $M$  of modes overlapping in the -3 dB modal bandwidth.

Adopting the same approach we expand in appendix the derivation of  $E_{|\psi|^2|\psi|^2}$ , that turns out to be,

$$E_{|\psi|^2|\psi|^2} \simeq E_{|\psi|^4} \left( \frac{E_{|\psi|^2}^2}{E_{|\psi|^4}} - 1 \right) \quad (29)$$

Setting  $K_c = \mu_4/\mu_2^2$ , the relative variance for a single-tone excitation reads,

$$\text{RelVar}(|p(\mathbf{x}, \omega_w)|^2) = 1 + \frac{K_c - 2}{M_s}. \quad (30)$$

The usual  $K$  factor being defined as,

$$K = \frac{\langle p_m^4(\mathbf{x}) \rangle}{\langle p_m^2(\mathbf{x}) \rangle^2} = \frac{\langle p_m^4(\mathbf{y}) \rangle}{\langle p_m^2(\mathbf{y}) \rangle^2}, \quad (31)$$

we can relate  $K_c$  to the usual  $K$  factor such that  $K_c = K^2$  and the relative variance reads,

$$\text{RelVar}(|p(\mathbf{x}, \omega_w)|^2) = 1 + \frac{K^2 - 2}{M_s}. \quad (32)$$

Comparing (32) to Davy's (and Lyon's) formula that was found to be<sup>2</sup>,

$$\text{RelVar}(|p|^2) = 1 + \frac{K^2}{M_s}, \quad (33)$$

a clear difference appears in the second term of the right-hand term.

This difference is quite surprising since both models have been derived on an independence assumption of the eigenfrequencies. We explain the origin of this discrepancy in the next section.

#### IV. ORIGIN OF THE DISCREPANCY

Although both approaches assume a Poisson distribution, unlike in Davy's paper<sup>2</sup>, the derivation presented herein does not truncate the modal expansion defined in (9) at any stage. This has the major advantage to avoid the issue of defining an arbitrary criterion that will serve to truncate the modal expansion.

This notwithstanding, we need to clarify the origin of the discrepancy. Given the time that has elapsed since the publication of Ref.2 and Ref.8, the reader may be skeptical and surprised that this discrepancy had not been reported since then. In order to raise any possible doubts, an easy and irrefutable way of checking this inconsistency is to perform Monte Carlo (MC) simulations.

These consisted in computing (9). Specific statistical distributions for each modal parameter were assumed and eigenfrequencies were regarded as independent. An ensemble of values of the mean-square pressure was obtained. The corresponding relative variance was then computed and compared to the analytical expressions given by (32) and (33). We assumed  $p_m(\mathbf{x})$  and  $p_m(\mathbf{y})$  to be normally distributed; the resulting  $K$  factor is therefore equal to 3, which corresponds to the commonly accepted value<sup>18</sup>.

Concerning the MC computations, the question that arises deals with the frequency range over which the eigenfrequencies must be computed. Let us consider a frequency range of about  $k_M$  modal bandwidths about a given working frequency. Fig. 2 shows the evolution of

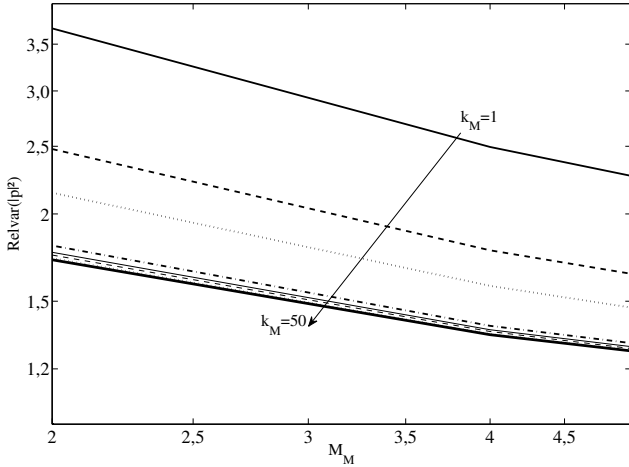


FIG. 2. Influence of the frequency range  $k_M B_M$  on the relative variance of the mean-squared pressure (y-axis) obtained by MC simulation as a function of the average number  $M_M$  of overlapping modes. Several values of  $k_M$  have been considered  $k_M = 1$  (bold solid black line),  $k_M = 2$  (bold dashed black line),  $k_M = 5$  (bold dotted line),  $k_M = 10$  (bold dashed-dotted line),  $k_M = 20$  (solid line),  $k_M = 30$  (dashed black line),  $k_M = 40$  (dotted black line),  $k_M = 50$  (extra bold dashed line).

the relative variance for different frequency ranges, i.e., different values of  $k_M$ . We can see that 50 modal bandwidths are enough to obtain non significant changes in the statistics. Note that  $k_M$  is all the more important to assess that an insufficient frequency range would lead to overestimated values of the variability of the mean-squared pressure.

For reverberation chambers whose reverberation time is around 10 s, this leads to a relative bandwidth of about 1%, which is sufficiently narrow to assume a local constant modal density. The average modal overlap parameter  $M_s$  was controlled by emulating different volumes at fixed working frequency of 1 kHz with an average damping constant of 0.7 rad/sec.

In order to check that the MC simulations are trustworthy we plot the mean values  $\langle U^2(\omega) \rangle$  and  $\langle W^2(\omega) \rangle$  that equal  $n\pi/2\gamma$ ; these mean values were expressed by relations (A45) and (A46) in Davy's work, respectively. Fig. 3 shows the values obtained by MC simulation of  $\langle U^2(\omega) \rangle$  (circles) and  $\langle W^2(\omega) \rangle$  (squares); the analytical expressions given by (A45) and (A46) are also reported (solid line), and this, as a function of the average number of modes  $M_M$  overlapping in the -3-dB modal bandwidth. The good agreement found allows us to consider that (A45) and (A46) are consistent.

The same simulations are used now to check the mean value of the cross product  $U^2(\omega) W^2(\omega)$  given by (A50/A53). Fig. 4 shows the values of  $\langle U^2(\omega) W^2(\omega) \rangle$  obtained by MC simulation (circles) and by using the analytical expression (solid line) given by (A53). The relative error (dashed line) is also reported in Fig. 4 (right y-axis). In order to raise possible doubts about the ana-

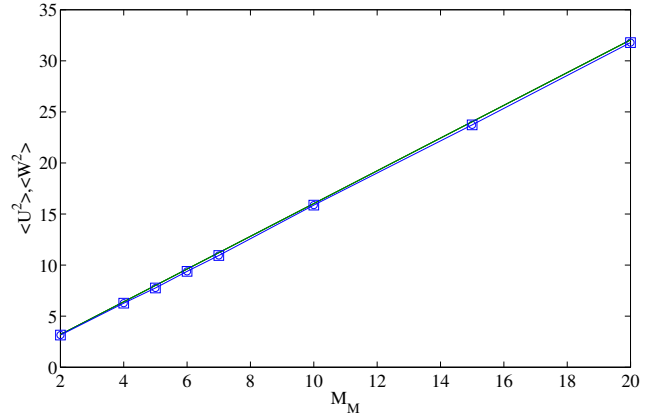


FIG. 3. MC simulation results of  $\langle U^2 \rangle$  (circles) and  $\langle W^2 \rangle$  (squares) as a function of the average number  $M_M$  of overlapping modes. The analytical expressions (which are identical for both quantities) have also been reported (solid line) and are given by eq. (A45) and (A46) of Davy's work<sup>2</sup>, respectively.

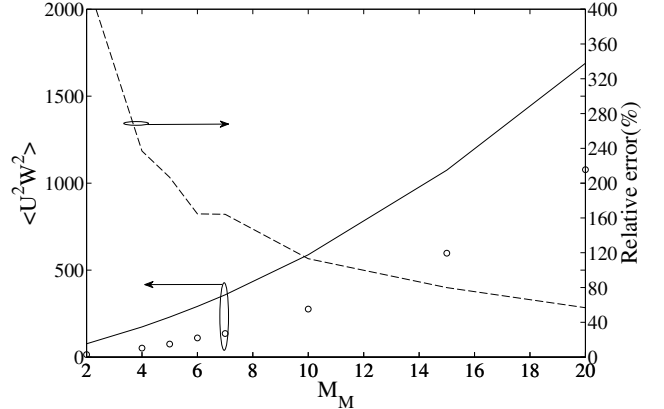


FIG. 4. Evolution of  $\langle U^2 W^2 \rangle$  (left y-axis) as a function of the average number  $M_M$  of overlapping modes obtained by MC simulation (circles) and by using the analytical expression (solid line) given by (A53) in Davy's work<sup>2</sup>. The relative error (right y-axis) is also reported (dashed line).

lytical expression of (A53) reported in Fig. 4, the reader can check that, in the case of single-tone excitation, equation (A53) can be simplified as follows,

$$\begin{aligned} \langle U^2(\omega) W^2(\omega) \rangle &= n \langle p_m^4(\mathbf{x}) \rangle \langle p_m^4(\mathbf{y}) \rangle (h^2 \# g^2(0)) \\ &+ n^2 \langle p_m^2(\mathbf{x}) \rangle^2 \langle p_m^2(\mathbf{y}) \rangle^2 (h \# h(0) g \# g(0)), \end{aligned} \quad (34)$$

since only one receiver and one emitter are considered and  $h \# g(0) = 0$  from (A39); note that  $\#$  refers to the convolution operator in Davy's notations.

We clearly see that the analytical expression of Davy overestimates  $\langle U^2(\omega) W^2(\omega) \rangle$ . The fact that we deal with a single receiver and a single source has the advantage of simplifying (A50) (from which ensues (A53)).

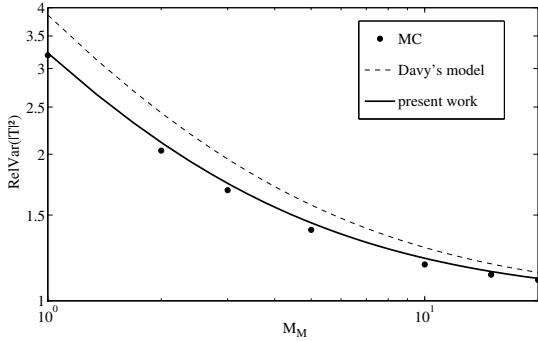


FIG. 5. Relative variances obtained by Monte Carlo simulation (black dots), Davy's model (dashed line) and the model derived in the present work (solid line) as a function of the average number  $M_M$  of overlapping modes. The shift shows that Davy's<sup>2</sup> and Lyon's<sup>8</sup> results are not consistent with the model assumed in their derivation, and overestimates the dispersion of the mean-squared pressure.

If we thoroughly analyze (A50), it appears that Davy double counted some elements in the last term. This double counting is at the origin of the overestimation of  $\langle U^2 W^2 \rangle$ . In other terms the double sum  $\sum_{m,l=1}^K$  should be replaced by  $\sum \sum_{m,l=1, m \neq l}^K$ , where  $K$  stands for a given number of modes spreading over an angular frequency range  $\Omega$ . This “local” overestimation is the cause of the relative-variance discrepancy.

Indeed, Fig. 5 shows resulting relative variances obtained by MC simulations (black dots) and Davy's expression (dashed line) given by (33). We can clearly see a shift that confirms the inconsistency due to the elements pointed out previously and an overestimation of the expected relative variance. Conversely, we can see that the model derived herein (solid line) is consistent with the MC simulations performed on the basis of the assumptions made upon the different modal parameters.

In order to be more accurate in the analysis of the inconsistency, the number of terms counted in the sum was  $K^2$  (that explains the  $n^2$  term in (A53)) instead of  $K(K - 1)$ . It is clear that at high modal overlap both can be confounded, but not at low modal overlap, which is the region of interest. This explains that the error is all the more important as the modal overlap lowers (see Fig. 4).

Now, we may wonder about the possibility to correct Davy's expression by taking into account  $K(K - 1)$  terms instead of  $K^2$  terms. If do so, given that Davy related the ratio  $K/\Omega$  to the modal density such that  $K/\Omega = n$ , it follows that relation (34) reads,

$$\begin{aligned} \langle U^2(\omega) W^2(\omega) \rangle &= n \langle p_m^4(\mathbf{x}) \rangle \langle p_m^4(\mathbf{y}) \rangle (h^2 \# g^2(0)) \\ &+ \left( n^2 - \frac{n}{\Omega} \right) \langle p_m^2(\mathbf{x}) \rangle^2 \langle p_m^2(\mathbf{y}) \rangle^2 (h \# h(0) g \# g(0)), \end{aligned} \quad (35)$$

with the inevitable question of assessing  $\Omega$ . In order to include all the modes in the modal expansion of the sound

field,  $\Omega$  was logically taken to infinity by Davy, but with the inability to isolate only the cross terms in the double sum of (A50/A53). So, where is the problem ?

The problem lays in the definition of the ensemble average of the frequency response that was defined, in the case of  $h^2(\omega - \omega_m)$  for instance, as follows

$$\langle h^2(\omega - \omega_m) \rangle = \frac{1}{\Omega} \int_0^\Omega h^2(\omega - \omega_m) d\omega_m. \quad (36)$$

This expression means that an eigenfrequency is uniformly distributed over  $\Omega$  defined as the frequency range over which the modal expansion of the sound field is considered. Recalling that the ensemble average applies to an ensemble of rooms that share approximately the same characteristics (volume, reverberation time,...), relation (36) means that the 10<sup>th</sup> and the 10000<sup>th</sup> eigenvalues, taken out from this ensemble, would be found to be uniformly distributed over the same frequency range  $\Omega$  that turns out to be infinite ! It is clear that it not so. Instead, each of these will be found to be uniformly distributed (on an ensemble of rooms) over frequency ranges that will likely not overlap. This is why the ensemble average of the frequency responses must be defined as in (25).

Moreover, setting  $K/\Omega = n$  is clearly incorrect for 3D structures for which the modal density is a quadratic function of frequency, i.e., the modal density is non linear. But one may wonder why the analytical expression of  $\langle U^2 \rangle$  and  $\langle W^2 \rangle$  were found to agree with MC simulation as shown in Fig. 3 ? This is due to the fact that  $n$  is indeed the right probability density function to set, but not for the reasons exposed in Ref.2. So, to deal with the cross terms, one need to follow the approach presented in appendix.

The next step consists in checking if the assumptions made on the different modal quantities allows us to find a good agreement with the relative variance of the mean-squared pressure estimated from experimental data.

## V. MODEL VALIDATION

Although the consistency of the model was checked, we need to verify if (32) still overestimates relative variances with respect to those obtained in practice.

To this end we performed measurements in a reverberation chamber at the Laboratoire National de métrologie et d'Essais, whose volume is 218 m<sup>3</sup>.

The ensemble average estimation was based on 64 realizations that consisted in displacing pairs of receiver/source positions. Although it is of common practice to characterize the chamber with noise signals such as the interrupted noise method<sup>19</sup>, we chose to use a calibrated pulse with a “witness” microphone close to the source in order to check the reproducibility of the emitted pulse. This pulse was such that no zero appears in the [0:10 kHz] frequency range.

The exits of the microphones were amplified and then plugged into a digital scope configured in such a way as to access 4 million temporal samples with a sampling frequency of 200 kHz. A 50 kHz anti-aliasing filter was used

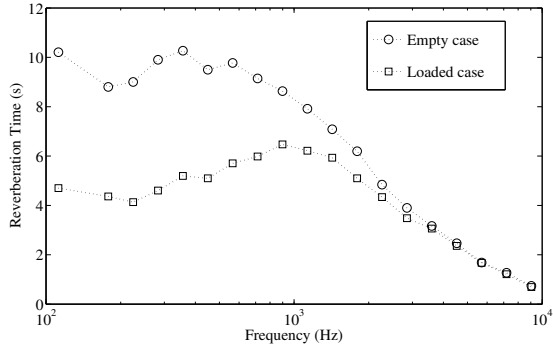


FIG. 6. Estimated reverberation times obtained when the reverberation chamber is empty (circles) and loaded (squares), respectively

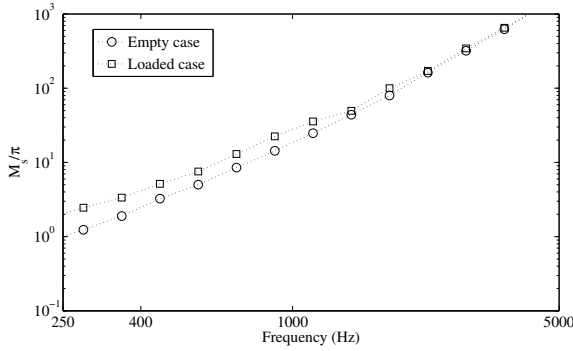


FIG. 7. Estimation of the average number of overlapping modes in the half-width bandwidth of a mode when the reverberation chamber is empty (circles) and loaded (squares), respectively.

and the spectra were computed by using Fast Fourier Transform. The resulting resolution was 0.05 Hz in the frequency domain.

The frequency range of interest has been reduced to [250:10kHz] in order to visualize the diffuse and non-diffuse regimes in the chamber, and this, with a minimum of one mode overlapping in the modal bandwidth.

The chamber was used in two configurations. In the first configuration the chamber was empty and in the second case, some absorbers were introduced (loaded case). Reverberation times, classically referred to as  $T_{60}$ , were computed over one-third octave bands and are shown in Fig. 6 for the empty (circles) and loaded (squares) cases, respectively.

Using the modal density given by (24), we estimated the average number  $M$  of overlapping modes; these are shown in Fig. 7 for the empty (circles) and loaded (squares) cases, respectively. The effect of the losses is especially observed at low frequencies.

As relative variances are estimated with no spatial averaging, the unavoidable dispersion is expected to be large. In order to lower this dispersion and to be able to extract the mean trend, we made use of frequency averag-

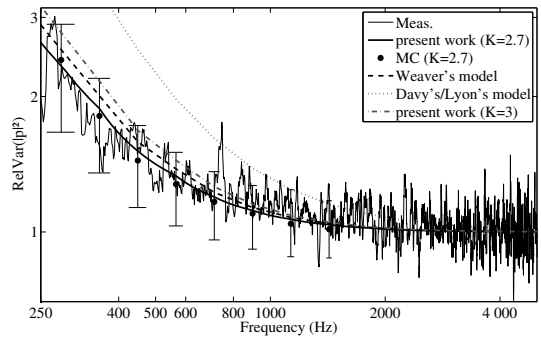


FIG. 8. Relative variances of the mean-squared pressure obtained experimentally (thin solid line), by the analytical expression given by (32) (bold solid line) and by MC simulation (black dots) with the corresponding uncertainty bars (vertical bars), for the empty (upper plot) and loaded cases (lower plot), respectively. Weaver's model (dashed line) given by (37) and Davy's/Lyon's model (dotted line) given by (33) are also reported.

ing. To that end, we assessed the larger modal bandwidth on the [250:1kHz] frequency range which turned out to be around 0.5 Hz. Consequently, we decimated the data by 2 Hz steps, i.e., four times the modal bandwidth in the worst case (and more in other cases), which allowed to consider uncorrelated data in the frequency domain. To reduce the experimental uncertainty we processed moving averages over ten contiguous points. We obtained the relative variances given by Fig. 8.

By minimizing the distance between experimental data and (32), i.e., by using a least-square method, we found optimized values for the K-factor of 2.75 and 2.63 for the empty and loaded cases, respectively. It turns out that these values are close to the value of 2.7 found by Langley and Brown<sup>18</sup>. Accordingly, we adopted the same value in (32). By using the results given in Fig. 7 we managed to assess  $M_s(f)$  to use in (32). The resulting curve is reported in Fig. 8 (solid line) for the empty case (upper plot) and the loaded case (lower plot). Note that the slight irregularity of solid lines is directly due to the slight irregularity of  $M_s(f)$  observed in Fig. 7.

We can note that the analytical result matches quite well with the average trend obtained experimentally. In order to check the consistency of our model, we performed MC simulations based on 50000 realizations. As

$K^2 \simeq 7.3$ , modal weights at the source and at the receiver, were assumed to follow triangular and normal distributions, respectively. It is worth emphasizing that this choice only aimed at ensuring  $K^2 \simeq 7.3$  and must not be regarded as a choice supported by any physical argument. Mean values of the resulting relative variances are reported in Fig. 8 (black dots) where quite a good consistency with the analytical model can be observed. The slight shift is likely due to the estimation uncertainty of the reverberation time which impacts on the estimation of  $M_s$ .

As experimental variances are deduced from sets made up of 64 samples, an unavoidable uncertainty has to be taken into account and is highlighted by the experimental dispersion observed in Fig. 8. To estimate this dispersion, MC simulations were used again; this merely consisted in computing 50000 times estimated relative variances obtained over sets composed of 64 realizations. In order to take into account the moving average over 10 (uncorrelated) contiguous points the data were grouped by 10 and averaged, so that 5000 resulting realizations were available. From these sets of data 95% confidence intervals were computed and reported by vertical bars for both configurations in Fig. 8. We can see that the experimental dispersion is quite coherent with the one obtained by MC simulation. In other terms, the assumptions of independence between the different modal parameters, including the independence between eigenfrequencies, on the one hand, and the  $K$  factor of 2.7, on the other hand, allows us to observe a good agreement, not only with mean values but also with the order of magnitude of the unavoidable experimental and statistical dispersion. As  $K = 3$  is the commonly accepted value, we plotted (32) in Fig. 8 for such case (dashed-dotted line). As it could be expected, the difference with respect to the previous  $K$  value, i.e.,  $K = 2.7$ , is all the more visible that the number of overlapping modes is weak, i.e., for the empty case (upper plot).

We superpose in Fig. 8 the expression of the relative variance derived by Weaver, whose expression is<sup>4</sup>,

$$\text{RelVar}(|p(\mathbf{x}, \omega_w)|^2) = 1 + \frac{K^2 - 3}{M_s}, \quad (37)$$

for  $K = 3$ . We observe the good agreement which made this model accepted in the community. However, as pointed out in Sec. II, the model cannot be regarded as able to properly take into account the repulsion effect of GOE systems. In terms of agreement, we can see that the model derived herein, based on an independence assumption between the eigenfrequencies, is able to predict the relative variance decrease observed at low modal overlap. Conversely, if we report Lyon and Davy's formula, given by (33), in Fig. 8 (dotted line), we can see that it overestimates indeed the relative variance obtained in practice and that the overestimation is statistically significant for reasons explained in section IV.

## VI. CONCLUSION

By revisiting Lyon and Davy's derivation of the relative variance of the mean-squared pressure where the mean-spacing distribution is assumed to follow a Poisson distribution, an inconsistency in the model was highlighted and was proved to be at the origin of the overestimation observed when compared to experimental data.

The resulting corrected model was analytically derived and comparisons with experimental and simulation data were found to be in good agreement. A special care to the dispersion was also taken into account and a good agreement was also found. This agreement shows that the repulsion effect has likely little influence at low modal overlap. Lyon had already proven that this effect was weak for the case of input impedances. The present work confirms in a way this finding for the case of the relative variance of transmission functions.

Finally, it was found that  $K \simeq 2.7$  provides the best fit to the experimental data and converges towards the figure proposed by Langley and Brown. The value of the  $K$  factor is however not yet understood and is still under investigation.

## APPENDIX: A

In order to derive  $E_{|\psi|^2|\psi|^2}$  defined by (18), it is worth noting that,

$$\langle \sum_n |\psi_n|^2 \rangle^2 = \sum_m \langle |\psi_m|^2 \rangle^2 + \sum_{i \neq j} \langle |\psi_i|^2 \rangle \langle |\psi_j|^2 \rangle. \quad (A.1)$$

Recalling the assumption of independence and considering (A.1) allows us to restate  $E_{|\psi|^2|\psi|^2}$  as follows,

$$\begin{aligned} E_{|\psi|^2|\psi|^2} &= \sum_{i \neq j} \langle |\psi_i|^2 \rangle \langle |\psi_j|^2 \rangle \\ &= \langle \sum_n |\psi_n|^2 \rangle^2 - \sum_m \langle |\psi_m|^2 \rangle^2 \\ &= E_{|\psi|^2}^2 - \sum_m \beta_m^2, \end{aligned} \quad (A.2)$$

where,

$$\begin{aligned} \beta_m &= \langle |\psi_m|^2 \rangle = \int_{\omega_k - \frac{\Delta\omega}{2}}^{\omega_k + \frac{\Delta\omega}{2}} \frac{1}{\Delta\omega} |\psi_k(\omega)|^2 d\omega \\ &\simeq \int_{\omega_k - \frac{\Delta\omega}{2}}^{\omega_k + \frac{\Delta\omega}{2}} \frac{1}{\Delta\omega} |\psi(\omega_k - \omega_w)|^2 d\omega \end{aligned} \quad (A.3)$$

A Taylor's expansion taken at first-order allows us to simplify  $\beta_m$  such that,

$$\beta_m = |\psi(\omega_k - \omega_w)|^2. \quad (A.4)$$

From a graphical point of view, it is worth noting that  $\beta_m$  corresponds to an area on a  $\Delta\omega$  interval centered at  $\omega_k$ . Consequently, we obtain,

$$\sum_m \beta_m^2 = E_{|\psi|^4}. \quad (A.5)$$

Finally,  $E_{|\psi|^2|\psi|^2}$  reads,

$$E_{|\psi|^2|\psi|^2} = E_{|\psi|^4} \left( \frac{E_{|\psi|^2}^2}{E_{|\psi|^4}} - 1 \right) \quad (\text{A.6})$$

## ACKNOWLEDGMENTS

Thanks to Christophe Conessa for his help during the measurements.

- <sup>1</sup> M. Schroeder, “Statistical parameters of the frequency response curves of large rooms”, *J. Audio Eng. Soc* **35**, 299–305 (1987).
- <sup>2</sup> J. Davy, “The relative variance of the transmission function of a reverberation room”, *Journal of Sound and Vibration* **77**, 455–479 (1981).
- <sup>3</sup> J. L. Davy, “Improvements to formulae for the ensemble relative variance of random noise in a reverberation room”, *Journal of sound and vibration* **115**, 145–161 (1987).
- <sup>4</sup> R. Weaver, “On the ensemble variance of reverberation room transmission functions, the effect of spectral rigidity”, *J Sound Vib* **130**, 487–491 (1989).
- <sup>5</sup> F. Jacobsen and A. Molares, “Sound power emitted by a pure-tone source in a reverberation room”, *J. Acoust. Soc. Am* **126**, 676 (2009).
- <sup>6</sup> F. Jacobsen and A. Molares, “The ensemble variance of pure-tone measurements in reverberation rooms”, *J. Acoust. Soc. Am* **127**, 233 (2010).
- <sup>7</sup> M. Schroeder, “Spatial averaging in a diffuse sound field and the equivalent number of independent measurements”, *J. Acoust. Soc. Am* **46**, 534 (1969).
- <sup>8</sup> R. Lyon, “Statistical analysis of power injection and response in structures and rooms”, *J. Acoust. Soc. Am* **45**, 545 (1969).
- <sup>9</sup> I. Gurevich and M. Pevsner, “Repulsion of nuclear levels”, *Nuclear Physics* **2**, 575–581 (1957).
- <sup>10</sup> H. Stöckmann, *Quantum chaos: an introduction*, chapter 3, (Cambridge University Press, New York) (2007).
- <sup>11</sup> H. Alt, C. Dembowski, H.-D. Gräf, R. Hofferbert, H. Rehfeld, A. Richter, R. Schuhmann, and T. Weiland, “Wave dynamical chaos in a superconducting three-dimensional sinai billiard”, *Physical review letters* **79**, 1026 (1997).
- <sup>12</sup> C. Ellegaard, T. Guhr, K. Lindemann, J. Nygård, and M. Oxborrow, “Symmetry breaking and spectral statistics of acoustic resonances in quartz blocks”, *Physical review letters* **77**, 4918–4921 (1996).
- <sup>13</sup> M. Davy, J. de Rosny, and M. Fink, “Focusing and amplification of electromagnetic waves by time reversal in an leaky reverberation chamber”, in *APSURSI'09*, 1–4 (IEEE) (2009).
- <sup>14</sup> F. Monsef and A. Cozza, “Average number of significant modes excited in a mode-stirred reverberation chamber”, *IEEE Transactions on Electromagnetic Compatibility* **PP(99)**, 1–7 (January 2014).
- <sup>15</sup> F. Monsef and A. Cozza, “Variability and confidence intervals of the power measured in a reverberation chamber”, *IEEE Transactions on Electromagnetic Compatibility* **PP(99)**, 1–4 (2014).
- <sup>16</sup> H. Kuttruff and M. Schroeder, “On frequency response curves in rooms. comparison of experimental, theoretical, and Monte Carlo results for the average frequency spacing between maxima”, *J Acoust Soc Amer* **34**, 76 (1962).
- <sup>17</sup> H. Kuttruff, *Room acoustics*, chapter 3, 5th edition (Spon Press, Oxon) (2009).

<sup>18</sup> R. Langley and A. Brown, “The ensemble statistics of the energy of a random system subjected to harmonic excitation”, *Journal of Sound and Vibration* **275**, 823–846 (2004).

<sup>19</sup> C. R. M. Passero and P. H. T. Zannin, “Statistical comparison of reverberation times measured by the integrated impulse response and interrupted noise methods, computationally simulated with odeon software, and calculated by sabine, eyring and arau-puchades formulas”, *Applied Acoustics* **71**, 1204–1210 (2010).

# Average Number of Significant Modes Excited in a Mode-Stirred Reverberation Chamber

Florian Monsef, *Member, IEEE*, and Andrea Cozza, *Senior Member, IEEE*

**Abstract**—Although the number of significant modes is intuitive, this concept has never been clearly defined, mainly because of the unbound number of modes involved in modal overlap. In the present paper, we show that, for a perfect stirring process, the effect of modal overlap can be modeled as an equivalent filtering formulation. By introducing the statistical-bandwidth concept, we show that the electromagnetic field statistics due to an infinite number of modes can be summarized by a finite number of significant modes. The case of the electric-energy density in an mode-stirred reverberation chamber has been considered and a new expression of its variability has been established. The good agreement found between the new expression and the experimental and simulation results support the several concepts introduced in this paper.

**Index Terms**—Cavity resonators, electromagnetic compatibility (EMC), modal analysis, parametric statistics, Reverberation chamber (RC).

## I. INTRODUCTION

MODE-STIRRED reverberation chambers (MSRC) are microwave complex environments in which it is of common use to regard the electromagnetic field as a random process. This approach is all the more justified when the chamber is overmoded, i.e., when a large number of modes of the chamber are excited. Indeed, in that case, tests indicate that the ratios of peak to average values of the field remain approximately the same [1]–[3] throughout the central part of the chamber. However, for metrology purposes, the degree of uniformity of such ratios need to be assessed, and this, even for the undermoded case, i.e., near the lowest usable frequency (LUF), for which field statistics differ from the overmoded case.

An important part of the measured-field uncertainty is directly due to the medium complexity. This is why the study of the MSRC is based on statistical tools [4]–[6] and aims at establishing statistical models able to describe the electromagnetic field from the undermoded to the overmoded regime. The most common approach in the community consists in finding probability density functions (pdf) able to describe the statistics of field-related quantities [7]–[9] from the LUF to the overmoded case. An alternative approach consists in modeling the field by

using a modal expansion [10], [11]; the pdfs to choose are this time those applied to modal parameters. In [10], the derivation was based on a finite number of modes to which a limit to infinity was applied as required by the modal theory, whereas in [11], the modal expansion was only including a finite number of contributing modes.

The notion of contributing mode is intuitively linked to the modal density but the concept has never been clearly defined. In [11] for instance, this number was arbitrarily set to the average number of modes overlapping in the average modal bandwidth. In [10], the bandwidth over which this number had to be considered was defined but not quantitatively specified as the aim was to include all the modes. The need to determine this significant number of modes is all the more important that it would provide a metric linked to the degree of overmodedness (or undermodedness) of an MSRC.

To clarify the significant mode concept, we need to regard modal overlap from an alternative point of view; to this end, we will present in Section II how the overlap in the frequency domain of an infinite number of modes can be summed up to the frequency response of a single mode. In Section III, we will show that the concept of statistical bandwidth provides a statistical criterion that highlights the frequency range over which the number of significant modes must be considered. This finding allows revising the expression of the variability of the electric energy density, referred to as  $\varsigma_W^2$ , derived in [10], by highlighting some key terms intervening in its expression. However, the number of significant modes cannot be directly assessed experimentally. This notwithstanding, as shown in Section IV, the validation of  $\varsigma_W^2$ 's law allows us to validate the assessment of the number of significant modes.

## II. REVISITING MODAL OVERLAP

The aim of this section is to revisit the way in which we commonly represent and regard the modal overlap effect. To this end, it is convenient to consider the statistics of a field-related quantity, such as the square modulus of the field in an MSRC or, equivalently, its corresponding electric-energy density referred to as  $W$ . This choice has the advantage to provide a link with a previous work [10] dealing with the problem of considering modal overlap in the derivations of the statistical moments of  $W$ ; to improve the readability with that previous work, we adopt the same notations as much as possible and we invite the reader to refer to the aforementioned paper.

To conduct this study, we need to consider a modal approach in which the electric field  $\mathbf{E}$  at a position  $\mathbf{r}$  and at an operating

Manuscript received February 17, 2013; revised July 26, 2013; accepted September 19, 2013. Date of publication January 9, 2014; date of current version March 24, 2014.

The authors are with the Département de Recherche en Electromagnétisme, Laboratoire des Signaux et Systèmes, UMR8506, Univ Paris-Sud, SUPELEC, CNRS, 91190 Gif-sur-Yvette, France (e-mail: florian.monsef@lss.supelec.fr; andrea.cozza@supelec.fr).

Color versions of one or more of the figures in this paper are available online at <http://ieeexplore.ieee.org>.

Digital Object Identifier 10.1109/TEMC.2013.2284924

frequency  $f_w$  can be expanded as follows:

$$\mathbf{E}(\mathbf{r}, f_w) = \sum_{n=1}^{\infty} \gamma_n \psi_n(f_w) \mathbf{e}_n(\mathbf{r}), \quad (1)$$

where  $\mathbf{e}_n(\mathbf{r})$  is the eigenvector of the  $n$ th mode,  $\gamma_n$  is the modal weight, i.e., the coupling constant of the excitation source to the  $n$ th eigenmode, and  $\psi_n$  is the frequency response of the  $n$ th mode.

If we express, on the one hand,  $\mathbf{e}_n(\mathbf{r}) = e_n(\mathbf{r})\hat{\xi}_n(\mathbf{r})$ , where  $\hat{\xi}_n(\mathbf{r})$  is the unitary polarization vector of the  $n$ th mode, and use, on the other hand,  $\{\tilde{\gamma}_n\}$  referred to as equivalent modal weights and defined as

$$\tilde{\gamma}_n(\mathbf{r}) = \gamma_n e_n(\mathbf{r}), \quad (2)$$

expression (1) can be expressed in the following convenient form

$$\mathbf{E}(\mathbf{r}, f_w) = \sum_{n=1}^{\infty} \tilde{\gamma}_n(\mathbf{r}) \psi_n(f_w) \hat{\xi}_n(\mathbf{r}), \quad (3)$$

where the frequency response  $\psi_n(f)$  reads

$$\psi_n(f) = \frac{-jf}{f^2 - f_n^2 - jf f_n / Q_n}. \quad (4)$$

Under the composite quality factor approximation [12],  $Q_n \simeq Q(f_n)$ , where  $Q(f)$  is the composite quality factor, a function of frequency. High Q resonances obtained in the MSRC are such that the most contributing part of  $\psi_n(f)$  come from working frequencies “close” to the eigenfrequency  $f_n$ , so that (4) can be approximated by

$$\psi_n(f) \simeq \frac{2(f - f_n) + jB_M}{4(f - f_n)^2 + B_M^2} \quad (5)$$

where  $B_M$  is the modal bandwidth related to the composite quality factor. As it will be stressed hereafter,  $B_M$  will be approximated by the modal bandwidth assessed at working frequency, i.e.,  $B_M \simeq f_w/Q(f_w)$ .

The concept of significant mode is studied here in a statistical sense. To position the problem of modal overlap within this framework, let us consider the average of  $W$  (see [10, eq. (19)]) expressed herein as follows:

$$\begin{aligned} \mathbb{E}[W] &\equiv \mathbb{E}_{f_n, |\tilde{\gamma}_n|^2} [W] \\ &= \mathbb{E}_{f_n, |\tilde{\gamma}_n|^2} \left[ \sum_{n=1}^{\infty} |\tilde{\gamma}_n|^2 |\psi_n(f_w)| \right] \end{aligned} \quad (6)$$

where  $\mathbb{E}_x[\cdot]$  stands for the ensemble-average operator linked to the stirring process and applied to the random variable  $x$ ; note that the spatial dependence of the  $|\tilde{\gamma}_n|^2$  has been omitted for the sake of brevity.

The difficulty of defining the number of significant modes lies in the infinite number of tails of frequency responses that overlap at the working frequency. The upper plot in Fig. 1 depicts the case of a random realization based on a set of frequency responses of excited modes, weighted by a set of equivalent squared modal weights  $|\tilde{\gamma}_n|^2$  (vertical arrows); the excitation

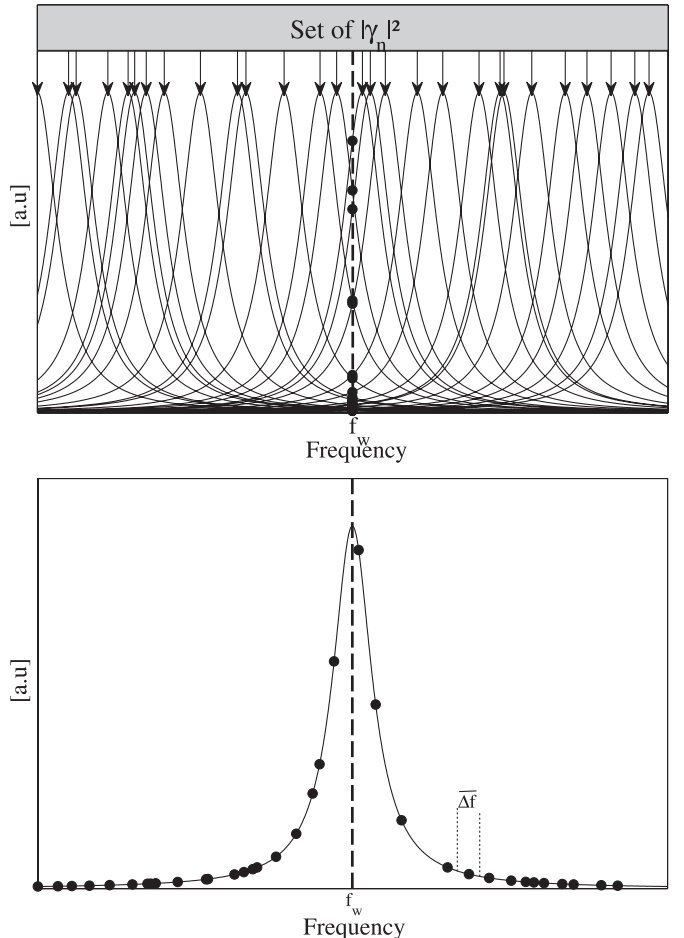


Fig. 1. Due to modal overlap, all resonant frequencies  $f_n$  are involved in the ensemble statistics of a given field-related quantity at given working frequency  $f_w$  (black dots in the upper plot). Each frequency response is weighted by a corresponding  $|\tilde{\gamma}_n|^2$  (vertical arrows). As illustrated, the black dots of the upper plot are contained in the template  $|\psi_0(f - f_w)|^2$  (lower plot). This illustrates the ergodic principle stating that expected values on the eigenfrequencies ensemble converges to the one found using a single-mode frequency response in the whole frequency domain.

level of the frequency responses at working frequency are highlighted by black dots.

Now, the discrete sum in (6) consists in summing the values indicated by the black dots weighted by the corresponding  $|\tilde{\gamma}_n|^2$ . As already done in [10], each frequency response in Fig. 1 is expressed by means of a frequency template  $\psi_0(f)$  defined as

$$\psi_n(f) \simeq \psi_0(f - f_n). \quad (7)$$

The use of such template could appear as a way of simplifying the derivation with a degree of approximation that can be questioned, because of the well known variation of the composite Q-factor with frequency. In fact, as shown in (4) and (5), the important parameter to consider in  $\psi_n(f)$  is the modal bandwidth (i.e., the ratio  $f_n/Q_n$ ) which, given the local quasi-linear variation of  $Q$  with frequency, does not change significantly. The experimental data presented in Section V show that the deviation of the average modal bandwidth is of 0.7% over a 100-MHz bandwidth centered about 800 MHz. So, the results obtained by using (7) are expected to ensure a reasonable level of accuracy.

Using (7) in (6) allows us to approximate the discrete sum (of (6)) as follows:

$$\sum_{n=1}^{\infty} |\tilde{\gamma}_n|^2 |\psi_n(f_w)|^2 \simeq |\tilde{\gamma}(f)|^2 |\psi_0(f - f_w)|^2, \quad (8)$$

where  $|\tilde{\gamma}(f)|^2$  is a discrete random signal for a given realization.

In order to further recast (6), it is worth recalling that the ensemble-average operator stands for an average over an ideally infinite number of stirring states. Moreover, since a stirring process consists in displacing resonance frequencies over a small frequency range, referred to as  $\overline{\Delta f}$  (see lower plot of Fig. 1), the vertical dashed line in the upper plot of Fig. 1, as well as the initially discrete frequency template, will both become continuous under perfect stirring conditions.

Note that the random signal  $|\tilde{\gamma}(f)|^2$  is analog to a power spectrum density (PSD). This one will become continuous in the frequency domain with an average amplitude  $\mu_2 = E[|\tilde{\gamma}_n|^2]$ .

Accordingly, the ensemble average over  $W$  can be approximated by a frequency average expressed as follows:

$$E[W] \simeq \lim_{B_e \rightarrow \infty} \frac{1}{\overline{\Delta f}} \int_{(B_e)} |\tilde{\gamma}(f)|^2 |\psi_0(f - f_w)|^2 df, \quad (9)$$

where  $B_e$  is the frequency range centered about  $f_w$ ; an infinite  $B_e$  allows including all the modes.

If (6) is compared to (9), an ergodic-like property is exhibited. When dealing with the first-order moment, this property consists usually (in its strict sense) in considering that a statistical average coincide with a temporal average; in the present case, the statistical average can be approximately assessed by a frequency average.

Equation (9) shows that the modal overlap effect can be restated as a simple filtering formulation of a random signal characterized by a PSD  $|\tilde{\gamma}(f)|^2$  applied to a filter with a frequency response  $|\psi_0(f - f_w)|^2$ .

The approach presented in this section can be extended to other statistical moments. For instance, it is easy to show that  $E[W^2]$  can be restated in a similar way to (9) where the filter response would be  $|\psi_0(f - f_w)|^4$  and the PSD would be  $|\tilde{\gamma}(f)|^4$  with an average value  $\mu_4 = E[|\tilde{\gamma}_n|^4]$ .

Note that if one is interested in the derivation of relative or normalized variance of  $W$ , one will have to deal with the following typical ratio

$$\mathcal{R} = \frac{\langle |\tilde{\gamma}(f)|^4 |\psi_0(f - f_w)|^4 \rangle_{\mathcal{F}}}{(\langle |\tilde{\gamma}(f)|^2 |\psi_0(f - f_w)|^2 \rangle_{\mathcal{F}})^2} \quad (10)$$

where  $\langle \cdot \rangle_{\mathcal{F}}$  stands for the frequency average as defined in (9).

### III. STATISTICAL BANDWIDTH AND SIGNIFICANT MODES

According to the previous section,  $|\psi_0(f - f_w)|^2$  and  $|\psi_0(f - f_w)|^4$  can be regarded as weighting functions acting on  $|\tilde{\gamma}(f)|^2$  and  $|\tilde{\gamma}(f)|^4$ , respectively.

The weighting functions are common tools in signal processing and instrumentation. A classic application deals with the estimation of the PSD of a signal [13] based on analog signal processing. The estimation of the PSD at a given frequency  $f_w$  consists in measuring the power of the signal at the output of a

perfect filter, i.e., a filter with an ideally flat frequency response of width  $B_1$ . Due to the finite bandwidth of the filter, the estimation error is unavoidable and is characterized by its normalized relative error. In practice however, the filter used for such estimation is of Lorentzian shape and the resulting estimated error may vary. To relate the impact of using such filter instead of the ideal one, the concept of statistical bandwidth, referred to as  $B_s$ , is introduced. The latter corresponds to the bandwidth  $B_1$  that would provide the same relative variance (RV) than the one obtained in practice.

Although the application is different in the present context, the scenario is quite similar if the normalized relative error is regarded as the RV of an unbiased estimator. Moreover, as stated previously,  $|\tilde{\gamma}(f)|^2$  being the PSD of a random signal, we can easily show that the RV to compute corresponds to  $\mathcal{R}$  given by (10). By using the statistical bandwidth concept it follows that

$$\mathcal{R} = \frac{\overline{\Delta f} \mu_4}{B_s \mu_2^2} \quad (11)$$

where  $B_s$  is the statistical bandwidth defined as [13], [14]

$$B_s = \frac{\left( \int_0^{\infty} |\psi_0(f - f_w)|^2 df \right)^2}{\int_0^{\infty} |\psi_0(f - f_w)|^4 df}. \quad (12)$$

Considering the frequency response given by (5) we obtain

$$B_s = \pi B_M. \quad (13)$$

The interest of the statistical bandwidth lies in the fact that the contribution, in a statistical sense, of an infinite number of  $|\tilde{\gamma}_n|^2$  weighted by a Lorentzian spreading on an infinite frequency range, can be summed up by a finite number of unweighted  $|\tilde{\gamma}_n|^2$  in a finite bandwidth  $B_s$ .

Within the statistical bandwidth model, it follows that the number of significant modes, referred to as  $M$ , reads finally

$$M = \pi M_M \quad (14)$$

where  $M_M$  refers to the number of modes overlapping in the modal bandwidth  $B_M$  that can be expressed as

$$M_M = m(f) B_M \quad (15)$$

where  $m(f)$  is the modal density in  $\text{Hz}^{-1}$ .

The condition  $V(f/c)^3 \gg 1$  being met, the simplest form of the modal density [15] can be used, such that

$$m(f) \simeq \frac{8\pi V f^2}{c^3}, \quad (16)$$

where  $V$  and  $c$  are the volume of the MSRC and the speed of light, respectively.

It is worth stressing that the modal density is, in a strict way, a fluctuating quantity whose variance will not be taken into account in the present study. We will only consider its approximated median value given by (16).

### IV. ASSESSMENT OF $M$

The concept and the number of significant modes is difficult to validate since it cannot be “counted” in practice. However, as shown in [10], the variability of  $W$  is governed by the number

of modes  $M_M$ . With the concepts introduced in the previous sections, studying the variability of  $W$  consists in assessing  $\varsigma_W^2$  for a finite number  $M$  of modes spreading over  $B_s$ . This is exactly the result given by (24) in [10], where  $B_e$  was at that stage regarded as a finite bandwidth over which  $M$  modes spread. Adapting the result is then straightforward, yielding

$$\begin{aligned}\varsigma_W^2 &= \frac{B_s}{M} \frac{\mu_4}{\mu_2^2 \pi B_M} + \frac{M-4}{3M} \\ &= \frac{1}{3} + \frac{2}{3\pi M_M}\end{aligned}\quad (17)$$

for  $\mu_4/\mu_2^2 = 2$ , keeping the assumption that  $\tilde{\gamma}_i$  are normally-distributed complex random variables.

A quick glance at the final expression of  $\varsigma_W^2$  in [10] shows a difference of a factor 3 in the second term of the right-hand term. In fact, in order to include all the modes, the initially finite bandwidth  $B_e$  was logically extended to infinity, but  $M/B_e$  was improperly substituted by the modal density  $m(f)$ —indeed this substitution can only be justified if  $B_e$  is sufficiently small. This is the advantage provided by the statistical-bandwidth concept which, given the order of magnitude of  $B_s$ , allows substituting  $B_s/M$  by  $1/m(f)$  in (17).

Since  $B_s$  and  $M$  only exist in the framework of an equivalent statistical model, the validation of these as pertinent (and useful) quantities cannot be performed, but indirectly, by validating the analytical expression of  $\varsigma_W^2$ .

## V. CONCEPTS AND MODEL VALIDATION

In order to validate the analytical expression of  $\varsigma_W^2$  found in (17), we will compare the RV to the one obtained, on the one hand, by Monte Carlo (MC) simulations and on the other hand, experimentally.

### A. MC Simulation Setup

The importance of the results obtained by the MC simulation should not be underestimated over those obtained experimentally. Indeed, beyond the flexibility that the MC method allows, it is a very convenient way to check the self-consistency of our analytical expressions with respect to the assumptions made on the different parameters intervening in (3).

The statistical distributions are such that the real and imaginary parts of the equivalent modal weights were assumed to follow a normal law; a uniform distribution was assumed for both the polarization of the modes, over  $4\pi$  sr.

As stated by (17), the only parameter that can vary is the number of modes overlapping in the modal bandwidth  $B_M$ . As shown by (16), this number can be modified by considering a variable volume and/or a variable frequency. As shown in [16], the two approaches are equivalent. In order to simplify the MC computations, we pick out the method consisting in fixing a modal bandwidth and adapting a (virtual) volume to ensure the desired number of overlapping modes. In the present study, a 1-MHz modal bandwidth is arbitrarily set.

Each MC simulation consisted in generating twenty sets of 50 000 independent random realizations of the electric field de-

scribed by (3), and this for the following values of  $M_M$ : 1, 2, 3, 5, 10, 15, 20, 25, 30, 35. The number of simulated modes was taken over a bandwidth of  $51B_M$  [16]. The resulting estimated variance was averaged over the twenty values.

### B. Experimental Setup and Chamber Characterization

In order to make the comparison more sensible with [10], the same measurements are considered herein. As a brief reminder, and to provide some more details, the setup takes place in the  $13.3 \text{ m}^3$  ( $3.08 \text{ m} \times 1.84 \text{ m} \times 2.44 \text{ m}$ ) RC equipped with a 100-step mechanical stirrer blade of 50 cm width; its LUF is around 550 MHz. The RV is studied over the frequency range of 0.7–3 GHz.

The reverberation chamber (RC) was used in two configurations. In the first one, the RC was empty; in the second one, it was loaded by inserting an hybrid absorber made up of four pyramids of about 30 cm high, standing in the center of the RC.

The loaded and empty cases provide respective advantages. When the RC is not loaded, the losses are minimized, allowing us to visualize, as clearly as possible, the transition of  $\varsigma_W^2$  toward its well known asymptotic value of  $1/3$ . The interest of the loaded case is to provide another configuration of the chamber and to have enough overlapping modes in order to approach the asymptotic value, i.e., to attain very well-overmoded conditions.

For the empty and loaded scenarios, we can show that the maximum average modal bandwidths are 150 and 375 kHz, respectively. On the frequency range of interest, 1000 linearly-spaced frequency bins are used, inducing a 2.3-MHz frequency space between each point. This frequency space is much larger than the maximum value of the modal bandwidths previously mentioned, allowing each measured point to be considered as uncorrelated between one another.

The variability  $\varsigma_W^2$  will be estimated with an inevitable uncertainty. The latter, i.e., the uncertainty, can be minimized by applying a moving average over five contiguous points, followed by a decimation whose factor equals 5 accordingly. The average values are therefore obtained over 10-MHz bandwidths.

It is worth recalling that the modal bandwidths and the modal density are two parameters that can fluctuate considerably. The moving average followed by the decimation aim at extracting the average trend, in order to be consistent with the model used herein that neither takes into account the variance of the number of modes [17] nor the variance of the quality factors [15], [18].

In order to make the validation reliable, we need to estimate some useful preliminary quantities such as the number of uncorrelated stirrer positions, referred to as  $N_{sp}$ .

The number of uncorrelated stirrer positions can be assessed when the correlation coefficient is below a certain threshold that depends on the number of stirrer positions [1]. For 100 positions, the threshold is found around 20%. For this correlation level, Fig. 2 shows the resulting number of “independent” number of stirrer positions as a function of frequency for the empty (solid line) and loaded (dashed line) scenarios, respectively.

In the validation process, the number of overlapping modes  $M_M$  is also a key quantity resulting from the knowledge of the composite quality factor. Accordingly, a special care must

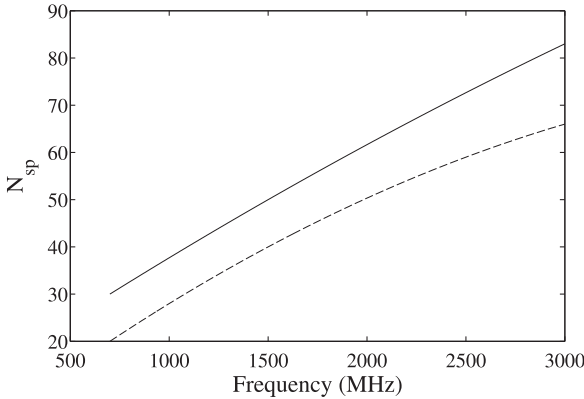


Fig. 2. Estimated number of independent stirrer positions as a function of frequency for the empty (solid line) and the loaded (dashed line) cases, respectively.

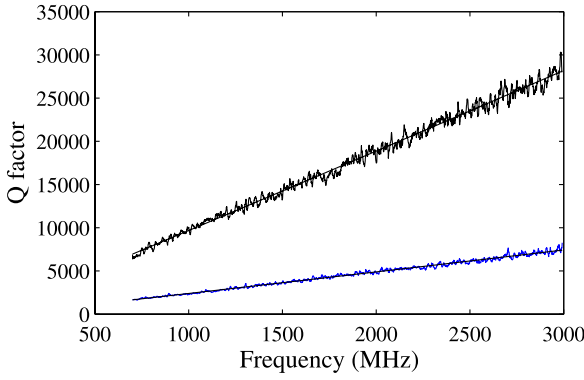


Fig. 3. Composite quality factor obtained by averaging over 10-MHz bandwidths in the empty case (black upper curve) and the loaded case (grey lower curve), respectively. The straight lines stand for first-order approximated median values in a least-square sense.

be taken with the estimation of  $Q$ . As the field probe used was phase sensitive, we were able to compute the composite quality factor for the chamber over the entire frequency range of test, by postprocessing the frequency-spectrum data in time domain. The frequency spectrum used was made up of 60 000 bins over the entire frequency range of interest. The composite quality factors were estimated on 1-MHz frequency bands. In order to be consistent with the process applied to  $\zeta_W^2$ ,  $Q$  values were averaged on 10-MHz frequency bands; the uncertainty was further minimized by using the data obtained on the three field components.

Fig. 3 shows the resulting composite quality factors obtained for the empty (black upper curve) and loaded cases (grey lower curve), respectively. In order to extract the mean trend for both cases, a first-order fit was performed in a least-square sense (straight lines). The measured quality factors, as a function of frequency, allow to compute modal bandwidths.

The knowledge of (average) modal bandwidths allowed us to derive the number  $M_M$  of overlapping modes by using (15). Accordingly, Fig. 4 shows the number  $M_M$  for the empty (black lower curve) and loaded cases (grey upper curve), respectively. The solid lines provide the mean trends resulting from those obtained for  $Q$ . Note that the fluctuations of  $M_M$  observed in Fig. 4 results from the fluctuations of the estimated composite

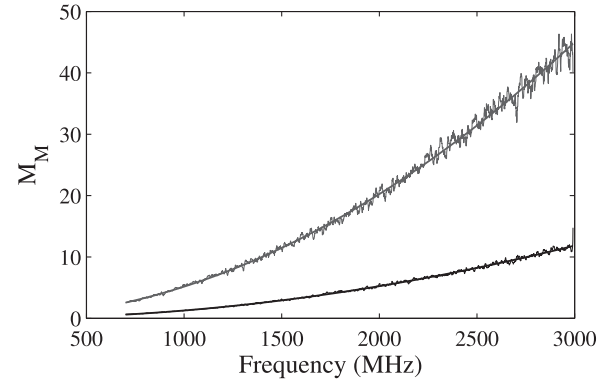


Fig. 4. Number of overlapping modes in the  $-3$ -dB bandwidth obtained when the RC is empty (black lower curve) and loaded (grey upper curve). The solid lines are the first-order approximated median values in a least-square sense.

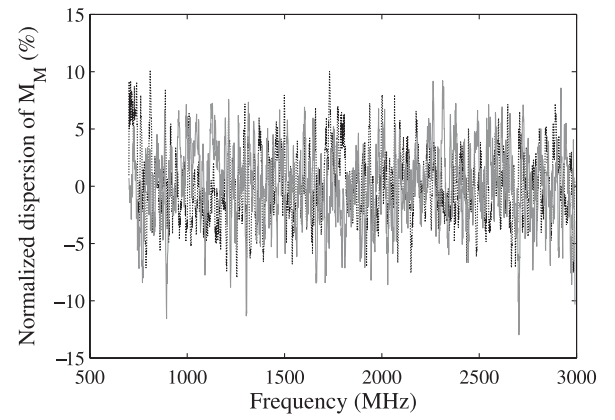


Fig. 5. Fluctuations of the estimated  $M_M$  values, obtained in Fig. 4, about the approximated median values, for the empty case (solid grey line) and the loaded case (black dotted line), respectively.

quality factor and are not due to local modal-density fluctuations; as explained in section III, these have not been considered in the present study.

In order to have an estimation of the fluctuations of  $M_M$  about mean values, Fig. 5 shows the normalized dispersion obtained for the empty case (solid grey line) and the loaded case (black dotted line), respectively. A dispersion of about  $\pm 7\%$  is observed for both cases.

This characterization of the chamber in both scenarios allows us to proceed to the validation of the RV of the electric-energy density.

### C. Results

We present in Fig. 6 the estimated values of  $\zeta_W^2$ , referred to as  $\hat{\zeta}_W^2$ , obtained experimentally (left y-axis) as a function of frequency (grey markers) with the corresponding relative deviation from its asymptotic value (right y-axis). For clarity, and in order to well visualize the transition of the RVs toward their asymptotic values, only the empty case is reported in Fig. 6. We superimposed the analytical expression obtained in (17) (solid line) and the analytical result obtained in [10] (dashed line). We can observe that the expression given by (17) is in very good agreement with measurements, whereas the RV  $\zeta_W^2$

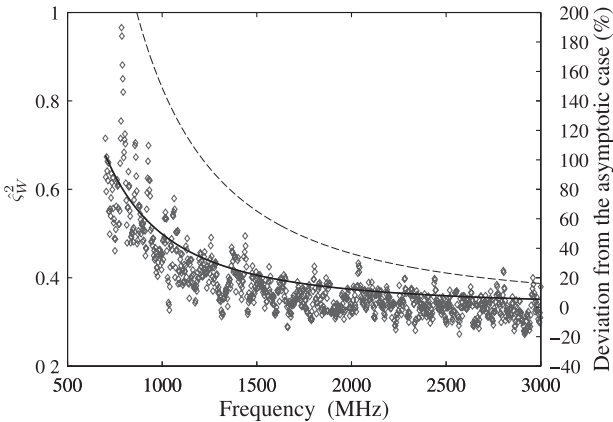


Fig. 6. Estimated RV  $\hat{\zeta}_W^2$  of the electric-energy density (left y-axis) and the relative deviation from the asymptotic value of  $1/3$  (right y-axis), as a function of frequency. The experimental results (grey markers) and analytical results (solid line) are reported; dashed line stands for the analytical expression derived in [10].

obtained in [10] (dashed line) tends to overestimate the degree of nonuniformity of  $W$ .

In order to compare these results to those obtained with the MC approach, the number of modes assessed experimentally for the empty and loaded scenarios (see Fig. 4) must be used. This allows to transpose and superimpose the experimental results to those obtained by the MC simulation. The variabilities are shown (left y-axis) accordingly in Fig. 7, where the experimental results (grey markers), MC results (black dots), and analytical results (solid line) have been reported. The deviation of  $\hat{\zeta}_W^2$  from its asymptotic value is also shown (right y-axis).

However, when experimental variances are estimated from sets made up of finite number of samples, directly related herein to the number  $N_{sp}$  of independent stirrer positions, an unavoidable uncertainty has to be taken into account. To estimate the latter, the MC simulations were used again; this merely consisted in computing 5000 times, for a given  $M_M$  value, estimated the RVs of  $W$  obtained over sets composed of  $N_{sp}$  realizations.

Recalling that  $\hat{\zeta}_W^2$  plotted in Fig. 6 was deduced from averages performed over five contiguous points, the 5000 MC values were rearranged in  $5 \times 1000$  values in order to perform averages over five contiguous points. From these averages, 95% confidence intervals of  $\hat{\zeta}_W^2$  have been computed, and correspond to the uncertainty bars reported in Fig. 7, for the empty case (upper plot) and the loaded case (lower plot), respectively.

Finally, we need to recall that  $M_M$  are mean estimated values for which 7% fluctuations were observed (see Fig. 5); accordingly, horizontal uncertainty bars on  $M_M$  have been added in Fig. 7.

We can observe a very good agreement between the results obtained analytically, numerically, and those obtained experimentally. For the latter, we note remarkable agreement even with uncertainty bars, especially for the empty case.

We stress the interest of using an MC approach, since the good agreement found ensures in some way that the analytical results are consistent with the assumptions made on the different parameters and their related statistical laws.

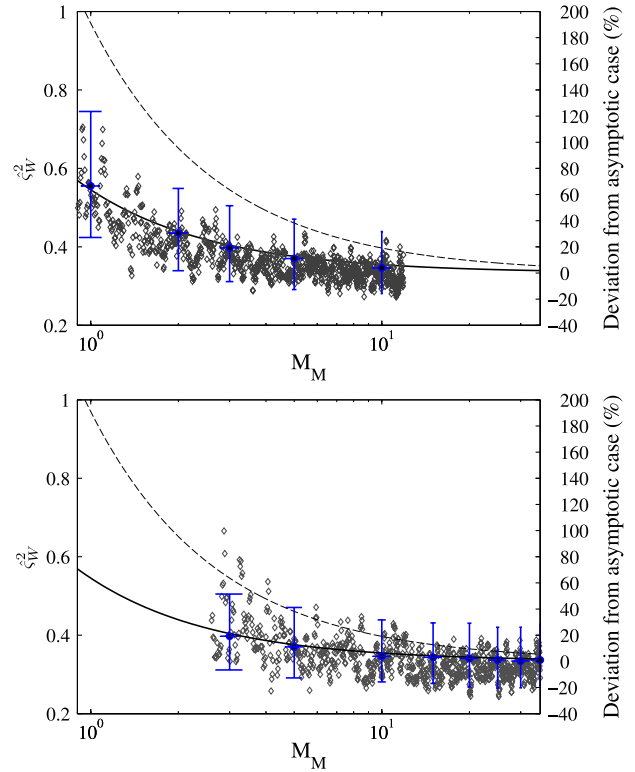


Fig. 7. Estimated RV  $\hat{\zeta}_W^2$  (left y-axis) of the electric-energy density, as a function of the number of modes  $M_M$  for the empty (upper plot) and loaded (lower plot) scenarios, respectively. The corresponding relative deviation from the asymptotic value of  $1/3$  (right y-axis). The experimental results (grey symbols), MC results (black dots) and analytical results (solid line) are reported. The dashed line stands for the analytical expression derived in [10]. The vertical bars are related to the uncertainty of the experimental measurements considered on a 95% confidence interval. The horizontal bars stand for the dispersion of  $M_M$  around its mean value.

## VI. CONCLUSION

The concept of significant modes has been revisited and highlighted. The bandwidth over which this number is defined, depends inevitably on the statistical quantity of interest. In the present study, a quantitative assessment of this number has been carried out on the basis of the variability of the electric-energy density. This notwithstanding, the approach presented in the present study can be extended to other statistical quantities.

Linking the concept of significant modes to previous work allowed us to derive a new expression of the variability of the electric-energy density. The good agreement found between the experimental results and simulation supports the different concepts introduced in the present paper. From a more practical point of view, it provides an answer to the pending question dealing with the assessment of the average number of significant modes to consider at a given frequency in an MSRC.

## REFERENCES

- [1] *Reverberation chamber test methods*, International Electrotechnical Commission (IEC), Std. 61 000-4-21, 2011.
- [2] J. Kostas and B. Boverie, "Statistical model for a mode-stirred chamber," *IEEE Trans. Electromagn. Compat.*, vol. 33, no. 4, pp. 366–370, Nov. 1991.

- [3] M. Hoijer, "Maximum power available to stress onto the critical component in the equipment under test when performing a radiated susceptibility test in the reverberation chamber," *IEEE Trans. Electromagn. Compat.*, vol. 48, no. 2, pp. 372–384, May 2006.
- [4] C. Lemoine, P. Besnier, and M. Drissi, "Investigation of reverberation chamber measurements through high-power goodness-of-fit tests," *IEEE Trans. Electromagn. Compat.*, vol. 49, no. 4, pp. 745–755, Nov. 2007.
- [5] C. Lemoine, P. Besnier, and M. Drissi, "Estimating the effective sample size to select independent measurements in a reverberation chamber," *IEEE Trans. Electromagn. Compat.*, vol. 50, no. 2, pp. 227–236, May 2008.
- [6] R. Serra, F. Leferink, and F. Canavero, "'Good-but-imperfect' electromagnetic reverberation in a VIRC," in *Proc. Int. Symp. Electromagn. Compat.*, 2011, pp. 954–959.
- [7] C. F. Bunting, "Statistical characterization and the simulation of a reverberation chamber using finite-element techniques," *IEEE Trans. Electromagn. Compat.*, vol. 44, no. 1, pp. 214–221, Feb. 2002.
- [8] L. Arnaut, "Compound exponential distributions for undermoded reverberation chambers," *IEEE Trans. Electromagn. Compat.*, vol. 44, no. 3, pp. 442–457, Aug. 2002.
- [9] G. Orjubin, E. Richalot, S. Mengue, and O. Picon, "Statistical model of an undermoded reverberation chamber," *IEEE Trans. Electromagn. Compat.*, vol. 48, no. 1, pp. 248–251, Feb. 2006.
- [10] A. Cozza, "The role of losses in the definition of the overmoded condition for reverberation chambers and their statistics," *IEEE Trans. Electromagn. Compat.*, vol. 53, no. 2, pp. 296–307, May 2011.
- [11] L. Arnaut, "Limit distributions for imperfect electromagnetic reverberation," *IEEE Trans. Electromagn. Compat.*, vol. 45, no. 2, pp. 357–377, May 2003.
- [12] B. H. Liu, D. C. Chang, and M. T. Ma, "Eigenmodes and the composite quality factor of a reverberating chamber," Tech. Rep. Tech. Note 1066, U.S. National Bureau of Standards, 1983.
- [13] J. Bendat and A. Piersol, *Random Data: Analysis and Measurement Procedures*. New York, NY, USA: Wiley-Interscience, 1971.
- [14] W. Stanley and S. Peterson, "Equivalent statistical bandwidths of conventional low-pass filters," *IEEE Trans. Commun.*, vol. 27, no. 10, pp. 1633–1634, Oct. 1979.
- [15] L. Arnaut and G. Gradoni, "Probability distribution of the quality factor of a mode-stirred reverberation chamber," *IEEE Trans. Electromagn. Compat.*, vol. 55, pp. 35–44, Feb. 2013.
- [16] F. Monsef, "Why a reverberation chamber works at low modal overlap," *IEEE Trans. Electromagn. Compat.*, vol. 54, no. 6, pp. 1314–1317, Dec. 2012.
- [17] A. Cozza, "Probability distributions of local modal-density fluctuations in an electromagnetic cavity," *IEEE Trans. Electromagn. Compat.*, vol. 54, no. 5, pp. 954–967, Oct. 2012.
- [18] L. Arnaut, "Statistics of the quality factor of a rectangular reverberation chamber," *IEEE Trans. Electromagn. Compat.*, vol. 45, no. 1, pp. 61–76, Feb. 2003.



**Florian Monsef** (M'12) received the Masters degree from the Université Paris-Sud, Orsay, France. He entered the Ecole Normale Supérieure de Cachan, Cachan, France, in electrical engineering and computer science. He did a thesis on electron transport in IV-IV heterostructures and received the Ph.D. degree in electronics from the Université Paris-Sud, Orsay, France, in 2002.

From 2002 to 2009, he was a Teacher in electrical engineering at the Technical Institute of the Université Paris X, Nanterre, France. Since 2009, he is currently an Assistant Professor with the Laboratoire des Signaux et Systèmes (Université Paris-Sud). His topics in research since 2009 include EMC, reverberation chambers, and time-reversal applications.



**Andrea Cozza** (S'02–M'05–SM'12) received the Laurea degree (*summa cum laude*) in electronic engineering from Politecnico di Torino, Turin, Italy, in 2001, and the Ph.D. degree in electronic engineering jointly from the Politecnico di Torino and the University of Lille, Lille, France, in 2005.

In 2007, he joined the Département de Recherche en Électromagnétisme, SUPELEC, Gif sur Yvette, France, where since 2013, he is a Full Professor. He is a reviewer for several scientific journals, including those of the IET and IEEE. His current research interests include reverberation chambers, statistical electromagnetics, wave propagation through complex media, and applications of time reversal to electromagnetics.

Dr. Cozza was awarded the 2012 Prix Coron-Thévenet by the Académie des Sciences, in France.

# Letters

## A Possible Minimum Relevance Requirement for a Statistical Approach in a Reverberation Chamber

Florian Monsef, *Member, IEEE*, and Andrea Cozza, *Senior Member, IEEE*

**Abstract**—Modal overlap in a reverberation chamber (RC) involves, strictly speaking, an infinite number of modes in the field statistics. The degree of overmodedness of an RC is often assessed by introducing an arbitrary reference bandwidth in which a number of overlapping modes is computed. We introduce a statistical model of the field in which the number of modes is rigorously finite. The model is chosen such that the number of degrees of freedom (DOF) of the field can be assessed. The number of DOF is assessed by considering the degree of homogeneity of the average power received by a linearly polarized antenna. It is considered that a statistical approach requires at least a single degree of freedom. Based on this criterion, the minimum frequency at which a statistical approach would make sense is evaluated and compared to the lowest useable frequency (LUF) commonly considered in EMC.

**Index Terms**—Cavity resonators, electromagnetic compatibility (EMC), modal analysis, parametric statistics, reverberation chamber (RC).

### I. INTRODUCTION

In order to deal with the complexity of the electromagnetic (EM) field inside reverberation chambers (RCs), a statistical approach is commonly used to estimate the degree of homogeneity of the mean and maximum power level that can be expected [1]–[3]. The power, referred to as  $P$ , is meant as being measured on a given rectangular field component by a linearly polarized antenna.

Due to wall losses and other loss mechanisms, the EM field results from the superposition of modes regarded as random normal modes. As soon as a certain number of modes is efficiently excited, the field can be assumed to follow a Gaussian law, a direct result from the central-limit theorem [4]. If the number of excited modes happened to raise, fluctuations of  $P$  about its mean value, i.e., its relative variance (or variability), would remain steady. It corresponds to an overmoded regime for which an infinite number of modes is ideally and theoretically assumed. The relative variance of the measured mean power tends to unity, as  $P$  follows a  $\chi^2_2$  law. A recent study [5] has highlighted the rate at which power variability tends toward its asymptotic value.

Each contributing mode could be thought of acting as a degree of freedom (DOF). The larger the number of DOF, the more Gaussian the field will be. Although intuitive, the correspondence between the number of excited mode and the number of DOF is not straightforward for the following reason. The frequency response of the modes are of Lorentzian shape. This means that the number of overlapping modes is rigorously infinite. One could bound the number of overlapping modes by setting a bandwidth of reference. In [6] for instance, the  $-3$  dB modal bandwidth was chosen. This choice can be a metric that provides the degree of modal overlap, but does not provide the number of modes that contribute to a given level of field homogeneity [7]. In any case, whatever the chosen bandwidth, the modal overlap involves theoretically an infinite number of modes.

This study tackles the problem in another way. It proposes an equivalent statistical model that, on the one hand, makes not possible the modal overlap to be infinite, and on the other hand, provides the same degree of homogeneity in a chamber, i.e., leads to the expected power variability. It is essentially a way to circumvent the problem of the tails of the frequency response of the modes. As we will see, the bandwidth over which the modal overlap is regarded is however related to the choice of some model parameters. Interestingly, this proposed approach allows us to define properly the concept of DOF and highlights the results derived in [8]. Finally, the model allows us to propose a criterion that could be a possible answer to the pending question dealing with the frequency from which a statistical approach makes sense in an RC.

After defining what is meant by DOF in Section II, the equivalent statistical model of the electric field will be exposed. The assessment of the number of DOF will also be presented. Section III will focus on the validation of the proposed model by means of Monte Carlo (MC) simulation. Finally, the frequency from which a statistical approach makes sense in an RC will be presented in Section IV.

### II. MODAL OVERLAP AND DEGREES OF FREEDOM

#### A. Degrees of Freedom: Definition

It is important to define what is meant by DOF in order to understand the interest of the approach presented herein. Let us consider a random variable  $Y$  expressed as follows:

$$Y = \sum_{i=1}^N X_i \quad (1)$$

Manuscript received June 29, 2015; accepted July 15, 2015.

The authors are at the GeePS Lab, UMR8507, Université Paris-Sud, CentraleSupélec, CNRS, UPMC, 91192 Gif-sur-Yvette, France (e-mail: florian.monsef@u-psud.fr).

Color versions of one or more of the figures in this paper are available online at <http://ieeexplore.ieee.org>.

Digital Object Identifier 10.1109/TEMC.2015.2464318

where  $X_i$  are independent and identically distributed (i.i.d.) random variables. The number  $N$  is defined as the number of DOF of  $Y$ .

A typical example of such definition is met with a  $\chi_N^2$  variable where the  $X_i$  are  $\chi_1^2$  distributed.

The basic idea of the paper is to introduce a way to express the electric field on the model given by (1), the interest of it will become clearer thereafter.

### B. Matching a Physical Model to a Statistical Field Model

The first step of the proposed approach consists in recalling the physics that describes the electric field in an RC. To that aim, a modal approach is used, and the electric field  $\mathbf{E}$  at a position  $\mathbf{r}$  and at a frequency  $f$  can be expressed as follows [8], [9]:

$$\mathbf{E}(\mathbf{r}, f) = \sum_{i=1}^{\infty} \gamma_i \psi_i(f) \mathbf{e}_i(\mathbf{r}) \quad (2)$$

where  $\mathbf{e}_i$  is the eigenvector of the  $i$ th mode, which is assumed not to have a specific form,  $\psi_i$  is the frequency response of the  $i$ th mode, and  $\gamma_i$  is the modal weight, i.e., the coupling constant of the source to the  $i$ th eigenmode.

Limiting the analysis to a single position  $\mathbf{r}$ , the following factorization for the modal topographies can be used:

$$\mathbf{e}_i(\mathbf{r}) = e_i(\mathbf{r}) \hat{\xi}_i(\mathbf{r}) \quad (3)$$

where  $\hat{\xi}_i(\mathbf{r})$  is a unitary polarization vector assumed to be uniformly distributed over  $4\pi$  sr.

As explained in [9], it is convenient to regard the set  $\{\gamma_i e_i(\mathbf{r})\}$  as a set of a single random variable  $\tilde{\gamma}_i$  defined as

$$\tilde{\gamma}_i = \gamma_i e_i(\mathbf{r}) \quad (4)$$

referred to as equivalent modal weights [9]. The real and imaginary parts of  $\tilde{\gamma}_i$  are assumed to follow a centered normal law.

As done in [5], [8], and [9], we consider three sets of modal parameters, i.e.,  $\tilde{\gamma}_i$ ,  $\psi_i$ , and  $\hat{\xi}_i$  as random variables. The main assumptions required are at two levels. First, the modal parameters of different sets are independent, second, the parameters within the same set are i.i.d.

Now, the electric field described by (2) corresponds to a sum of weighted random variables, the weight function being  $\psi_i(f)$ . If we want to highlight the number of DOF for the case of the electric field, a rectangular shaped weight function has to be considered; the weight function, referred to as  $\psi_{i,e}(f)$ , would be of width  $B_w$  and of height  $A_{eq} \forall i$ .

By doing so, we are introducing fictitious modes that have rectangular shaped frequency response. So, these modes are, or totally excited, or not at all. When these are excited, their contribution is equal to their neighbors.

In other terms, we are introducing an arbitrary electric field model. Accordingly, an equivalent electric field, referred to as  $\mathbf{E}_e(\mathbf{r}, f)$  must be considered; it is still expressed as a modal expansion as follows:

$$\mathbf{E}_e(\mathbf{r}, f) = \sum_{i=1}^{\infty} \tilde{\gamma}_{i,e} \psi_{i,e}(f) \hat{\xi}_{i,e}(\mathbf{r}) \quad (5)$$

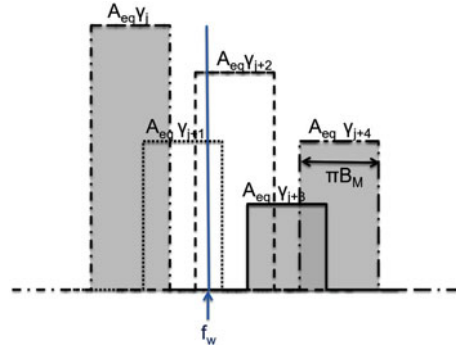


Fig. 1. Illustration of the overlap using the fictitious-modes model. Given the shape of their frequency response, only a finite number of those is excited—two in the illustrated case.

where  $\tilde{\gamma}_{i,e}$ ,  $\hat{\xi}_{i,e}(\mathbf{r})$  and  $\psi_{i,e}(f)$  refer to equivalent modal quantities. However, these do not follow necessarily the same statistics as the modal quantities in (2) as they are related to fictitious modes.

The infinite modal-overlap issue at given frequency  $f_w$  is then circumvented as shown in Fig. 1. The sketch highlights indeed that only a finite number of fictitious modes intervene in (5). It follows that  $\mathbf{E}_e(\mathbf{r}, f)$  can be simplified and reads

$$\mathbf{E}_e(\mathbf{r}, f) = \sum_{i=1}^N \tilde{\gamma}_{i,e} \hat{\xi}_{i,e}(\mathbf{r}) \quad (6)$$

where  $N$  is the number of DOF, i.e., of fictitious modes, whose number will be specified in the next section. It is worth noting that the expression in (6) follows indeed the form given by (1).

Provided that the degree of homogeneity of the average power is the quantity of interest, its variability, referred to as  $\varsigma_P^2$ , must remain the same no matter what model is used. In other terms, (2) and (6) must lead to the same expression of the variability. This one was shown to be expressed in [5] as

$$\varsigma_P^2 = 1 + \frac{8}{5\pi M_M} \quad (7)$$

where  $M_M$  stands for the average number of real modes overlapping in the  $-3\text{dB}$  modal bandwidth.

We chose  $\tilde{\gamma}_{i,e}$  and  $\hat{\xi}_{i,e}(\mathbf{r})$  to share  $\tilde{\gamma}_i$  and  $\hat{\xi}_i(\mathbf{r})$  properties, respectively. This choice is motivated by the fact that the main issue is only linked to the tails of the frequency responses. Accordingly, we do not have any reason to consider that  $\tilde{\gamma}_{i,e}$  and  $\hat{\xi}_{i,e}(\mathbf{r})$  follow different probability laws than  $\tilde{\gamma}_i$  and  $\hat{\xi}_i(\mathbf{r})$ .

Now, if (6) is considered, by using the approach used in [5], it is easy to show that  $\varsigma_P^2$  reads

$$\varsigma_P^2 = 1 + \frac{\Gamma - 2}{N} \quad (8)$$

where  $\Gamma$  is defined as

$$\Gamma = \frac{\mu_4 \nu_4 \kappa_4}{\mu_2^2 \nu_2^2 \kappa_2^2} \quad (9)$$

From [5] and [9],  $\mu_n = E_{\tilde{\gamma}_{i,e}} [|\tilde{\gamma}_{i,e}|^n]$ ,  $\kappa_n = E_{u_{i,e}} [|u_{i,e}|^n]$ , and  $\nu_n = E_{\psi} [|\psi_{i,e}(f)|^n]$ , where  $E_x [\cdot]$  is the ensemble average operator applied to  $x$ .

Given that  $\tilde{\gamma}_{i,e}$  and  $u_{i,e}$  follow a Gaussian and a uniform law, respectively, we can show that  $\Gamma$  reads

$$\Gamma = \frac{18}{5} \frac{\nu_4}{\nu_2^2}. \quad (10)$$

Moreover, the frequency responses of the model being of rectangular shape, we can easily show that

$$\nu_2 = m(f_w) A_{eq}^2 B_w \quad (11a)$$

$$\nu_4 = m(f_w) A_{eq}^4 B_w \quad (11b)$$

where  $m(f_w)$  is the modal density in mode/Hz at working frequency  $f_w$ .

If we use the real-modes model, we have  $\nu_2$  and  $\nu_4$  such that [5]

$$\nu_2 = \frac{\pi m(f_w)}{2B_M} \quad (12a)$$

$$\nu_4 = \frac{\pi m(f_w)}{4B_M^3}. \quad (12b)$$

In order to match (11) to (12), the frequency responses of the fictitious modes must be chosen such that

$$A_{eq} = \frac{1}{B_M \sqrt{2}} \quad (13)$$

and

$$B_w = \pi B_M. \quad (14)$$

We can make a total analogy with the equivalent noise bandwidth, referred to as  $B_N$ , of a filter;  $B_N$  is the bandwidth of an ideal filter (rectangular response) for which the power noise is the same than the one that we have with a real filter. This concept has been transposed herein such that the equivalent bandwidth provides the same statistical moments. This bandwidth may be referred to as the statistical bandwidth as proposed in [8].

If we had taken the electric energy density  $W$  as quantity of interest, as done in [9] for instance, the related variability, referred to as  $\varsigma_W^2$  would be the metric to consider. In order to match the two first moments of  $W$ , we can show that the conditions needed on  $A_{eq}$  and  $B_w$  remain unchanged.

It is worth stressing that other shapes (triangles, etc.) of frequency responses could have led to finite modal overlap, but those would still have behaved as weighting functions. In a strict sense, the bandwidth, over which modal overlap is estimated, depends on the shape of the frequency response. However, the assessment of the number of DOF would not be possible for nonrectangular shapes. So the coupling of the DOF constraint enforces a single bandwidth value, the one given by (14).

### C. Number of Degrees of Freedom

Now that the bandwidth  $B_w$  is identified as being  $\pi$  times the modal bandwidth, the sketch of Fig. 1 allows us to assess easily the number of fictitious modes, or in other words, the number of DOF.

<sup>1</sup>See [5, Sec. III].

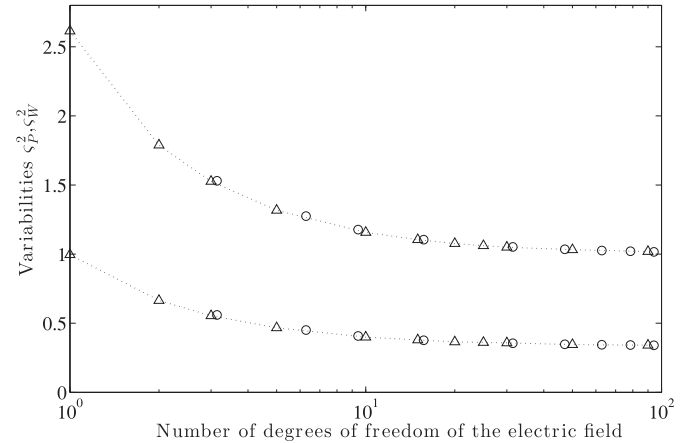


Fig. 2. Relative variances of the power measured along a given cartesian component (upper curve) and of the electric-energy density (lower curve) obtained by MC simulations using (2) (circles) and (6) (triangles). These are plotted as a function of the number of degrees of freedom of the field.

The average distance between continuous modes being  $1/m(f_w)$ , the number  $N$  of DOF is such that

$$N = m(f_w) B_w = \pi M_M. \quad (15)$$

This number corresponds to what was called the “effective number” of excited modes in [8]. The problem is tackled here from another angle, highlighting that these “modes” correspond in fact, from a statistical point of view, to a number of DOF.

We emphasize that the number  $N$  must not be regarded as a number of real modes that contribute to the field statistics otherwise leading to an improper variability level as shown in [7]. This is especially striking at low modal overlap. For this case, the modes that contribute to the statistics are poorly excited due to their Lorentzian-shaped frequency response. This impose to consider real modes spreading over a wide frequency band ( $50B_M$  according to [7] for  $M_M = 1$ ); with the DOF model, the fictitious modes are entirely excited and the statistics does not need such a wide frequency band to converge.

### III. MODEL VALIDATION

The form obtained in (6) can make one skeptical about the validity of such a simple equivalent model of the electric field. In order to raise doubts, we have computed, on the one hand,  $\varsigma_P^2$  and  $\varsigma_W^2$  using MC simulations for the following number of DOF: 1, 2, 3, 5, 10, 15, 20, 25, 30, 50, and 90. On the other hand, we have computed MC simulations by using the real-modes model given by (2). Fig. 2 shows the resulting relative variances, i.e., those obtained using the physical model (circles) and the equivalent model (triangles), respectively. In this procedure, 5000 realizations and 500 independent stirrer states were considered.

When using physical modes, the computation of the moments of  $P$  assumes that a sufficient number of (real) modes is considered in the simulation as explained in [7]. In a strict manner, the number of real modes included is always truncated. This does not happen with the equivalent model, since this one is defined as being composed of a finite number of DOF as expressed in

(6). Besides, it is clear that the number of DOF taken into account in the simulations are integer values since the sum in (6) is discrete. It allows us not to run into the question of setting a sufficiently large bandwidth.

Relative variances obtained with the physical model on the one hand, and with the statistical model on the other hand, are found to be in good agreement. This allows us to validate the fact that the relative variance obtained using (6) matches the “real” one obtained by using classical modal theory.

#### IV. DOF AND RELEVANCE OF A STATISTICAL APPROACH

The advantage of the statistical model lies in the simple overlap model that it provides. If a single DOF is excited would not it be a reasonable criterion to consider it as the minimum requirement to consider the relevance of a statistical approach? We propose to regard the frequency for which a single DOF is considered as the minimum frequency from which a statistical modeling of the field makes sense.

We emphasize to distinguish this frequency, referred to as  $f_m$ , from the lowest useable frequency (LUF). This one is indeed defined over a homogeneity criterion of the maximum stress [10]. The link between the variabilities considered herein and the maximum stress being not straightforward,  $f_m$  and the LUF are clearly different quantities. Note however that  $f_m$  is likely to be lower than the LUF.

In the light of the above,  $f_m$  is such that

$$\mathbf{E}_e(\mathbf{r}, f_m) \triangleq \mathbf{E}_e(\mathbf{r}, f), N = 1. \quad (16)$$

In order to determine  $f_m$ , we must solve the following equation:

$$N(f_m) = m(f_m) \pi B_M = 1. \quad (17)$$

Recalling that  $B_M = f_m/Q$ , where  $Q \equiv Q(f_m)$  is the composite quality factor [11], relation (17) can be recast and  $f_m$  must satisfy

$$m(f_m) \pi f_m = Q(f_m). \quad (18)$$

The frequency range under consideration corresponds to the case where the RC is undermoded. Accordingly, we prefer to adopt the following modal-density expression:

$$m(f) \simeq \frac{8\pi V f^2}{c_0^3} - \frac{a + b + c}{c_0} \quad (19)$$

valid for the cuboid case, note that the second term is a correcting term for low frequencies [11] where  $a$ ,  $b$ , and  $c$  correspond to the cuboid edges.

We observed in [8] that the quality factor of the chamber was quite linear with the frequency. The study was performed for a minimum frequency of 700 MHz, i.e., for a frequency above the 550 MHz LUF of the chamber. In order to have a more accurate insight on the value of  $f_m$ , we processed measurements between 200 MHz and 1 GHz. Note that for these measurements, the RC was empty. Fig. 3 shows the evolution of the quality factor, the left-hand term of (18) is superimposed. The intersection point provides the solution for  $f_m$  which turns out to be about 250 MHz, i.e., well below the LUF as expected.

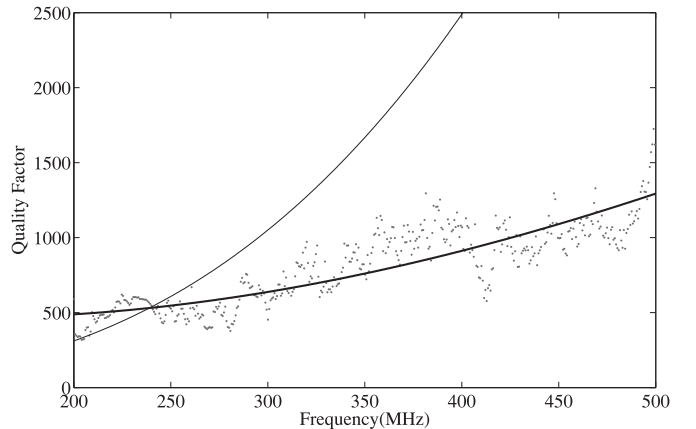


Fig. 3. Estimated  $Q$  factor (symbols) with the average trend (bold line).  $m(f) * \pi f$  (thin solid line) has been superposed. The intersection point highlights the frequency for which a single DOF is found.

#### V. CONCLUSION

A statistical model of the electric field has been presented. It is based on a square frequency response of the modes which allows us to highlight the number of DOF of the field. The interest of this choice lies in the fact that only a strictly finite number of modes overlap. The number of DOF is defined over a criterion based on the variability of the power measured along a linearly polarized antenna and/or of the electric energy density.

If less than a single DOF is considered, the relevance of a statistical approach is cut down. Accordingly the frequency at which a single DOF is excited was proposed to be regarded as the lower bound from which a statistical approach would make sense in a reverberation chamber. The frequency is expected to be smaller than the LUF commonly considered in EMC.

#### REFERENCES

- [1] *Reverberation Chamber Test Methods*, IEC Standard 61000-4-21, 2003.
- [2] T. H. Lehman, “A statistical theory of electromagnetic fields in complex cavities,” Interaction Notes, USAF Phillips Laboratory, NM, USA, Note 494, May 1993.
- [3] J. Kostas and B. Boverie, “Statistical model for a mode-stirred chamber,” *IEEE Trans. Electromagn. Compat.*, vol. 33, no. 4, pp. 366–370, Nov. 1991.
- [4] A. Papoulis, *Probability, Random Variables, and Stochastic Processes*, 2nd ed. New York, NY, USA: McGraw-Hill, 1984, p. 168.
- [5] F. Monsef and A. Cozza, “Variability and confidence intervals of the power measured in a reverberation chamber,” *IEEE Trans. Electromagn. Compat.*, vol. 56, no. 5, pp. 1238–1241, Oct. 2014.
- [6] L. Arnaut and G. Gradoni, “Probability distribution of the quality factor of a mode-stirred reverberation chamber,” *IEEE Trans. Electromagn. Compat.*, vol. 55, no. 1, pp. 35–44, Feb. 2013.
- [7] F. Monsef, “Why a reverberation chamber works at low modal overlap,” *IEEE Trans. Electromagn. Compat.*, vol. 54, no. 6, pp. 1314–1317, Dec. 2012.
- [8] F. Monsef and A. Cozza, “Average number of significant modes excited in a mode-stirred reverberation chamber,” *IEEE Trans. Electromagn. Compat.*, vol. 56, no. 2, pp. 259–265, Apr. 2014.
- [9] A. Cozza, “The role of losses in the definition of the overmoded condition for reverberation chambers and their statistics,” *IEEE Trans. Electromagn. Compat.*, vol. 53, no. 2, pp. 296–307, May 2011.
- [10] *Reverberation Chamber Test Methods*, IEC Standard 61000-4-21, 2011.
- [11] B. Liu, D. Chang, and M. Ma, “Eigenmodes and the composite quality factor of a reverberating chamber,” U.S. Nat. Bur. Stand., Tech. Rep. 1066, 1983.

# CHAPITRE 3

## Retournement Temporel

Les travaux sur le retournement temporel (RT) se sont intégrés dans les travaux amorcés au laboratoire par Andrea Cozza. Ces travaux portent sur le RT classique dans deux types d'environnements principaux : les milieux *indoor* et les chambres réverbérantes.

Un deuxième volet concerne le développement du RT dit généralisé qui peut être vu comme un prolongement et/ou une généralisation du RT classique. On entend par RT classique la technique développée dans les années 90 par l'équipe de Matthias Fink de l'ESPCI et permettant de focaliser une onde en un point (FINK 1992; WU, THOMAS et al. 1992; CASSEREAU et FINK 1992).

### I Retournement Temporel classique

Pour situer l'intérêt des travaux menés dans le cadre du RT, il convient de rappeler les performances offertes par le RT classique et les questions ouvertes dans ce domaine.

Le RT classique est une technique dont le protocole classique s'effectue en deux phases. La première phase consiste à émettre un signal par le biais d'une source (acoustique ou électromagnétique). Dans sa version d'origine, on considère cette source entourée de transducteurs qui reçoivent et enregistrent les signaux propagés<sup>9</sup>; Dans la partie gauche de la Fig. 3.1, on représente cette première phase. Ces transducteurs sont communément appelés *Miroirs à Retournement Temporel (MRT)*. Si  $x(t)$  est le signal envoyé,  $y(t)$  correspond au signal reçu par un transducteur et  $h(t)$  correspond à la réponse impulsionnelle, on a,

$$y(t) = h(t) * x(t), \quad (3.1)$$

où  $*$  est l'opération de convolution.

La deuxième phase consiste à renverser les signaux acquis dans le temps et à les réinjecter dans les *MRT* entourant la source initiale, comme illustré dans la partie droite de la Fig. 3.1. On réinjecte alors  $y(-t)$ ; si le milieu est réciproque la réponse impulsionnelle (R.I) est inchangée et on obtient alors un signal, noté  $s(t)$ , au niveau du point source initial tel que,

$$s(t) = h(t) * h(-t) * x(-t), \quad (3.2)$$

Une onde se propage alors vers la source initiale autour de laquelle elle se focalise sur le point source (puis diffracte). On peut y voir une forme de rétro propagation sous réserve que la R.I

9. définie par M-Fink comme Cavité dite à *Retournement Temporel* cf. Ref. (CASSEREAU et FINK 1992)

### 3 Retournement Temporel

est une distribution de Dirac. En toute rigueur, ce n'en est pas une dans la mesure où le signal qui se focalise est affecté par le milieu et n'est donc pas une réplique exacte de ce qui a été émis.

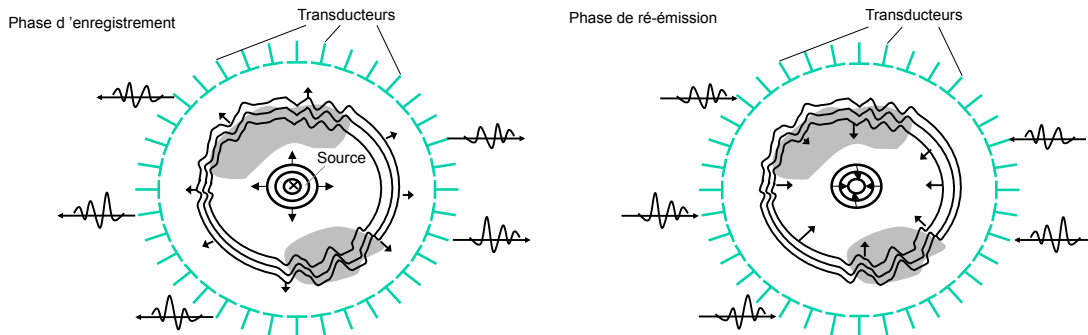


FIGURE 3.1 – Phase d'émission et d'enregistrement des signaux par les MRT (gauche) et réémission par réinjection des signaux dans les MRT (droit) dans le protocole du RT classique (d'après *Tourin (ESPCI)* ).

Le milieu de propagation ne permet pas en effet de transmettre les composantes réactives du champ, i.e., les composantes au nombre d'onde élevé. On pourrait donc modéliser le signal focalisant comme le signal initial entâché d'un *bruit de reconstruction*, noté  $N(f)$  dans l'espace des fréquences et  $n(t)$  dans l'espace des temps.

Il a été montré que le cas de la cavité à RT peut être drastiquement simplifié dans des milieux complexes (LEROSEY, DE ROSNY et al. 2004) ... tels qu'une chambre réverbérante. La simplification réside dans le fait de ne plus avoir besoin d'autant de transducteurs. L'idée est que l'on puisse collecter le maximum d'informations sur l'onde émise. Un raisonnement avec le principe des images permet de mettre en évidence cet atout. Ainsi, dans un milieu complexe, la deuxième phase, peut, à l'extrême, s'appuyer sur un seul récepteur ! L'apparition d'un champ focalisant se fera durant un laps de temps, ou *fenêtre temporelle*, pendant lequel aucune réflexion sur les parois n'aura lieu.

Dans le cas de milieux complexes tels que les chambres réverbérantes le bruit de reconstruction est encore plus important du fait des résonances du milieu : certaines fréquences sont filtrées par le milieu. Le signal focalisant pourra d'autant moins être une réplique du signal émis initialement. Le fait que certaines fréquences soient filtrées amène à ne pas considérer le RT en régime monochromatique, le risque étant de ne rien obtenir dans le cas où la fréquence coïncide avec un zéro de transmission ; le fonctionnement du RT dans un tel régime serait très aléatoire et fortement lié à l'emplacement de la source et du récepteur.

Plus la bande passante du signal augmente, plus la fonction de transfert est complexe. Il est alors adapté de la décrire de manière statistique. L'augmentation de la bande passante accroît la complexité de la réponse en fréquence. Toutefois les moments de celle-ci deviennent indépendants du point source et du TRM. Ceci est illustré Fig. 3.2 pour laquelle 4 fonctions de transfert  $|S_{21}|^2$  sont reportées. Celles-ci ont été prises en quatre points distants d'un mètre les uns des autres ; on considère une bande de 300 MHz centrée autour de 1.5 GHz. On voit que les moments d'ordre 1 et 2 fluctuent de 10 à 15% - la variance relative (variabilité) y figure également car on évalue un peu plus loin son influence sur le bruit de reconstruction. On peut percevoir que les variabilités abordées au chapitre précédent se retrouvent dans le cadre de cette application.

L'étude des signaux dans l'espace des fréquences met en évidence que le RT classique est un

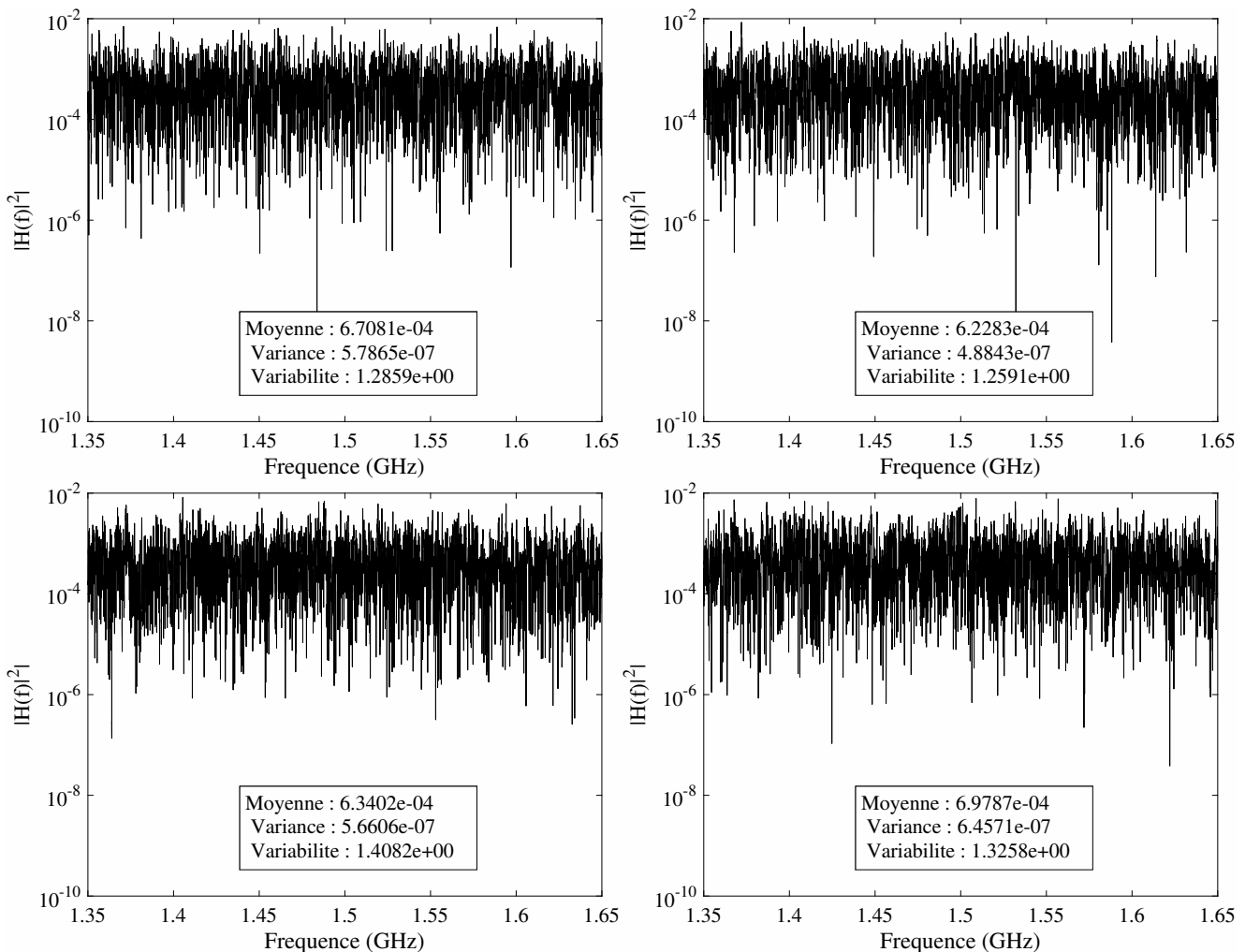


FIGURE 3.2 – Relevés expérimentaux de  $|S_{21}|^2$  en quatre points de la CR pour une position de brasseur fixe. On constate que les moments statistiques ont des valeurs proches pour ces quatre positions.

filtre adapté pour lequel la conjugaison de phase permet de rattraper le déphasage subi lors de la première phase. Il est donc commode de travailler avec la transformée de Fourier de la relation (3.2), et obtenir la réponse suivante dans l'espace des fréquences,

$$S(f) = |H(f)|^2 X^*(f), \quad (3.3)$$

où  $S(f)$ ,  $H(f)$  et  $X(f)$  sont respectivement les transformées de Fourier de  $s(t)$ ,  $h(t)$  et  $x(t)$ .

Si l'on pose,

$$|H(f)|^2 = \bar{H}^2 + \delta H^2, \quad (3.4)$$

où  $\bar{H}^2$  est une constante, le signal refocalisé peut être vu comme la superposition d'une image du *template* initial ( $\bar{H}^2 X^*(f)$ ) et d'un bruit de reconstruction ( $N(f) = \delta H^2 X^*(f)$ ) à valeur moyenne nulle. Ce bruit est multiplicatif, i.e., augmenter la puissance de  $x(t)$  amènerait à amplifier également le bruit. La partie utile dans le domaine des fréquences, notée  $S_c(f) = |\bar{H}^2| X(f)$ , est qualifiée de *partie cohérente* au sens de la cohérence de phase inhérente au filtre adapté et la partie bruit est notée  $N(f)$  comme introduit précédemment ;  $s_c(t)$  et  $n(t)$  correspondent aux notations temporelles.

### 3 Retournement Temporel

Il est intéressant de souligner que l'intégralité de mes travaux sur le RT s'est faite à partir de mesures dans l'espace des fréquences. L'intérêt est de s'affranchir des bruits autres que le bruit intrinsèque à la technique elle-même. Tous les signaux temporels sont donc obtenus par post-traitement en prenant une transformée de Fourier inverse. Afin de juger de l'allure des signaux émis et focalisé, on donne un exemple Fig. 3.3 pour laquelle on reporte la fonction de transfert pondérée par une fonction gaussienne (haut), le template temporel, le signal focalisé. On constate que le signal focalisé porte un bruit que l'on isole dans le graphe donnant  $n(t)$ .

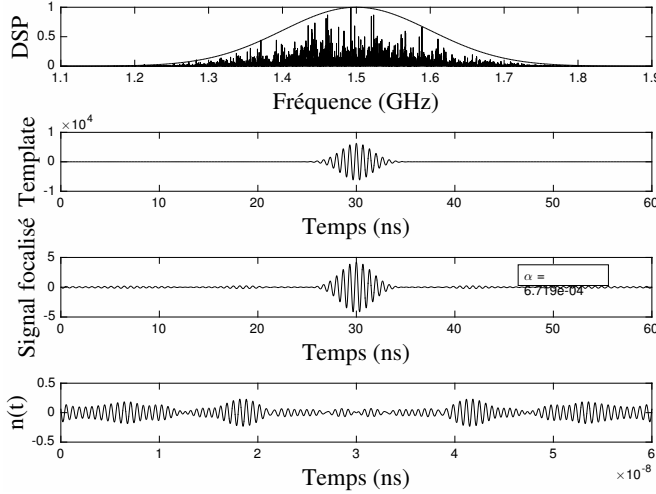


FIGURE 3.3 – La fonction de transfert (haut) est pondérée par une gaussienne. On obtient le signal focalisé pour un template du type impulsion gaussienne. Le bruit du signal focalisé est extrait et représenté sur le graphe du bas.

## II Métrique utile : le contraste en énergie et le contraste pic

Suivant les applications, deux visions sont à considérer quant aux métriques utiles. Pour les applications pour lesquelles le critère important est de pouvoir délivrer une énergie intense à l'instant de focalisation, on cherche à quantifier de combien l'énergie à l'instant de focalisation sort du niveau du bruit ; on parle alors de *contraste pic*, noté  $\Lambda_p$  dans la suite du manuscrit. Ce contraste est défini tel que,

$$\Lambda_p = \frac{s_c^2(0)}{n_{eff}^2} \quad (3.5)$$

où  $t = 0$  est pris comme l'instant de focalisation,  $n_{eff}^2$  représente la puissance de bruit et  $s_c^2(0)$  la puissance instantanée de la partie cohérente à l'instant de focalisation.

Pour les applications pour lesquelles la forme de l'impulsion à l'instant de focalisation a une importance, le contraste en énergie, noté  $\Lambda$  est alors plus utile pour quantifier ce que l'on qualifierait de SNR dans les télécommunications. Si l'on considère  $\mathcal{E}_c$  l'énergie de la partie cohérente et  $\mathcal{E}_f$  l'énergie de la partie fluctuante (bruit), on a  $\Lambda$  tel que,

$$\Lambda = \frac{\mathcal{E}_c}{\mathcal{E}_f}. \quad (3.6)$$

Les deux contrastes ont été reliés dans (COZZA 2009) ; il y a été montré comment la forme de l'impulsion envoyée impacte les contrastes. Nous verrons une manière différente de les relier, notamment en présence de plusieurs MRT.

## III Contributions au RT classique

Dans le cadre des travaux menés, une partie a porté sur le RT classique dans plusieurs contextes. Le cas des milieux hétérogènes ou multi-trajets a été considéré avec une attention particulière portant sur l'influence du nombre de MRT. Le cas de milieux *indoor* a également été étudié pour analyser les performances de transmissions point à point basées sur le RT pour des applications Telecom. Enfin, le cas de perturbation dans un milieu a été dérivé afin d'en mesurer l'impact sur les performances de RT.

### III.1 Influence du nombre de sources

L'étude de l'influence du nombre de sources nous a amené à reconsidérer la manière d'exprimer le contraste en énergie et le contraste pic. Pour une source, le contraste en énergie est par définition le rapport de l'énergie du *template* sur l'énergie de bruit , soit une image de  $\bar{H}^2/\delta H^2$ . Il en découle aisément que le contraste en énergie est directement relié à la variabilité du milieu tel que :  $\Lambda = 1/\varsigma_W^2(f_c)$ , où  $f_c$  est la fréquence centrale de la bande occupée de l'impulsion émise. Le calcul mené dans (COZZA et MONSEF 2014) met en évidence que ce résultat suppose que le spectre de l'impulsion soit lentement variable devant la bande de cohérence  $B_c$ .

En outre pour relier les contrastes entre eux, on a montré que  $\Lambda_p = \Lambda \times B_T/B_c$  (COZZA et MONSEF 2014). On peut voir dans le rapport  $B_T/B_c$  le nombre de degrés de liberté (modes significatifs) du champ EM généré. A l'instant de focalisation, le bruit étant nul, la partie cohérente bénéficie des contributions en phase de chaque mode équivalent. Ainsi, on observe que le contraste pic est lié à la bande occupée de l'impulsion, contrairement à  $\Lambda$ . Pour ce dernier on s'est intéressé à sa dépendance avec le nombre de MRT.

Intuitivement, plus le nombre de MRT augmente plus on pourrait s'attendre à une amélioration monotone des contrastes. Pour s'en convaincre, un déploiement des images de ces MRT permettrait de mettre en évidence que le système se ramènerait au cas de la cavité à retournement temporel de la Fig. 3.1. La différence est toutefois que les transducteurs seraient agencés de manière désordonnée et donc pas forcément optimale ; chaque miroir aurait néanmoins une contribution. Cette intuition s'avèrera vraie dans le cas où les MRT seraient totalement indépendantes. Or dans un milieu réverbérant, il existe une corrélation spatiale (HILL et LABDURY 2002). En d'autres termes, les signaux reçus par certains MRT portent une information partiellement contenue dans le signal reçu par le MRT voisin. Si l'on considère un niveau de corrélation moyen  $\bar{\mu}_r$  l'intérêt d'augmenter le nombre  $N_A$  de MRT va diminuer car une partie de l'information portée par chaque MRT deviendra redondante. Vu d'un point de vue fluctuations, celles-ci deviendront corrélées de telle sorte que la somme globale  $\delta H^2$  ne sera pas à moyenne nulle, menant à une performance « plafond » ; au contraire si elles étaient vraiment indépendants, la somme tendrait vers zéro.

Pour rendre compte de ce phénomène, nous nous sommes intéressés à l'amélioration du contraste en énergie obtenue après l'introduction d'un MRT supplémentaire ; on s'y réfère à travers la notion d'amélioration *incrémentale* sachant  $N_A$  sources déjà présentes. Ce rapport

### 3 Retournement Temporel

est tel que (COZZA et MONSEF 2014)

$$\frac{\Delta\Lambda}{\Lambda^0} = \frac{1 - \bar{\mu}_r}{1 - \bar{\mu}_r + N_A \bar{\mu}_r (2 - \bar{\mu}_r)}, \quad (3.7)$$

où  $\Lambda^0$  représente le contraste mono-MRT, i.e., pour  $N_A = 1$ . Pour la validation du modèle

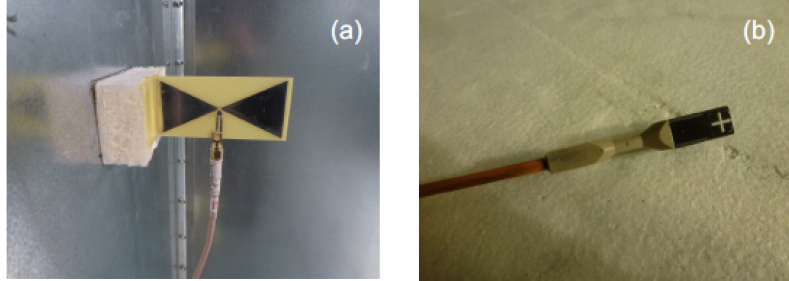


FIGURE 3.4 – Setup expérimental : (a) une des 12 antennes papillons, montées sur les parois de la chambre réverbérante, avec un espaceur de 3 cm en polystyrène; (b) La sonde électro-optique Enprobe's EFS105, équipée d'une tête de mesure de 6.6 mm de large.

trouvé, on a procédé à un protocole expérimental incluant douze antennes papillons (cf. Fig. 3.4). Ces antennes ont été conçues pour travailler sur une plage de 500 MHz à 2 GHz. Pour une position de brasseur, douze fonctions de transfert ont ainsi été mesurées sur cette plage de fréquence. Afin de générer un ensemble de réalisations, 50 positions du brasseur ont été utilisées. Il est important de souligner qu'un post-traitement des fonctions de transfert a été effectué afin de soustraire la contribution de ligne directe (*Line of sight*) commune aux fonctions de transfert, et ce, afin de respecter l'hypothèse de milieu diffusif. Pour plus de détails, on renvoie à la publication jointe en annexe.

Un des paramètres importants qui ressort de (3.7) est la corrélation moyenne existant entre les différentes antennes. On montre Fig. 3.5 l'évolution du gain incrémental en fonction du nombre d'antennes présentes dans la chambre, les courbes étant paramétrées par le niveau moyen de corrélation. On peut voir à quelle vitesse l'introduction d'un nouveau MRT perd de son efficacité sur le contraste en fonction du niveau de corrélation moyen.

Pour estimer le gain incrémental attendu dans le cas du setup proposé, nous avons estimé le niveau de corrélation moyen entre les fonctions de transfert sur des bandes de fréquence de 5%. On montre l'estimation de niveau de corrélation sur la Fig. 3.6. Comme attendu, le niveau de corrélation baisse avec la fréquence, et ce, à cause du degré de surmodage qui augmente jusqu'à 1,5 GHz puis plafonne. Dans la configuration considérée, on passe d'un niveau moyen d'environ 25% vers 500 MHz pour plafonner autour de 5% à plus haute fréquence.

De telles performances sont possibles dans un milieu réverbérant. Un certain nombre d'auteurs, voient dans les milieux multi-trajets une forme de réverbération. Nous avons rejoint l'intérêt porté à l'étude de la viabilité du retournement temporel dans des milieux indoors.

### Transmissions par RT en milieux *indoor*

L'étude sur la viabilité du RT en milieu indoor a été essentiellement expérimentale et a donné lieu à deux conférences internationales (MONSEF, COZZA et ABOUD 2010 ; MONSEF et COZZA

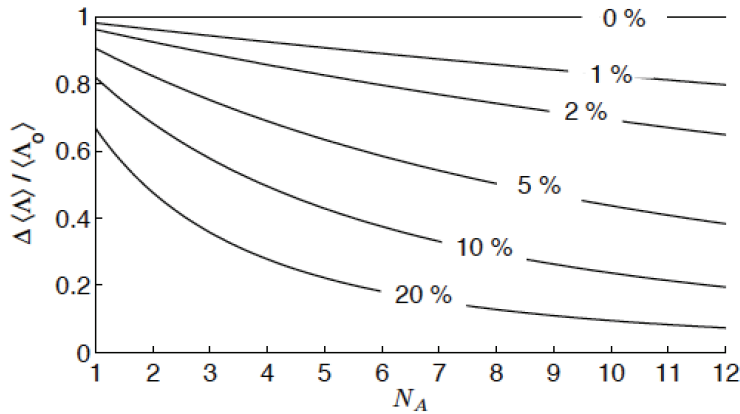


FIGURE 3.5 – Apport incrémental à l’ajout d’un MRT sachant  $N_A$  MRT déjà présents, en considérant un niveau moyen de cohérence  $\bar{\mu}_r$  (en pourcentage sur chaque ligne).

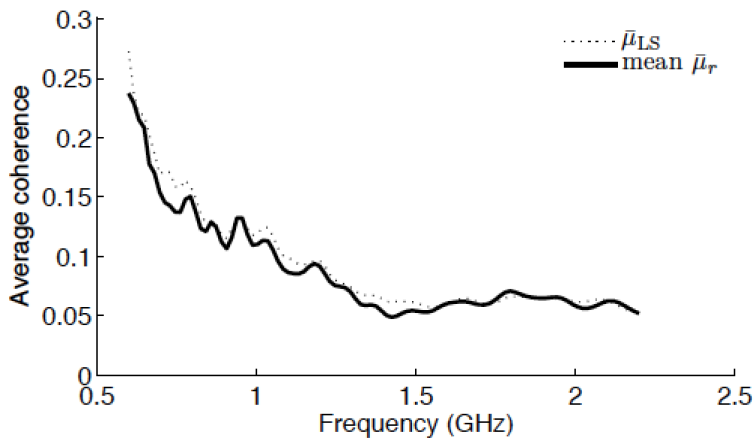


FIGURE 3.6 – Corrélation moyenne estimée entre différentes fonctions de transfert (trait plein) ; régression au sens des moindres carrés est superposée (pointillés).

2011).

Les études trouvées dans la littérature portent sur l’utilisation des caractéristiques de focalisation du RT pour permettre des transmissions point à point, sécurisées le cas échéant. L’étude a consisté à considérer des milieux standards tels que des couloirs, des halls et des bureaux pour juger de la qualité de focalisation et d’étudier de plus près les aspects « transmissions sécurisées ».

Plusieurs milieux *indoor* ont été étudiés. La richesse du canal est directement liée à la complexité et à la durée  $T_{RMS}$  de la réponse impulsionale (prise à -60dB) du milieu considéré ; on obtient les réponses impulsionales Fig. 3.8.

Nous introduisons deux métriques afin d’estimer les performances du RT. La première est un SNR défini comme le taux de réjection du deuxième écho par rapport à l’impulsion utile (cf Fig. 3.9). Ce critère est utile pour limiter les interférences inter-symboles. La deuxième métrique est un gain défini comme le rapport du SNR obtenu par RT et du SNR obtenu sans RT.

Si l’on considère que le temps de réponse est un paramètre associé à la complexité du milieu,

### 3 Retournement Temporel

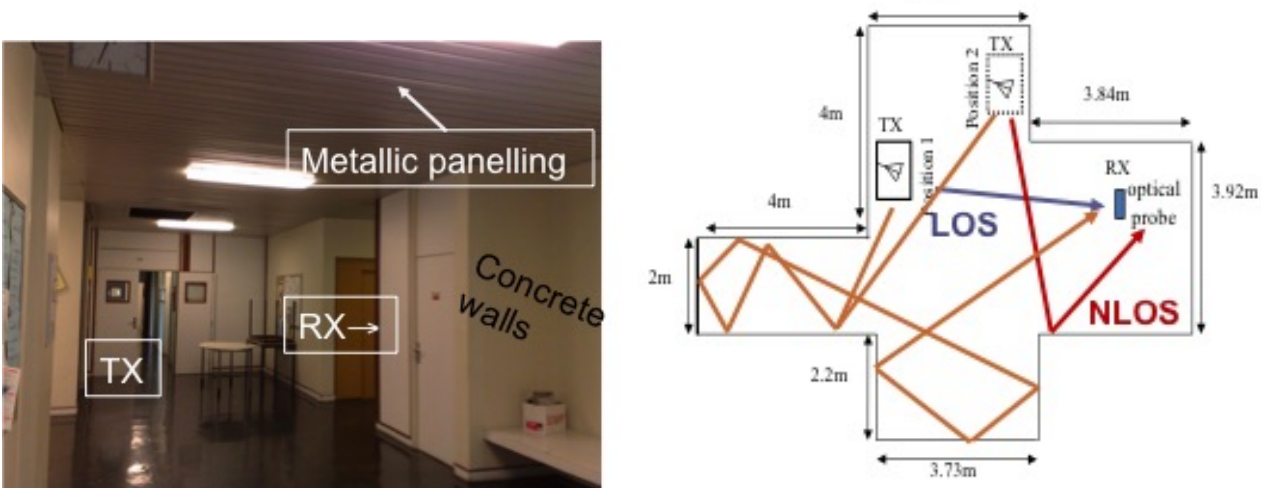


FIGURE 3.7 – Exemple de milieu indoor dans lequel les performances du RT ont été étudiées (gauche) avec les dimensions et positionnement(s) des émetteurs/récepteur (droite). On constate des trajets directs (*LOS*) et des parcours multi-trajets (*NLOS*).

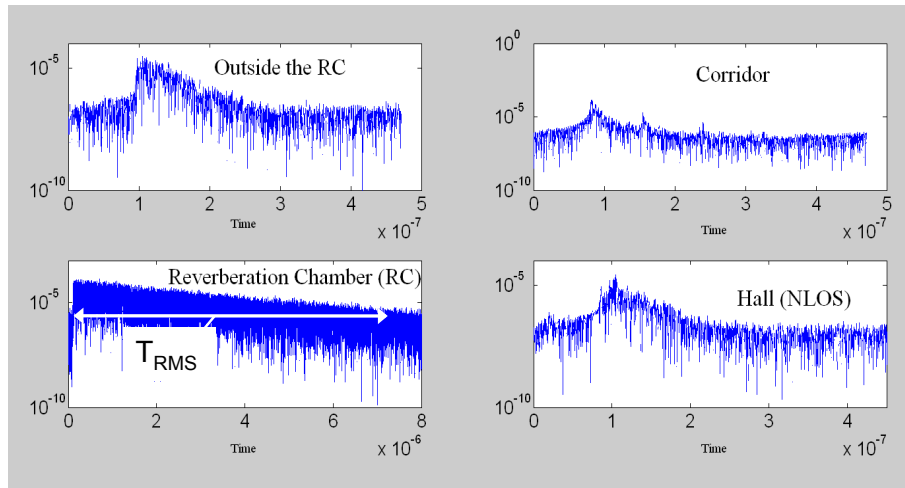


FIGURE 3.8 – Réponses impulsionnelles des différents milieux étudiés : en-dehors de la chambre (en haut à gauche), dans un couloir (en haut droite), dans la chambre réverbérante (en bas à gauche) et dans le hall illustré Fig. 3.7.

il est intéressant d'évaluer le SNR obtenu pour le RT. On résume les résultats Fig. 3.10. Les mesures ont été effectuées pour trois fréquences centrales avec des bandes relatives de ??

Le degré de complexité étant illustré par le temps de réverbération  $T_{RMS}$ , on observe Fig. 3.10 une certaine corrélation entre la degré de complexité du milieu et la valeur du SNR (gauche) ainsi que le gain (droite).

Il s'avère que la richesse des échos en milieu *indoor* est insuffisante pour que l'effet auto-moyennant du RT permette de focaliser le signal de manière à pouvoir transmettre sur des récepteurs proches les uns des autres sans « baver » sur le récepteur adjacent.

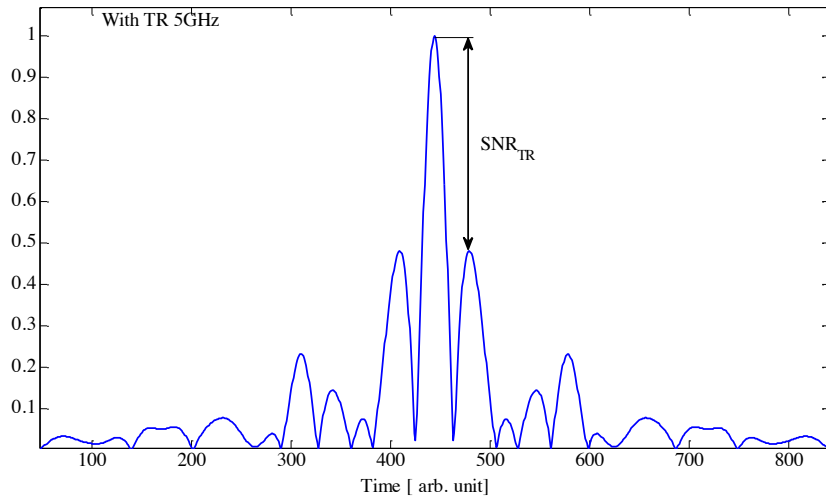


FIGURE 3.9 – Illustration du SNR obtenu par RT avec une fréquence de 5 GHz : rapport des deux pics considérés (écho et impulsion utile).

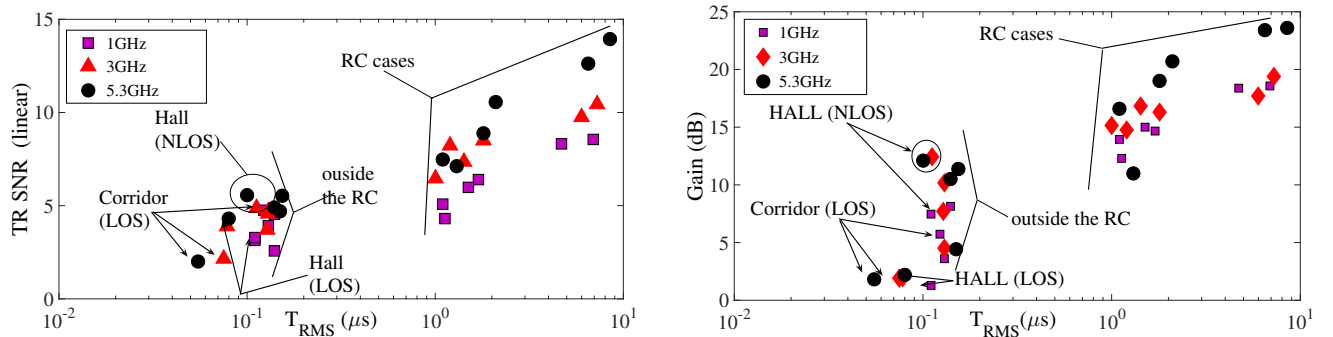


FIGURE 3.10 – SNR obtenus (gauche) dans les différents milieux *indoor* étudiés et le gain qu’apporte le RT (droite) par rapport une transmission classique.

### III.2 RT pour la synthèse de front d’ondes : la TREC

Le RT a été étendu à l’idée de pouvoir générer un front d’onde contrôlé en termes de polarisation, direction d’incidence et de forme, ce dernier point sera discuté plus en détail. Ayant vu précédemment que la complexité du milieu était synonyme de bonnes performances du RT, une chambre réverbérante a été considérée pour l’étude de cette extension du RT. Ce dispositif est appelé *TREC* pour (*Time-Reversal Electromagnetic Chamber*) (COZZA et MOUSSA 2015) et le principe a été formalisé par Andrea Cozza dans (COZZA 2012).

Contrairement au RT classique il n’y a pas d’étape initiale pendant laquelle une vraie source émet. En fait, une manière simple d’appréhender l’idée derrière la TREC est de partir de ce que l’on veut : créer un front d’onde incident sur un dispositif sous test. L’étape initiale du RT suppose que ce front d’onde est émis par une source ... virtuelle !

Dans un tel scénario, considérons une surface ( $S$ ) que le front d’onde traverse. En discréteisant cette surface, on peut y mesurer le champ électrique  $\mathbf{E}_s$  et magnétique  $\mathbf{H}_s$ , l’indice  $s$  renvoyant à la surface considérée. En utilisant le principe d’équivalence, cela revient à considérer que des sources électriques et magnétiques, notées respectivement  $\mathbf{J}_s$  et  $\mathbf{M}_s$ , placées en ces points génér-

### 3 Retournement Temporel

reraient le front d'onde à l'extérieur de cette surface ... dans l'étape initiale du RT. Finalement, les « vraies » sources à considérer dans le cas de la TREC sont en fait ces sources  $\mathbf{J}_s$  et  $\mathbf{M}_s$ . Dans le cas de front d'onde directif, la surface (S) peut être vue comme un ensemble de sources électriques et magnétiques croisées, ou coupleurs directifs, qui rayonnent le champ désiré. Cette phase doit rester néanmoins virtuelle sous peine de ne pouvoir créer le front d'onde incident sur l'objet sous test, car la surface (S) doit évidemment rester électromagnétiquement « transparente », i.e., ne doit pas comporter d'éléments diffractants. « L'astuce » consiste alors à utiliser le principe de réciprocité : les éléments rayonnants seront les MRT et la mesure du champ se fera sur la surface (S) ; cette mesure doit être la moins perturbante possible.

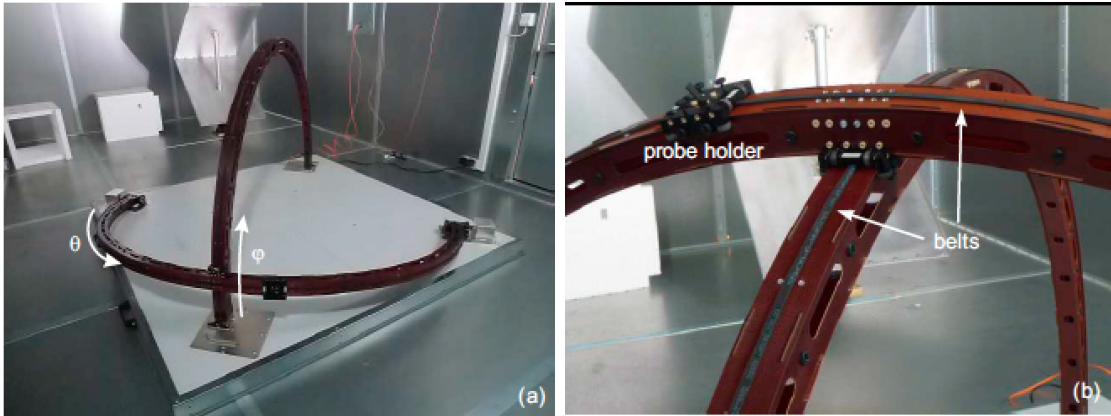


FIGURE 3.11 – L'arche constituant le coeur de la TREC consiste en un échantillonneur spatial du champ suivant les coordonnées polaires  $\theta$  et  $\varphi$  (a) - Un zoom met en évidence le système de courroie utilisé ainsi que le chariot accueillant la sonde électro-optique (b).

Comme montré Fig. 3.11 la TREC est constitué d'un échantillonneur du champ sur une surface de Huyghens hémisphérique. Pour remplir la contrainte d'être le moins perturbant possible, l'arche est constitué de matériaux dont la permittivité est proche de l'air et la mesure du champ se fait via la sonde électro-optique présentée Fig. 3.4. Le but est de pouvoir retrouver des conditions d'espace libre pendant un laps de temps donné en recréant un front d'onde émis par une source. En pratique, ceci nécessite d'échantillonner le champ sur une surface de Huyghens et ainsi, mesurer un ensemble de fonctions de transfert entre les points d'échantillonnage de cette surface et les MRT. Il est important de rappeler que les bras du système robotisé sont en diélectrique. De ce fait, le déplacement de ceux-ci engendrent en toute rigueur une perturbation. Le degré de perturbation est présenté en détail dans (COZZA, MASCIOVECCHIO et al. 2017) et permet de conclure à la viabilité du dispositif.

La mesure d'un ensemble de fonctions de transfert est le prix à payer pour pouvoir générer des fronts d'onde arbitraires. Dit autrement, c'est la contrainte à considérer pour pouvoir émuler un milieu anéchoïque dans un environnement tel qu'une chambre réverbérante. La contrepartie positive est de pouvoir générer des séries de tests où les directions d'incidence, les polarisations, les fronts d'onde sont configurables électroniquement.

On montre Fig. 3.12a un exemple de front d'onde gaussien 3D obtenu dans la TREC. Deux angles d'ouverture ont été considérés :  $10^\circ$  et  $40^\circ$ . Pour un détail des conditions expérimentales on renvoie à l'article (COZZA et MONSEF 2017b) joint en annexe. On illustre également la qualité de synthèse de front d'onde avec la TREC en présentant les coupes de composantes cartésiennes du champ Fig. 3.12b ; les topographies attendues sont sur la partie gauche tandis

que les topographies obtenues sont sur la partie droite respectivement. Un coefficient linéaire de corrélation de 97% témoigne de la bonne qualité de synthèse des fronts d'onde.

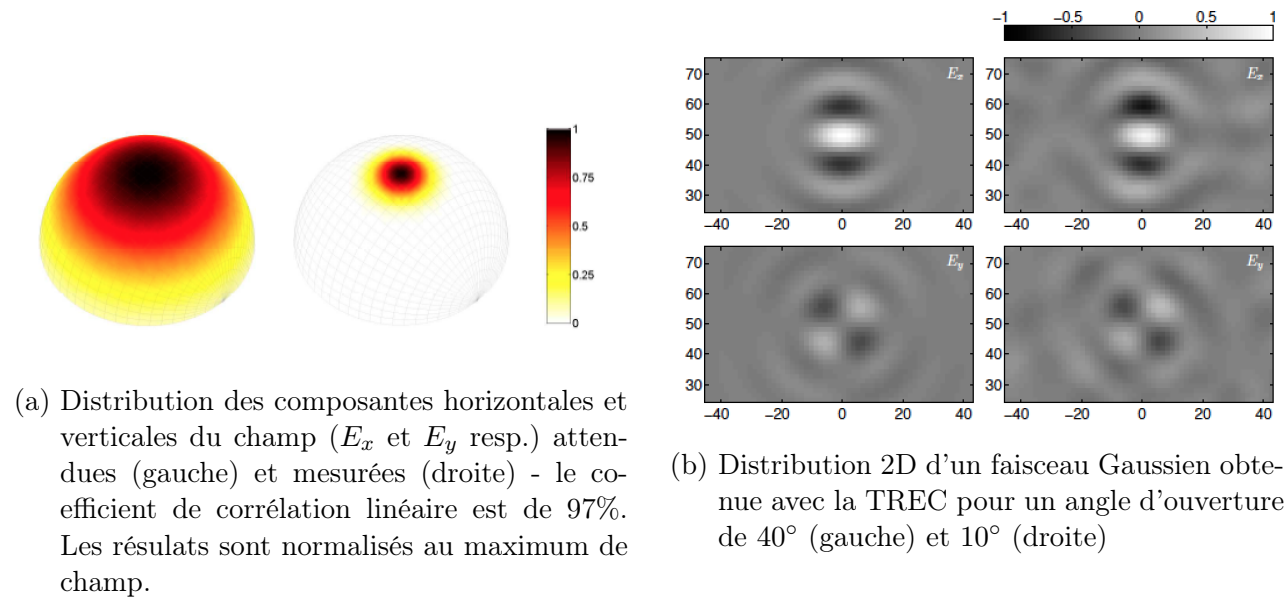


FIGURE 3.12 – Topographies 3D (gauche) et coupe 2D (droite) obtenues avec la TREC

Une des applications intéressantes de la TREC porte sur la mesure d'antenne hors chambre anéchoïque. Pour ce type d'application, un front d'onde plan (type onde plane) est souvent désiré. La thèse menée par Philippe Méton a permis d'explorer la faisabilité en la matière : générer un front d'onde plan avec une extension spatiale maîtrisée ... dans une chambre réverbérante ...

Le concept d'onde plane n'intègre pas la notion d'extension spatiale. En pratique, on considère souvent des ondes localement planes, qui pré-suppose que l'onde émise est (en général) divergente. Cela pose le problème d'une intensité qui diminue avec la distance. Si l'on veut contraindre l'extension spatiale du front d'onde, cela posera inévitablement, de par le principe d'incertitude, un étalement spectral théoriquement infini.

La problématique posée a donc porté sur la possibilité de décomposer les signaux émis dans les MRT sur une base de fonctions dont les extensions spatiales et spectrales puissent être limitées. Pour simplifier la formalisation, on a considéré l'étude de la concentration de l'onde incidente dans un plan focal 1D comme montré Fig. 3.13 où le champ est polarisé suivant  $z$  et un demi-angle d'ouverture  $\Theta$ . Le champ électrique, noté  $\mathbf{E}(\mathbf{r})$ , étant confiné suivant  $x$  uniquement, peut être alors décomposé en un spectre d'ondes planes, tel que,

$$\mathbf{E}(\mathbf{r}) = \int \tilde{\mathbf{E}}(k_x) \exp(-jk_x x) \exp\left(-j\sqrt{k_0^2 - k_x^2}y\right) dk_x, \quad (3.8)$$

où  $k_0$  est le nombre d'onde,  $\tilde{\mathbf{E}}(k_x)$  est le spectre onde plane à déterminer, relié au champ dans le plan focal  $\mathbf{E}(x, y = 0)$ , tel que :  $\tilde{\mathbf{E}}(k_x) = \mathcal{F}(\mathbf{E}(x, y = 0))$ , où  $\mathcal{F}(\cdot)$  est la transformée de Fourier.

Pour que le champ soit d'une part, confiné spatialement, et d'autre part confiné spectralement pour éviter toute dispersion du milieu, on introduit un opérateur respectant ces deux critères. Si l'on note  $\mathcal{C}$  l'opérateur de concentration, la fonction recherchée devra obéir à l'équation aux

### 3 Retournement Temporel

valeurs propres suivantes (SLEPIAN et POLLAK 1961) :

$$\mathcal{C}E_{x,n}(x) = \lambda_n E_{x,n}(x) \quad (3.9)$$

où la valeur propre  $\lambda_n$  correspond à la fraction d'énergie de la fonction confinée sur un intervalle fermé (spectral ou spatial). Les fonctions propres  $E_{x,n}(x)$  sélectionnées seront donc celles pour lesquelles  $\lambda_n \simeq 1$ . La notion d'énergie est entendue ici au sens d'une norme  $L2$ .

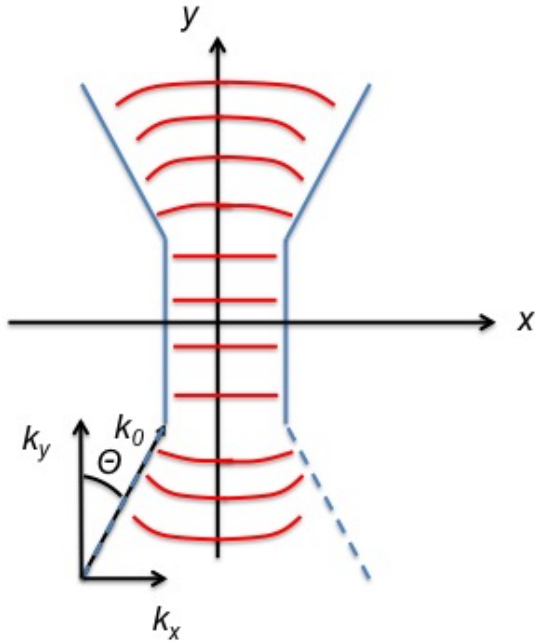


FIGURE 3.13 – Topographie de champ visé où la concentration de l'onde est confinée spatialement et localement plane.

Le nombre  $N_{sl}$  de Slepian « parfaitement » concentrées dans un intervalle  $[-W; +W]$  peut être estimé en sommant les valeurs propres, tel que (SIMONS 2010) :

$$N_{sl} \simeq \sum_{n=1}^{\infty} \lambda_n = 2W \sin \Theta \quad (3.10)$$

Pour  $W = 5$  et un angle  $\Theta = 20^\circ$ , on montre Fig. 3.14 les fonctions satisfaisant l'équation aux valeurs propres ; on peut constater que 5 fonctions peuvent être vues comme concentrées. Pour chaque fonction, on a reporté la valeur propre associée. On peut remarquer que pour une valeur propre inférieure à 0.5 les fonctions débordent en-dehors de la zone de confinement attendue. En fonction de la répartition optimale désirée  $E_{opt}$ , on en déduit les coefficients  $\alpha_n$  de projection de  $E_{opt}$  sur les fonctions de base. On obtiendra alors un champ  $E \simeq \sum_n \alpha_n E_n$ .

Supposons que l'on souhaite que  $E_{opt}$  corresponde à une fonction porte de largeur  $2W$ . Pour les 4 Slepian considérées Fig. 3.15, on détermine que le jeu de coefficients doit avoir les valeurs suivantes :  $\alpha_n = 0.2241, 0.1522, 0.1238, 0.08$  ; on obtient alors la topographie du champ total comme montrée Fig. 3.16.

Cette procédure 1D est à transposer en 3D pour le cas d'une TREC réelle. La synthèse des signaux à générer dans les MRT prendra comme base le champ échantillonné sur la surface de Huyghens évoqué lors de la présentation de la TREC. Le cas 3D est laissé en perspective.

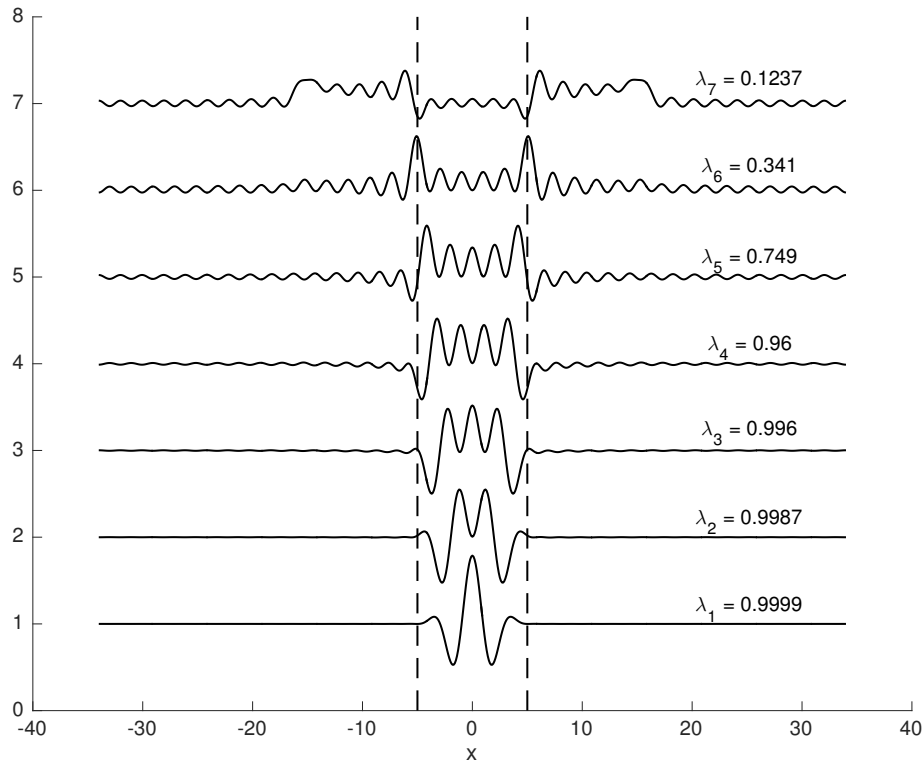


FIGURE 3.14 – Pour une largeur  $W=5$  et un angle  $\Theta = 30^\circ$ , on illustre les fonctions propres résultantes avec les valeurs propres  $\lambda_n$  correspondantes.

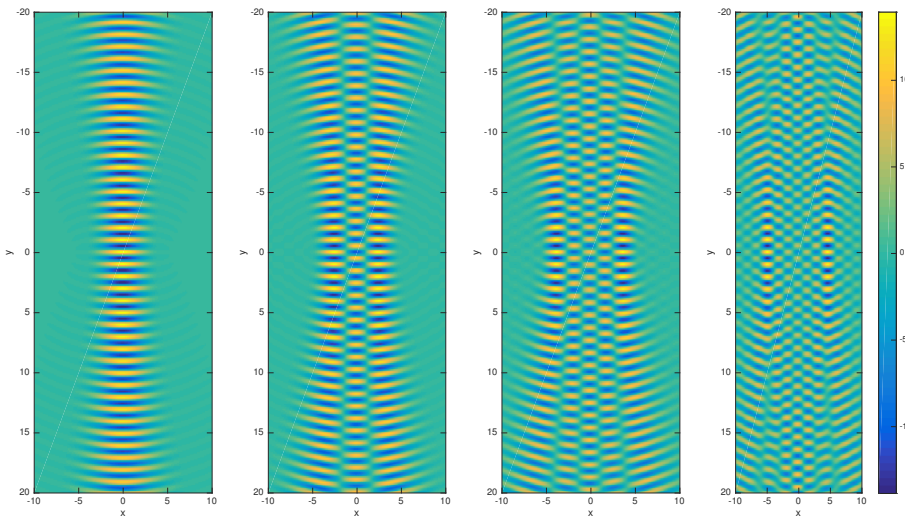


FIGURE 3.15 – Topographies des fonctions Slepian pour  $W = 5$  et un angle  $\Theta = 20^\circ$ .

L'étude s'est limitée au cas de milieux complexes tels que les chambres réverbérantes à brassage de modes. Lorsque un objet est déplacé dans un tel milieu, le déplacement ne modifie pas la statistique du milieu ; en revanche, les fonctions de transfert considérées pour une phase

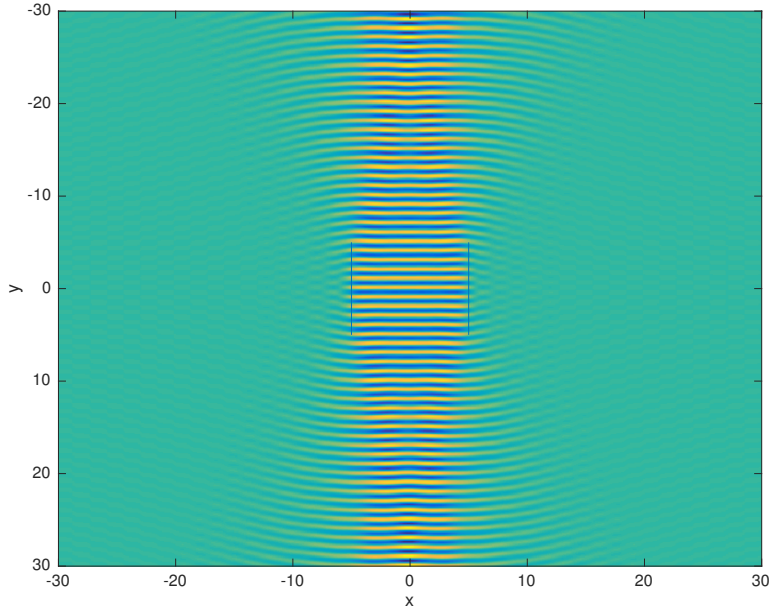


FIGURE 3.16 – Topographie de champ obtenue en incluant 4 Slepians

de RT sont modifiées. Suivant le degré de perturbation, la question est de savoir comment les énergies des parties cohérentes et fluctuantes sont modifiées par rapport au cas non perturbé.

Formellement cela revient à considérer la fonction de transfert modifiée, notée  $H(\nu)$ , en fonction de la fonction de transfert non perturbée, notée quant à elle  $H_0(\nu)$ , telle que

$$H(\nu) = \rho H_0(\nu) + \delta H(\nu) \quad (3.11)$$

où  $\rho$  est le facteur de corrélation linéaire entre la fonction de transfert perturbée et non perturbée ;  $\delta H(\nu)$  et  $H_0(\nu)$  sont donc orthogonaux. Dans le cadre de ce modèle, il est aisément de montrer que :

$$\mathcal{E}_c = \rho^2 \mathcal{E}_{c_0}, \quad (3.12)$$

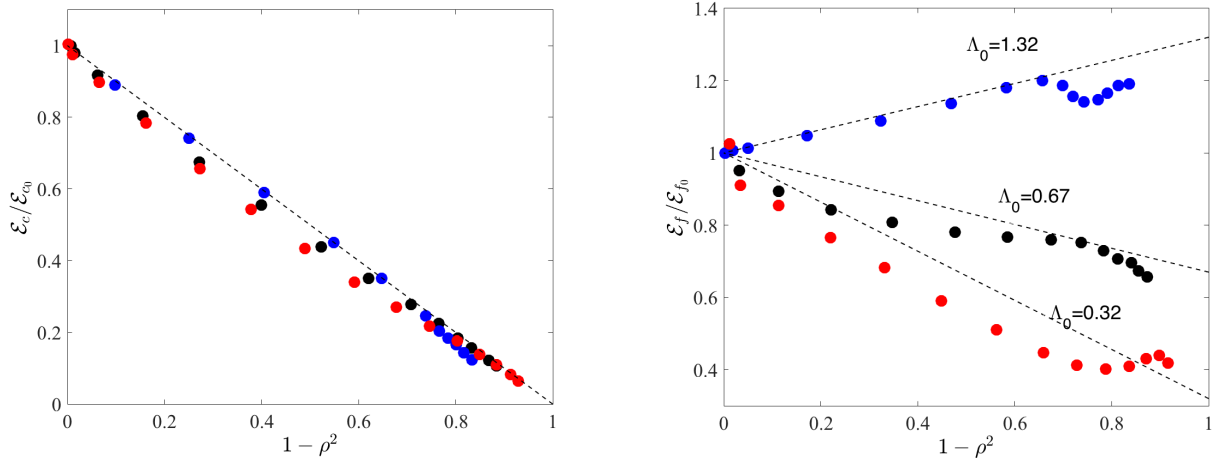
où  $\mathcal{E}_{c_0}$  et  $\mathcal{E}_c$  correspondent aux énergies de la partie cohérente avant et après perturbation. Dans le cadre de l'étude menée la perturbation était associée à la rotation du brasseur.

De la même manière on peut montrer (COZZA et MONSEF 2017a) que l'évolution de l'énergie des fluctuations est telle que :

$$\mathcal{E}_f / \mathcal{E}_{f_0} = \rho^2 (1 - \Lambda_0) + \Lambda_0, \quad (3.13)$$

où  $\Lambda_0$  est le contraste du milieu initial, i.e., du milieu non perturbé.

Pour cette étude, trois configurations de la chambre ont été adoptées menant à des contrastes initiaux de 0.32, 0.67 et 1.32. Pour ce dernier cas, la chambre est surmodée ou diffusive. Pour le détail de la façon dont ces configurations ont été mises en place on renvoie à la Ref. (COZZA et MONSEF 2017a). On représente Fig. 3.17a l'évolution du rapport exprimé dans (III.2) (tirets), en attirant l'attention que l'axe des abscisses est gradué en fonction de  $(1 - \rho^2)$ , i.e., gradué en fonction du niveau de perturbation introduit dans le milieu ; les résultats expérimentaux sont représentés par des cercles pleins de couleurs rouge, noir et bleu associés respectivement aux contrastes initiaux de 0.32, 0.67 et 1.32.



(a) Evolution du rapport de l'énergie de la partie cohérente en fonction du degré de perturbation pour trois conditionnements de la chambre. Les couleurs rouge, noire et bleue sont associées respectivement à des contrastes initiaux  $\Lambda_0$  de 0.32, 0.67 et 1.32.

(b) Evolution de l'énergie des fluctuations en fonction du degré de perturbation pour trois conditionnements de la chambre donnant lieu à des contrastes initiaux  $\Lambda_0$  différents.

FIGURE 3.17 – Evolution du rapport des parties cohérentes et fluctuantes en fonction du degré de perturbation illustré par le coefficient  $(1 - \rho^2)$ . Les résultats expérimentaux sont représentés par les symboles pour trois statistiques différentes de chambre ; les modèles théoriques sont représentés par les courbes en tirets.

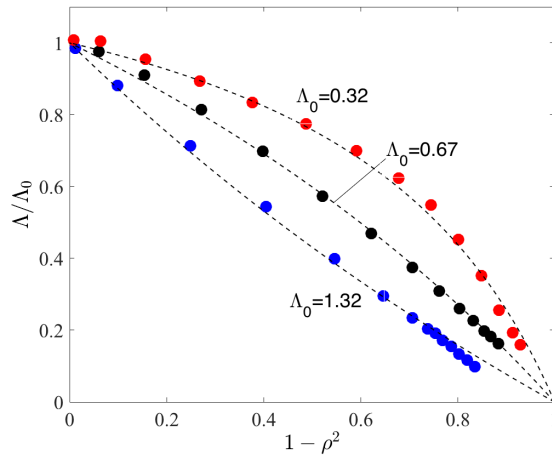


FIGURE 3.18 – Evolution relative du contraste en fonction du niveau de perturbation de la chambre, et ce, pour trois statistiques différentes.

On constate, que quelque soit la statistique initiale de la chambre (surmodée, partiellement surmodée,...), l'énergie de la partie cohérente décroît avec le niveau de perturbation comme on pouvait intuitivement s'y attendre. La Fig. 3.17b, quant à elle, met en évidence l'évolution de l'énergie de la partie fluctuations (en fonction du degré de perturbation également). On constate, comme montré par (III.2) (tirets), que l'évolution de celle-ci obtenue expérimentalement est fonction de la statistique initiale de la chambre (cercles de couleurs). Plus le milieu est diffusif

### 3 Retournement Temporel

au départ, plus l'énergie des fluctuations augmente (par rapport à ce qu'elle était initialement) avec le degré de perturbation ; a contrario, l'énergie des fluctuations tend à diminuer si le milieu n'est pas complètement diffusif au départ, i.e., si le contraste  $\Lambda_0$  est inférieur à 1.

Sachant que dans certains cas, l'énergie des fluctuations peut augmenter ou au contraire diminuer par rapport à la situation initiale, on peut se demander comment évolue le contraste. La Fig. 3.18 met en évidence l'évolution de  $\Lambda/\Lambda_0$  en fonction du degré de perturbation, et ce, avec comme paramètre le contraste initial de la TREC. Il en ressort que le contraste en cas de perturbation se dégrade mais la vitesse à laquelle se produit cette dégradation est fonction de la statistique initiale du milieu.

## IV Conclusion et perspectives

Les travaux menés sur les milieux indoors standard ont permis de montrer que le degré de complexité du milieu est vraiment fondamental dans l'obtention d'une focalisation spatiale satisfaisante.

Les travaux sur le retournement temporel ont permis de mettre en évidence les limites mais aussi les possibilités offertes par cette technique dans le cadre de la TREC notamment. Le travail sur l'intérêt du multi-source a permis quant à lui de mettre en évidence comment la statistique des grandeurs liées au champ, vues au chapitre 2, est directement impliquée dans le contraste de la partie cohérente et du bruit de reconstruction. De plus, bien que restreinte à un cas 2D, on a pu voir de quelle manière confiner une extension spatiale d'un front d'onde. Le cas 3D est laissé en perspective.

## Références

- CASSEREAU, D. et M. FINK (1992). « Time-Reversal of ultrasonic fields. III. Theory of the closed Time-Reversal cavity ». *IEEE Trans Ultrason Ferroelectr Freq Controll* 39.5, p. 579-592 (cf. p. 65).
- COZZA, A. (2009). « Statistics of the performance of Time Reversal in a lossy reverberating medium ». *Phys Rev E* 80.5, p. 56604 (cf. p. 69).
- COZZA, A. et F. MONSEF (2017a). « Influence of Medium Statistics on Robustness of Time-Reversal Transmissions ». *IEEE Antennas Wireless Propagat. Lett.* 16, p. 38-41. ISSN : 1536-1225. DOI : 10.1109/LAWP.2016.2553148 (cf. p. 78).
- COZZA, A. (2012). « Emulating an anechoic environment in a wave-diffusive medium through an extended Time-Reversal approach ». *IEEE Trans. Antennas Propagat.* 60.8, p. 3838-3852 (cf. p. 73).
- COZZA, A., F. MASCIOVECCHIO, C. DORGAN, M. SERHIR, F. MONSEF et D. LECOINTE (2017). « A Dielectric Low-Perturbation Field Scanner for Multi-Path Environments ». *IEEE Trans. Antennas Propagat.* 65.4, p. 1978-1987 (cf. p. 74).
- COZZA, A. et F. MONSEF (2014). « Multiple-source Time-Reversal transmissions in random media ». *IEEE Trans. Antennas Propagat.* 62.8, p. 4269-4281 (cf. p. 69, 70).
- COZZA, A. et F. MONSEF (2017b). « Steering Focusing Waves in a Reverberation Chamber with Generalized Time Reversal ». *IEEE Trans. Antennas Propagat.* 65.3, p. 1349-1356 (cf. p. 74).
- COZZA, A. et M. H. MOUSSA (2015). *Method of checking the directivity and polarization of coherent field distributions in a reverberant medium*. US Patent 9,103,862 (cf. p. 73).

- FINK, M. (1992). « Time Reversal of ultrasonic fields. I. Basic principles ». *IEEE Trans Ultrason Ferroelectr Freq Control* 39.5, p. 555-566 (cf. p. 65).
- HILL, D. A. et J. M. LADBURY (2002). « Spatial-correlation functions of fields and energy density in a reverberation chamber ». *IEEE Trans. Electromagn. Compat.* 44.1, p. 95-101 (cf. p. 69).
- LEROSEY, G., J. DE ROSNY, A. TOURIN, A. DERODE, G. MONTALDO et M. FINK (2004). « Time reversal of Electromagnetic waves ». *Phys. Rev. Lett.* 92.19, p. 193904 (cf. p. 66).
- MONSEF, F. et A. COZZA (2011). « Analysis of Time-Reversal-based propagation for spatial focusing and multiplexing ». *Antennas and Propagation in Wireless Communications (APWC), 2011 IEEE-APS Topical Conference on*. IEEE, p. 827-830 (cf. p. 70).
- MONSEF, F., A. COZZA et L. ABOUD (2010). « Effectiveness of Time-Reversal technique for UWB wireless communications in standard indoor environments ». *ICECom, 2010 Conference Proceedings*. IEEE, p. 1-4 (cf. p. 70).
- SIMONS, F. J. (2010). « Slepian functions and their use in signal estimation and spectral analysis ». *Handbook of geomathematics*. Springer, p. 891-923 (cf. p. 76).
- SLEPIAN, D. et H. O. POLLAK (1961). « Prolate spheroidal wave functions, Fourier analysis and uncertainty—I ». *Bell Labs Tech. J.* 40.1, p. 43-63 (cf. p. 76).
- WU, F., J.-L. THOMAS et M. FINK (1992). « Time Reversal of ultrasonic fields. II. Experimental results ». *IEEE Trans Ultrason Ferroelectr Freq Control* 39.5, p. 567-578 (cf. p. 65).

# Multiple-Source Time-Reversal Transmissions in Random Media

Andrea Cozza, *Senior Member, IEEE* and Florian Monsef, *Member, IEEE*

**Abstract**—The ability of time-reversed signals in reproducing a given time-dependence of the electromagnetic field within random media is investigated. A general setup consisting of multiple sources cooperating in providing the best transmission is considered, where the constructive interference of their individual contributions is meant to improve the quality of the field generation with respect to a single-source setup. The medium response is described by means of tools from random-process theory, for the case of stationary media complex enough to ensure a large number of multi-path contributions. It is shown that even a very weak spatial coherence in the medium is sufficient to significantly hinder the improvement expected from the use of multiple-source scenarios. Experimental results obtained in a reverberation chamber support the validity of the proposed theory. Direct applications of these results can be found in recent proposals about the potential benefits of time-reversed signals used in wireless communications, imaging techniques, as well as in pulsed-field generation devices based on energy compression through dispersive media.

**Index Terms**—Time-reversal transmissions, spatial correlation, complex media, multi-path propagation, statistical electromagnetism.

## I. INTRODUCTION

Time-reversal transmissions were first introduced in acoustics [1], [2] and initial applications dealt mainly with open media with local inhomogeneities leading to relatively weak propagation aberrations with respect to free-space configurations. In the case of free-space configurations time-reversal can be interpreted as a direct application of Huygens' principle [3]: as well known from the equivalence theorem [4], sampling over a closed surface the field distribution generated by a radiating source allows defining equivalent currents that can recreate on their own a wavefront identical to the one originally generated by the source, be it outward or inward propagating, according to the sign of the time variable. In this respect, time reversal is predicated by earlier work in nonlinear optics, particularly on phase-conjugation techniques [5], reminiscent of the ideas behind retrodirective (also known as Van Atta) arrays [6].

For the large family of quasi free-space (or weakly echoic) configurations, time-reversed wavefronts will therefore be a close (time-reversed) replica of the propagative part of the original wavefront, as long as the spatial sampling criterium [7] is fulfilled, by using a sufficient number of field transducers/sources [1], [8]. Conversely, in the case of more complex media, e.g., multiple-scattering media [9]–[14], dominated

A. Cozza and F. Monsef are with the Département de Recherche en Électromagnétisme, Laboratoire des Signaux et Systèmes (L2S), UMR 8506 SUPELEC - Univ Paris-Sud - CNRS, 3 rue Joliot-Curie, 91192 Gif-sur-Yvette, France.

Contact e-mail: andrea.cozza@supelec.fr

by discrete scattering phenomena (e.g., collections of small scatterers [15], [16], multi-path environments [17]) or spatially distributed ones (e.g., turbulent media [16], inhomogeneous soils [18]), where field propagation can be modeled by means of random-process tools [16], [19], time-reversed wavefronts are affected by incoherent fluctuations [9], [11], [20], [21].

Although the appearance of these fluctuations could put off users of time-reversed signals in complex media, this nuisance is counterbalanced by a major advantage, since it is no longer necessary to satisfy the spatial sampling criterium. As a matter of fact, single-source configurations have been demonstrated to be capable of recreating high-fidelity versions of a wavefront, when operated by time-reversed signals in a complex medium [20], [22]–[26]. In this case the use of more than one emitter is no longer justified on the basis of the equivalence theorem, but rather on the need to mitigate the level of these fluctuations, by averaging them out thanks to spatial/angle/polarization diversity. Previous results about this topic are available in the literature [27]–[30], but are more concerned with the ability to obtain space-time focusing within random media, rather than assessing the quality of signals thus received.

It is the aim of this paper to understand how multiple-source implementations of time-reversed transmissions in complex media allow to control the relative intensity of the fluctuations, depending on the number of emitters and the statistical properties of the propagation medium, in particular spatial and frequency coherence (or correlation). To this end, a general theoretical approach is developed in section III, based on the concept of energy contrast introduced in section II.

The proposed theory confirms that while multiple sources can improve the quality of the transmission, residual spatial coherence in the medium can significantly reduce the overall effectiveness in mitigating the level of fluctuations. A quantitative analysis of the effects of these predictions is discussed in section IV; experimental results validating them are presented in section V. The results shown are intended to serve as quantitative predictive tools in the design of applications based on the transmission of time-reversed signals, such as in wireless communications, non-destructive testing, remote-sensing and imaging techniques.

In this respect, two families of setups for the application of time-reversal transmissions (TRTs) can be defined, both involving the need to generate a faithful reproduction of a template signal  $p(t)$  at the receiver-end: (a) a scalar component of the electromagnetic field is the quantity of interest or (b) the output signal observed at the electric port of a receiver. Clearly, these two setups can be regarded as belonging to the same class of problem, by considering that the first case implies the use of an ideal receiver generating an output

signal  $b(t) = \mathbf{h} \cdot \mathbf{E}(\mathbf{r}, t)$ , where  $\mathbf{h}$  is the vector effective length of the receiving transducer found at the position  $\mathbf{r}$ . This kind of response translates the use of an ideal non-dispersive elementary dipole, oriented along the electric-field component of interest  $\mathbf{h}/\|\mathbf{h}\|$ .

## II. TRT : COHERENT AND INCOHERENT CONTRIBUTIONS

We consider a set of  $N_A$  sources, not necessarily identical, found at the positions  $\{\mathbf{r}_m\}$ . Depending on the application, an observer or a receiver is present at the position  $\mathbf{r}_o$ ; no assumption is made on the reciprocal orientations of the sources and the observer. Input signals  $\{a_m(t)\}$  applied to the transmitting antennas and the overall output signal  $b(t)$  are chosen to be represented as power waves, in accordance with standard scattering-parameter formalism [31]. Assuming the medium to be linear, the individual contributions  $\{b_m(t)\}$  provided by the excitation of the  $m$ th source is given by  $b_m(t) = a_m(t) \star h_m(t)$ , with  $\star$  the time-convolution integral operator and  $h_m(t)$  the impulse response between the  $m$ th source and the receiver output.

The goal of transmission systems is typically to ensure the ability to generate at the receiver output a signal as close as possible to a reference signal  $p(t)$ , hereafter referred to as the template signal, which is typically taken to be a short pulse in time-reversal literature, but it is not necessarily so; no assumption will be made about this point in this paper since in practical settings, particularly for wireless communications, waveforms are typically more complex and not pulse-like.

When dealing with complex media, if the template signal  $p(t)$  were directly applied to an emitter, as soon as its time support  $T_p$  is shorter than the relaxation time of the medium, any received signal would risk being significantly distorted. Time-reversal transmissions act as a generalization of matched filter, by requiring the use of excitation signals

$$a_m(t) = p(t) \star h_m(-t). \quad (1)$$

This is the standard definition of time-reversed excitation signals, as originally formulated in acoustics [1]. Unlike for matched-filter theory, the reason for this result is not the maximization of the output signal-to-noise ratio for an additive white gaussian noise channel, but rather to produce the strongest focusing of energy around the receiver [27], [29].

It is well-known that applications of time-reversed signals are limited by the assumption of a stationary medium, in order to ensure the best performance with respect to the quality of reproduction of the template signal; please refer to the papers cited in the introduction for more details. Hence, this property will be assumed throughout this paper.

In order to assess the quality of the output signals generated by this kind of procedure, the mathematical analysis presented in this paper is developed within the framework introduced in [23], where each individual contribution  $b_m(t)$  to the output signal is expressed as

$$b_m(t) = \alpha_m p(t) + f_m(t), \quad (2)$$

i.e., as composed of a coherent part  $\alpha_m p(t)$ , with  $\alpha_m \geq 0$ , proportional to the template signal and a residual part  $f_m(t)$ , orthogonal to  $p(t)$ .

The overall signal  $b(t)$  resulting from the superposition of the  $N_A$  contributions can therefore be written as

$$b(t) = p(t)\alpha + f(t) = p(t) \sum_{m=1}^{N_A} \alpha_m + \sum_{m=1}^{N_A} f_m(t). \quad (3)$$

From (1),  $b_m(t) = h_m(t) \star h_m(-t) \star p(t)$ , so that for  $H_m(\nu)$  the Fourier transform of the impulse response of the medium, with  $\nu$  the frequency variable, it is convenient to introduce the equivalent transfer functions  $W_m(\nu) = |H_m(\nu)|^2$ , relating the Fourier spectrum  $P(\nu)$  of the template signal to the actual output signals received when using (1);  $P(\nu)$  will be assumed to have a compact support, centered at the frequency  $\nu_c$  and covering a bandwidth  $B_T$ . The coherent coefficients  $\{\alpha_m\}$  can therefore be computed by projecting  $b(t)$  over  $p(t)$ , i.e.,

$$\alpha_m = \mathcal{E}_p^{-1} \int_{B_T} W_m(\nu) |P(\nu)|^2 d\nu, \quad (4)$$

with  $\mathcal{E}_p$  the energy of the template signal  $p(t)$ .

## III. THEORY OF PEAK AND ENERGY CONTRASTS

Arguably, the most important figures of merit in TRTs are those measuring its ability to generate a received signal dominated by the coherent part  $\alpha p(t)$ , at the expenses of the residual part  $f(t)$ . This feature is commonly assessed by measuring the ratio between the peak value of the received signal and the average intensity of the fluctuations [20], [32]. While this kind of definition makes sense as long as  $p(t)$  is expected to be a narrow pulse, it is not general enough in electrical engineering, since one could be interested in transmitting more complex signals, e.g., when dealing with wireless communications; it is therefore necessary to apply a different definition, as the one introduced in section III-A, which can be extended to any kind of signals. More importantly, it is simply related to another figure of merit, the energy contrast. This last quantity is shown in section III-B to only depend on the statistical behavior of the medium's Green's function, independently from the specific choice of the template signal  $p(t)$  and more importantly from its bandwidth.

### A. Peak contrast

For the sake of simplicity, it will be assumed that  $p(t)$  reaches its peak intensity at  $t = 0$ . We can then introduce the following definition of the peak contrast,

$$\Lambda_p = \frac{\alpha^2 p^2(0)}{\max_t \langle f^2(t) \rangle}, \quad (5)$$

as a direct measure of the relative contribution of the coherent and incoherent parts; the latter is measured by the average power of the fluctuations, defined by means of an ensemble-average operator, represented by the brackets. As proven by our derivation, the shape of the template has a non-negligible impact on the performance of time reversal and its role should

therefore be explicitly accounted for. For this reason we introduce the shape factors  $\chi_p$  and  $\kappa_2$ , defined as

$$\chi_p = \frac{|p(0)|^2}{\mathcal{E}_p} \quad (6a)$$

$$\kappa_2^2 = \frac{1}{B_T} \frac{\left( \int_{B_T} |P(\nu)|^2 d\nu \right)^2}{\int_{B_T} |P(\nu)|^4 d\nu}, \quad (6b)$$

where Cauchy-Schwarz inequality indicates that  $\kappa_2 \leq 1$ ;  $\chi_p$  measures whether the energy of the template signal is distributed in a narrow span of time as a pulse, or rather as a longer signal. It has dimensions of a bandwidth and its definition implies that  $\chi_p \leq B_T$ , where the extreme value is reached only for a sinc pulse, corresponding to a constant power spectral density over  $B_T$ .

In a similar manner, we introduce  $\chi_f$ , defined as

$$\chi_f = \frac{\max_t \langle f^2(t) \rangle}{\langle \mathcal{E}_f \rangle} \quad (7)$$

in order to relate the overall energy of the residual fluctuations to their peak average intensity. The use of ensemble averages in (7) is due to the random nature of the residual fluctuations  $f(t)$ , inherited from the description of the medium Green's functions as random processes. The major difference between (6) and (7) is that the latter is mostly dependent on the medium and not on the template signal.

From (5), (6) and (7)

$$\langle \Lambda_p \rangle = \langle \Lambda \rangle \frac{\chi_p}{\chi_f}, \quad (8)$$

where

$$\Lambda = \frac{\mathcal{E}_c}{\mathcal{E}_f} = \frac{\alpha^2 \mathcal{E}_p}{\int_{B_T} |F(\nu)|^2 d\nu}, \quad (9)$$

is the energy contrast, defined as the ratio of the energy  $\mathcal{E}_c$  of the coherent portion of the received signal and the energy  $\mathcal{E}_f$  of the fluctuating residual part;  $F(\nu)$  in (9) is the Fourier transform of the overall fluctuating part  $f(t)$ . The energy contrast, as it will be proven in section III-B, is practically independent from the choice of the template signal, but strongly related to the statistical properties of the medium and the number of sources used. As a result, (8) allows separating the respective contributions of the medium and the sources from the choice of the template signal, with respect to the quality of the received signals. In particular, the impact of the number of sources used in the transmission only appears in  $\Lambda$ , hence it is sufficient to study this quantity, as done in the next section.

### B. Energy contrast

In order to compute the ensemble average of the energy contrast  $\Lambda$ , the following approximation of (9) will be applied:

$$\langle \Lambda \rangle \simeq \frac{\langle \mathcal{E}_c \rangle}{\langle \mathcal{E}_f \rangle} = \frac{\langle \alpha^2 \rangle \mathcal{E}_p}{\int_{B_T} \langle |F(\nu)|^2 \rangle d\nu}, \quad (10)$$

justified by applying the delta method [33] to the definition of  $\Lambda$ , with respect to the energies of the coherent and fluctuating parts. It is expected to hold with good precision as long as the number of degrees of freedom underlying the field distribution is much larger than one, as shown in [23]. This condition is not conservative, since it is required when time reversal is applied to complex media, as discussed in [20], [32]. The experimental results presented in V-B prove that this approximation is very robust, as they are derived frequency by frequency, without requiring the definition of a bandwidth, as initially stated in the introduction.

From (3)

$$\langle \alpha^2 \rangle = \left\langle \left( \sum_{i=1}^{N_A} \alpha_i \right)^2 \right\rangle = \sum_{i=1}^{N_A} \langle \alpha_i^2 \rangle + \sum_{i \neq j} \langle \alpha_i \alpha_j \rangle, \quad (11)$$

while

$$\begin{aligned} \int_{B_T} \langle |F(\nu)|^2 \rangle d\nu &= \sum_{i=1}^{N_A} \int_{B_T} \langle |F_i(\nu)|^2 \rangle d\nu \\ &\quad + \sum_{i \neq j} \int_{B_T} \langle F_i(\nu) F_j^*(\nu) \rangle d\nu. \end{aligned} \quad (12)$$

As it will be shown later, the residual correlation existing between mixed terms in (12) should not be neglected, lest we overestimate the actual performance of the transmission system.

In order to compute these four sets of terms, it is necessary to consider the mutual moments  $\langle W_i(\nu_1) W_j(\nu_2) \rangle$ . As argued in the appendix, the functions involved in these moments, though defined for discrete indexes (i.e., the source identifiers) can be interpreted as continuous parametric fields, i.e.,  $W_i(\nu) = W(\mathbf{r}_i, \nu; \mathbf{h}_i)$ , parameterized by the vector effective height of each respective source. While this would mean dealing with a set of  $N_A$  different fields, it is possible to simplify our derivation by noticing that a common feature of complex media is that they generate depolarized fields, i.e., on average they do not present dominant polarization components [16], [34], independently from the way the medium was first excited; non-line-of-sight propagation channels comply with this kind of description, which is one of the reasons for the use of reverberation chambers as channel emulators [35]. This property leads to a strong simplification in the statistical representation of Green's function. Under this assumption, if the sources are arbitrarily oriented versions of the same antenna, all the parametric fields share the same statistical moments. This property, discussed in the appendix, is instrumental in our derivation, since it allows dropping the effective heights as parameters, i.e.,

$$\langle W_i(\nu_1) W_j(\nu_2) \rangle = \langle W(\mathbf{r}_i, \nu_1) W(\mathbf{r}_j, \nu_2) \rangle. \quad (13)$$

As a result the moments  $\langle W_i(\nu_1)W_j(\nu_2) \rangle$  can now be related to the space-frequency coherence function of what will be referred to as the TRT field  $W(\mathbf{r}, \nu)$ . There should be no confusion at this point that even though (13) is no more dependent on the effective heights  $\{\mathbf{h}_m\}$ , there is no such a thing as a single TRT field, but a set of fields, depending on the characteristics of each source. The TRT field  $W(\mathbf{r}, \nu)$  considered hereafter should therefore be regarded as an auxiliary function that makes sense only when considering its statistical moments, as those in (13).

We need to recall that

$$\begin{aligned} \langle W(\mathbf{r}_i, \nu_1)W(\mathbf{r}_j, \nu_2) \rangle &= \langle W(\mathbf{r}_i, \nu_1) \rangle \langle W(\mathbf{r}_j, \nu_2) \rangle + \\ &\mu(\mathbf{r}_i, \mathbf{r}_j, \nu_1, \nu_2) \sqrt{\sigma_W^2(\mathbf{r}_i, \nu_1)\sigma_W^2(\mathbf{r}_j, \nu_2)}, \end{aligned} \quad (14)$$

where  $\sigma_W^2(\mathbf{r}, \nu) = \langle |W(\mathbf{r}, \nu)|^2 \rangle - |\langle W(\mathbf{r}, \nu) \rangle|^2$  is the variance of the TRT field and  $\mu(\mathbf{r}_i, \mathbf{r}_j, \nu_1, \nu_2)$  is its spectral degree of coherence [36].

In practical scenarios involving complex media where the field can be represented as a large collection of plane waves, e.g., those involving multiple-scattering propagation and interactions with rough surfaces, some further properties can be invoked. First, statistical moments of the Green's dyadic functions can be approximated as being independent from the point of observation, in the same way as wide-sense stationarity is assumed for random time-series, but with respect to space rather than time. As a result  $\sigma_W^2(\mathbf{r}, \nu) \simeq \sigma_W^2(\mathbf{r}_o, \nu), \forall \mathbf{r}$  so that in the following the argument  $\mathbf{r}$  will be dropped.

Furthermore, by introducing  $\nu_d = \nu_1 - \nu_2$ ,  $\nu_c = (\nu_1 + \nu_2)/2$ ,  $\mathbf{r}_c = (\mathbf{r}_i + \mathbf{r}_j)/2$  and  $\Delta r_{ij} = \|\mathbf{r}_i - \mathbf{r}_j\|$ , the degree of coherence can be factorized as

$$\mu(\mathbf{r}_i, \mathbf{r}_j, \nu_1, \nu_2) \simeq \mu_\nu(\mathbf{r}_c, \nu_d)\mu_r(\nu_c, \Delta r_{ij}), \quad (15)$$

as argued in [36, section 5.3] for quasi-homogeneous random fields. The two resulting functions in (15),  $\mu_\nu(\mathbf{r}_c, \nu_d)$  and  $\mu_r(\nu_c, \Delta r_{ij})$ , separately account for the degree of frequency and spatial coherence, respectively. While this property can be expected to hold over relatively wide regions of the medium when observed at a single frequency at the time, frequency invariance is a reasonable approximation only when required over a limited bandwidth  $B_W$ . We will assume in the rest of this paper that  $B_W \gg B_T$ .

The rationale for approximation (15) is provided by the observation that for complex media the degree of coherence falls to negligible levels if one of two conditions is met: a) as soon as  $|\nu_2 - \nu_1| > B_c$ , with  $B_c$  the coherence bandwidth of the medium, as defined later on, or; b) when  $\Delta r_{ij} > D_c$ , the coherence distance (or length) of the medium. When  $|\nu_2 - \nu_1| \simeq 0$ , the degree of coherence is dominated by the spatial coherence, while the opposite holds when  $\Delta r_{ij} \simeq 0$ .

Finally, by assuming that the template signal  $p(t)$  operates over a frequency range  $B_T \gg B_c$ , the frequency degree of coherence will dominate (15), independently of the observer position, by virtue of the stationarity property; this condition is known to be necessary to ensure effective TRTs in complex media [32]. Hence,  $\mu_\nu(\mathbf{r}_c, \nu_d) = \mu_\nu(\nu_d)$  in the following. The existence of three separate frequency scales is therefore

assumed throughout this work, subject to the condition

$$B_W \gg B_T \gg B_c. \quad (16)$$

The term  $\langle \alpha_i \alpha_j \rangle$  in (11) can now be computed by using (4), (14) and (15)

$$\begin{aligned} \mathcal{E}_p^2 \langle \alpha_i \alpha_j \rangle &= \iint_{B_T} |P(\nu_1)|^2 |P(\nu_2)|^2 \times \\ &\left\{ \sigma_W^2(\nu_c)\mu_\nu(\nu_d)\mu_r(\nu_c, \Delta r_{ij}) + \langle W(\nu_1) \rangle \langle W(\nu_2) \rangle \right\} d\nu_1 d\nu_2. \end{aligned} \quad (17)$$

Switching to  $\nu_c$  and  $\nu_d$ , the first part of the integral can be written as

$$\begin{aligned} \iint_{B_T} |P(\nu_1)|^2 |P(\nu_2)|^2 \sigma_W^2(\nu_c)\mu_\nu(\nu_d)\mu_r(\nu_c, \Delta r_{ij}) d\nu_1 d\nu_2 = \\ \int \sigma_W^2(\nu_c)\mu_r(\nu_c, \Delta r_{ij}) \times \\ \int |P(\nu_c - \nu_d/2)|^2 |P(\nu_c + \nu_d/2)|^2 \mu_\nu(\nu_d) d\nu_d d\nu_c \end{aligned} \quad (18)$$

where the second integral is significantly different from zero only for  $\nu_d < B_c \ll B_T$ , resulting into

$$\begin{aligned} \iint_{B_T} |P(\nu_1)|^2 |P(\nu_2)|^2 \sigma_W^2(\nu_c)\mu_\nu(\nu_d)\mu_r(\nu_c, \Delta r_{ij}) d\nu_1 d\nu_2 \simeq \\ \sigma_W^2(\nu_c)B_c \int \mu_r(\nu_c, \Delta r_{ij}) |P(\nu_c)|^4 d\nu_c, \end{aligned} \quad (19)$$

having extracted  $\sigma_W^2(\nu_c)$  from the integral because of (16), while

$$B_c = \int \mu_\nu(\nu_d) d\nu_d \quad (20)$$

is the coherence bandwidth of the medium. By introducing the variability  $\varsigma_W^2(\nu)$  of the TRT field

$$\varsigma_W^2(\nu) = \sigma_W^2(\nu) / \langle W(\nu) \rangle^2 \quad (21)$$

we obtain

$$\begin{aligned} \langle \alpha_i \alpha_j \rangle \simeq \langle W(\nu_c) \rangle^2 \left[ 1 + \right. \\ \left. \mathcal{E}_p^{-2} B_c \varsigma_W^2(\nu_c) \int_{B_T} \mu_r(\nu_c, \Delta r_{ij}) |P(\nu_c)|^4 d\nu_c \right]. \end{aligned} \quad (22)$$

This expression can be further simplified by noticing that

$$\mathcal{E}_p^{-2} B_c \int_{B_T} \mu_r(\nu_c, \Delta r_{ij}) |P(\nu_c)|^4 d\nu_c \leq \frac{B_c}{B_T \kappa_2^2}. \quad (23)$$

We can therefore conclude that

$$\langle \alpha_i \alpha_j \rangle \simeq \langle W(\nu_c) \rangle^2, \quad (24)$$

as long as  $\kappa_2^2 \gg B_c/B_T$ . The computation of  $\langle \alpha_i^2 \rangle$  goes along the same lines, with the difference that now  $\Delta r_{ij} = 0$ . It results into  $\langle \alpha_i^2 \rangle = \langle W(\nu_c) \rangle^2$ , so that the average coherent energy is

$$\langle \mathcal{E}_c \rangle = N_A^2 \langle W(\nu_c) \rangle^2, \quad (25)$$

a result that corresponds to the case of individual coherent contributions  $\{\alpha_i\}$  always constructively interfering, implying a unitary positive correlation. In other words, the spatial invariance of the moments of the TRT field translates into individual coherent contributions that asymptotically behave as deterministic rather than random quantities; this result can be ascribed to the property of self-averaging well known in time-reversal applications [32].

From (2) and (4), the term involving mutual moments in (12) is made up of four contributions

$$\begin{aligned} \int_{B_T} \langle F(\mathbf{r}_i, \nu) F^*(\mathbf{r}_j, \nu) \rangle d\nu = \\ \int_{B_T} \langle W(\mathbf{r}_i, \nu) W(\mathbf{r}_j, \nu) \rangle |P(\nu)|^2 d\nu + \int_{B_T} \langle \alpha_i \alpha_j \rangle |P(\nu)|^2 d\nu \\ - \int_{B_T} \langle W(\mathbf{r}_i, \nu) \alpha_j \rangle |P(\nu)|^2 d\nu - \int_{B_T} \langle W(\mathbf{r}_j, \nu) \alpha_i \rangle |P(\nu)|^2 d\nu. \end{aligned} \quad (26)$$

Recalling (14) and (15)

$$\begin{aligned} \int_{B_T} \langle W(\mathbf{r}_i, \nu) W(\mathbf{r}_j, \nu) \rangle |P(\nu)|^2 d\nu = \\ \sigma_W^2(\nu_c) \int_{B_T} \mu_r(\Delta r_{ij}, \nu) |P(\nu)|^2 d\nu + \langle W(\nu_c) \rangle^2 \mathcal{E}_p, \end{aligned} \quad (27)$$

a result also appearing in the integrand functions in the last two terms in (26)

$$\begin{aligned} \langle \alpha_i W(\mathbf{r}_j, \nu) \rangle = \mathcal{E}_p^{-1} \int_{B_T} \langle W(\mathbf{r}_j, \nu) W(\mathbf{r}_i, \nu') \rangle |P(\nu')|^2 d\nu' \\ \simeq \mathcal{E}_p^{-1} \sigma_W^2(\nu) \mu_r(\Delta r_{ij}, \nu) B_c |P(\nu)|^2 + \langle W(\nu) \rangle^2, \end{aligned} \quad (28)$$

having applied the same line of reasoning as in the derivation of (24). Hence,

$$\begin{aligned} \int_{B_T} \langle \alpha_i W(\mathbf{r}_j, \nu) \rangle |P(\nu)|^2 d\nu = \\ = \mathcal{E}_p^{-1} \sigma_W^2(\nu_c) B_c \int_{B_T} \mu_r(\Delta r_{ij}, \nu_c) |P(\nu_c)|^4 d\nu_c + \langle W(\nu_c) \rangle^2 \mathcal{E}_p \\ \simeq \mathcal{E}_p \langle W(\nu_c) \rangle^2, \end{aligned} \quad (29)$$

as long as  $\kappa_2^2 \gg B_c/B_T$ ; this result also holds when the indexes  $i$  and  $j$  are switched. Stitching together these results yields

$$\int_{B_T} \langle F(\mathbf{r}_i, \nu) F^*(\mathbf{r}_j, \nu) \rangle d\nu \simeq \sigma_W^2(\nu_c) \int_{B_T} \mu_r(\Delta r_{ij}, \nu) |P(\nu)|^2 d\nu. \quad (30)$$

Applying essentially the same procedure, the remaining term needed is

$$\int_{B_T} \langle |F(\mathbf{r}_i, \nu)|^2 \rangle d\nu \simeq \sigma_W^2(\nu_c) \mathcal{E}_p. \quad (31)$$

Finally, (10) becomes

$$\langle \Lambda \rangle \simeq \frac{\varsigma_W^{-2}(\nu_c) N_A}{1 + \mathcal{E}_p^{-1} N_A^{-1} \sum_{i \neq j} \int_{B_T} \mu_r(\Delta r_{ij}, \nu) |P(\nu)|^2 d\nu}. \quad (32)$$

It can be noticed that

$$\mu_{ij} = \mathcal{E}_p^{-1} \int_{B_T} \mu_r(\Delta r_{ij}, \nu) |P(\nu)|^2 d\nu \quad (33)$$

in (32) represents the degree of spatial coherence between the single-source contributions averaged over  $B_T$ , weighted by  $|P(\nu)|^2$ , while the average energy contrast expected for a single-source configuration is

$$\langle \Lambda^o \rangle = \langle \Lambda \rangle \Big|_{N_A=1} = \varsigma_W^{-2}(\nu_c), \quad (34)$$

allowing to restate (32) as

$$\langle \Lambda \rangle \simeq \langle \Lambda^o \rangle D(N_A, \bar{\mu}_r), \quad (35)$$

with

$$D(N_A, \bar{\mu}_r) = \frac{N_A}{1 + (N_A - 1)\bar{\mu}_r} \quad (36)$$

the improvement provided by exploiting spatial/polarization diversity from  $N_A$  sources, in an arrangement presenting an average spatial coherence  $\bar{\mu}_r$

$$\bar{\mu}_r = \frac{\sum_{i \neq j} \mu_{ij}}{N_A(N_A - 1)}. \quad (37)$$

#### IV. PERFORMANCE ANALYSIS

The derivation of (35) highlights how the average energy contrast obtained by means of TRT depends on two independent contributions: the average single-source contribution,  $\langle \Lambda^o \rangle$ , and a multiplicative factor  $D(N_A, \bar{\mu}_r)$ , hereafter referred to as the diversity factor. In this section the relative roles of these two terms are discussed.

##### A. Single-source configurations

The individual contributions  $\langle \Lambda^o \rangle$  appear only to depend on the statistical variability  $\varsigma_W^2(\nu)$  of the TRT field and therefore on the statistical properties of the Green's function of the medium, and not on the characteristics of the template signal (bandwidth, shape factor  $\chi_p$ ). The fact that the bandwidth of the template has no impact on  $\langle \Lambda^o \rangle$  implies that the energy efficiency of TRT is firmly constrained by the type of medium we have to deal with.

These limitations in the energy performance (energy contrast) do not apply to the peak contrast, which on the contrary yields more easily to design needs. As a matter of fact, the shape factor  $\chi_p$  introduced in (6) allows to increase the average peak contrast, since Wiener-Khinchin theorem implies that (8) goes like

$$\langle \Lambda_p \rangle \sim \langle \Lambda^o \rangle \frac{T_f}{T_p} \sim \langle \Lambda^o \rangle \frac{B_T}{B_c}, \quad (38)$$

where  $T_p$  and  $T_f$  are the effective time-domain supports (e.g., the half-power durations) of the template (coherent part)

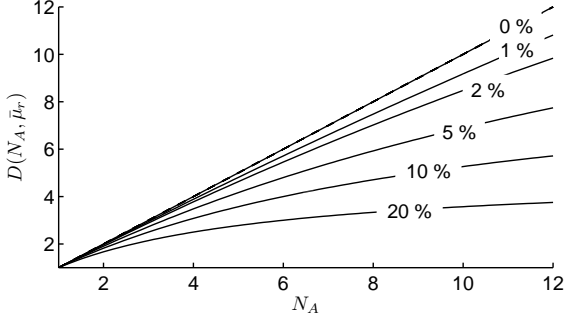


Fig. 1: The diversity factor  $D(N_A, \bar{\mu}_r)$  as a function of the number of sources  $N_A$  and the average spatial degree of coherence  $\bar{\mu}_r$  (in percent units over each line).

and residual fluctuation signals (incoherent part related to the relaxation time of the medium), respectively. In other words, the closer the template to a short pulse, the better the performance of TRTs. The interest of our approach is that it makes clear that while a higher peak contrast can be generated by acting on  $B_T$  (hence reducing  $T_p$ ), the overall energy efficiency of TRTs is not under control in complex media; these two quantities act as complementary metrics of the performance of TRTs.

### B. Multiple-source configurations

The function  $D(N_A, \bar{\mu}_r)$  can have a multiplicative effect on the energy contrast of a single-source configuration, since (36) implies that  $D(N_A, \bar{\mu}_r) \geq 1$ . In the ideal case of  $\bar{\mu}_r = 0$ , we expect  $D(N_A, \bar{\mu}_r) = N_A$ , resulting in a potentially dramatic improvement of the energy contrast. Since (25) proves that the coherent parts of each individual contribution are hardly distinguishable, the improvement of the energy contrast should not be interpreted as solely due to an increase in the overall coherent transmission. The reasons for the improvement in the overall energy contrast is rather to be found in the perfect decorrelation between the residual fluctuations contributed by each source. Under these circumstances, the average energy of the incoherent fluctuations will sum up as a linear function of  $N_A$ , to be compared with the  $N_A^2$  increase expected for the coherent part.

In the more realistic case of  $\bar{\mu}_r > 0$ , the trend of  $D(N_A, \bar{\mu}_r)$  as a function of  $N_A$  and  $\bar{\mu}_r$  is shown in Fig. 1. It can be observed that as the number of sources increases, the incremental improvement in the overall energy contrast decreases with  $N_A$ . Moreover, as  $N_A \rightarrow \infty$ , there exists a maximum attainable improvement given by

$$\lim_{N_A \rightarrow \infty} D(N_A, \bar{\mu}_r) = \frac{1}{\bar{\mu}_r}. \quad (39)$$

Even a relatively weak average spatial coherence leads to an upper limit to the improvement: e.g.,  $\bar{\mu}_r = 0.1$ , usually regarded as a negligible level of coherence, directly leads to a maximum improvement of a factor 10 which, though not negligible, implies that it is not possible to do better than the performance that would be obtained with 10 independent

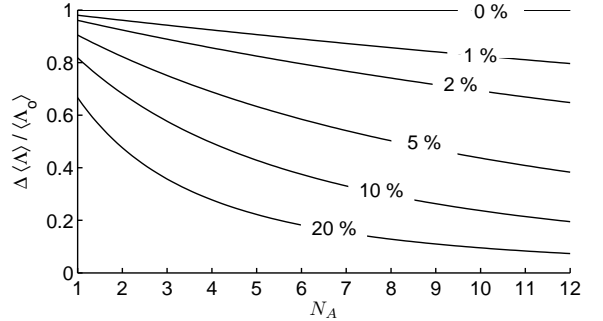


Fig. 2: Incremental contribution to the average overall energy contrast  $\langle\Lambda\rangle$  from a source added to  $N_A$  pre-existing sources, as a function of the average spatial degree of coherence  $\bar{\mu}_r$  (in percent units over each line).

sources in an idealized setup. Hence,  $D(N_A, \bar{\mu}_r)$  can be interpreted as an equivalent number of uncorrelated sources taking part to the transmission.

By far worse is the fact that (39) requires an infinite number of real sources excited at the same time, thus implying a huge redundancy level. The limited contribution of each individual source is better observed by computing the incremental improvement due to a single source added to  $N_A$  already existing, normalized to that of a single source, i.e.,

$$\frac{\Delta\langle\Lambda\rangle}{\langle\Lambda\rangle_0} = D(N_A + 1, \bar{\mu}_r) - D(N_A, \bar{\mu}_r), \quad (40)$$

hence

$$\frac{\Delta\langle\Lambda\rangle}{\langle\Lambda\rangle_0} = \frac{1 - \bar{\mu}_r}{1 - \bar{\mu}_r + N_A \bar{\mu}_r (2 - \bar{\mu}_r) + N_A^2 \bar{\mu}_r^2}. \quad (41)$$

Since (41) goes like  $O(N_A^{-2})$ , it appears that the realized improvement in the performance of TRT after adding a new source decreases relatively fast as  $N_A$  increases, even for rather low values of  $\bar{\mu}_r$ , as shown in Fig. 2.

It is important to stress the fact that spatial coherence has no link with the more common concept of antenna coupling. Spatial coherence rather implies that the random TRT between one source and the receiver/observer and those of other sources are not entirely uncorrelated random processes. Moreover, spatial coherence is a property that is independent of the structure of the sources and rather depends on the complexity of the medium.

In the design of TRT schemes, it is therefore important to acknowledge this loss of effectiveness of the sources. As a result, there exists a maximum number of sources  $N_A^*$  such that each relative contribution to the overall contrast is higher than a given value  $s < 1$ . Fig. 3 shows how  $N_A^*$  evolves with  $\bar{\mu}_r$  and  $s$ . Notice how for a requirement of a loss of less than 10 % in the incremental improvement, i.e.,  $s \geq 90 \%$ , it is worthwhile to switch from 1 to 2 sources only if  $\bar{\mu}_r \leq 5 \%$ , a very low level of residual correlation/coherence.

In the case of  $\bar{\mu}_r \ll 1$  the results in Fig. 3 are well approximated by

$$N_A^* \simeq 1 + \frac{s^{-1/2} - 1}{\bar{\mu}_r}. \quad (42)$$

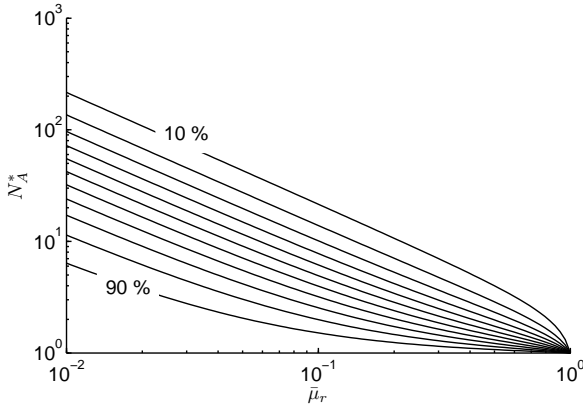


Fig. 3: The maximum number of sources allowed in order to ensure that all of them provide a contribution to the overall contrast at least equal to  $s \langle \Lambda^0 \rangle$ . The 9 curves correspond to values of  $s$  going from 10 % to 90 %, with a 10% step.

## V. EXPERIMENTAL VALIDATION

In order to assess the validity of (35) we chose a reverberation chamber as test case. The rationale for such a choice is threefold: 1) reverberation chambers are routinely used to emulate the effects of wave propagation in complex media of practical interest, such as indoor and outdoor environments, e.g., for hand-held mobile set testing [35], [37], [38]. In this respect, they provide a natural setting for testing our theory; 2) reverberation chambers often come with mechanical field stirrers, intended to modify the boundary conditions for waves propagating through them. A stirrer comes in handy here, as a simple way of generating a large number of random configurations, i.e., an ensemble of media sharing the same statistical properties; 3) it was found in [39] that the variability of the field within a reverberation chamber is far from being a constant value, and can be expected to take rapidly changing values in the lower-frequency range. This property is here interesting as it allows testing our predictions against different values of  $\zeta_W^2$ , i.e., varying random-field statistics, depending on the central frequency of operation; by the same token, spatial coherence is also expected to be a function of frequency [40], so that our predictions can be tested against a whole range of values of  $\bar{\mu}_r$ .

The effectiveness of TRTs is better appreciated in the time domain. In order to simplify the experimental validations, we rather carried out the measurements in the frequency domain; time-domain signals were then post-processed by means of discrete Fourier transforms. Transfer functions were measured with a vector network analyzer, as discussed in section V-A.

Mechanical stirring can only affect that portion of the field (and therefore of the transfer functions) that interacts with it, i.e., submitted to multiple scattering interactions. As a result, line-of-sight propagation between the sources and the receiver position appear as a deterministic contribution shared by each realization of  $\{H_m(\nu)\}$  [35]. In order to ensure realizations as independent as possible, line-of-sight contributions were subtracted from the original transfer functions, defining a new

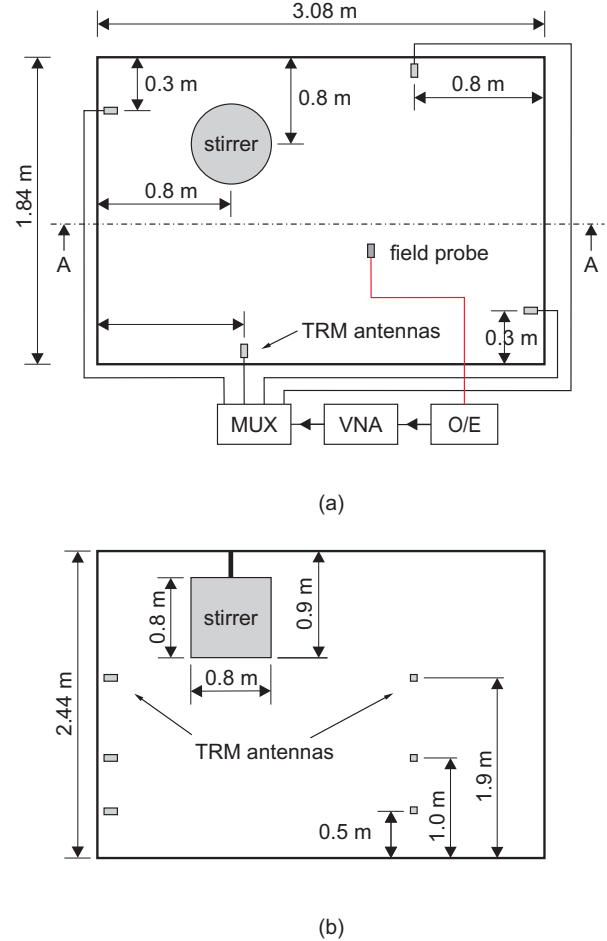


Fig. 4: The experimental setup used for the validation of the proposed theory. A total of 12 transmitting antennas (see Fig. 5(a)) were mounted over the 4 walls of a reverberation chamber, equipped with a field stirrer (paddle): (a) top view; (b) front view from the AA cut.

set of results as  $\{H_m(\nu) - \langle H_m(\nu) \rangle\}$ . It is important to stress that this procedure is in no way related to the assumptions invoked throughout our derivation, but is merely a matter of ensuring a set of independent realizations. At the same time this procedure also removes eventual couplings appearing through the excitation circuit.

### A. Experimental setup

A schematic description of the chamber is given in Fig. 4. A total of 12 sources were included into the chamber; the sources were identical and consisted of printed bow-tie antennas perpendicularly mounted over the walls of the chamber, as shown in Fig. 5(a). Their input ports were connected to a multiplexer through coaxial cables. These antennas were chosen in order to cover the frequency range from 0.5 to 2.0 GHz.

The receiver was an electro-optical probe (Enprobe's EFS-105) positioned at the center of the chamber, resting on a 1 m high styrofoam column. The probe, shown in Fig. 5(b), has

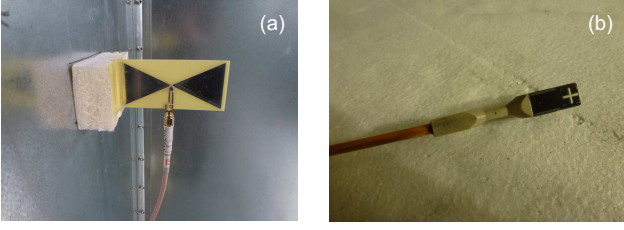


Fig. 5: Experimental setup: (a) one of the 12 bow-tie transmitting antennas, mounted over the walls of the reverberation chamber, kept 3 cm away from them by a piece of styrofoam; (b) Enprobe's EFS105 optical probe, measuring head 6.6 mm wide, connected to a optical-fiber cable.

the particularity of presenting a negligible scattering cross-section, while behaving as an ideal Hertzian dipole. Its ability to measure phase-shift angles makes it ideally suited for time-domain post-processing. This configuration corresponds to the case where the sources are employed in the generation of a field at the probe position. The probe was operated as a receiver by connecting it to a vector network analyzer (Rohde & Schwarz ZVB8) through an optic-to-electric converter, while the sources were independently excited one-by-one by means of a multiplexer, as shown in Fig. 4. In this way 12 transfer functions were collected for each realization, corresponding to a single stirrer position. The stirrer consisted of four tilted paddles mounted around a vertical axis; 50 angular positions were considered, in order to generate a corresponding number of sets of transfer functions between the sources and the observation point.

Preliminary results from this setup are given in Fig. 6, where an estimate of the variability of the TRT is shown. This quantity spans values going from 1.1 to 1.7; the lower value is close to what is expected for an ideal diffuse-field configuration, related to Rayleigh fading in wireless communications [17], [41], while the higher value is a measure that field propagation is less complex than expected, with a reduced number of degrees of freedom [39]. Moreover,  $\varsigma_W^2 \neq 1$  implies that the underlying field cannot be described as a Gaussian process, and therefore neither as a Rayleigh propagation. This fact is important in proving that the agreement between results discussed in the next section and the proposed theory is not limited to simplified configurations (e.g., Rayleigh propagation), but also in intermediary cases closer to practical settings.

Complementary information is provided by the power density results shown in Fig. 7 as a black line, estimated from the 50 realizations of the first of the 12 sources. The received fields appear as essentially behaving as random processes, weakly dependent on the frequency of observation (frequency stationarity). These results are of interest since they imply that condition (16) is satisfied: as a matter of fact, the average power density (black curve) evolves rather smoothly along the frequency axis, while the fast random fluctuations of each realization provide a direct assessment of the frequency coherence of the medium, which is of the order of 100 kHz. Furthermore, Fig. 7 does not give away any clue about the fact that the statistics of the medium is fundamentally different at the two ends of the frequency axis, as opposed to Fig. 6. The importance of the information derived from the variability, already exposed in section III-B, will be confirmed in the next section.

### B. Output field statistics

Throughout this section we will consider a gaussian template signal  $p(t)$ , with a -20 dB bandwidth  $B_T$  modulating a harmonic carrier at the frequency  $\nu_c$ ; the values of  $B_T$  were chosen in order to be much larger than the coherence bandwidth  $B_c$ , as required in the derivation of our theory. The received signals were computed by means of inverse discrete Fourier transforms of the spectra  $B_m(\nu) = |H_m(\nu)|^2 P(\nu)$ ;

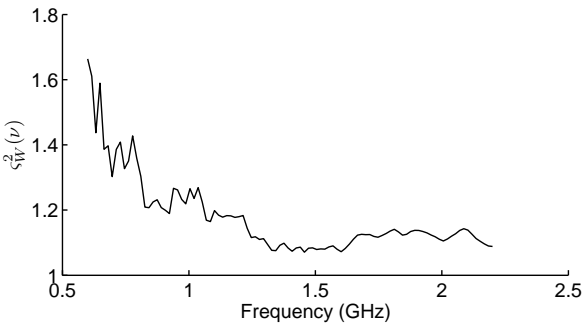


Fig. 6: Estimate of  $\varsigma_W^2$ , averaged over the results obtained with 12 sources, smoothed over a 5 % bandwidth.

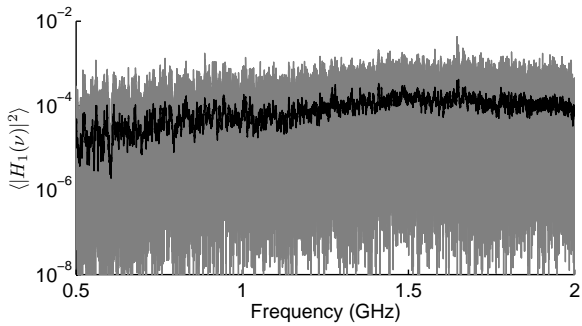


Fig. 7: Plots of the 50 realizations of  $W_1(\nu) = |H_1(\nu)|^2$  (gray) and of their ensemble average  $\langle W_1(\nu) \rangle$  (black curve). Fast fluctuations on a short range in the  $\{W_1(\nu)\}$  are a consequence of the narrow coherence bandwidth of the medium, as opposed to the smoother evolution of  $\langle W_1(\nu) \rangle$ , a direct indication of the existence of two separate scales of frequency-related phenomena.

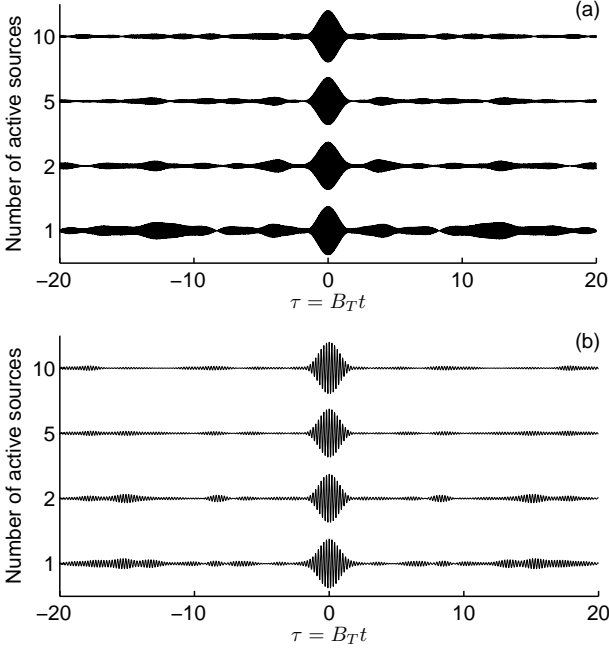


Fig. 8: A single realization of signals received for an increasing number of active sources, for  $\nu_c = 0.7$  GHz and: (a)  $B_T/\nu_c = 5\%$ ; (b)  $B_T/\nu_c = 20\%$ . The peak values attained by the signals are practically independent of the number of sources involved.

overall signals were then computed by summing over a chosen subset of individual contributions. For the sake of simplicity, the following convention will be used: for a configuration with  $N_A$  active sources, the resulting signals correspond to the sum of the first  $N_A$  sources, without considering all the available combinations. In order to allow a direct comparison of signal amplitude in different configurations, the output signals are always normalized to  $N_A$ , while  $p(t)$  has unit energy.

Examples of these signals are given in Fig. 8, for  $\nu_c = 0.7$  GHz and two relative bandwidths  $B_T/\nu_c$ , namely 5 % and 20 %, when exciting an increasing number of sources. While increasing  $B_T$  leads to a clear improvement in the peak contrast, as already well documented in the available literature about TRT, a further important information is that the resulting fields are practically independent of the number of sources involved. This observation confirms the results obtained in (25), stating that the peak-value of the coherent part is proportional to  $N_A$ , i.e., the individual contributions are practically identical. Still, Fig. 8 also shows that the ratio between the peak coherent value and the background fluctuations does not improve as fast when  $N_A$  increases; in other words, while the peak received signal increases, its quality is not improving as fast as would be expected for ideally incoherent fluctuations. This behavior is better understood by switching from the intuitive peak contrast to the energy contrast, as argued in section III.

In this respect, we needed to compute the empirical probability density functions (epdf) obtained for the single-source

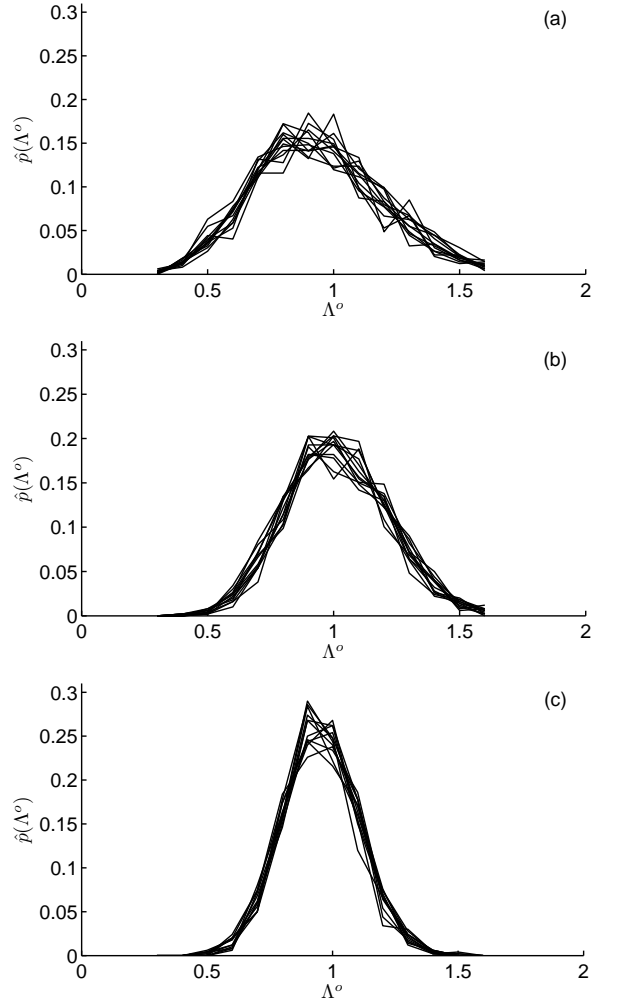


Fig. 9: Empirical probability density functions for  $\Lambda^o$  for three values of the central frequency  $\nu_c$  : (a) 0.7 GHz; (b) 1.3 GHz and (c) 2.0 GHz, for a 5 % relative bandwidth. Twelve results are shown on each graph, corresponding to the results obtained from the use of each transmitting antenna.

$\Lambda^o$ , shown in Fig. 9, derived for the 12 sources and the data collected for the 50 realizations. These results confirm that the epdfs are practically independent of the source, supporting the arguments presented in the appendix.

The main interest in the use of the energy contrast is that its average value  $\langle \Lambda^o(\nu) \rangle$  does not depend on the specific choice of  $p(t)$ , but only on the medium; evidence for this claim is provided in Fig. 10, where  $\langle \Lambda^o(\nu) \rangle$  is computed either applying its definition (9), based on output signals, or from (34), based on estimates of medium statistics; a good agreement is found within a few percent points over the entire frequency range and for three different relative bandwidths, while minor disagreements are likely due to the approximation applied in (10). In particular, going from  $B_T/\nu_c = 5\%$  to 20 %, e.g., a fourfold increase, does not lead to any improvement in  $\langle \Lambda^o(\nu) \rangle$ , as predicted from the proposed theory. Of notable interest is the fact that the agreement is extended to the lower

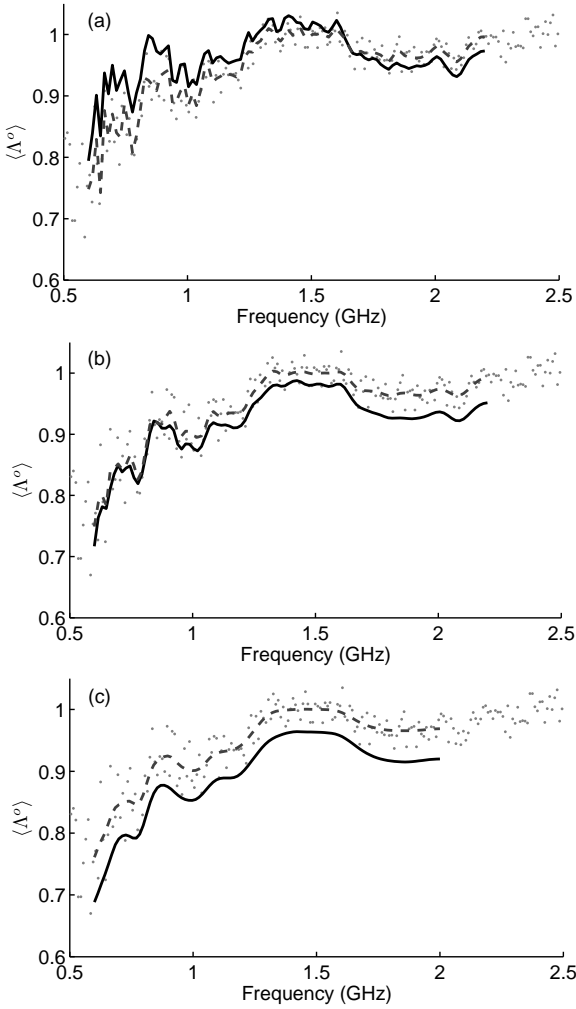


Fig. 10: Comparisons between several estimates of  $\langle \Lambda^o \rangle$ , computed from : the arithmetic average over the 50-realization dataset (solid line); the reciprocal of the variability, i.e.,  $\varsigma_W^{-2}(\nu)$  (gray dots), as predicted by (34); its smoothed version computed by averaging with  $|P(\nu)|$  as a weighting function (dashed line). The three graphs relate to three different relative bandwidths: (a) 5 %; (b) 10 %; (c) 20 %.

frequency range, where the field statistics are not compatible with those of a gaussian distribution law, since  $\varsigma_W^2 \neq 1$ .

Equation (36) states that in order to predict the improvement brought in by the use of multiple-source excitations, the only needed quantity to be computed is  $\bar{\mu}_r$ , according to (37), starting from the residual correlations between the  $\{W_m(\nu)\}$  equivalent transfer functions; results are shown in Fig. 11. As expected for a complex medium, the residual spatial correlation is rather low and could be dismissed as negligible.

The predictions given by (36) about the improvement  $D(N_A, \bar{\mu}_r)$  are compared in Fig. 12 against the measured ratio  $\langle \Lambda \rangle / \langle \Lambda^o \rangle$ , for three values of  $\nu_c$  and three relative bandwidths. As predicted, the realized improvement is smaller what would be expected from the deterministic behavior of the individual contributions to the coherent part, i.e.,

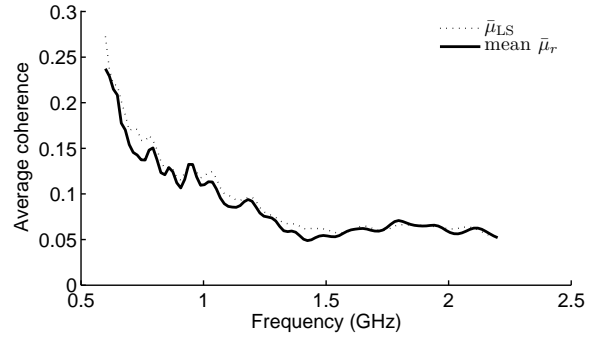


Fig. 11: Estimate of the mean-value of  $\bar{\mu}_r(\nu)$ , computed over the 50 realizations, obtained from the  $\{W_m(\nu)\}$  for a 5 % relative bandwidth (solid line), compared to the least-square estimate  $\bar{\mu}_{LS}(\nu)$  derived by fitting the diversity factor to the measured data.

$D(N_A, \bar{\mu}_r) = N_A$ . The reduction in  $\langle \Lambda \rangle / \langle \Lambda^o \rangle$  is accurately predicted by (36), based on the  $\bar{\mu}_r$  estimates in Fig. 11. The divergence between the theoretical predictions and the experimental results can be explained in terms of residual uncertainties in the estimation of  $\bar{\mu}_r$ : assuming a 10 % uncertainty provides mutually compatible results.

A more general comparison is possible by computing the least-squares fit of  $\langle \Lambda \rangle / \langle \Lambda^o \rangle$ , yielding an optimal  $\bar{\mu}_{LS}$ , compared in Fig. 11 and Fig. 12 with the estimate of  $\bar{\mu}_r$ . A good agreement is observed over the entire frequency range, supporting the proposed theory as capable of predicting the performance of TRTs in complex media.

## VI. CONCLUSIONS

In this paper we have introduced a theory describing the ability of multiple-source TRT in generating coherent signals in complex media. This theory shows how inevitable spatial correlation puts an upper bound on the improvement brought by the introduction of additional transmitting sources, even for values of coherence that are often regarded as negligible.

The introduction of the energy contrast, as opposed to the more intuitive peak contrast, allows appreciating limitations of the energy efficiency that have been seldom discussed; this topic deserves further research for its practical importance in the optimal design of transmission systems.

Overall, experimental results strongly support the theoretical model presented in section III, and in particular the possibility of factorizing the peak contrast into three separate contributions: a) the ratio between the template bandwidth  $B_T$  and the coherence bandwidth of the medium; b) the variability of the TRT field supported by the medium; c) the diversity factor  $D(N_A, \bar{\mu}_r)$ , depending on the residual spatial coherence and the number of sources.

These two last points make clear that albeit allowing remarkable performances, time reversal is profoundly affected by physical limitations that cannot be easily compensated by means of signal-processing techniques.

## ACKNOWLEDGEMENTS

Part of the work here reported was funded by the French National Research Agency through the grant ANR-12-ASTR-0005-01, within the framework of the 2012 ASTRID program.

## REFERENCES

- [1] M. Fink, "Time reversal of ultrasonic fields. I. Basic principles," *IEEE Transactions on Ultrasonics, Ferroelectrics and Frequency Control*, vol. 39, no. 5, pp. 555–566, 1992.
- [2] M. Fink, D. Cassereau, A. Derode, C. Prada, P. Roux, M. Tanter, J. Thomas, and F. Wu, "Time-reversed acoustics," *Reports on Progress in Physics*, vol. 63, p. 1933, 2000.
- [3] B. Baker and E. Copson, *The mathematical theory of Huygens' principle*. Chelsea Pub Co, 2003.
- [4] R. Harrington, *Time-Harmonic Electromagnetic Fields*. McGraw-Hill, New York, NY, 1961.
- [5] A. Yariv, "Phase conjugate optics and real-time holography," *IEEE Journal of Quantum Electronics*, vol. 14, no. 9, pp. 650–660, 1978.
- [6] E. Sharp and M. Diab, "Van Atta reflector array," *IRE Transactions on Antennas and Propagation*, vol. 8, no. 4, pp. 436–438, 1960.
- [7] E. Joy and D. Paris, "Spatial sampling and filtering in near-field measurements," *IEEE Transactions on Antennas and Propagation*, vol. 20, no. 3, pp. 253–261, 1972.
- [8] M. Fink and C. Prada, "Acoustic time-reversal mirrors," *Inverse Problems*, vol. 17, p. R1, 2001.
- [9] A. Derode, P. Roux, and M. Fink, "Robust acoustic time reversal with high-order multiple scattering," *Physical Review Letters*, vol. 75, no. 23, pp. 4206–4209, 1995.
- [10] P. Roux, B. Roman, and M. Fink, "Time-reversal in an ultrasonic waveguide," *Applied Physics Letters*, vol. 70, p. 1811, 1997.
- [11] C. Draeger, J. Aime, and M. Fink, "One-channel time-reversal in chaotic cavities: Experimental results," *The Journal of the Acoustical Society of America*, vol. 105, p. 618, 1999.
- [12] A. Derode, A. Tourin, J. de Rosny, M. Tanter, S. Yon, and M. Fink, "Taking advantage of multiple scattering to communicate with time-reversal antennas," *Physical Review Letters*, vol. 90, no. 1, p. 14301, 2003.
- [13] K. Sarabandi, I. Koh, and M. Casciato, "Demonstration of time reversal methods in a multi-path environment," in *IEEE Antennas and Propagation Society International Symposium*, vol. 4. IEEE, 2004, pp. 4436–4439.
- [14] I. Vellekoop, A. Lagendijk, and A. Mosk, "Exploiting disorder for perfect focusing," *Nature Photonics*, vol. 4, no. 5, pp. 320–322, 2010.
- [15] H. C. Van De Hulst, *Light Scattering by Small Particles*. Dover Pubn Inc, 2010.
- [16] A. Ishimaru, *Wave propagation and scattering in random media*. Wiley-IEEE Press, 1999, vol. 12.
- [17] R. Vaughan and J. B. Andersen, *Channels, propagation and antennas for mobile communications*. Institution of Electrical Engineers, 2003.
- [18] M. Yavuz and F. Teixeira, "Full time-domain DORT for ultrawideband electromagnetic fields in dispersive, random inhomogeneous media," *IEEE Transactions on Antennas and Propagation*, vol. 54, no. 8, pp. 2305–2315, 2006.
- [19] R. Bourret, "Stochastically perturbed fields, with applications to wave propagation in random media," *Il Nuovo Cimento Series 10*, vol. 26, no. 1, pp. 1–31, 1962.
- [20] G. Lerosey, J. de Rosny, A. Tourin, A. Derode, G. Montaldo, and M. Fink, "Time reversal of electromagnetic waves," *Physical Review Letters*, vol. 92, no. 19, p. 193904, 2004.
- [21] J. Fouque and G. Papanicolaou, *Wave Propagation and Time Reversal in Randomly Layered Media*. Springer Verlag, 2007.
- [22] S. Kim, W. Kuperman, W. Hodgkiss, H. Song, G. Edelmann, and T. Akal, "Echo-to-reverberation enhancement using a time reversal mirror," *The Journal of the Acoustical Society of America*, vol. 115, p. 1525, 2004.
- [23] A. Cozza, "Statistics of the performance of time reversal in a lossy reverberating medium," *Physical Review E*, vol. 80, no. 5, p. 56604, 2009.
- [24] A. Cozza and A. Abou El Aileh, "Accurate Radiation-Pattern Measurements in a Time-Reversal Electromagnetic Chamber," *IEEE Antennas and Propagation Magazine*, vol. 52, no. 2, pp. 186–193, 2010.
- [25] H. Moussa, A. Cozza, and M. Cauterman, "Experimental demonstration of directive pulsed waveform generation in reverberation chambers," *Electronics Letters*, vol. 46, no. 9, pp. 623–624, 2010.
- [26] A. Cozza, "Emulating an anechoic environment in a wave-diffusive medium through an extended time-reversal approach," *Antennas and Propagation, IEEE Transactions on*, vol. 60, no. 8, pp. 3838–3852, 2012.
- [27] C. Oestges, A. Kim, G. Papanicolaou, and A. Paulraj, "Characterization of space-time focusing in time-reversed random fields," *IEEE Transactions on Antennas and Propagation*, vol. 53, no. 1, pp. 283 – 293, 2005.
- [28] H. C. Song, W. Hodgkiss, W. Kuperman, W. Higley, K. Raghukumar, T. Akal, and M. Stevenson, "Spatial diversity in passive time reversal communications," *The Journal of the Acoustical Society of America*, vol. 120, no. 4, pp. 2067–2076, 2006.
- [29] J. de Rosny, G. Lerosey, and M. Fink, "Theory of electromagnetic time-reversal mirrors," *IEEE Transactions on Antennas and Propagation*, vol. 58, no. 10, pp. 3139–3149, 2010.
- [30] P. Blomgren, P. Kyritsi, A. D. Kim, and G. Papanicolaou, "Spatial focusing and intersymbol interference in multiple-input-single-output time reversal communication systems," *IEEE Journal of Oceanic Engineering*, vol. 33, no. 3, pp. 341–355, 2008.
- [31] K. Kurokawa, "Power waves and the scattering matrix," *IEEE Transactions on Microwave Theory and Techniques*, vol. 13, no. 2, pp. 194–202, 1965.
- [32] A. Derode, A. Tourin, and M. Fink, "Random multiple scattering of ultrasound. II. Is time reversal a self-averaging process?" *Physical Review E*, vol. 64, no. 3, p. 36606, 2001.
- [33] C. G. Small, *Expansions and asymptotics for statistics*. CRC Press, 2010.
- [34] L. Tsang and J. A. Kong, *Scattering of Electromagnetic Waves: Advanced Topics*. Wiley-Blackwell, 2001, vol. 26.
- [35] C. Holloway, D. Hill, J. Ladbury, P. Wilson, G. Koepke, and J. Coder, "On the use of reverberation chambers to simulate a Rician radio environment for the testing of wireless devices," *IEEE Transactions on Antennas and Propagation*, vol. 54, no. 11, pp. 3167 –3177, 2006.
- [36] E. Wolf, *Introduction to the Theory of Coherence and Polarization of Light*. Cambridge University Press, 2007.
- [37] P. Kildal, "Overview of 6 years R&D on characterizing wireless devices in Rayleigh fading using reverberation chambers," in *International Workshop on Antenna Technology: Small and Smart Antennas Metamaterials and Applications, 2007. IWAT'07*. IEEE, 2007, pp. 162–165.
- [38] K. Rosengren and P.-S. Kildal, "Radiation efficiency, correlation, diversity gain and capacity of a six-monopole antenna array for a mimo system: theory, simulation and measurement in reverberation chamber," *Microwaves, Antennas and Propagation, IEE Proceedings*, vol. 152, no. 1, pp. 7–16, 2005.
- [39] A. Cozza, "The Role of Losses in the Definition of the Overmoded Condition for Reverberation Chambers and Their Statistics," *IEEE Transactions on Electromagnetic Compatibility*, no. 53, pp. 296–307, 2010.
- [40] D. Hill and J. Ladbury, "Spatial-correlation functions of fields and energy density in a reverberation chamber," *IEEE Transactions on Electromagnetic Compatibility*, vol. 44, no. 1, pp. 95–101, 2002.
- [41] M. K. Simon and M.-S. Alouini, *Digital communication over fading channels*. Wiley-Interscience, 2005, vol. 95.

## APPENDIX

The derivation presented in section III-B rests on the idea that while each transmitting antenna generates a different time-reversal field distribution, their statistical moments are independent of the orientation of the sources, as long as they are rotated replicas of the same type of source. In this respect, it is necessary to prove that the first- and second-order moments of the TRT fields only depend on  $\{\|\mathbf{h}_m\|\}$  and are rather dominated by the medium statistics. The main assumption is that the medium generates depolarized fields.

The transfer functions  $\{H_m(\nu)\}$  can be related to the vector effective heights of the transmitters and receiver,  $\{\mathbf{h}_m\}$  and  $\mathbf{h}_o$ , respectively. For the sake of simplicity it will be assumed that the transmitters and the receiver are electrically small, whence

$$H_m(\nu) = C(\nu) \mathbf{h}_o(\nu) \cdot \underline{\mathbf{G}}_{ee}(\mathbf{r}_o, \mathbf{r}_m, \nu) \cdot \mathbf{h}_m(\nu), \quad (43)$$

where  $\underline{G}_{ee}$  is the electric-electric Green's dyadic function of the medium, while  $C(\nu)$  is a function depending on the reference impedance used in the definition of the scattering parameters; in the following we will set  $C(\nu) = 1$ , with no loss of generality. From (43), we can interpret each transfer function as a continuous parametric field

$$H_m(\nu) = H(\mathbf{r}_m, \nu; \mathbf{h}_m), \quad (44)$$

not only defined for the actual position of the  $m$ th source, but for a general  $\mathbf{r}_m$ .

With no loss of generality, in our derivation it will be assumed that the reference system relating to the observer in  $\mathbf{r}_o$  is defined such that  $\mathbf{h}_o = h_o \hat{\mathbf{u}}_k$ , i.e., the observer is aligned to the  $k$ th axis  $\hat{\mathbf{u}}_k$ . The frequency variable is here dropped for the sake of space. From (43)

$$W_m = \left| \sum_{i,j=1}^3 h_o^i h_m^j G_{ee}^{ij}(\mathbf{r}_o, \mathbf{r}_m) \right|^2, \quad (45)$$

where  $\{G_{ee}^{ij}\}$  are the scalar components of the dyadic Green's function. For  $\mathbf{h}_o = h_o \hat{\mathbf{u}}_k$  (45) reduces to

$$W_m = |h_o|^2 \left| \sum_{i=1}^3 h_m^i G_{ee}^{ki}(\mathbf{r}_o, \mathbf{r}_m) \right|^2, \quad (46)$$

which, using the convention  $X_i = G_{ee}^{ki}(\mathbf{r}_o, \mathbf{r}_m)$ , leads to

$$W_m = |h_o|^2 \sum_{i,j} h_m^i h_m^{j*} X_i X_j^*, \quad (47)$$

where  $*$  stands for the complex conjugate. The ensemble average  $\langle W_m(\nu) \rangle$  is therefore

$$\langle W_m \rangle = |h_o|^2 \sum_{i,j} h_m^i h_m^{j*} \langle X_i X_j^* \rangle. \quad (48)$$

Following the depolarized-field assumption,  $\langle G_{ee}^{ij}(\mathbf{r}_o, \mathbf{r}_m) G_{ee}^{pq*}(\mathbf{r}_o, \mathbf{r}_m) \rangle = \delta_{ij} \delta_{pq} \sigma_G^2$ , with  $\sigma_G^2$  the variance of each scalar component of the dyadic Green's function; in practical terms, a rotational symmetry or isotropy is introduced in the statistics of the components of the dyadic Green's function. Hence

$$\langle W_m \rangle = |h_o|^2 \|\mathbf{h}_m\|^2 \sigma_G^2, \quad (49)$$

which does not depend on the orientation of the  $m$ th source. Field statistics for complex media can be assumed, at least at the first order, as following a complex-valued circular normal distribution, i.e., with zero-mean real and imaginary parts normal distributed and iid, with variances  $\sigma_0^2$ , thus  $\sigma_G^2 = 2\sigma_0^2$ , quantities directly related to the spectral density  $\sigma_W^2(\mathbf{r})$ . As argued in section III-B, spatial dependence is here assumed to be negligible at least in the region of space where the sources are found, so that the argument  $\mathbf{r}$  will be dropped.

In the same way the second-order moment  $\langle |W_m|^2 \rangle$  can be computed as

$$\langle |W_m|^2 \rangle = |h_o|^4 \sum_{i,j,p,q} h_m^i h_m^{j*} h_m^p h_m^{q*} \langle X_i X_j^* X_p X_q^* \rangle. \quad (50)$$

The assumption of a depolarized field implies that of the four sums above only the terms involving  $\{i = j = p = q\}$ ,  $\{i = j \wedge p = q\}$  and  $\{i = q \wedge j = p\}$  contribute non-zero moments

$$\begin{aligned} \langle |W_m|^2 \rangle |h_o|^{-4} &= \sum_i |h_m^i|^4 \langle |X_i|^4 \rangle + \\ &2 \sum_{i \neq j} |h_m^i|^2 |h_m^j|^2 \langle |X_i|^2 |X_j|^2 \rangle, \end{aligned} \quad (51)$$

which can be shown to yield

$$\langle |W_m|^2 \rangle = 8\sigma_0^4 |h_o|^4 \|\mathbf{h}_m\|^4 \quad (52)$$

and hence

$$S_W = 4\sigma_0^4 |h_o|^4 \|\mathbf{h}_m\|^4 \quad (53)$$

The last moment to consider is  $\langle W_m(\nu) W_n(\nu) \rangle$ , which will bring into play the spatial degree of coherence of the medium Green's function. First, it can be shown that

$$\begin{aligned} \langle W_m W_n \rangle |h_o|^{-2} &= \sum_i |h_m^i|^2 |h_n^i|^2 \langle |X_i(\mathbf{r}_m)|^2 |X_i(\mathbf{r}_n)|^2 \rangle + \\ &\sum_{i \neq j} |h_m^i|^2 |h_n^i|^2 \langle |X_i(\mathbf{r}_m)|^2 \rangle \langle |X_j(\mathbf{r}_n)|^2 \rangle + \\ &\sum_{i \neq j} h_m^i h_n^{i*} h_m^j h_n^{j*} \langle X_i(\mathbf{r}_m) X_i^*(\mathbf{r}_n) \rangle \langle X_j^*(\mathbf{r}_m) X_j(\mathbf{r}_n) \rangle. \end{aligned} \quad (54)$$

This expression can be simplified by recalling that

$$\langle |X_i(\mathbf{r})|^2 \rangle = 2\sigma_0^2 \quad \forall \mathbf{r} \quad (55a)$$

$$\langle X_i(\mathbf{r}_m) X_i^*(\mathbf{r}_n) \rangle = 2\sigma_0^2 \rho'_i(\mathbf{r}_m, \mathbf{r}_n) \quad (55b)$$

$$\langle |X_i(\mathbf{r}_m)|^2 |X_i(\mathbf{r}_n)|^2 \rangle = 4\sigma_0^4 [1 + \rho''_i(\mathbf{r}_m, \mathbf{r}_n)] \quad (55c)$$

where  $\rho'_i(\mathbf{r}_m, \mathbf{r}_n)$  and  $\rho''_i(\mathbf{r}_m, \mathbf{r}_n)$  are the spatial degree of coherence of the  $i$ th scalar component of the electric field and its squared modulus, respectively. In order to further simplify our derivation, it is convenient to assume a diffuse-field propagation [16]; in this case, by choosing a reference system pertaining to the source part of Green's dyadic function such that the  $i$ th axis is either parallel or perpendicular to the direction  $\mathbf{r}_m - \mathbf{r}_n$ , then  $\rho''_i(\mathbf{r}_m, \mathbf{r}_n) = [\rho'_i(\mathbf{r}_m, \mathbf{r}_n)]^2$ , as demonstrated in [40].

This results, after some algebraic manipulations, into

$$\frac{\langle W_m W_n \rangle}{4|h_o|^4 \sigma_0^4} = \|\mathbf{h}_m\|^2 \|\mathbf{h}_n\|^2 + \left[ \sum_{i=1}^3 h_m^i h_n^{i*} \rho'_i(\mathbf{r}_m, \mathbf{r}_n) \right]^2. \quad (56)$$

This last expression is actually dependent on the angles between  $\mathbf{h}_m$  and  $\mathbf{h}_n$ ; depending on the direction cosines of  $\mathbf{h}_m$  and  $\mathbf{h}_n$ , the functions  $\rho'_i(\mathbf{r}_m, \mathbf{r}_n)$  will be linearly combined according to different weights. Two special cases can be invoked in order to understand when the final result is not affected by the orientation of the sources.

First, consider the case of identical sources, aligned along a straight line. In this case the direction cosines will be the same independently of the couple  $(m, n)$ , hence  $\langle W_m(\nu) W_n(\nu) \rangle$  will only depend on the medium coherence functions. This configuration is often employed in practice, particularly when dealing with linear arrays of sources.

The second case is that of a more complex geometry, where sources are not necessarily parallel to each other and distributed either along a two- or three-dimensional grid, or randomly. In either case, depending on  $(m, n)$ , the direction cosines will span any possible value, since even for identical sources their projections over the local reference system defined around the direction  $\mathbf{r}_m - \mathbf{r}_n$  will change. By modeling the angles as uniformly distributed over all possible directions, the average value of  $h_m^i h_n^{i*}$  observed for any  $(m, n)$  is expected to be  $\langle h_m^i h_n^{i*} \rangle = \|\mathbf{r}_m\| \|\mathbf{r}_n\| / 3$ , hence (56) will be, according to the law of large numbers, asymptotically equal to

$$\frac{\langle W_m W_n \rangle}{4|h_o|^4 \sigma_0^4} = \|\mathbf{h}_m\|^2 \|\mathbf{h}_n\|^2 \left[ 1 + \left( \frac{1}{3} \sum_{i=1}^3 \rho'_i(\mathbf{r}_m, \mathbf{r}_n) \right)^2 \right], \quad (57)$$

which only depends on the degree of coherence of the medium.

Recalling the definition of the spatial coherence functions in (15) and making use of (49), (53) and (56) yields

$$\mu_r(\Delta r_{mn}) = \left[ \sum_{i=1}^3 h_m^i h_n^{i*} \rho'_i(\mathbf{r}_m, \mathbf{r}_n) \right]^2 = \left[ \frac{\sin(k_o \Delta r_{mn})}{k_o \Delta r_{mn}} \right]^2 \quad (58)$$

where the last result holds for the case of a diffusive medium [16], as demonstrated in [40], with  $k_o = \nu/c_o$  the wavenumber and  $c_o$  the average speed of light through the medium. Equation (58) also proves that  $\mu_{mn} \geq 0, \forall m, n$ , so that the  $\bar{\mu}_r$  cannot be smaller than the smallest individual coherences  $\{\mu_{ij}\}$ , i.e., they cannot compensate themselves reducing the overall average coherence of the transmission system.

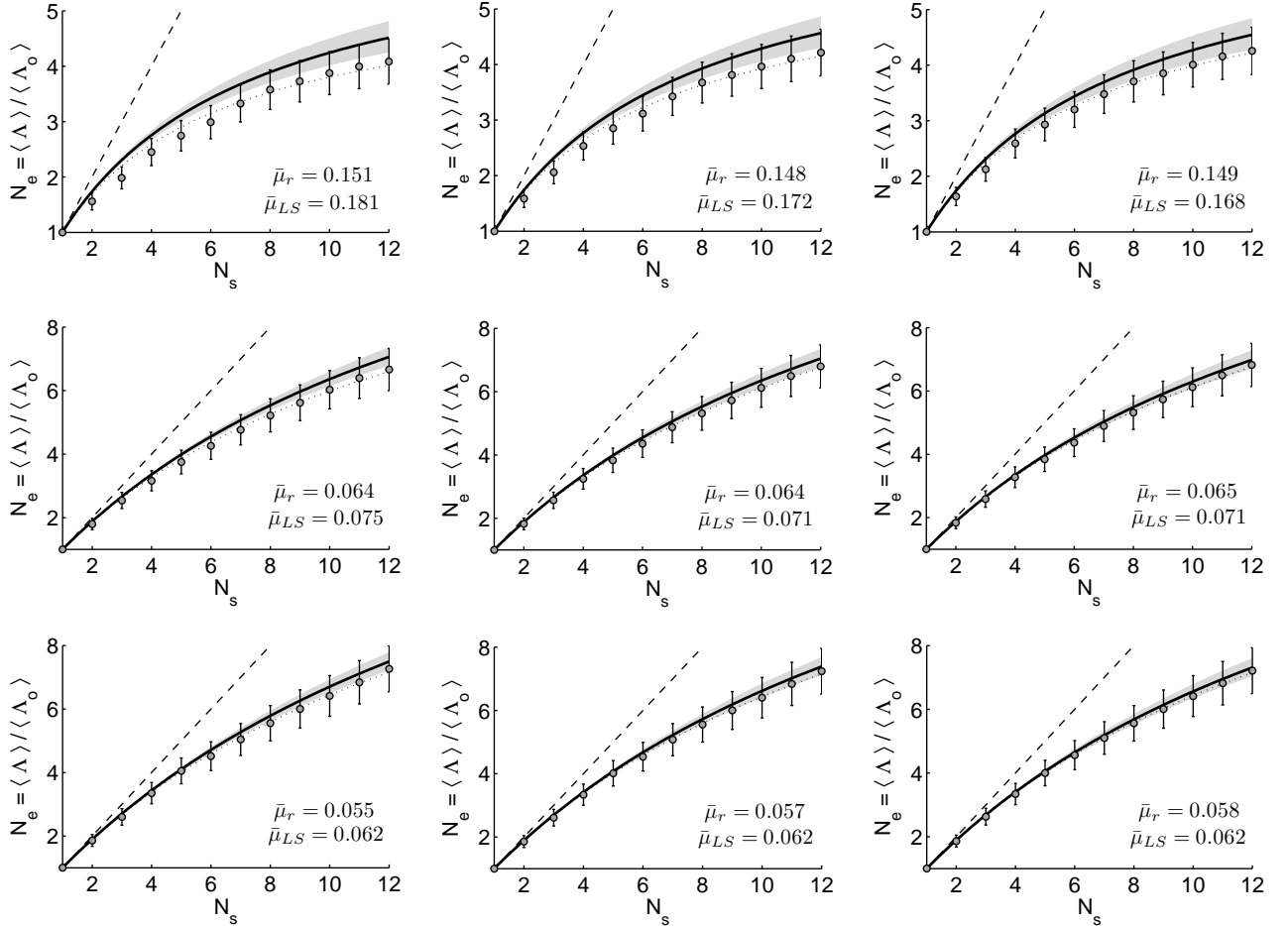


Fig. 12: Equivalent number of independent sources, or diversity factor, as estimated from measurements, for three values of the central frequency  $\nu_c$  (top to bottom: 0.7, 1.3 and 2.0 GHz) and three relative bandwidths (left to right: 5, 10 and 20 %). Each graph presents experimental results as circles, to be compared with the theoretical prediction from (36), shown as a thick solid line, based on the average coherence  $\bar{\mu}_r$  estimated in Fig. 11. Dotted lines correspond to the use of an optimal average coherence, derived by least-square fitting, while dashed lines are the results that would be expected if the propagation medium presented no spatial coherence. The effects of experimental uncertainties are shown at two levels: 1) a 10 % uncertainty over the estimate of  $\bar{\mu}_r$ , affecting the model prediction, as shown by the shaded area; 2) a 10 % uncertainty over the estimate of  $\langle \Lambda \rangle$ , as vertical bars.

# Steering Focusing Waves in a Reverberation Chamber with Generalized Time Reversal

Andrea Cozza, *Senior Member, IEEE*, Florian Monsef, *Member, IEEE*

**Abstract**—Generalized time reversal was introduced in a previous paper from a theoretical point of view. In this paper experiments are conducted to demonstrate its application to a reverberation chamber, as a method for generating coherent wavefronts in a medium displaying random propagation. Wavefronts thus generated were sampled over a planar surface, confirming that they propagate as if in a free-space environment. The accuracy with which they match their free-space counterpart is not affected by changing their features, e.g., direction of arrival and focus. These results prove that a single excitation antenna can generate complex wavefronts when coupled to diffusive wave propagation.

**Index Terms**—Time reversal, diffusive media, reverberation chamber, wavefront synthesis.

## I. BACKGROUND AND MOTIVATIONS

Time reversal (TR) was first introduced in acoustics as a method for generating wavefronts focusing back the field distribution initially radiated by a source [1]. Its intrinsical ability to compensate distortions introduced by heterogeneous and complex media with no need for active equalization is perhaps its most striking feature [2]–[4]. Indeed, beam-forming methods require a priori information about the propagation of waves in a given medium; this need is avoided in TR applications by the fact that the wave radiated by the source (which would afterwards be focused back at it) acts as a sort of medium sounding, and thus brings in itself information about the medium. Moreover, contrarily to methods based on inverse problems, TR is not affected by any ill-posedness, as opposed to dereverberation methods [5]. Other beam-forming techniques, such as wave field synthesis [6], require a very large number of synchronous sources, which would typically be prohibitively expensive at microwave frequencies.

Still, TR suffers from an obvious drawback: focusing waves cannot be synthesized arbitrarily, as they can only reproduce previously radiated wavefronts. This is particularly problematic when thinking about applications of TR for testing the response to impinging wavefronts of a device under test.

Generalized TR (GTR) was first tested in an embryonic version in [7], [8], where direct wavefront synthesis was not yet formalized, as later done from a theoretical point of view in [9]. It is based on the use of the equivalence theorem as a way of avoiding the introduction of a source, in order to directly synthesize signals capable of generating focusing

Part of the work here reported was funded by the French National Research Agency through the grant ANR-12-ASTR-0005, MIMOCHEC project, within the framework of the 2012 ASTRID program. The design and manufacturing of the robot were funded by Digiteo, under the AUTOTREC project.

A. Cozza and F. Monsef are with PIEM | GeePs, UMR 8507, CentraleSupélec, Univ Paris Sud, UPMC, CNRS, 1 rue Joliot-Curie, 91192 Gif-sur-Yvette, France. Contact e-mail: andrea.cozza@ieee.org.

wavefronts with arbitrary features. GTR is entirely dependent on the availability of a medium capable of supporting diffuse-field propagation, a statistically isotropic case of multipath propagation, also known as Rayleigh diffusion. Reverberation chambers comply with these requirements and bring at the same time a further advantage, energy efficiency, being closed systems with weak losses; when used with TR signals their efficiency can be further increased [10].

This paper shows validation results obtained with a fully automated system. Experimental results of wavefronts generated within a reverberation chamber are compared to theoretically computed distributions. Sequences of wavefronts varying in the position of their focal region and direction of arrival are generated, confirming that the diffusive nature of the medium ensures an excellent reproducibility of wavefronts at any position.

The conclusions of this study imply that GTR can accurately generate arbitrary pulsed focusing wavefronts with a single antenna. Moreover, generating similar focusing wavefronts in open media could require a potentially large number of sources, depending on the angular spectrum of the wavefront, i.e., its focusing power. These sources would need to be excited coherently over a relatively large bandwidth, an operation which is complex and expensive, as it requires synchronizing a number of modulators or signal generators, which can hardly handle high peak-power levels, were them required.

Applications of GTR-based synthesis are currently in progress and range from hardening shielded systems to high-power microwaves, imaging and generating stable high-intensity fields without the statistical uncertainty found in standard reverberation chambers [10].

The paper is organized as follows. GTR is briefly explained in Sec. II, as an intuitive application of first principles well-known in electromagnetics. Sec. III provides some details about the way wavefront-related data is generated. The experimental setup is described in Sec. IV, while Sec. V explains how generated fields are imaged. Reproducibility and robustness to varying conditions are tested and commented in Sec. VI.

## II. A SHORT SUMMARY OF GTR

This section presents a very short description of how GTR works. The simplest way to understand it is by going through the different steps at its origin. The interested reader can refer to [9] for a much more detailed discussion.

Suppose a source radiates a free-space field distribution  $\mathbf{E}_s(\mathbf{r}, t)$ . When excited within a medium supporting diffusive propagation, the resulting field distribution would be

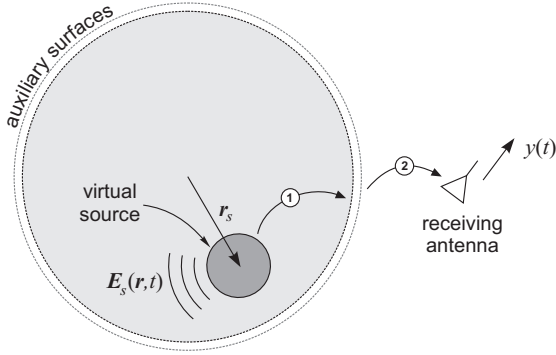


Fig. 1: Relevant quantities in the derivation of direct synthesis of excitation signals with GTR. The auxiliary surfaces are shown to act as an interface between the virtual source radiation (1) and its propagation through the medium (2).

underpinned by a rich plane-wave spectrum, due to a large number of scattering events over its boundaries [11]–[13]. Standard time-reversal would require measuring the signal  $y(t)$  received by a further antenna present in the medium [1], [14]. Injecting the time-reversed signal  $x(t) = y(-t)$  into what was the receiving antenna, eventually corrected for its dispersive response, can generate a close replica of  $\mathbf{E}_s(\mathbf{r}, -t)$ , i.e., the converging counterpart to the originally diverging wavefront  $\mathbf{E}_s(\mathbf{r}, t)$ , stripped of its reactive, i.e., non-propagating, components. A single source can support an entire wavefront thanks to self-averaging ensured by the multipath propagation of the medium, if excitation bandwidths cover several coherence bandwidths of the medium [15]. Stated in other terms, complex media can present frequency responses that become weakly interdependent when observed at frequencies spanning at least one coherence bandwidth. The result is the existence of degrees of freedom that can be roughly measured by taking the ratio of the bandwidth of the excitation signal divided by the coherence bandwidth of the medium. TR signals work by controlling these degrees of freedom such that at the time of focusing they cooperate to create coherent wavefronts, out of individual random contributions from each frequency. This property, known as self-averaging, is fundamentally equivalent to the mechanisms behind Van Cittert-Zernike theorem [16], where degrees of freedom are in space rather than in the frequency domain, and result in overall coherent field distribution generated from random spatial distributions.

The problem with the TR approach is that a focusing wavefront can be generated only if a source radiates a corresponding divergent wavefront in the first place. Clearly, if several focusing wavefronts were to be generated, not only the source would have to be modified (e.g., orientation, position) and made to radiate, but also an array of sources with different characteristics may be required (e.g., directivity, polarization).

GTR bypasses this problem by getting rid of the need for physical sources. The excitation signal  $x(t)$  is directly synthesized, according to the wished characteristics of the focusing wavefront. In order to do that,  $y(t)$  is obtained in

two steps. With reference to Fig. 1, first the field radiated by the source is sampled over (at least) an auxiliary surface  $\Sigma$ . From these samples, equivalent currents are defined, capable of reproducing the outgoing field that would have reached the receiving antenna, were the source real. In the second step,  $y(t)$  is computed from an assumed knowledge of the Green's functions on the medium, acting as transfer functions between the equivalent sources over  $\Sigma$  and the receiving antenna, hereafter referred to as  $\mathbf{N}_e(\mathbf{r}, \omega)$  and  $\mathbf{N}_m(\mathbf{r}, \omega)$ , respectively for the electric and magnetic field Green's functions. The result is a direct synthesis formula for the Fourier spectrum of the received signal  $y(t)$  [9]

$$Y(\omega) = \int_{\Sigma} d\mathbf{r} \left[ \frac{\mathbf{N}_e(\mathbf{r}, \omega)}{\zeta} + \hat{\mathbf{r}} \times \mathbf{N}_m(\mathbf{r}, \omega) \right] \cdot \mathbf{E}_s(\mathbf{r}, \omega). \quad (1)$$

The derivation of (1) means that the auxiliary surfaces act as a relay in the synthesis of the signal  $y(t)$  generated by a given virtual source. Moreover, since the field radiated by the virtual source is not sampled over  $\Sigma$  for its own sake, but rather in order to propagate it to the receiver, there is no need to include reactive contributions [17], [18], due to an eventually near-field configuration. As a result, far-field representations of  $\mathbf{E}_s(\mathbf{r}, t)$  can be used, as done in Sec. V.

If the Green's functions were known, then the first step could be accomplished numerically, with no need of a source in the first place, just by defining firsthand the field distribution expected over  $\Sigma$ . In fact, since the medium is reciprocal, the Green's functions can be measured by exciting the receiving antenna and sampling the electromagnetic field distribution it excites over  $\Sigma$ . This operation is carried out in our case by a low-perturbation robot developed in our laboratory, as discussed in Sec. IV.

In practice, weakly perturbative field probes are needed. Since most often electric-field probes have a better performance in this respect, equivalent currents can be defined from electric field samples only, if a further auxiliary surface is introduced. As demonstrated in [19], this is possible if specific weights  $\{A_i\}$ ,  $i \in [1, L]$  are applied to the field distributions sampled over each auxiliary surface  $\Sigma_l$ , yielding

$$Y(\omega) = \zeta^{-1} \sum_{l=1}^L A_l \int_{\Sigma_l} d\mathbf{r} \mathbf{N}_e(\mathbf{r}, \omega) \cdot \mathbf{E}_s(\mathbf{r}, \omega) \quad (2)$$

For the case  $L = 2$ ,  $A_1 = -\exp(-2jk\Delta R)/[1 - \exp(-2jk\Delta R)]$ ,  $A_2 = -A_1 \exp(2jk\Delta R)$ , with  $\Delta R$  the difference between the radii of the two spherical auxiliary surfaces, required to satisfy  $\Delta R < \lambda/2$ , with  $\lambda$  the working wavelength.

### III. REFERENCE FIELD DISTRIBUTIONS

With reference to Fig. 2, the definition of the virtual source is based on a Gaussian far-field radiation pattern, with phase center  $\mathbf{r}_s$

$$\mathbf{E}_s(\mathbf{r}, \omega) = \hat{\varphi} G(\mathbf{r} - \mathbf{r}_s, \omega) e^{-\psi^2/2\psi_s^2} P(\omega) \quad (3)$$

and  $\psi = \cos^{-1}(\hat{\mathbf{r}}' \cdot \hat{\mathbf{y}})$ , for an angular divergence  $\psi_s$ ;  $G(\mathbf{r}, \omega)$  is the scalar Green's function for free space; the polarization is set equal to  $\hat{\varphi}$ ;  $P(\omega)$  is the Fourier spectrum of  $p(t)$ , the time evolution of the radiated field, usually chosen to be a pulse.

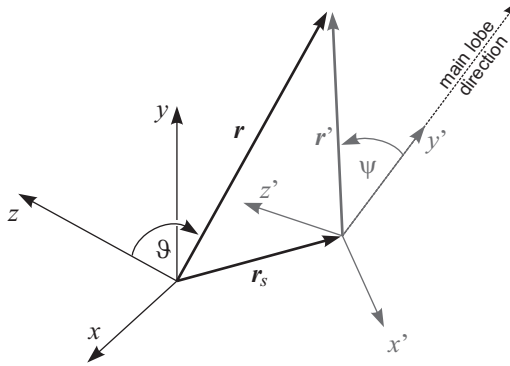


Fig. 2: Global and local reference frames for the computation of the vector field distribution at  $\mathbf{r}$ , radiated by a source centered over  $\mathbf{r}_s$ .

A Gaussian pulse will be used throughout the paper, with a Fourier spectrum

$$P(\omega) = e^{-(\omega - \omega_c)^2 / 2B_e^2}, \quad (4)$$

with  $B_e$  the equivalent bandwidth of the pulses.

In order to orient the main lobe along any direction  $\hat{\mathbf{r}}_{\text{inc}}$ , with arbitrarily oriented polarization, (3) is considered as defined within the local reference frame shown in Fig. 2 in grey with primed quantities, reoriented with respect to the global reference frame through a rotation matrix  $\mathbf{R}$ .

The spherical unit vectors  $\hat{\mathbf{u}}_i(\mathbf{r})$  of the global reference frame are juxtaposed into a matrix  $\mathbf{U}(\mathbf{r})$ , and the same is done for the unit vectors  $\hat{\mathbf{u}}'_i(\mathbf{r}')$  of the local reference frame into a matrix  $\mathbf{U}'(\mathbf{r}')$ . The local-frame field  $\mathbf{E}'(\mathbf{r}')$  then appears to the global frame as  $\mathbf{R}\mathbf{E}'(\mathbf{r}')$  and can be decomposed into the global unit-vector representation as

$$\mathbf{E}_s(\mathbf{r}, \omega) = \mathbf{U}^T(\mathbf{r}) \mathbf{R} \mathbf{U}'(\mathbf{r}') \mathbf{E}'_s(\mathbf{r}', \omega), \quad (5)$$

knowing that  $\mathbf{E}'_s(\mathbf{r}', \omega) = E_s(\mathbf{r}', \omega)\hat{\varphi}$ , as of (3); T is the matrix transpose.

Since (3) makes use of the scalar Green's function, it can only account for far-field radiation. This is not an issue, since the source-radiated field distribution over the auxiliary surfaces has a relay role, as recalled in Sec. II.

Eq. (3) is also needed in order to predict the reference (theoretical) field distribution that GTR is expected to produce. It can be computed by using a plane-wave spectrum (PWS) representation of the radiated field, which corresponds to the far-field radiation [18], and thus coincides with (3) as sampled over a spherical surface centered at the origin of the global reference frame. The value chosen for the radius  $R$  of this test surface has no impact on the PWS computation, as long as  $R$  is much larger than the radii of the auxiliary surfaces.

The refocused field distribution can then be computed by switching the direction of the plane waves from outbound to inbound, yielding

$$\mathbf{E}_{\text{GTR}}(\mathbf{r}, t) = \frac{1}{2\pi} \int d\omega e^{j\omega t} \int d\hat{\mathbf{k}} \mathbf{E}_s^*(R\hat{\mathbf{k}}, \omega) e^{j\hat{\mathbf{k}} \cdot \mathbf{r}}, \quad (6)$$

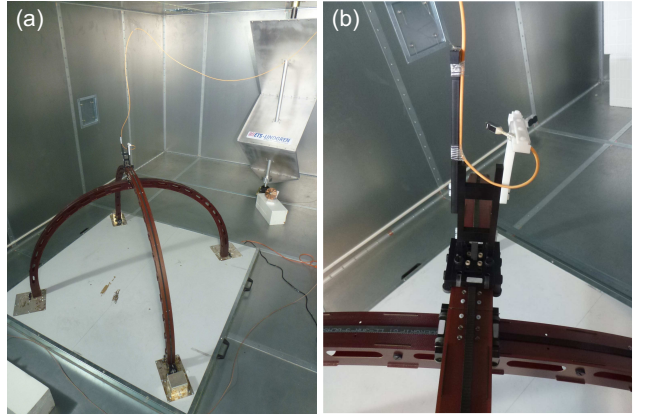


Fig. 3: The hemispherical field scanner with the excitation antenna (a) and the electro-optical probe (b) used during the experimental validation. Notice that the scanner has two arms, one mobile and the other used as a mechanical support, passing through the  $xy$  plane.

with  $*$  the complex conjugation,  $k$  the propagation constant and  $\hat{\mathbf{k}}$  the direction of propagation of each plane wave composing the wavefront. The integration over  $\hat{\mathbf{k}}$  is limited to the directions covered by the auxiliary surfaces, in this case only the  $2\pi$  steradian of the upper half space, i.e., the region spanned by the field scanner described in Sec. IV.

#### IV. EXPERIMENTAL SETUP

Experimental tests were based on the setup shown in Fig. 3. It consisted of a reverberation chamber, of dimensions  $6 \times 3.5 \times 2.5 \text{ m}^3$ , made of galvanised steel. A mechanical stirrer is present but not rotated during the tests, in order to have a static environment, which is a fundamental requirement in order to ensure the best performance in a complex environment [20]. A stirrer can still be of practical interest, as it effectively reduces degeneracies in the modal response of a medium, as due to symmetries.

The electric Green's function, underpinning the synthesis of the excitation signals discussed in Sec. II, is sampled thanks to a dielectric robot. The robot was designed in order to weakly perturb a propagation medium as it moves a probe over a hemispherical surface [21]. The radius of this surface is equal to 1.18 m and can be modified manually, by operating on the probe holder, in order to sample the electric Green's function over two concentric surfaces, as required by Sec. II.

The electric field tangential to the hemispherical surface was sampled with an electro-optical probe, manufactured by Enprobe (model EFS-105). These probes have a flat frequency response up to 3 GHz and are sensitive to phase shifts, making them capable of capture information necessary for time-domain analysis. They are also linearly polarized, with a cross-polarization rejection higher than 40 dB. The  $\vartheta$  and  $\varphi$  tangential scalar components of the electric field were sampled by repeating the scan after rotating the probe by 90 degrees.

Choosing a frequency range for these experiments is a critical decision. On the one hand, increasing frequency enables

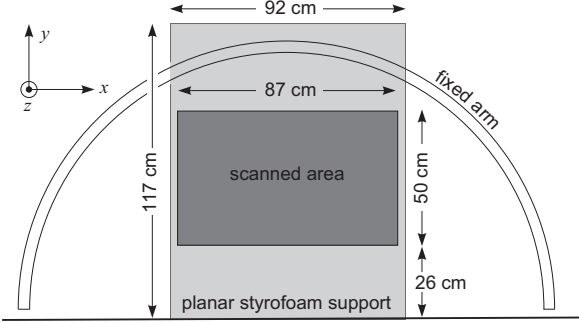


Fig. 4: Layout of the scanned planar area, as part of the  $xy$  plane.

the synthesis of finer focal spots, which would be interesting to test as capable of higher spatial resolution; on the other hand, the robot would introduce stronger perturbations and thus risk degrading the coherence of the field [21]: it would then be harder to understand if errors were due to limitations in GTR or perturbations from the robot. Moreover, the frequencies should be chosen as to ensure that the chamber stays diffusive, i.e., avoiding extended frequency regions where no resonant mode is accessible. For the above chamber, a minimum frequency of about 500 MHz can be considered as safe in this respect, as modal overlapping, partly enabled by moderate losses, ensures that enough degrees of freedom are available [22]. These considerations should be regarded as a conservative requirement, being based on the behaviour of a reverberation chamber excited by a single harmonic signal. As TR applications cover bandwidths that would span a large number of resonant modes of a chamber, standard requirements for modal overlapping can be relaxed. Losses also have an impact on the efficiency of TR and GTR, as they directly control the intensity of the generated wavefront for a given input peak power [10].

For our experiments we settled for the bandwidth  $1.5 \div 2.5$  GHz as a good compromise between spatial resolution and robot perturbation. The two hemispherical surfaces were then set 3.5 cm apart, i.e., about a quarter of wavelength at 2 GHz; this choice ensures that for all the frequencies considered the sampled field distributions will be maximally uncorrelated, in order to avoid any redundancy [23]. The angular sampling was set to 2 degrees, corresponding to a spatial sampling of about 4 cm, in order to have data close enough to ensure a meaningful spatial interpolation. Robot movements are fully automated and controlled through an optical-fiber interface linked to a personal computer.

A single excitation antenna was used, close to the stirrer, as visible in Fig. 3. The antenna was a conical monopole, about 30 cm about the metallic floor, set obliquely. In fact, because of the diffusive nature of waves propagating in the chamber, the features of the antenna have no importance on the final results, though different excitation signals would then be needed (see Sec. II); the orientation chosen was in fact motivated by the need to avoid any symmetry in the setup, which could reduce the number of degrees of freedom on the field.

Transfer functions between the antenna and the field probe were measured by means of a vector network analyzer (Rohde & Schwarz ZVB8). Frequency sampling needs to be chosen carefully, in order to avoid time aliasing, due to the relatively long relaxation time of the chamber, around  $1 \mu\text{s}$ ; 5000 frequency samples were acquired, with a step of 200 kHz, thus a maximum time window of  $5 \mu\text{s}$ .

The data thus collected were used for the synthesis of the excitation signals, using (2). Equally important are the data needed in order to image the field distributions generated by these excitation signals. In order to avoid scanning a surface for each excitation signal used, as it would be necessary for a time-domain excitation, we rather used a two-step approach, requiring a post-processing phase. The idea is again to sample the electric Green's function but this time over the surface over which the wavefront generated with GTR is to be imaged. These samples are therefore no longer used for synthesis, but rather for checking the accuracy of theoretical predictions. Knowing these samples, later referred to as  $\Pi(\mathbf{r}, \omega)$ , the field distributions can be computed as explained in Sec. V.

To this effect, a styrofoam block was introduced, oriented as to have one of its surfaces tangent to the  $xy$  plane, hereafter referred to as the planar monitor. It was used for holding the electro-optical probe over a Cartesian grid graved over its surface; the sampling distance was set to 3.1 cm. The region shown in Fig. 4 was manually scanned, measuring the two tangential polarizations at each point. The normal component was not measured, since it was already proven that time-reversed wavefronts excited in a reverberation chamber present the same accuracy in the three field components, independently of the source used [24].

## V. IMAGING WAVEFRONTS

Given the transfer functions  $\Pi(\mathbf{r}, \omega)$  between the excitation antenna and a position  $\mathbf{r}$  over the planar monitor, the time-domain field generated by an excitation signal  $x(t)$  with a Fourier spectrum  $X(\omega)$  can be retrieved by computing

$$\mathbf{E}(\mathbf{r}, t) = \frac{1}{2\pi} \int d\omega \, \Pi(\mathbf{r}, \omega) X(\omega) e^{j\omega t}. \quad (7)$$

The analysis of the accuracy of the wavefronts generated by GTR is based on sources with  $\psi_s = 40$  degrees (see Sec. III); Sec. VI-C also considers the case  $\psi_s = 10$  degrees. The angular distributions of these two wavefronts, i.e., the modulus of their PWS, are shown in Fig. 5.

Apart from Sec. VI-C, all the results involve wavefronts evolving in time as Gaussian pulses with  $B_e = 500$  MHz, in order to ensure a high contrast between the coherent wavefronts and the background diffuse contribution. The rationale is to create the conditions for judging unambiguously if the wavefronts generated with GTR do indeed evolve as in free-space conditions. The effects of reducing the bandwidth and/or the focusing power are discussed in Sec. VI-C, where they are shown to be two facets of the same problem.

In this section we first consider the generation of a Gaussian wavefront propagating along the direction  $\vartheta = \varphi = 90$  degrees, towards the floor. Its polarization is set to be tangent

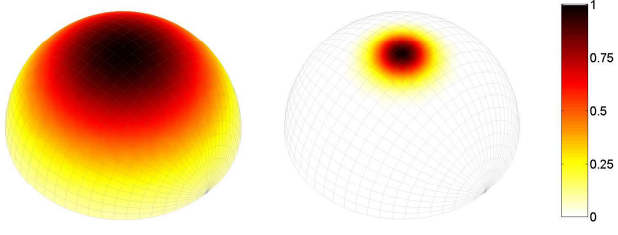


Fig. 5: Angular distribution of the Gaussian beams used throughout the experimental validation: (a)  $\psi_s = 40$  degrees, (b)  $\psi_s = 10$  degrees.

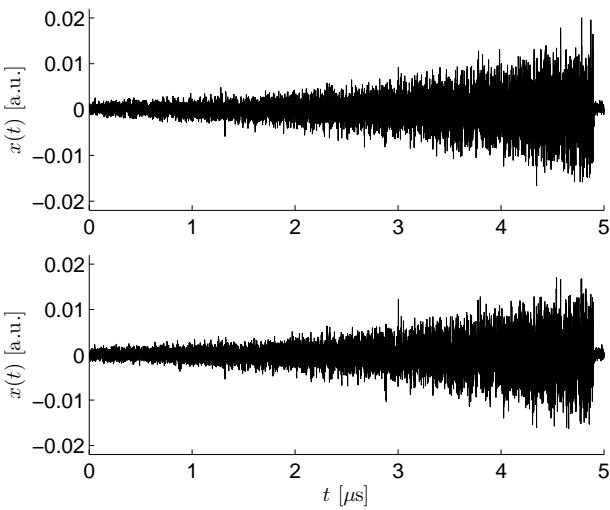


Fig. 6: An example of excitation signals obtained with GTR, for the wavefronts shown in Fig. 11, for a normal incidence along the  $y$  axis (top figure) and an oblique one, tilted by 40 degrees along the  $xy$  plane (bottom figure).

to the planar monitor, i.e., to the plane  $xy$ , or a  $\hat{\varphi}$ -polarized wave. The focus is set in the center of the imaged region.

Combining the data collected with the setup described in Sec. IV together with the theoretical wavefront distribution at the auxiliary surfaces  $\Sigma_i$  as in (2), we obtained the excitation signals expected to reproduce the wavefront within the chamber. Two examples of such signals are presented in Fig. 6, encoding the information needed for generating focusing wavefronts along two directions of incidence. They share the same envelope, as this is directly controlled by the relaxation response of the medium.

Rather than synthesizing these signals in time domain and injecting them into the chamber through the antenna, we proceeded as explained at the beginning of this section. The field distribution over the planar monitor was then computed at a few time instants, in order to observe the focusing wavefront as it approaches the focal region.

Figs. 7 and 8 present the evolution of the  $E_x$  component of the field, respectively theoretically and experimentally. The results closely agree both in the time and space evolution.

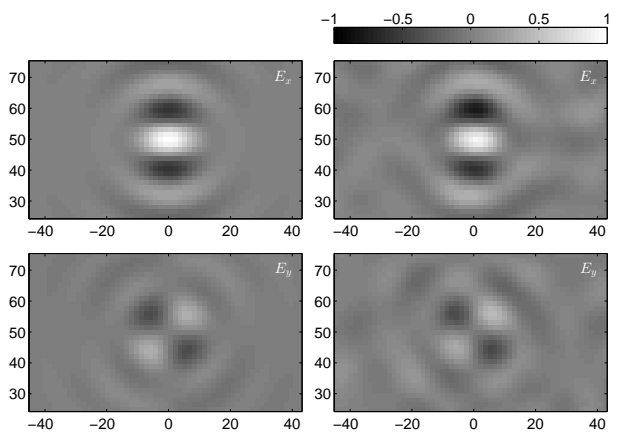


Fig. 9: Distributions of the horizontal ( $E_x$ ) and vertical ( $E_y$ ) field components expected (left column) and measured (right column) at  $t = 0$ . Linear correlation between the theoretical and experimental results is 97% for  $E_x$  and 94% for  $E_y$ . Results normalized to the peak of the norm of the respective electric fields.

The existence and intensity of the background fluctuations can be appreciated in Fig. 8 for  $t = -5$  ns, when the wavefront is expected to be negligible. The field distribution then resembles closely a speckle distribution, with cells about half a wavelength wide.

The coherent evolution of the generated wave is further confirmed in Fig. 8 at  $t = 3$  ns, where the distribution matches that of a wavefront reflected by the floor and moving back upwards. The divergence and delay are in good accordance with the total distance travelled from the focus.

Hereafter only results for  $t = 0$  will be discussed. The focal instant can be regarded as the most important one, as it shows the wavefront that would impinge onto an system if it was present in the chamber in the first place, also during the sampling of Green's functions. It would be impossible to image the impinging field distribution in this last case, since the scattered field would overlap with it; tests carried out in the conditions described in this paper therefore provide precious information for the definition of applications that could benefit from GTR performance.

Fig. 9 shows the two measured field components for  $t = 0$ , compared to those expected for the convergent version of the Gaussian wavefront. Data match very closely, providing an explanation for our showing only the horizontal component  $E_x$  of the electric field, which is also the dominant one.

## VI. WAVEFRONT FIDELITY

Having verified the accurate reproduction of the convergent wavefront, it is fundamental to assess whether GTR can generate it with the same accuracy even when its focus and directions of arrival are changed. The theoretical derivations in [9] concluded that the homogeneous characteristics of diffusive media should ensure a comparable reproduction for any set of parameters, at least on average.

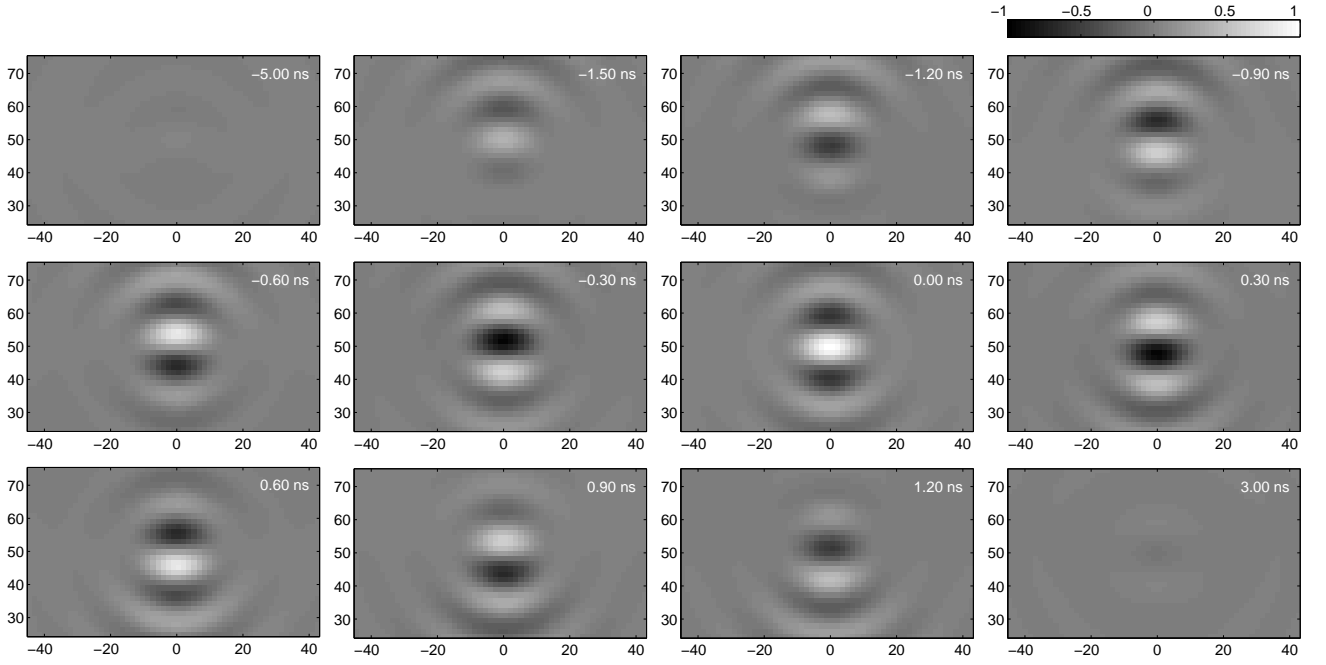


Fig. 7: Theoretical distributions of the horizontal field component  $E_x$  expected over the region shown in Fig. 4, for  $\psi_s = 40$  degrees,  $B_e = 500$  MHz. Results normalized to the peak of the norm of the electric field at  $t = 0$ .

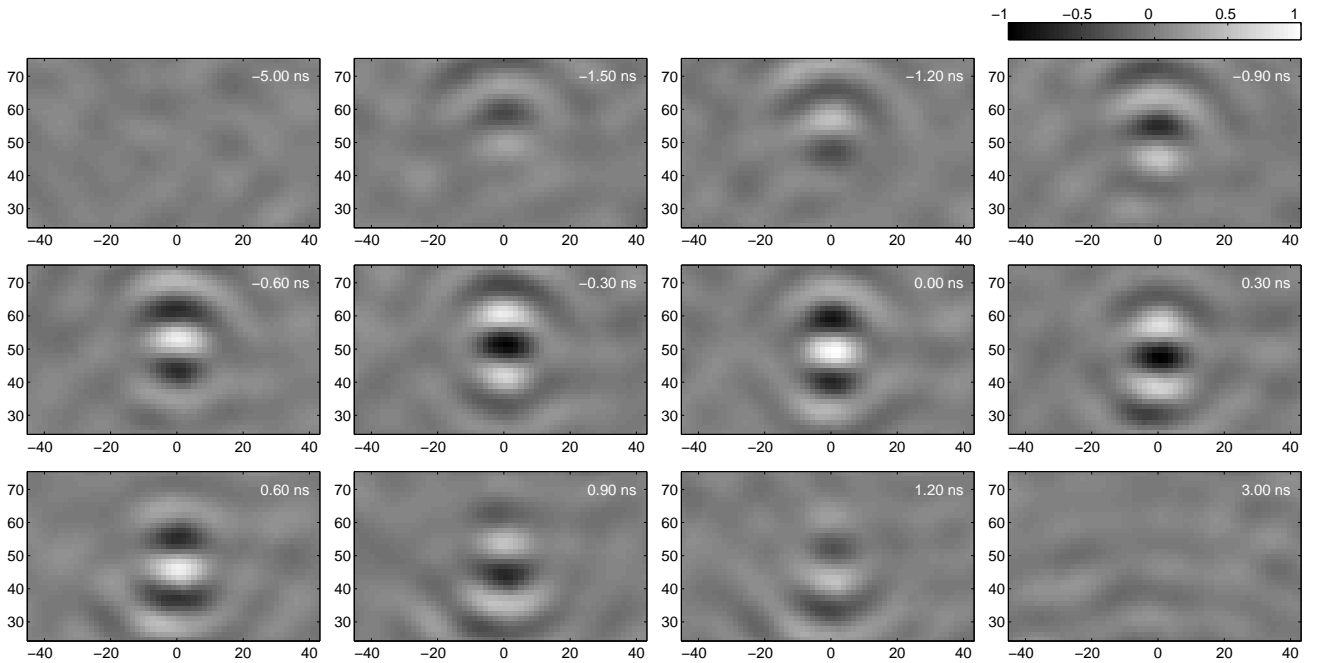


Fig. 8: Field distributions of  $E_x$  measured over the region shown in Fig. 4, for  $\psi_s = 40$  degrees,  $B_s = 500$  MHz. At  $t = -5$  ns, only background fluctuations are visible; at  $t = 3$  ns the wavefront propagates back after reflecting on the metallic floor. Results normalized to the peak of the norm of the electric field at  $t = 0$ .

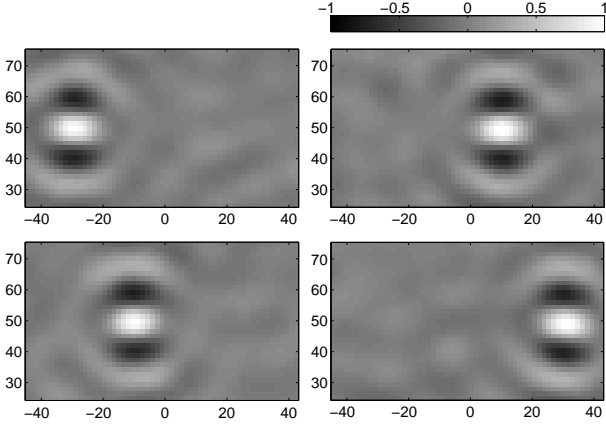


Fig. 10: Measured field distributions for  $E_x$ , for  $\psi_s = 40$  degrees,  $B_e = 500$  MHz and  $t = 0$ , as the position of their focus is displaced horizontally, by 20 cm steps. Linear correlation between the four field distributions is above 95%. Results normalized to the peak of the norm of the electric field at  $t = 0$  for the original central position shown in Fig. 9.

#### A. Moving the focal spot

The field distribution observed at  $t = 0$  was studied as the position of the focal spot changes. Four positions were considered, following a sequence of 20 cm horizontal displacements. The results are shown in Fig. 10 for the dominant field component,  $E_x$ . An excellent fidelity was found, with both the field structure and its amplitude practically unchanged.

#### B. Changing direction of arrival

The next test was to verify the wavefront fidelity when the direction of arrival changes. Since rotations would also affect the orientation of the main polarization, it is now necessary to study the polarization vector of the field. Five directions were considered, for  $\varphi$  changing from -40 to 40 degrees around the initial direction, in steps of 20 degrees.

The results are shown in Fig. 11, where theoretical field distributions are compared with those found in practice. The agreement is again satisfying, with the focal regions practically identical to theoretical predictions. As discussed in Sec. VI-C, the regions outside the focal region are more strongly affected by random fluctuations inherent in the use of a diffusive medium; as a result, the agreement is not perfect outside the focal region.

#### C. Focusing and contrast

Previous results were obtained in optimal conditions, choosing wavefronts both confined in time (wide bandwidth) and in space (high values of  $\psi_s$ ). The reason for the optimal performance for this case can be understood by recalling that wavefront-related quantities (e.g., received signals) present a mixture of coherent components, i.e., the wavefront meant to be generated, and incoherent ones, i.e., the random background fluctuations observed in the field distributions. It was shown

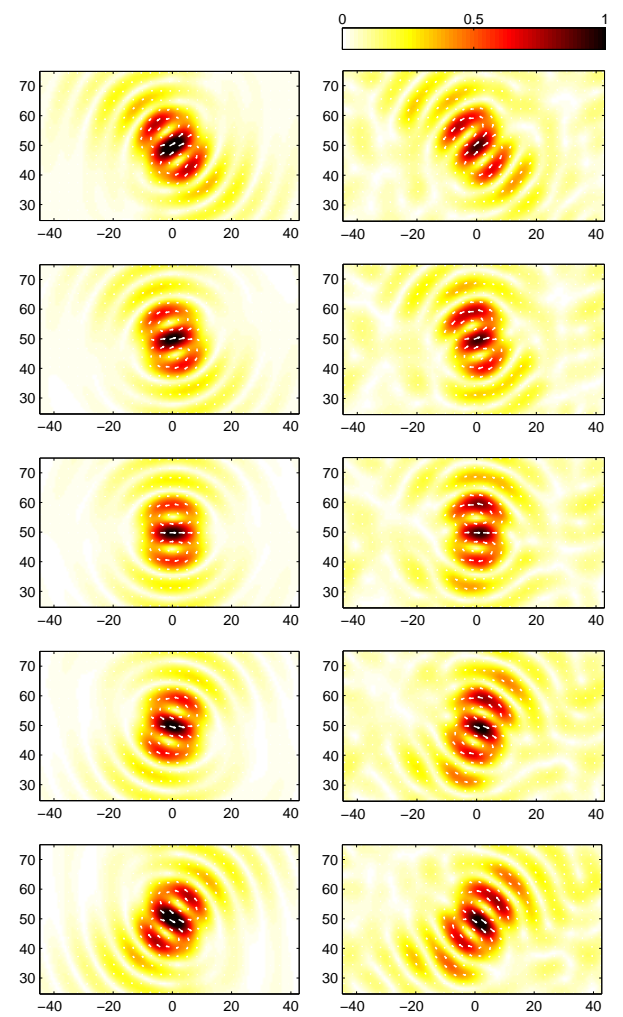


Fig. 11: Vector field distributions (theoretical on the left and measured on the right), for  $\psi_s = 40$  degrees,  $B_e = 500$  MHz and  $t = 0$ , for wavefronts impinging along a direction of arrival  $\hat{r}_{\text{inc}} \in xy$ , rotated by 20 degree steps, from -40 degrees to 40 degrees with respect to the  $\hat{y}$  axis. Results are normalized to the peak value of each field distribution. Linear correlation coefficients between experimental and theoretical spatial distributions of the field norm are 95%, 94%, 93%, 93% and 92%, from top to bottom.

in [25] that the ratio between the average energy densities conveyed by these two components is fixed by the statistical properties of the medium itself; e.g., for a diffusive medium it is equal to one.

This result has a very practical implication: if the coherent energy is fixed, then depending on how it is shaped, the instantaneous power can take very different values. For instance, if energy is shaped into a short pulse, the peak to energy ratio will be maximized, leading to a peak in the coherent component, making it stay well above the background fluctuations. On the contrary, if a narrower bandwidth is chosen, the energy will be spread over a larger time interval,

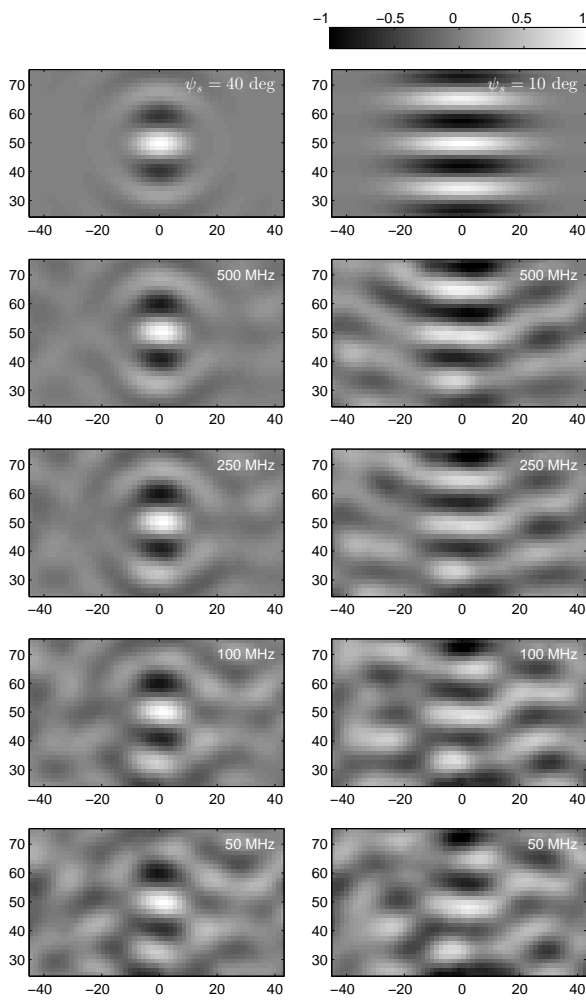


Fig. 12: Comparison between  $E_x$  field distributions obtain for two Gaussian beams, with  $\psi_s = 40$  degrees (left column) and  $\psi_s = 10$  degrees (right column), as the equivalent bandwidth  $B_e$  changes. Notice how the focal region is hardly affected for  $\psi_s = 40$  degrees, even for a relatively narrow bandwidth, as opposed to the case for  $\psi_s = 10$  degrees. Results are normalized to the peak value of each field distribution. Linear correlation coefficients between experimental and theoretical spatial distributions are, from top to bottom, 97%, 95%, 94% and 93%, for  $\psi_s = 40$  degrees and 94%, 93%, 87% and 73%, for  $\psi_s = 10$  degrees.

hence a lower peak instantaneous power, with a subsequent risk of having it drowned into the background fluctuations.

This reasoning leads to conclude that both time and spatial focusing play the same role: weakly converging wavefronts, somewhat closer to plane waves over regions spanning several wavelengths, also spread energy over space. Examples going in this sense are shown in Fig. 12, where wavefronts with different combinations of bandwidth and angular convergence are considered. For the same bandwidth, the focal region can be shown to be about 6 times larger when  $\psi_s = 10$  degrees than for  $\psi_s = 40$  degrees. As a result, in order to maintain

a similar contrast between the coherent wavefront and the background in the two cases, a bandwidth about 6 times larger is required for  $\psi_s = 10$  degrees. This conclusion is consistent with the observation of similar background fluctuations in the results for  $B_e = 250$  MHz (for  $\psi_s = 10$  degrees) and  $B_e = 50$  MHz (for  $\psi_s = 40$  degrees).

In short, bandwidth and angular divergence do not put into question the ability of GTR to generate accurate wavefronts, but rather need to be regarded as design parameters that impact the margin between the wavefront and the background fluctuations.

## VII. CONCLUSIONS

GTR was applied to a reverberation chamber, as a way of generating coherent focusing wavefronts. These were proven to create focal regions very close to those theoretically computed. Moreover, their features were practically independent of their direction of arrival or position.

The results shown make clear that the appearance of the wavefronts is not due to a local compensation of the medium response, but corresponds to an actual wavefront interacting with the medium boundaries, as proven by the reflections shown in Fig. 8.

GTR is therefore an effective way of generating arbitrary focusing wavefronts with a single antenna. Its main limitations are the need for a low-perturbation field scanner and sufficiently high space-time focusing, which make it better suited to the generation of pulsed wavefronts.

## REFERENCES

- [1] D. Cassereau and M. Fink, "Time-reversal of ultrasonic fields. III. Theory of the closed time-reversal cavity," *IEEE Transactions on Ultrasonics, Ferroelectrics, and Frequency Control*, vol. 39, no. 5, pp. 579–592, 2002.
- [2] P. Roux, B. Roman, and M. Fink, "Time-reversal in an ultrasonic waveguide," *Applied Physics Letters*, vol. 70, p. 1811, 1997.
- [3] W. Kuperman, W. Hodgkiss, H. Song, T. Akal, C. Ferla, and D. Jackson, "Phase conjugation in the ocean: Experimental demonstration of an acoustic time-reversal mirror," *The Journal of the Acoustical Society of America*, vol. 103, p. 25, 1998.
- [4] M. Fink and C. Prada, "Acoustic time-reversal mirrors," *Inverse Problems*, vol. 17, p. R1, 2001.
- [5] P. A. Naylor and N. D. Gaubitch, *Speech dereverberation*. Springer Science & Business Media, 2010.
- [6] E. W. Start, *Direct sound enhancement by wave field synthesis*. TU Delft, Delft University of Technology, 1997.
- [7] H. Moussa, A. Cozza, and M. Cauterman, "Directive wavefronts inside a time reversal electromagnetic chamber," in *Electromagnetic Compatibility, 2009. EMC 2009. IEEE International Symposium on*, Aug 2009, pp. 159–164.
- [8] ———, "Experimental demonstration of directive pulsed wavefront generation in reverberation chambers," *Electronics Letters*, vol. 46, no. 9, pp. 623–624, 2010.
- [9] A. Cozza, "Emulating an anechoic environment in a wave-diffusive medium through an extended time-reversal approach," *Antennas and Propagation, IEEE Transactions on*, vol. 60, no. 8, pp. 3838–3852, 2012.
- [10] H. Vallon, A. Cozza, F. Monsef, and A. S. Chauchat, "Time-reversed excitation of reverberation chambers: Improving efficiency and reliability in the generation of radiated stress," *IEEE Transactions on Electromagnetic Compatibility*, vol. 58, no. 2, pp. 364–370, April 2016.
- [11] D. Hill, "Plane wave integral representation for fields in reverberation chambers," *IEEE Transactions on Electromagnetic Compatibility*, vol. 40, no. 3, pp. 209–217, aug 1998.
- [12] H. Kuttruff, *Room acoustics*. Taylor & Francis, 2000.

- [13] C. Holloway, D. Hill, J. Ladbury, P. Wilson, G. Koepke, and J. Coder, “On the use of reverberation chambers to simulate a Rician radio environment for the testing of wireless devices,” *IEEE Transactions on Antennas and Propagation*, vol. 54, no. 11, pp. 3167–3177, 2006.
- [14] C. Draeger, J. Aime, and M. Fink, “One-channel time-reversal in chaotic cavities: Experimental results,” *The Journal of the Acoustical Society of America*, vol. 105, p. 618, 1999.
- [15] A. Derode, P. Roux, and M. Fink, “Robust acoustic time reversal with high-order multiple scattering,” *Physical Review Letters*, vol. 75, no. 23, pp. 4206–4209, 1995.
- [16] M. Born and E. Wolf, “Principles of opticspergammon press,” *New York*, 1980.
- [17] R. Collins and F. Zucker, *Antenna Theory*. McGraw-Hill, New York, 1969.
- [18] T. Hansen and A. D. Yaghjian, *Plane-wave theory of time-domain fields*. IEEE Press, 1999.
- [19] A. Cozza and F. Monsef, “Layered electric-current approximations of cylindrical sources,” *Wave Motion*, vol. 64, pp. 34–51, 2016.
- [20] ——, “On the influence of medium statistics on the robustness of time-reversal transmissions,” *IEEE Antennas and Wireless Propagation Letters*, vol. PP, no. 99, pp. 1–1, 2016.
- [21] A. Cozza, F. Masciovecchio, C. Dorgan, M. Serhir, F. Monsef, and D. Lecointe, “A dielectric low-perturbation field scanner for sensitive environments,” *Antennas and Propagation, IEEE Transactions on*, 2016, under review.
- [22] A. Cozza, “The role of losses in the definition of the overmoded condition for reverberation chambers and their statistics,” *IEEE Transactions on Electromagnetic Compatibility*, vol. 53, no. 2, pp. 296–307, May 2011.
- [23] D. Hill and J. Ladbury, “Spatial-correlation functions of fields and energy density in a reverberation chamber,” *IEEE Transactions on Electromagnetic Compatibility*, vol. 44, no. 1, pp. 95–101, 2002.
- [24] A. Cozza and H. Moussa, “Enforcing deterministic polarisation in a reverberating environment,” *Electronics Letters*, vol. 45, no. 25, pp. 1299–1301, 2009.
- [25] A. Cozza and F. Monsef, “Multiple-source time-reversal transmissions in random media,” *Antennas and Propagation, IEEE Transactions on*, vol. 62, no. 8, pp. 4269–4281, Aug 2014.

# On the Influence of Medium Statistics on the Robustness of Time-Reversal Transmissions

Andrea Cozza, *Senior Member, IEEE*, Florian Monsef, *Member, IEEE*

**Abstract**—The problem of predicting the performance of Time-Reversal Transmissions (TRT) in a time-varying complex medium is addressed in this paper. The loss of coherence in the propagation medium and its nominal energy contrast are proven sufficient to predict the average loss of quality in received signals. In particular, it is shown how a perturbation in the medium affects in a different way coherent focusing and background fluctuations. In the extreme case of a diffusive medium (e.g., Rayleigh channels), the fluctuations intensity is unaltered. The predictions of the proposed theoretical models are validated against experimental results measured in a reverberation chamber, where a mechanical paddle (stirrer) acts as the source of perturbation in the medium. It is confirmed that, depending on the medium statistics, perturbations can have a varying impact on TRT performance.

**Index Terms**—Time-reversal transmissions, complex media, perturbation analysis.

## I. INTRODUCTION

Waves propagating through complex media are subjected to a potentially large number of scattering events, generating multiple propagation paths and ultimately leading to phenomena like time-spreading of pulses and frequency selectivity, making signal transmissions less predictable and reliable.

Time-reversal transmissions (TRT) have been studied in the last few years as a potential solution to counter these effects, by providing the best replica of a target signal at the receiver, while at the same time focusing a substantial portion of the energy around it [1], [2]. Most applications are based on a direct implementation of standard time reversal as described in [3]. In short, in order to have a received signal as close as possible to a target signal  $p(t)$ , the transmitted signal has a Fourier spectrum of the kind  $P(\nu)H^*(\nu)M(\nu)$ , where  $\nu$  is the frequency variable and  $H(\nu)$  is the transfer function between the transmitter and the receiver.  $M(\nu)$  is a weighting function that represents the effects of equalization and compensation schemes that have been used for improving TRT [4].

The main weakness of TRT is that even in collaborative configurations, where it makes sense to assume  $H(\nu)$  to be known, propagation media may change over time. As a matter of fact, real-life propagation scenarios are hardly static, as they often involve moving people/vehicles, and also receiving and transmitting antennas can change position/orientation, e.g., when hand-held mobile terminals are used. Time-varying propagation can be taken into account, by periodically sounding the

Part of the work here reported was funded by the French National Research Agency through the grant ANR-12-ASTR-0005, MIMOCHEC project, within the framework of the 2012 ASTRID program.

A. Cozza and F. Monsef are with PIEM, GeePs (UMR 8507), 11 rue Joliot-Curie, 91192 Gif-sur-Yvette, France. Contact e-mail: andrea.cozza@ieee.org.

medium response and transfer functions, but this can clearly be done only at discrete times. In between them, TRT risk using signals that no longer represent an accurate description of the medium, resulting in a loss of coherence and ultimately a reduced performance. This problem has been addressed in a few papers, mostly empirically and essentially with the aim of assessing what degree of perturbation would still provide an acceptable performance [5]–[8]. In diffusive media, such as large cavities, indoor propagation and heavily built urban structures, TRT can be so sensitive that it has been proposed for detecting perturbations in the first place [9].

A case therefore exists to understand under what conditions TRT are more or less sensitive to perturbations. This paper brings some insight into this issue, by demonstrating how the statistical behavior of a medium results into a different sensitivity to perturbations. The predictions of the proposed models are validated against experimental results, confirming their accuracy.

## II. RESIDUAL FLUCTUATIONS AND CONTRAST

Signals received with TRT in static media can be expressed as

$$y(t) = \int_{B_T} d\nu P(\nu)|H(\nu)|^2 e^{j2\pi\nu t} \quad (1)$$

where  $H(\nu)$  is the transfer function between the transmitting antenna and the receiver and  $B_T$  is the bandwidth over which the spectrum  $P(\nu)$  of the target signal  $p(t)$  is defined. For any medium significantly different from free space,  $H(\nu)$  would not be a monotonous function of frequency, presenting minima or even nulls over certain frequencies due to reflections and in general interactions with boundary elements. Modelling  $H(\nu)$  as a random process, fluctuations in  $y(t)$  appear as the result of deviations from line-of-sight transmissions.

The effectiveness of TRT can be measured by first separating the received signal  $y(t)$  as done in [10]

$$y(t) = \alpha p(t) + f(t), \quad (2)$$

i.e., as made up of a coherent portion proportional to  $p(t)$  and residual fluctuations  $f(t)$ . Projecting the received signal onto the target one yields

$$\alpha = \langle Y(\nu), P(\nu) \rangle = \int_{B_T} d\nu Y(\nu)P^*(\nu), \quad (3)$$

choosing  $p(t)$  to have unit energy, here meant as for a mathematical signal, i.e., the square of its  $L_2$  norm. A direct consequence of (2) is the orthogonality of  $f(t)$  and  $p(t)$ .

A natural metric is therefore the energy contrast  $\Lambda$  [10], which measures the ratio between the energy  $\mathcal{E}_c = \alpha^2$  of the

the case of a Rayleigh or diffusive medium. Introducing the TRT function  $W(\nu) = |H(\nu)|^2$ , [10] demonstrated that the second-order statistics of  $W(\nu)$  provide a direct estimate of the energy contrast as  $\langle \Lambda \rangle = \varsigma_W^{-2}$ , where  $\varsigma$  is the square of the standard deviation normalized to the mean. This relationship is useful as it gives a straightforward understanding of the performance of TRT as a function of the medium statistics and complexity. Nevertheless, it only holds for the average behavior of a medium, so that  $\Lambda$  can exceed the value one on a local basis, as observed in Sec. IV.

Once the energy contrast is known, it can be translated into a peak contrast, measuring the ratio of the peak of coherent focusing and the rms amplitude of the background fluctuations [10].

### III. EFFECTS OF PERTURBATIONS ON TRT

We consider a nominal transfer function  $H_o(\nu)$  for the unperturbed medium and  $H(\nu)$  the one found at the time of transmission, after the perturbation event has occurred. It is convenient to express this modified function as a linear combination of the original function plus a random process  $\delta H(\nu)$  modelling the effect of the perturbation, i.e.,

$$H(\nu) = \rho H_o(\nu) + \delta H(\nu), \quad (5)$$

with  $\rho$  the linear correlation coefficient between the original and modified functions. By definition,  $\delta H(\nu)$  is orthogonal to  $H_o(\nu)$ , i.e., their projection

$$\langle \delta H(\nu), H_o(\nu) \rangle = \int_{B_T} d\nu \delta H(\nu) H_o^*(\nu) = 0. \quad (6)$$

The perturbation is assumed not to affect the statistical moments of field-related quantities, but only their specific random realizations. This assumption makes sense when the perturbation does not change either the complexity of the medium or the overall rate of energy dissipated. Under this assumption, introducing the average energies of  $H(\nu)$  and  $H_o(\nu)$ , in the sense of squared  $L_2$  norms, i.e., defined as the

$$\mathcal{E}_H = \int_{B_T} d\nu \langle |H(\nu)|^2 \rangle, \quad (7)$$

with  $\langle \cdot \rangle$  the expected value, it is therefore straightforward to prove that

$$\mathcal{E}_{\delta H} = (1 - \rho^2) \mathcal{E}_{H_o}, \quad (8)$$

by enforcing the condition

$$\mathcal{E}_H = \mathcal{E}_{H_o} \quad (9)$$

and (6).

In case of no perturbation, the Fourier spectrum of the received signal is

$$Y_o(\nu) = |H_o(\nu)|^2 P(\nu), \quad (10)$$

while, after a perturbation occurs, one would obtain

$$Y(\nu) = H(\nu) H_o^*(\nu) P(\nu), \quad (11)$$

yielding, after (5),

$$Y(\nu) = \rho |H_o(\nu)|^2 P(\nu) + \delta H(\nu) H_o^*(\nu) P(\nu). \quad (12)$$

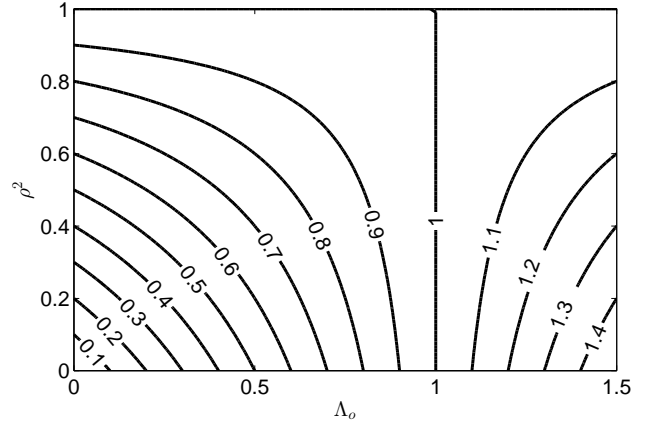


Fig. 1:  $\mathcal{E}_f/\mathcal{E}_{f,o}$  as a function of  $\rho$  and  $\Lambda_o$ .

The degradation in the energy contrast in case of a perturbation is naturally measured by the ratio  $\Lambda/\Lambda_o$ , for which we need to compute the new energies for the coherent part of the received signal and the background fluctuations. The coherent energy  $Y_c$  after the perturbation has occurred is given by

$$\mathcal{E}_c = \rho^2 \mathcal{E}_{c,o}, \quad (13)$$

by recalling (5), (6) and using (19).

The average energy of the background fluctuations in the perturbed case reads

$$\mathcal{E}_f = \int_{B_T} d\nu |Y(\nu) - Y_c(\nu)|^2, \quad (14)$$

which can be simplified, thanks to (19), into

$$\mathcal{E}_f = \rho^2 \mathcal{E}_{f,o} + \int_{B_T} d\nu \langle |\delta H(\nu)|^2 \rangle \langle |H_o(\nu)|^2 \rangle. \quad (15)$$

Following (8),

$$\mathcal{E}_f = \rho^2 \mathcal{E}_{f,o} + (1 - \rho^2) \mathcal{E}_{c,o}, \quad (16)$$

so that

$$\mathcal{E}_f/\mathcal{E}_{f,o} = \rho^2 (1 - \Lambda_o) + \Lambda_o. \quad (17)$$

Eq. (17) implies that the level of fluctuations in signals received in the perturbed medium should not be expected to be same experienced in the nominal configuration. Fig. 1 show a contour-level plot of (17); it should be noticed how, for any  $\Lambda_o \neq 1$ , perturbing the medium could either lead to weaker or stronger fluctuations, for a same loss of coherence.

Still, even in the case of a reduction in the fluctuations for  $\Lambda_o < 1$ , the contrast systematically reduces after a perturbation, as found by combining (13) and (17)

$$\Lambda/\Lambda_o = \left[ 1 + \left( \frac{1}{\rho^2} - 1 \right) \Lambda_o \right]^{-1}. \quad (18)$$

Fig. 2 shows how the above ratio depends on the nominal energy contrast and  $\rho$ . According to (17), the dependence on  $\Lambda_o$  is purely due to the changing intensity of background fluctuations, since the received coherence energy is not expected to depend on  $\Lambda_o$ .

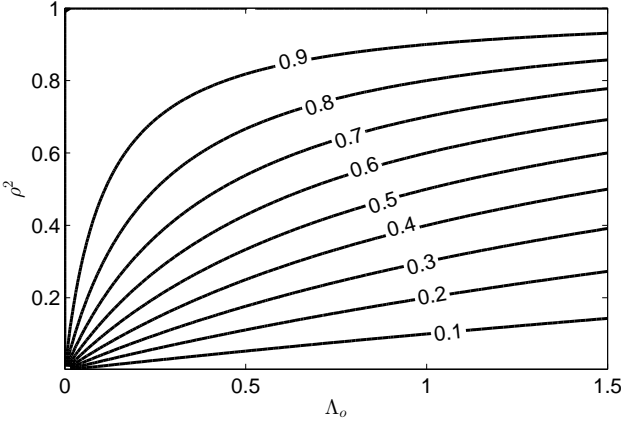


Fig. 2:  $\Lambda/\Lambda_o$  as a function of  $\rho$  and  $\Lambda_o$ .

#### IV. EXPERIMENTAL VALIDATION

In order to validate the implications of our models, access to a medium capable of supporting different field statistics is needed. A reverberation chamber is the ideal facility for these tests since, depending on the degree of overlapping in the frequency responses of its resonant modes, it can support field propagations with a varying  $\Lambda_o$ . Modal overlapping, and as a consequence  $\Lambda_o$ , can be controlled by changing frequency, as demonstrated in [11], [12].

Moreover, reverberation chambers are routinely equipped with at least one metallic paddle acting as a field stirrer, which is a practical way of perturbing the medium in a controllable and reproducible way. But stirrers are usually designed and operated in order to (ideally) generate independent random realizations when rotated. This would ideally lead to only two values of  $\rho$ , either 0 or 1. We rather need to define rotation steps in the stirrer in order to evenly sample the entire range of values taken by  $\rho$ . As a result, the fact that the chosen angles of rotation of the stirrer are small should not come as a surprise.

Two monocone antennas were used as receiver and transmitter. They were positioned on either side of the stirrer, in order to reduce the incidence of line-of-sight paths, so that modifications in the stirrer position would have an impact on the maximum number of propagation paths within the chamber.

The transfer function between the two antennas was measured with a vector network analyzer from Rohde & Schwarz, model ZVB8, operated between 200 MHz and 700 MHz; the transfer functions were sampled with 40 kHz steps. This approach allows a sufficiently fine frequency step, in order to avoid any aliasing in the relatively long impulse responses of the chamber, around 4  $\mu$ s.

The  $\Lambda_o$  that the setup can produce were assessed from the transfer functions  $H(\nu)$ , as explained in [10], by estimating the normalized variance of  $W(\nu) = |H(\nu)|^2$ . Three central frequencies were chosen, 300, 510 and 695 MHz, where the chamber behaves in a distinctly different way. A bandwidth  $B_T = 30$  MHz was chosen for the excitation around each frequency, as a compromise between spectral resolution and

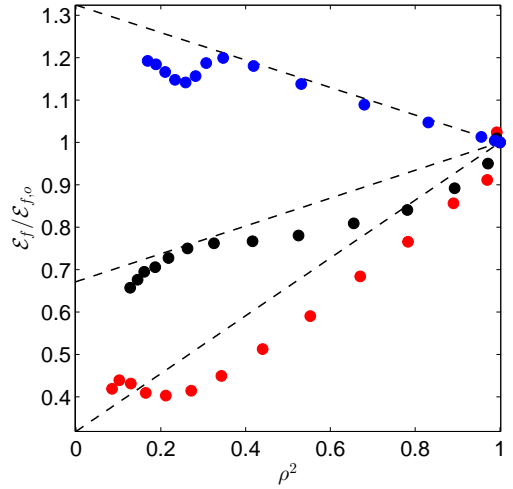


Fig. 3: Comparison between experimental (circles) and theoretical (dashed lines) relationships for the effect of a perturbation in a medium and the energy of the fluctuations at the receiver, for  $\Lambda_o$  equal to 0.32 (red), 0.67 (black) and 1.32 (blue).

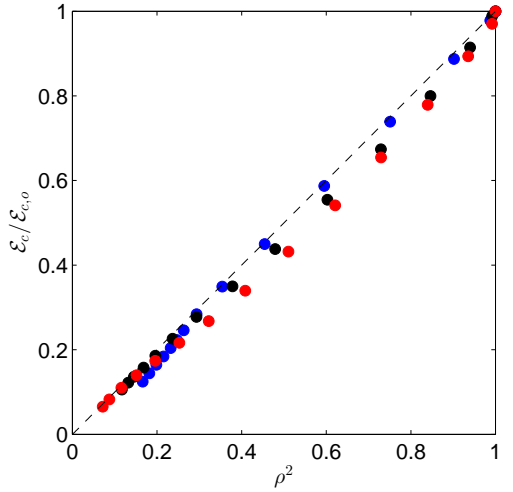


Fig. 4: As in Fig. 3, but here studying the modifications in the coherent energy at the receiver.

statistical uncertainty. For this choice,  $\Lambda_o$  was found to be equal to 0.32, 0.67 and 1.32, respectively, for the three central frequencies. These values correspond to the stirrer parked at its original position, in static conditions.

The stirrer was then put in motion by 1-degree steps. For each step, the transfer function was measured, and the procedure repeated 14 times. For each frequency the linear correlation between the original transfer function and the perturbed ones was computed, together with the resulting modification in energy contrast, coherent and background-fluctuation energy at the receiver. Notice that these quantities were computed by directly observing the received signals; no approximation was considered here. These results are shown in Figs. 3, 4 and 5 and compared to the theoretical models

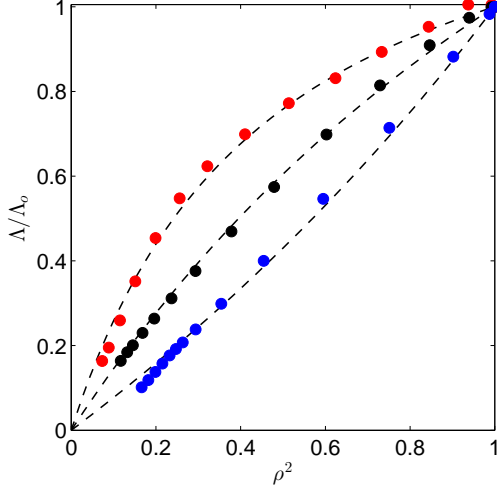


Fig. 5: As in Fig. 3, but here studying the modifications in the energy contrast at the receiver.

derived before.

The models appear to be accurate, as they correctly predict the strong dependence of the background-fluctuation energy on different values of the static  $\Lambda_0$ . Also, the coherent energy at the receiver is also confirmed to be practically insensitive to  $\Lambda_0$  and proportional to  $\rho^2$ . It is therefore confirmed that the main reason for a varying robustness is the changing level of background fluctuations.

## V. CONCLUSIONS

Simple theoretical models here derived predict accurately how perturbations in the transfer functions of a complex medium affect TRT. The main result is the strong sensitivity of the intensity of background fluctuations to the statistics of the unperturbed medium; the coherent energy at the receiver is on the contrary unaffected by the medium statistics and directly controlled by the level of perturbation of the medium.

The accuracy of these models implies that knowing second-order statistics of a medium transfer functions and its level of potential loss of coherence are sufficient to predict the degradation in TRT schemes and related applications.

## APPENDIX

This appendix proves that given a random process  $G(\nu)$  and a piece-wise smooth spectrum  $P(\nu)$  of mathematical energy  $\mathcal{E}_P$ , the following approximation holds

$$\int_{B_T} d\nu G(\nu)|P(\nu)|^2 \simeq \int_{B_T} d\nu \langle G(\nu) \rangle |P(\nu)|^2 \simeq \langle G(\nu_c) \rangle \mathcal{E}_P, \quad (19)$$

as long as the coherence bandwidth  $B_c^G$  of  $G(\nu)$  is much smaller than that of  $|P(\nu)|^2$ ,  $B_c^P$ . The integral can be computed over a sequence of  $N$  contiguous frequency bands  $B_i$  centered at  $\nu_i$ , covering the entire  $B_T$ , chosen such that

$B_c^P > B_i \gg B_c^G$ . In this way,  $|P(\nu_i)|^2$  can be approximated as a constant over each  $B_i$

$$\int_{B_T} d\nu G(\nu)|P(\nu)|^2 \simeq \sum_{i=1}^N |P(\nu_i)|^2 \int_{B_i} d\nu G(\nu). \quad (20)$$

Each integral acts as an estimator of the ensemble average of  $G(\nu_i)$ , since  $B_i$  spans a multitude of independent realizations, thus the first approximation in (19). In case of an average independent from frequency, the second approximation in (19) is obtained.

## REFERENCES

- [1] A. Derode, A. Tourin, J. de Rosny, M. Tanter, S. Yon, and M. Fink, "Taking advantage of multiple scattering to communicate with time-reversal antennas," *Physical Review Letters*, vol. 90, no. 1, p. 14301, 2003.
- [2] R. Qiu, C. Zhou, N. Guo, and J. Zhang, "Time reversal with MISO for ultrawideband communications: Experimental results," *Antennas and Wireless Propagation Letters, IEEE*, vol. 5, no. 1, pp. 269–273, Dec 2006.
- [3] M. Fink, "Time reversal of ultrasonic fields. I. Basic principles," *IEEE Transactions on Ultrasonics, Ferroelectrics and Frequency Control*, vol. 39, no. 5, pp. 555–566, 1992.
- [4] H. Song, W. Hodgkiss, W. Kuperman, M. Stevenson, and T. Akal, "Improvement of time-reversal communications using adaptive channel equalizers," *Oceanic Engineering, IEEE Journal of*, vol. 31, no. 2, pp. 487–496, April 2006.
- [5] A. Tourin, A. Derode, and M. Fink, "Sensitivity to perturbations of a time-reversed acoustic wave in a multiple scattering medium," *Physical review letters*, vol. 87, no. 27, p. 274301, 2001.
- [6] L. Liu, D. G. Albert, and D. K. Wilson, "The effect of changing scatterer positions on acoustic time-reversal refocusing in a 2D urban environment at low frequencies," *Journal of Geophysics and Engineering*, vol. 4, no. 3, p. 276, 2007. [Online]. Available: <http://stacks.iop.org/1742-2140/4/i=3/a=S06>
- [7] D. Liu, S. Vasudevan, J. Krolik, G. Bal, and L. Carin, "Electromagnetic time-reversal source localization in changing media: Experiment and analysis," *Antennas and Propagation, IEEE Transactions on*, vol. 55, no. 2, pp. 344–354, 2007.
- [8] M. Yavuz and F. Teixeira, "On the sensitivity of time-reversal imaging techniques to model perturbations," *Antennas and Propagation, IEEE Transactions on*, vol. 56, no. 3, pp. 834–843, March 2008.
- [9] B. T. Taddese, T. M. Antonsen, E. Ott, and S. M. Anlage, "Sensing small changes in a wave chaotic scattering system," *Journal of Applied Physics*, vol. 108, no. 11, p. 114911, 2010.
- [10] A. Cozza and F. Monsef, "Multiple-source time-reversal transmissions in random media," *Antennas and Propagation, IEEE Transactions on*, vol. 62, no. 8, pp. 4269–4281, Aug 2014.
- [11] A. Cozza, "The Role of Losses in the Definition of the Overmoded Condition for Reverberation Chambers and Their Statistics," *IEEE Transactions on Electromagnetic Compatibility*, no. 53, pp. 296–307, 2010.
- [12] F. Monsef and A. Cozza, "Average number of significant modes excited in a mode-stirred reverberation chamber," *Electromagnetic Compatibility, IEEE Transactions on*, vol. 56, no. 2, pp. 259–265, 2014.

# CHAPITRE 4

## Mesure d'antenne en milieu échogène

Le but de ce chapitre est de présenter les travaux réalisés dans le but de réduire les temps de mesure de diagramme de rayonnement d'antenne. Les protocoles de mesure proposés vont à l'encontre des principes classiques de ce type de mesures qui bannissent les échos. Ceux-ci sont vus comme des signaux intempestifs.

L'idée proposée consiste ici au contraire à utiliser l'information portée par les échos dans un milieu maîtrisé afin de pouvoir accélérer les mesures. Le travail a été proposé dans le cadre d'une thèse menée et soutenue par Mouad Djedidi en octobre 2016.

Le travail de thèse est parti d'une modélisation champ lointain avec une structure permettant l'exploitation d'échos. Le travail proposé a évolué et peut être subdivisé en trois étapes : la pertinence du modèle proposé par rapport aux distances mises en jeu dans un set-up de mesures, la manière d'appréhender la technique d'inversion du problème par rapport aux incertitudes de mesure, les configurations mettant en jeu plus d'un écho.

### I Modélisation du problème dans le cas monoécho

Dans les représentations que l'on propose, on adopte une approche d'optique géométrique où les ondes sont « vues » comme des rayons. On suppose donc que les dispositifs mis en jeu ont des dimensions grandes devant la longueur d'onde du signal émis. Le but est de pouvoir mesurer le diagramme de rayonnement, noté  $F_\Phi$  associé à une antenne. Le principe de la mesure proposée repose sur le fait de maîtriser l'environnement de mesure afin de générer des échos contrôlés. Le set-up de base consiste à placer une plaque réfléchissante (infiniment conductrice) sur un des côtés de l'antenne à caractériser. Dans un premier temps, on considère le cas d'école d'une plaque infinie. Deux scénarios ont été considérés : le cas d'une polarisation parallèle à la plaque (cas d'une polarisation  $TM$ ) et le cas d'une polarisation inscrite dans le plan perpendiculaire à la plaque (cas d'une polarisation  $TE$ ).

On a limité l'étude aux cas des antennes à polarisation linéaire. Les antennes sous test (AST) considérées sont une antenne biconique et un dipole demi longueur d'onde dont on donne les représentations, le paramètre  $S_{11}$  et les bandes de fonctionnement Fig. 4.1. En outre dans le cadre de cette section, une hypothèse de simple plaque a été utilisée, mettant en jeu comme précisé ci-après un écho utile à la mesure du diagramme de rayonnement.

L'exemple du cas  $TM$  est représenté Fig. 4.2. On y voit la sonde de mesure représentée par le carré bleu. On constate que le trajet direct entre l'AST et la sonde, caractérisé par une distance  $r_0$ , permet d'échantillonner la valeur de  $F_\Phi$  pour un angle donné  $\Phi_0$  et que l'écho (parcourant une distance  $r_1$ ) dû à la plaque réfléchissante permet d'échantillonner une autre

#### 4 Mesure d'antenne en milieu échogène

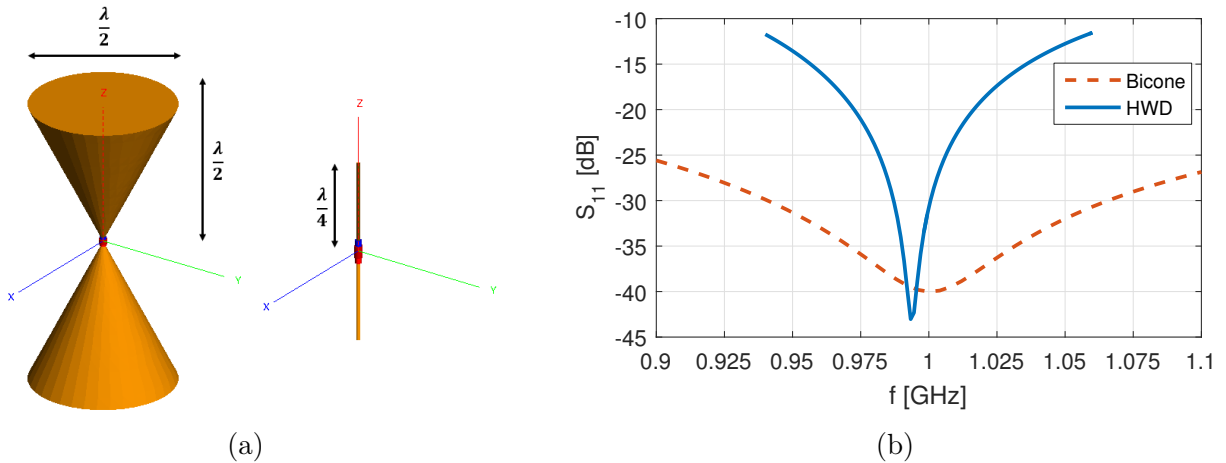


FIGURE 4.1 – Antennes utilisés pour l’analyse du concept proposé : (a) dimensions des AST  
(b) Coefficients de réflexion  $S_{11}$  correspondants et bandes de fonctionnement.

valeur de  $F_\Phi$  pour un angle distinct  $\Phi_1$ . L’hypothèse d’un plan infini permet de remplacer l’effet de la plaque réfléchissante par le placement d’une image comme représentée sur la partie droite de la Fig. 4.2. Les conditions limites sur la plaque amènent la source image à une polarisation inverse ; le diagramme  $F_\Phi$  est donc également inversé, l’inversion étant repérable par le petit ergo sur la Fig. 4.2. La distance séparant l’image de la sonde est notée  $r_1$ .

En supposant la fonction de Green en champ lointain, le set-up de mesure de la Fig. 4.2 (cas  $TM$ ) peut se résumer sous la forme matricielle suivante :

$$\begin{bmatrix} E_z(f_0) \\ E_z(f_1) \end{bmatrix} = \begin{bmatrix} -\frac{1}{r_0} e^{-j\frac{2\pi}{c} f_0 r_0} & \frac{1}{r_1} e^{-j\frac{2\pi}{c} f_0 r_1} \\ -\frac{1}{r_0} e^{-j\frac{2\pi}{c} f_1 r_0} & \frac{1}{r_1} e^{-j\frac{2\pi}{c} f_1 r_1} \end{bmatrix} \begin{bmatrix} F_\Phi(\phi_0) \\ F_\Phi(\phi_1) \end{bmatrix}, \quad (4.1)$$

ou en forme plus compacte,

$$\mathbf{E}_z = \mathbf{G}_{TM} \mathbf{F}_\Phi. \quad (4.2)$$

Comme on le constate, l’équilibrage du système algébrique nécessite d’avoir recours à deux fréquences  $\{f_0, f_1\}$  pour lesquelles le diagramme de rayonnement est supposé inchangé. Nous reviendrons sur ce point plus loin.

Le cas  $TE$  quant à lui ne nécessite pas de diversité fréquentielle dans sa version basique - on peut en effet montrer que cela revient à poser le système suivant :

$$\begin{bmatrix} E_x \\ E_y \end{bmatrix} = \begin{bmatrix} -\frac{1}{r_0} e^{-jk r_0} \sin \phi_0 & -\frac{1}{r_1} e^{-jk r_1} \sin \phi_1 \\ \frac{1}{r_0} e^{-jk r_0} \cos \phi_0 & -\frac{1}{r_1} e^{-jk r_1} \cos \phi_1 \end{bmatrix} \begin{bmatrix} F_\phi(\phi_0) \\ F_\phi(\phi_1) \end{bmatrix}, \quad (4.3)$$

soit,

$$\mathbf{E}_{xy} = \mathbf{G}_{TE} \mathbf{F}_\Phi. \quad (4.4)$$

Quel que soit le cas de polarisation considéré, le but est d’inverser les matrices de Green ( $\mathbf{G}_{TE}$  et  $\mathbf{G}_{TM}$ ) pour récupérer les diagrammes de rayonnement. Toutefois, avant de s’intéresser à la manière de procéder à l’inversion du problème, il est utile de souligner que la modélisation adoptée comporte des hypothèses dont il convient de vérifier le degré de justification.

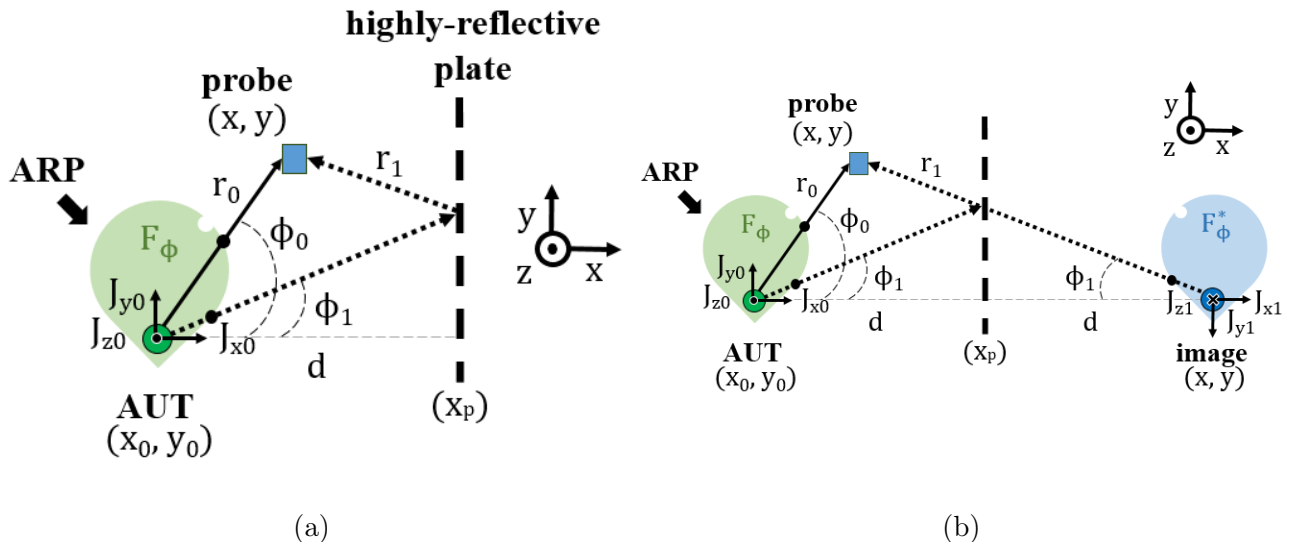


FIGURE 4.2 – Principe de la mesure exploitant les échos. (a) La sonde est placée à une distance  $r_0$  de l'AST et l'écho parcourt une distance  $r_1$ . (b) Schéma équivalent utilisant le principe des images mettant en évidence la mesure de deux points du diagramme en une mesure.

## II Pertinence du modèle proposé

La modélisation utilisée dans (4.2) et (4.4) suppose que la mesure effectuée est à champ lointain et que le champ résulte de deux sources émettant en espace libre. Dans cette section, nous allons aborder la pertinence des hypothèses soutenant le modèle proposé en analysant trois aspects. Le premier aspect porte sur l'estimation de la distance minimale à partir de laquelle l'hypothèse de champ lointain et comparer la distance trouvée à la distance de Fraunhofer ; cette dernière étant une distance régulièrement prise pour délimiter le début de zone de champ lointain (**balanis1992antenna**). Les deux autres aspects portent sur les effets de la plaque. D'une part, la simple présence de la plaque amène des réflexions intempestives. D'autre part, la plaque étant de taille finie, des risques de diffraction par les bords est à étudier.

### II.1 Hypothèse de Champ lointain

Pour cette étude on résume ici les résultats de simulation obtenus à l'aide du logiciel FEKO. Les deux types d'antennes (biconique et dipole) ont été considérées. Comme précédemment les cas TM (émission symétrique) et TE ont été mis en oeuvre. L'erreur, notée  $\epsilon_{FF}$ , est ici définie comme l'écart relatif entre le modèle champ lointain (associé à la fonction de Green notée  $\mathbf{G}$ ) et le champ obtenu par simulation, tel que :

$$\epsilon_{FF} = \frac{\|\mathbf{E}_{\text{sim}} - \mathbf{GF}_{\text{sim}}\|}{\|\mathbf{GF}_{\text{sim}}\|}, \quad (4.5)$$

où  $\mathbf{E}_{\text{sim}}$  est le champ obtenu par simulation et  $\mathbf{F}_{\text{sim}}$  est le diagramme de rayonnement de l'antenne en espace libre obtenu par une simulation distincte (en espace libre).

La Fig. 4.3 met en lumière les ordres de grandeur de  $\epsilon_{FF}$  obtenus pour le cas TM en espace libre. On constate que pour une distance de  $15\lambda_0$  on atteint des atténuations de -35 à -40 dB.

#### 4 Mesure d'antenne en milieu échogène

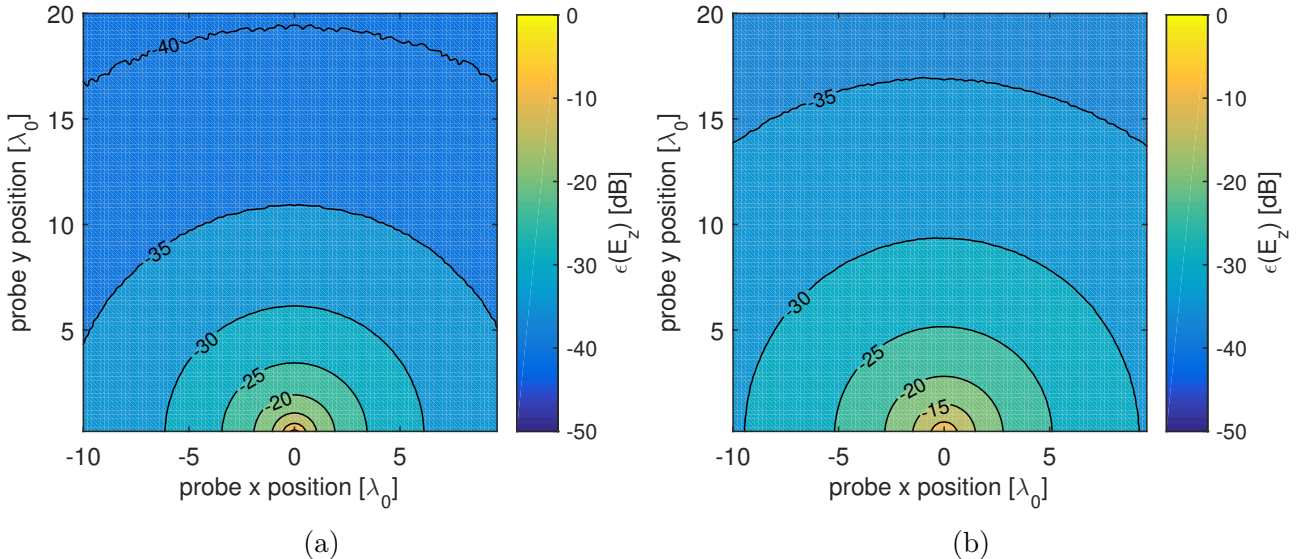


FIGURE 4.3 – Erreur  $\epsilon_{FF}$  en module (dB) pour le cas TM (isotrope) - (a) cas du dipole (b) cas de l'antenne biconique

Il est toujours difficile d'estimer si cette atténuation est en absolue « satisfaisante ». Il faudra la comparer aux autres sources d'erreur qui interviennent.

Le réflexe pour la communauté de la mesure d'antenne pourrait être de considérer la distance de Fraunhofer comme distance « seuil » pour le champ lointain. Il est intéressant de se rappeler d'où vient cette distance pour ne pas tomber dans un réflexe « recette ». La distance de Fraunhofer est une estimation de la distance à partir de laquelle le terme de phase de l'intégrale de rayonnement peut être vu comme indépendant de la distance - c'est cette hypothèse, rappelons-le, qui permet d'isoler le diagramme de rayonnement dans l'expression d'un champ lointain. En toute rigueur le terme de phase n'est pas indépendant de la distance (SELVAN et JANASWAMY 2017).

Considérons une ouverture circulaire de diamètre  $D$  et un point à une distance  $d$  pris dans la direction du maximum de rayonnement. On peut montrer qu'une erreur systématique de  $(kD^2/8.d)$  existe au premier ordre dans le terme de phase. La distance de Fraunhofer accepte une erreur de  $\pi/8$  menant à la distance typique  $d_{FF} = 2D^2/\lambda$ . Cette distance ne présuppose donc aucune atténuation spécifique. Pour les deux antennes considérées, antenne biconique et demi-longueur d'onde, on a respectivement  $d_{FF_{bicone}} = 2\lambda$  et  $d_{FF_{HWD}} = \lambda/2$ .

On reporte sur une ligne de coupe (face à l'AST) l'évolution du module de l'erreur relative<sup>1</sup> mais également l'évolution de l'erreur de phase<sup>2</sup> sur la Fig. 4.4. Pour le cas du dipole, on constate des erreurs de l'ordre de -20dB aux distances de Fraunhofer ; quant aux erreurs de phase on obtient 22° et 12° pour la HWD et la biconique respectivement ; pour obtenir une atténuation de -40 dB des distances proches de  $2\lambda_0$  et  $15\lambda_0$  doivent être considérées, soit 4  $d_{FF_{HWD}}$  et 7.5  $d_{FF_{bicone}}$  respectivement.

Nous nous sommes également intéressés au cas TE, i.e., le cas pour lequel les axes des antennes sont inscrits dans le plan perpendiculaire à la plaque supposée infinie. On s'intéresse

1.  $\epsilon_{||E_z||} = \left\| \frac{\|\mathbf{E}_{sim}\| - \|\mathbf{GF}_{sim}\|}{\|\mathbf{GF}_{sim}\|} \right\|$

2.  $\epsilon_{\angle E_z} = \angle E_z - \angle \mathbf{GF}_{sim}$

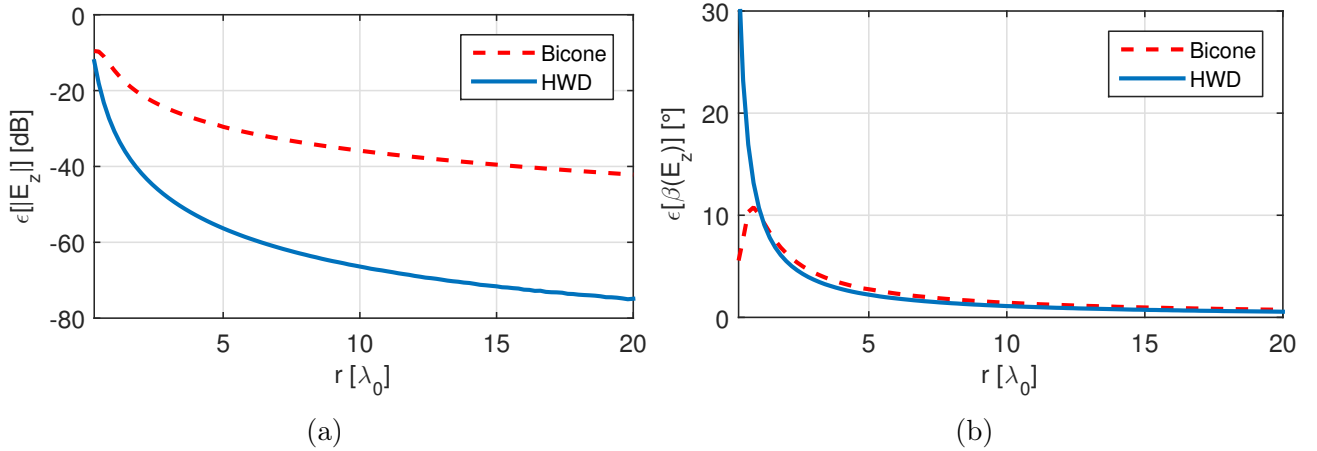


FIGURE 4.4 – Evolution des erreurs sur le module (a)  $\epsilon_{\parallel E_z \parallel}$  et la phase (b)  $\epsilon_{\angle E_z}$ , pour le cas TM isotrope.

aux coordonnées cartésiennes ( $x, y$ ) par souci de comparaison expérimentale ultérieure. La sonde électro-optique étant un dipôle linéaire, les coordonnées polaires type  $E_\theta$  sont décomposées sur les axes cartésiens. En procédant comme pour le cas de polarisation précédente, on obtient l'erreur, définie par (4.5), sur la Fig 4.5.

On constate que les niveaux d'erreur suivent une topographie anisotrope à l'image du diagramme de rayonnement. A ce stade il est difficile d'évaluer le niveaux d'erreur acceptable, i.e., de savoir à quel degré d'inexactitude on peut espérer une approximation permettant une inversion satisfaisante du problème. L'inversion du problème inclura d'autres sources d'erreur. L'idée est à ce stade de l'étude de dégrossir toutes les sources d'erreur avec un ordre de grandeur à l'appui. Une autre source d'erreur est liée à la diffraction par l'antenne.

## II.2 Diffraction de l'antenne

La présence de la plaque induit une réflexion qui se rétro-propage vers l'antenne sous test (AST). Quand cette réflexion atteint l'AST, il y a un effet de diffraction sur l'antenne. Le modèle considéré ne prend pas en compte cette contribution indésirable. Pour évaluer la contribution de cette partie diffractée, plusieurs simulations ont été menées. Deux simulations indépendantes en espace libre avec la présence de l'AST d'une part et de son image d'autre part - on obtient alors les champs notés respectivement  $\mathbf{E}_{\text{sim}}^{\text{LOS}}$  et  $\mathbf{E}_{\text{sim}}^{\text{im}}$ ; une troisième simulation incluant la présence de la plaque considérée infinie génère un champ noté  $\mathbf{E}_{\text{sim}}^{h\infty}$ . On peut alors isoler la partie diffractée, notée  $\mathbf{E}_d^{\text{AST}}$  telle que,

$$\mathbf{E}_d^{\text{AST}} = \|\mathbf{E}_{\text{sim}}^{h\infty} - \mathbf{E}_{\text{sim}}^{\text{LOS+im}}\|, \quad (4.6)$$

où  $\mathbf{E}_{\text{sim}}^{\text{LOS+im}} = \mathbf{E}_{\text{sim}}^{\text{LOS}} + \mathbf{E}_{\text{sim}}^{\text{im}}$

L'impact de l'AST est alors évalué en comparant le champ diffracté aux deux champs contrôlés  $\mathbf{E}_{\text{sim}}^{\text{LOS}}$  et  $\mathbf{E}_{\text{sim}}^{\text{im}}$  par l'intermédiaire de la variable  $\epsilon_i^d$  définie telle que,

$$\epsilon_i^d = \left\| \frac{\mathbf{E}_d^{\text{AST}}}{\mathbf{E}_i} \right\|^2, \quad i = 0, 1, \quad (4.7)$$

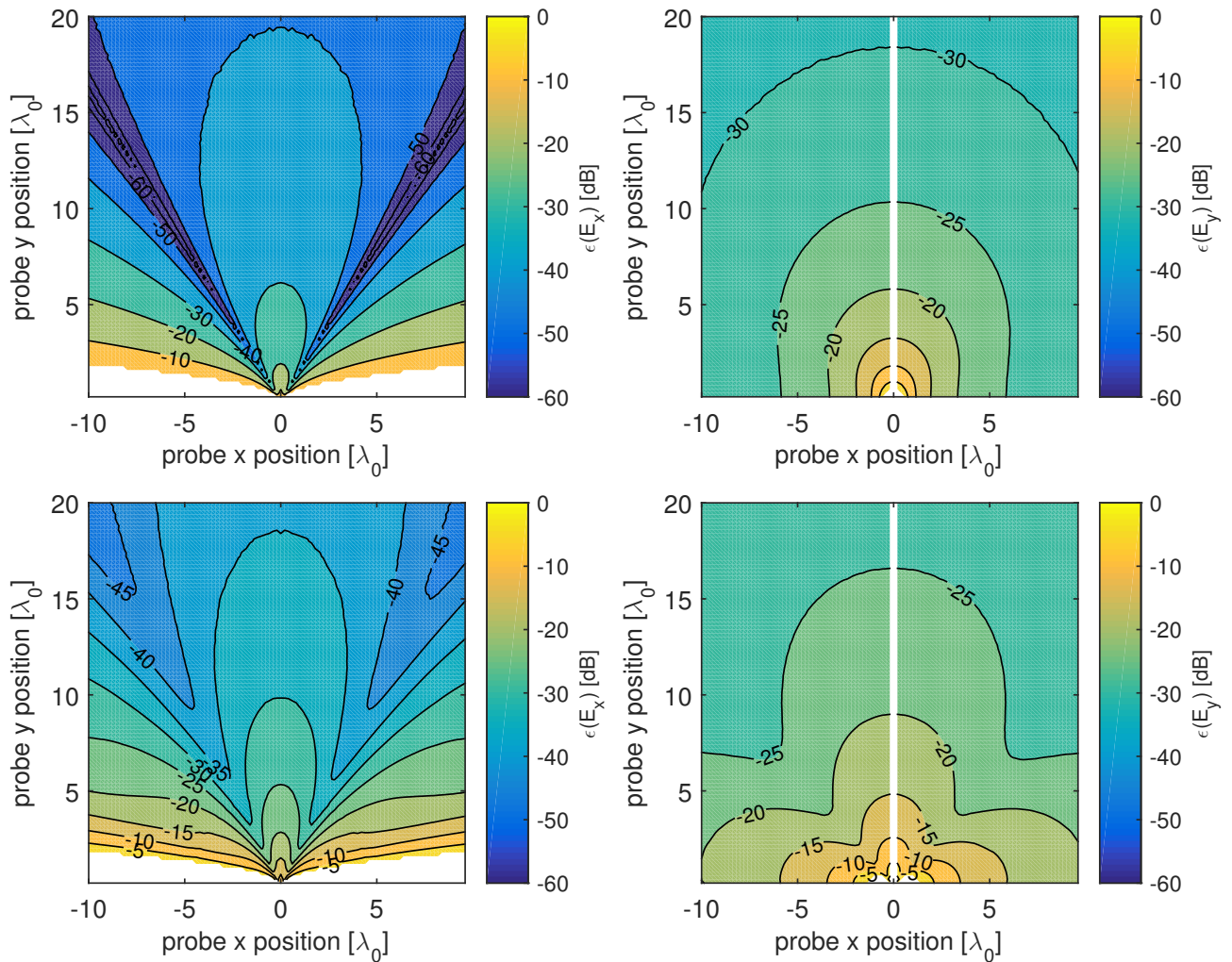


FIGURE 4.5 – Erreur obtenue en espace libre [dB] sachant l'hypothèse de champ lointain - cas TE : (a)  $\epsilon(E_x)_{\text{HWD}}$  (b)  $\epsilon(E_y)_{\text{HWD}}$  (c)  $\epsilon(E_x)_{\text{biconique}}$  (d)  $\epsilon(E_y)_{\text{biconique}}$

l'indice 0 renvoyant au cas du champ direct et l'indice 1 renvoyant au cas du champ émis par l'antenne image. La Fig. 4.6 met en évidence les rapports obtenus en dB pour les antennes étudiées dans le cas TM ; pour le cas TE les mêmes ordres de grandeur sont obtenus. En somme, on constate que les ordres de grandeur sont analogues au cas précédent, i.e., à l'erreur liée à l'hypothèse de champ lointain. En analysant de près les résultats on arrive au bilan suivant :

- L'influence de la plaque (effet ping-pong) sur le rayonnement de l'antenne en espace libre semble négligeable en première approximation sachant les dimensions de la zone de mesure.
- Comme attendu, les zones proches de l'AST montrent des niveaux élevés d'erreur sachant l'approximation champ lointain utilisée dans le modèle. Même la contribution de l'image est perturbée proche de l'AST à cause du champ diffracté, qui est alors du même ordre de grandeur.
- Le mode TE permet de voir que les directions pour lesquelles l'émission est faible (zeros de diagramme de rayonnement) sont très fortement entâchées d'erreur. Cela est dû à la superposition des composantes radiales de la partie réactive du champ ainsi qu'au champ diffracté par l'AST. On verra que l'utilisation d'une régression permet de contourner cet inconvénient.

### II.3 Plaque de dimension finie

Le modèle proposé s'appuie sur l'hypothèse d'une plaque de taille infinie. En pratique, les dimensions étant évidemment finies, un risque de diffraction par les bords a été étudié. L'idée a été de voir si les dimensions alignées sur les dimensions de la zone de test pouvaient être jugées comme suffisantes.

Pour cette étude, le dipôle a été utilisé en mode TE et TM. Une étude théorique type *GTD* (*Geometric Theory of Diffraction*) a été menée. Celle-ci prévoit un effet important de la diffraction par les bords proche de la paroi pour la partie directe ou *Line of Sight (LOS)*. On renvoie au manuscrit de thèse pour des détails<sup>3</sup>. Dans les résultats obtenus Fig. 4.8, il apparaît que la diffraction par les bords de la plaque a peu d'influence sur la partie rayonnée par l'AST (la partie *LOS*) pour laquelle l'erreur passe sous la barre des -40 dB, et ce, y compris proche de la paroi.

Par contre on constate que la diffraction par les bords a un sérieux impact sur la partie rayonnée par l'image avec des niveaux d'erreur<sup>4</sup> de l'ordre de -20 dB (voire supérieur, cf graphe en haut à droite de la Fig. 4.8) sur l'essentiel de la zone de test. Cela s'explique encore une fois par la divergence de l'onde émise par l'image qui atteint des niveaux semblables à la partie diffractée par les bords de la paroi. Il ressort de ces résultats préliminaires que même pour une plaque de dimension de 10 à 20  $\lambda_0$  l'effet de diffraction par les bords ne peut être négligé sur la partie image. On pourrait réduire la distance AST-paroi afin de réduire la distance de l'image et donc augmenter le contraste entre la partie image et la partie diffractée. Cela se ferait au profit de la partie diffractée par l'antenne, i.e., la partie diffractée par l'antenne augmente avec la réduction de la distance AST-paroi. Une approche plus efficace a consisté à modifier les bords de la plaque comme montré Fig. 4.9.

On obtient alors les résultats données Fig. 4.10. On constate une réelle amélioration dans le cas TM pour lequel l'erreur passe sous la barre des -40dB dans la majeure partie de la zone de test. Pour le cas TE les résultats sont également meilleurs que pour une plaque purement

3. p.83 du manuscrit de thèse

4. erreur définie de manière analogue à la relation (4.7) où  $\mathbf{E}_d^{AST}$  est remplacé par  $\mathbf{E}_d^{paroi}$ .

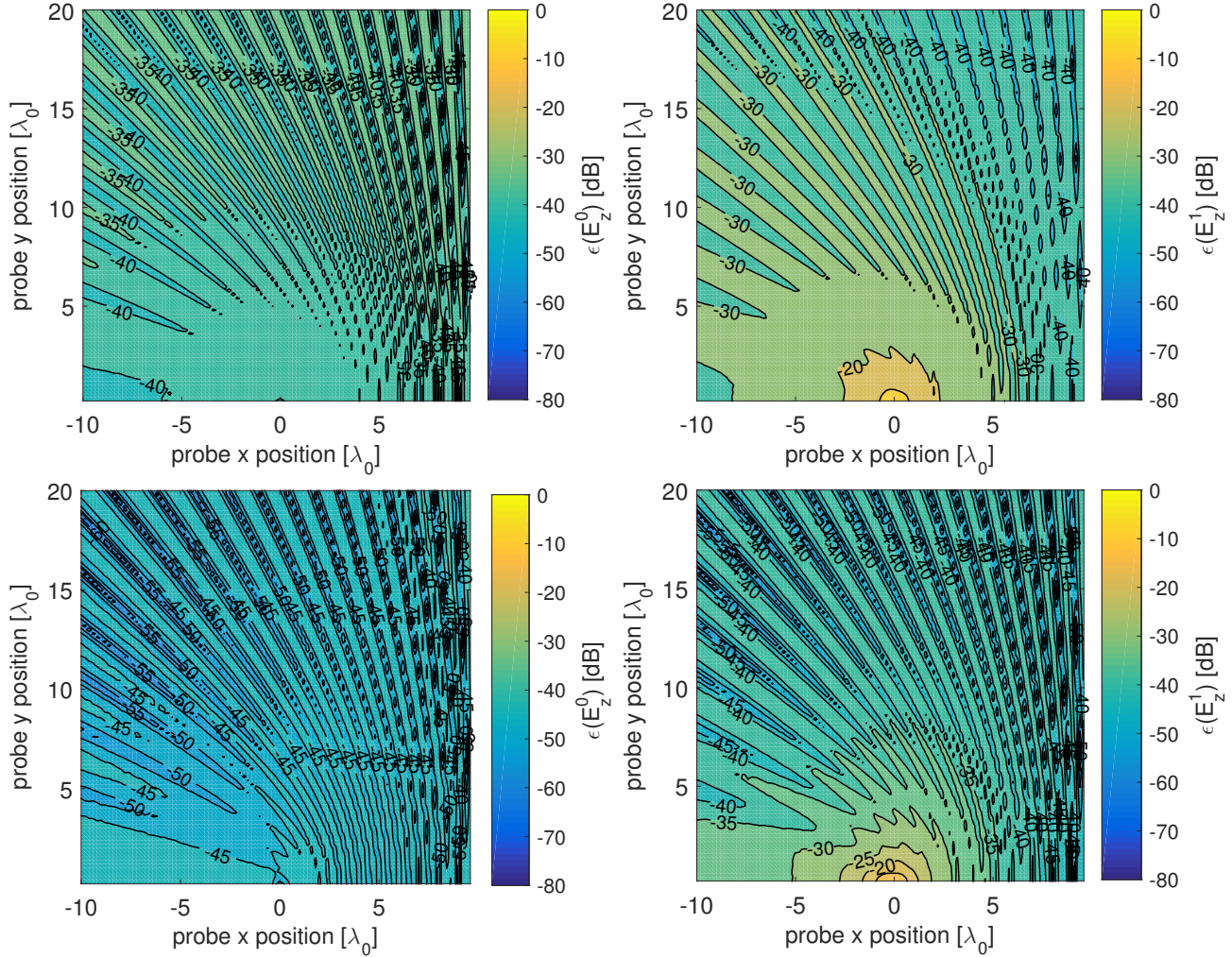


FIGURE 4.6 – Cartographie de l'erreur liée au champ diffracté par l'antenne sous test en mode TM ; plaque en  $x_p = 10\lambda_0$  : (a)  $\epsilon_0^d$ , (dipôle) (b)  $\epsilon_1^d$  (dipôle) (c)  $\epsilon_0^d$  (biconique) (d)  $\epsilon_1^d$  (biconique).

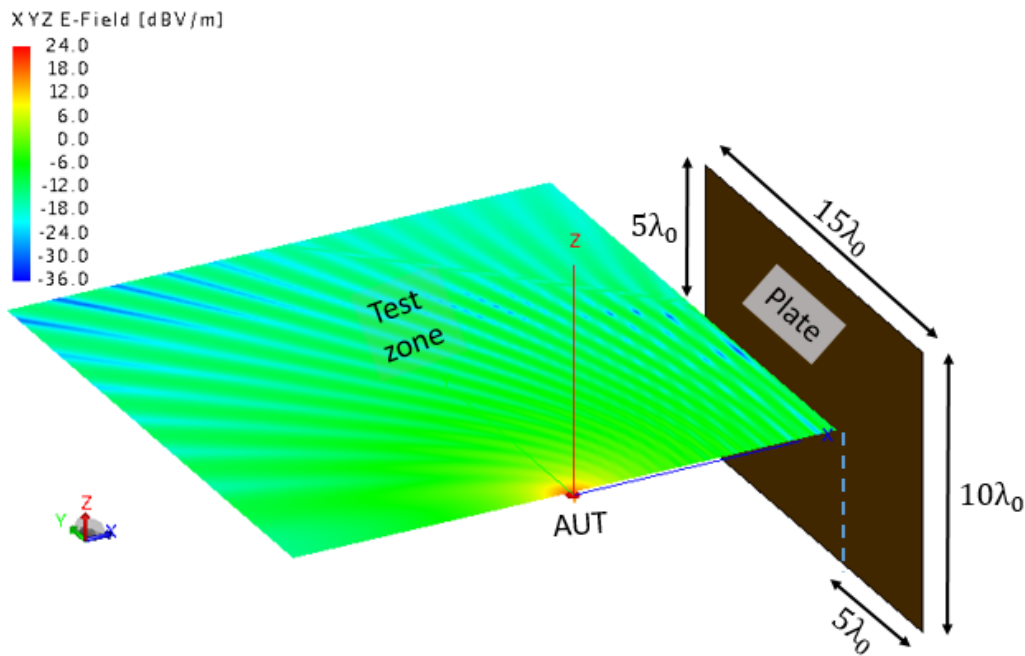


FIGURE 4.7 – Configuration considérée sachant une plaque de dimension finie afin d'en évaluer l'effet de diffraction par les bords.

rectangulaire ; en revanche la réduction des niveaux d'erreur est moins importante que pour le cas TM. Cela a nécessité de se pencher sur une méthode d'inversion suffisamment robuste et/ou d'utiliser d'autres degrés de liberté telle que la diversité fréquentielle pour cette polarisation. Ces points sont abordés un peu plus loin dans ce chapitre.

### III Inversion du problème

Ayant en main les ordres de grandeur des différences sources de perturbation par rapport au modèle champ lointain adopté, il convient de résoudre le système décrit par (4.2) et (4.4). Une première approche a consisté à s'intéresser au nombre de conditionnement<sup>5</sup> des matrices mises en jeu. Plusieurs idées ont été testées afin de d'améliorer le conditionnement des matrices de Green. Cette étude a permis de mettre en lumière des zones optimales pour le placement de la sonde de mesure. Une part importante de la thèse a porté sur cette partie.

#### III.1 Nombre de conditionnement dans l'approche classique

Comme présenté jusqu'ici on s'intéresse à deux types de polarisations (TM, TE) sachant que ces deux cas représentent la décomposition qui devra être prise en compte pour un cas 3D<sup>6</sup>.

Une partie du travail a consisté à pouvoir déterminer de manière analytique des lieux géométriques permettant d'assurer un nombre de conditionnement minimal afin de ne pas amplifier les erreurs et les incertitudes lors de l'inversion directe du problème. Pour rappel, le nombre de conditionnement, noté ici  $\kappa$ , est optimal s'il vaut 1 ; plus  $\kappa$  est grand plus les incertitudes et les erreurs risquent d'affecter le résultat issu de l'inversion.

5. dont nous rappelons l'intérêt peu après

6. Ce cas n'ayant pas été approfondi dans le cadre de la thèse encadrée

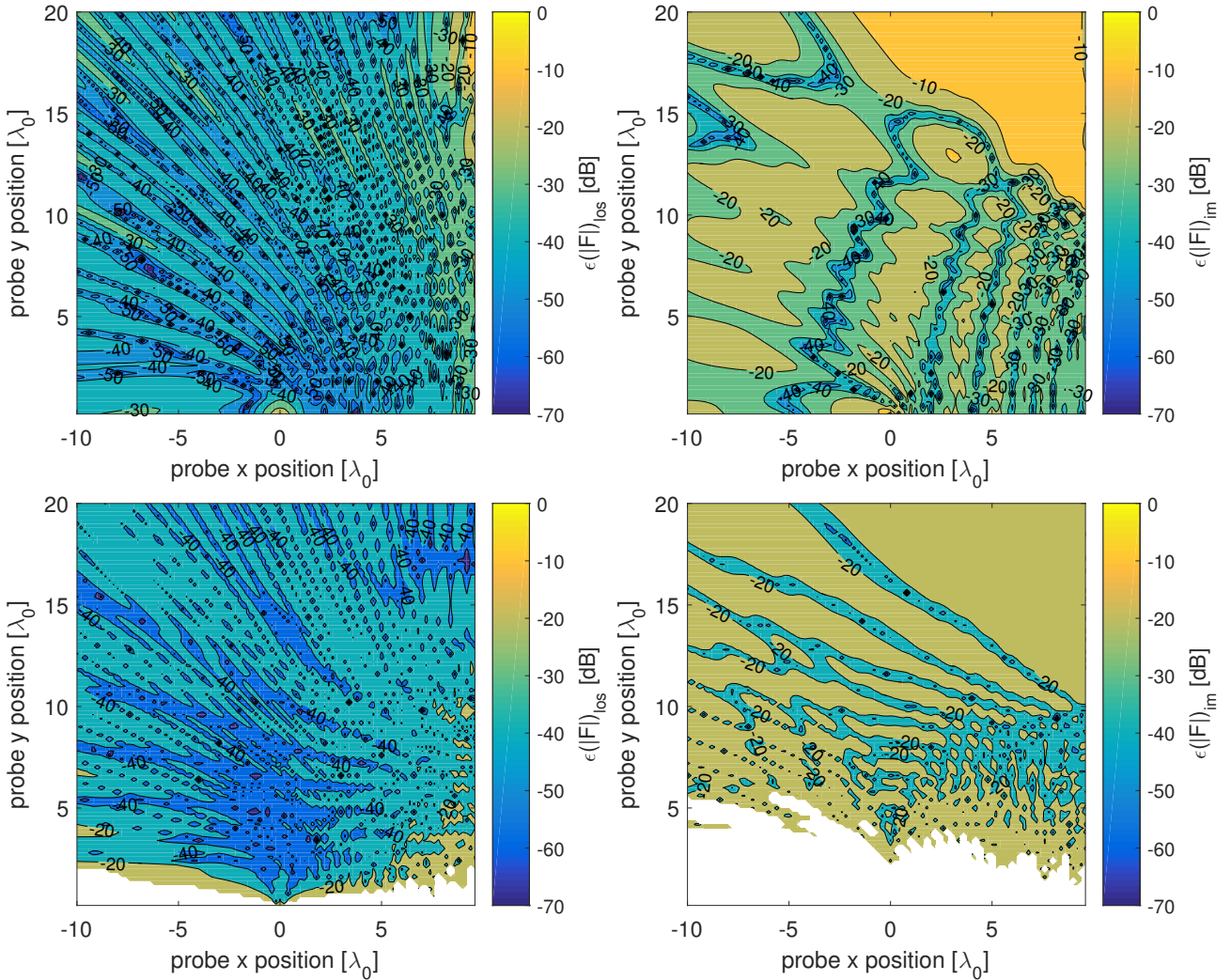


FIGURE 4.8 – Erreur obtenue sur le diagramme de rayonnement de l'antenne dipôle en fonction de la position de la sonde et impact des champs diffractés par les bords et les angles de coin. La plaque est tronquée en  $h_y = [-5\lambda_0, 10\lambda_0]$  et  $h_z = \pm 5\lambda_0$  et positionnée en  $x_p = 10\lambda_0$  (a) erreur sur l'amplitude de la partie directe (TM), UFBW = 4% (b) erreur sur l'amplitude UFBW = 4% (c) TE LOS amplitude error, basic model (d) TE image amplitude error, basic model.

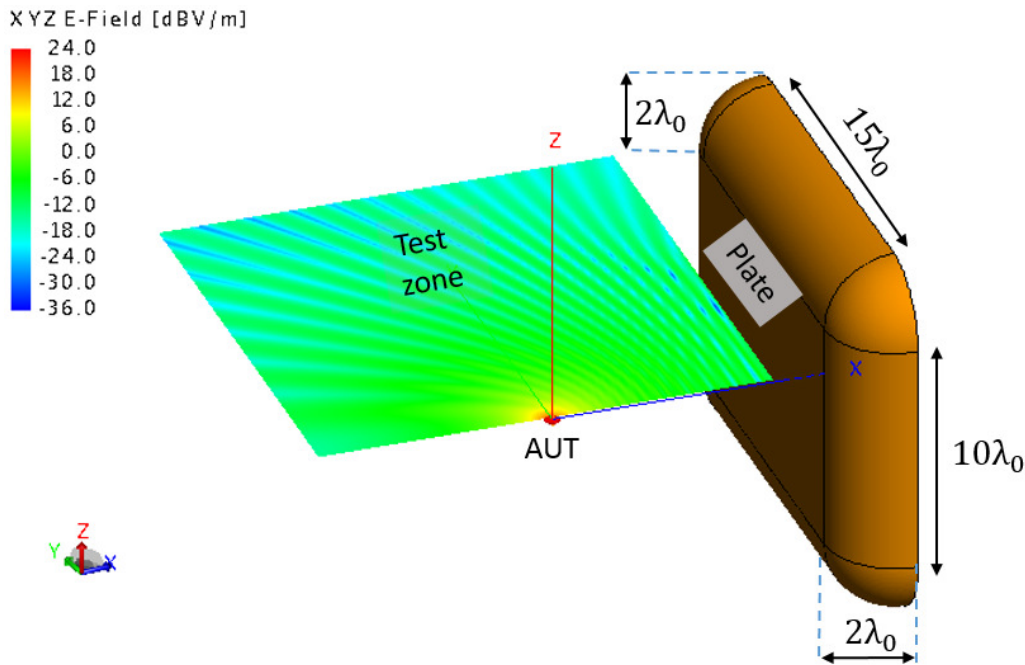


FIGURE 4.9 – Bords de la plaque arrondis afin de réduire la diffraction par les arêtes de la plaque.

Dans l'étude du cas TM il est ressorti que les intersections d'une hyperbole et d'un cercle d'Appolonius définissent les zones optimales. Ces lieux ont été mis en évidence par une approche où la corrélation, notée  $\rho$ , entre lignes de la matrice a été déterminée analytiquement à défaut de pouvoir le faire directement avec  $\kappa$  (DJEDIDI 2016). Dans le cas TE les lieux sont des cercles. On rappelle que le cas TM nécessite une diversité fréquentielle, i.e., une bande de fréquence  $\Delta f$  de travail, contrairement au cas TE.

La Fig. 4.11 met en évidence les zones optimales pour les deux cas de polarisation considérées. On constate comme montré Fig. 4.11a que les zones loin de la plaque (i.e. placée en  $x_p = 10\lambda_0$ ) sont à privilégier dans le cas TM. On constate également que le  $\kappa$  est minimal le long des intersections entre les lieux précités précédemment. Avec l'utilisation d'une bande relative plus large, on a alors un jeu d'hyperboles et plusieurs zones optimales apparaissent comme le montre la Fig. 4.11b ; les largeurs de ces zones dépendent de la bande utilisée. Pour le cas TE en revanche, on constate que la zone à privilégier se situe près de la plaque (cf. Fig. 4.11c). L'utilisation de la diversité fréquentielle pour ce cas là permet d'étendre les zones de bons conditionnements, donnant ainsi un plus grand degré de liberté quant au positionnement de la sonde de mesure (Fig. 4.11d).

Comme nous le verrons dans ce qui suit, la méthode d'inversion directe montre rapidement ses limites dans la mesure où chaque point est vu comme indépendant, permettant ainsi au diagramme obtenu d'avoir des discontinuités ou des sauts brusques. Pour éviter ce travers, une inversion par régression procure une robustesse bien adaptée au problème posé.

### III.2 Approche par Régresseurs

La régression linéaire est une technique de modélisation utilisée généralement pour fitter un modèle à des observables. La méthode de loin la plus utilisée est la fameuse régression par moindres carrés (*Least Mean Square* (LS)) (LAWSON et HANSON 1995)). Cette approche

#### 4 Mesure d'antenne en milieu échogène

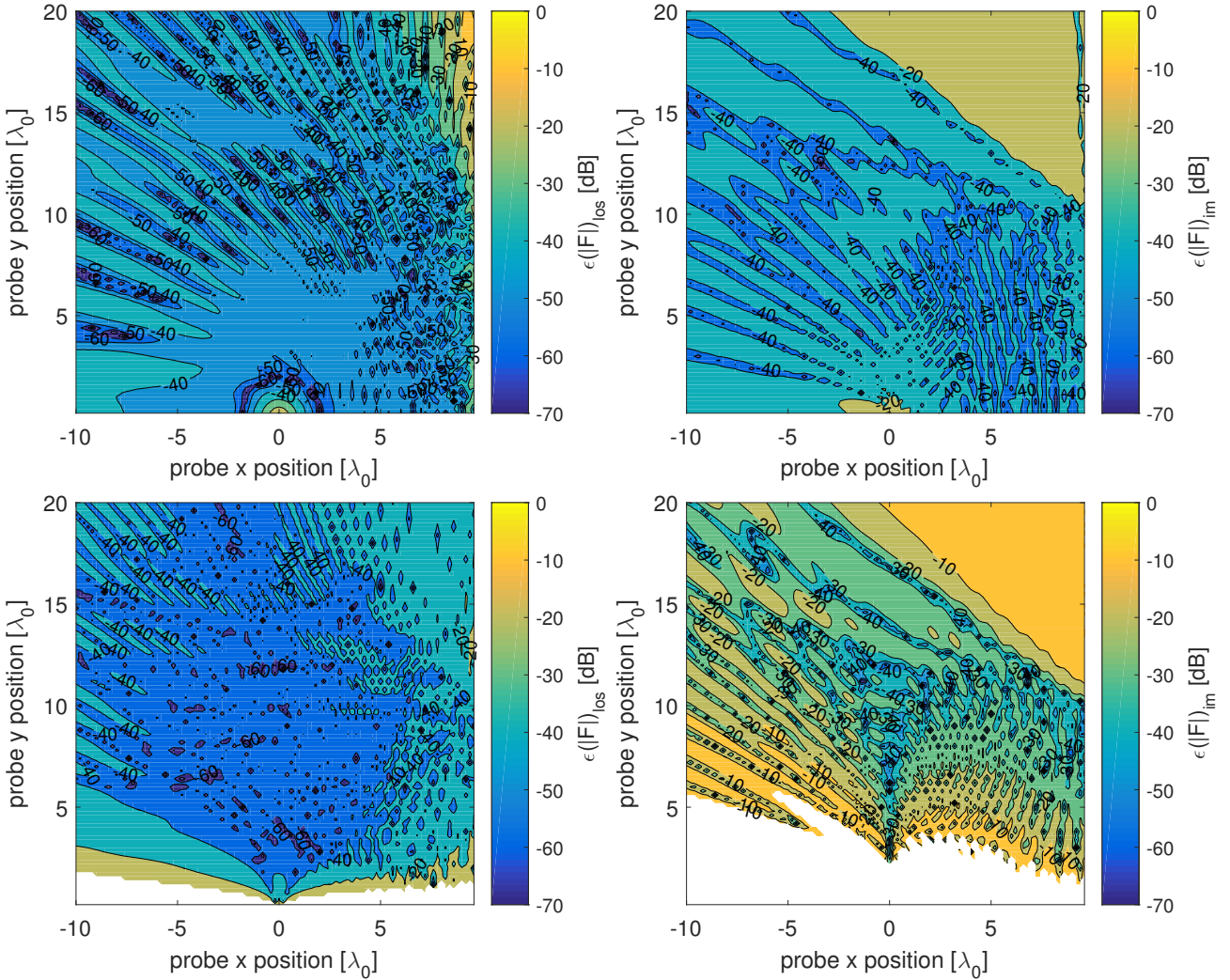


FIGURE 4.10 – Exemple de réduction du problème de diffraction par les bords en utilisant des bords recourbés. La partie plate de la plaque a les dimensions suivantes :  $h_y = [-5\lambda_0, 10\lambda_0]$  and  $h_z = \pm 5\lambda_0$ .  $x_p = 10\lambda_0$ . HWD. (a) Erreur sur l'amplitude de la partie LOS (TM, UFBW = 4%) (b) Amplitude de l'erreur de la partie image (TM, UFBW = 4%) (c) Amplitude de l'erreur de la partie LOS (TE) avec le modèle de base (d) erreur sur la partie image (TE) avec le modèle de base.

est d'autant plus adaptée que le nombre d'échantillons de mesure est important. Sachant  $N_m$  positions de mesure, on décompose le diagramme sur une base de  $N_r$  fonctions de régression ; la somme étant pondérée par une matrice  $\beta$ , telle que les expressions (4.2) et (4.4) prennent alors la forme suivante :

$$\mathbf{E} = \mathbf{GR}\boldsymbol{\gamma}, \quad (4.8)$$

où  $\mathbf{G}$  est la matrice de *Green* qui coïncide avec  $\mathbf{G}_{TE}$  ou  $\mathbf{G}_{TM}$  suivant le cas étudié ;  $\mathbf{R}$  est une matrice  $2N_m \times N_r$  et  $\boldsymbol{\gamma}$  un vecteur de pondération des fonctions de régression de dimension  $N_r$ .

Dans cette approche il convient d'avoir un nombre  $2N_m$  total d'angles différents bien supérieur au nombre  $N_r$  de fonctions de régression. Les poids  $\boldsymbol{\gamma}$  deviennent désormais les inconnues qui se déterminent par minimisation ; on a donc des estimations  $\hat{\boldsymbol{\gamma}}$  de ces poids au sens des moindres

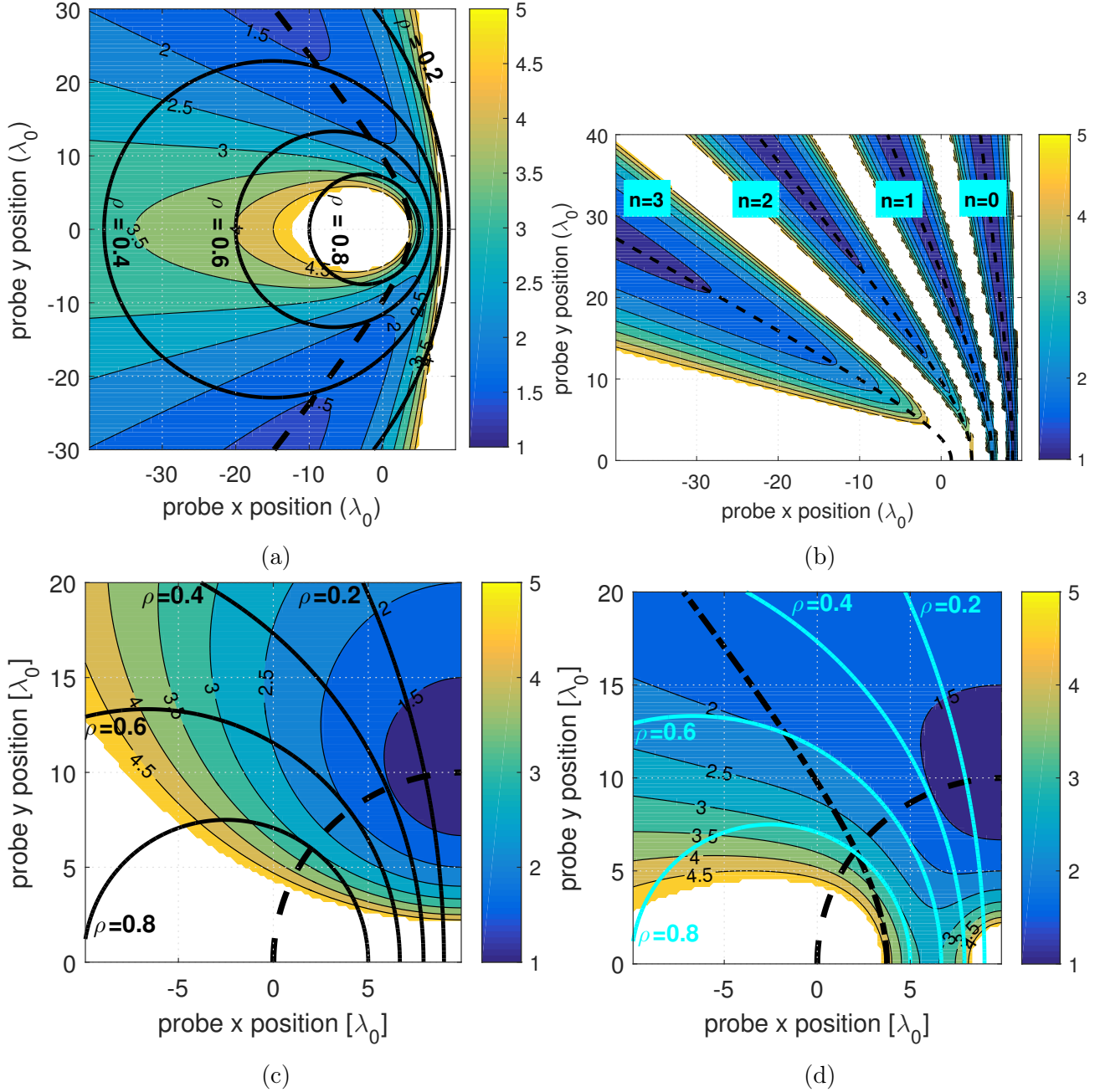


FIGURE 4.11 – Relation entre le facteur de projection  $\rho$  et le nombre de conditionnement  $\kappa(\mathbf{G}_{TM})$ . Mise en évidence des positions optimales montrant l’intérêt des hyperboles optimales (tirets) et des cercles de conditionnement (trait plein). La plaque se situe en  $x_p = 10\lambda_0$  et une bande relative  $\Delta f_b$  de 4% est utilisée : (a)  $\kappa(\mathbf{G}_{TM})$ ; (b)  $\Delta f_b = 20\%$ ,  $\kappa(\mathbf{G}_{TM})$ ; (c)  $\kappa(\mathbf{G}_{TE})$ ; (d)  $\kappa(\mathbf{G}_{TE})$  avec diversité fréquentielle (bande de 4%).

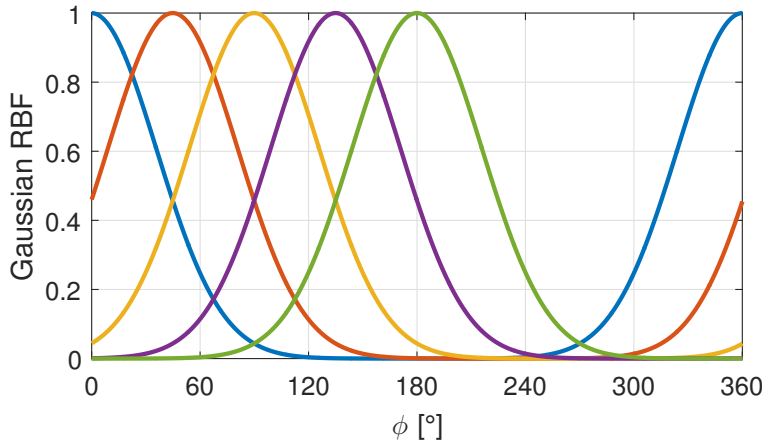


FIGURE 4.12 – Fonctions *RBF* définies sur un intervalle angulaire de  $180^\circ$ ,  $N_r = 5$ ,  $s = 36^\circ$ .

carrés telles que,

$$\hat{\gamma} = \text{Arg min} \|\mathbf{GR}\gamma - \mathbf{E}\|^2. \quad (4.9)$$

Plusieurs fonctions de régression ont été testées. Dans le cadre des antennes mises en oeuvre, les fonctions de type Gaussiennes (*Gaussian Radial Basis Functions* ou *RBF*), notées  $R_n(\phi)$ , ont été retenues et sont définies telles que,

$$R_n(\phi) = e^{-\frac{(\phi-\phi_n)^2}{2s^2}}, \quad (4.10)$$

où  $\phi_n$  correspond aux angles sur lesquels les *RBF* sont centrées ; la largeur à mi-hauteur de chacune des fonctions est fixée à  $2,355s$ . La Fig. 4.12 donne une représentation de ces fonctions pour  $N_r = 5$  et  $s = 36^\circ$ . Pour que la régression soit efficace il convient d'avoir un certain recouvrement entre les fonctions.

Une comparaison des résultats obtenus avec une inversion directe et une inversion par régression est illustrée Fig. 4.13. Nous avons considéré le cas de l'antenne dipole en polarisation TE. Pour émuler le bruit expérimental que 'on aurait en pratique, nous avons superposé *a posteriori* un bruit blanc aux données de simulation avec un *SNR* de 20 dB. Deux fréquences formant une bande relative de 4% et 10 points de mesure ont été utilisés, soit 20 angles au total. On observe Fig. 4.13a que la régression avec un jeu de 90 fonctions très étroites ( $s = 1^\circ$ ) n'a aucun intérêt par rapport à une inversion classique car chaque point est associé à une fonction et non à une combinaison linéaire de celles-ci. La Fig. 4.13b montre une amélioration par rapport à l'inversion directe avec un jeu de 10 fonctions. Toutefois sachant la largeur à mi-hauteur de chacune d'elle, on se retrouve à utiliser plus de fonctions que nécessaire sachant le diagramme de rayonnement à reproduire et l'inversion n'est alors pas optimale. Si l'on tombe dans l'autre extrême, à savoir prendre peu de fonctions on obtient le résultat de la Fig. 4.13c pour laquelle on a un jeu de trois fonctions - pour ce cas, le centre du diagramme est bien reconstruit pour peu qu'une des fonctions soit centrée sur le lobe principal ; les extrémités quant à elles sont mal reconstruites. Le compromis est trouvé Fig. 4.13d où, avec un jeu de 5 fonctions qui se recouvrent, on parvient à reconstruire le diagramme malgré le bruit. L'inversion du problème, on le rappelle, permet de retrouver les poids  $\hat{\gamma}$  pour retrouver le diagramme de rayonnement  $F_\phi$ .

On constate la robustesse de la technique par régression, notamment vis-à-vis du bruit, par rapport à l'inversion directe. Il est à souligner que le vecteur de bruit diffère d'une simulation

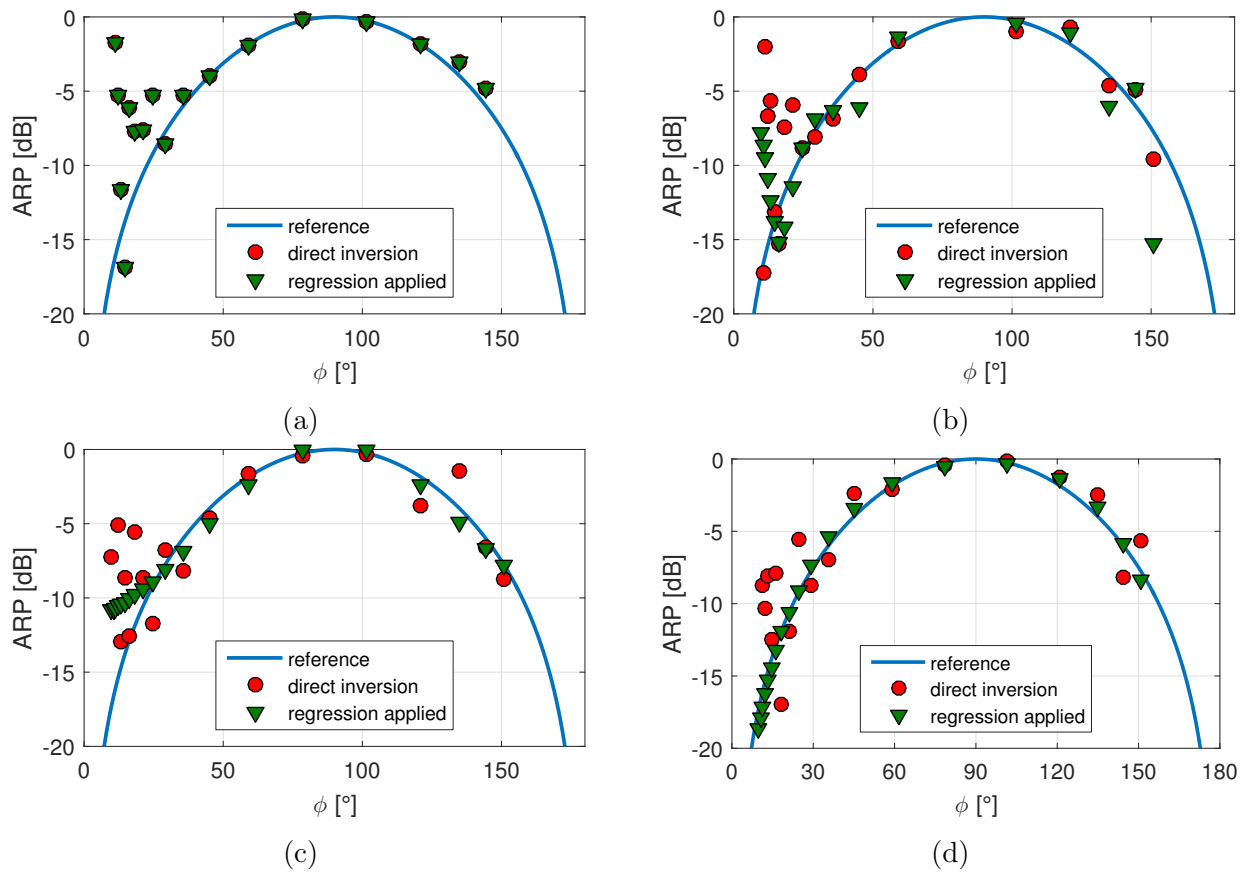


FIGURE 4.13 – Illustration de l'inversion par régression dans le cas du dipôle (cas TE) avec 10 points de mesure (soit 20 angles)  $(x, y) = (-9\lambda_0 : 2\lambda_0 : 9\lambda_0, 5\lambda_0)$ ,  $d = 10\lambda_0$ . Bruitage des données avec bruit blanc (SNR = 20dB).  $\Delta f = 4\%$  : (a) RBF regression,  $N_r = 90$ ,  $s = 1^\circ$ , (b) RBF regression,  $N_r = 10$ ,  $s = 36^\circ$ , (c) RBF regression,  $N_r = 3$ ,  $s = 36^\circ$ , (d) RBF regression,  $N_r = 5$ ,  $s = 36^\circ$

à l'autre ce qui explique que les résultats de l'inversion directe mène à des résultats qui diffère d'un graphe à l'autre.

L'utilisation de la régression a été étendue à l'étude de l'impact de la dépendance en fréquence du diagramme de rayonnement. Pour le cas TM pour lequel une diversité en fréquence est nécessaire pour équilibrer le système d'équations, l'hypothèse sous-jacente a été de regarder le diagramme de rayonnement comme une donnée indépendante de la fréquence. Même si dans certains cas cette hypothèse peut être justifiée, elle atteint rapidement des limites. On modifie alors le modèle proposé de la manière suivante,

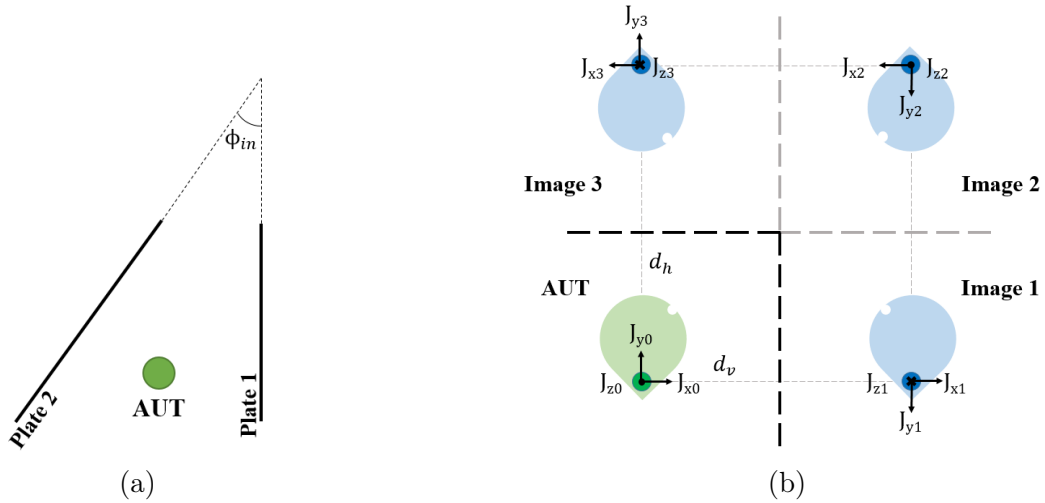


FIGURE 4.14 – Extension du cas simple plaque aux configurations permettant du multi-échos ;  
 (a) Configuration diédrale d'angle  $\phi_{in}$  (b) Configuration diédrale, avec  $\phi_{in} = 90^\circ$

$$\mathbf{E} = \boldsymbol{\alpha} \mathbf{G} \mathbf{F}, \quad (4.11)$$

$$\text{où } \boldsymbol{\alpha}_{TM} = \begin{bmatrix} 1 & 0 \\ 0 & \alpha \end{bmatrix}, \quad (4.12)$$

$$\text{et } \boldsymbol{\alpha}_{TE} = \left[ \begin{array}{c|c} \boldsymbol{\alpha}_{TM} & 0 \\ \hline \cdots & \cdots \\ 0 & \boldsymbol{\alpha}_{TM} \end{array} \right], \quad (4.13)$$

où  $\boldsymbol{\alpha}$  rend compte des variations éventuelles du diagramme à la deuxième fréquence choisie, et ce, en phase et en amplitude. Le problème de régression se transforme en un problème de minimisation non-linéaire d'une fonction coût avec deux grandeurs à estimer telles que (TORN et ZILINSKAS 1989),

$$(\hat{\boldsymbol{\beta}}, \hat{\boldsymbol{\alpha}}) = \text{Arg min} \|\boldsymbol{\alpha} \mathbf{G} \mathbf{R} \boldsymbol{\beta} - \mathbf{E}\|^2. \quad (4.14)$$

L'étude de cette partie en est restée à ses balbutiements car elle correspondait à la fin de la thèse et fait partie des points proposés dans la suite de ces travaux.

Tout ce qui a été présenté jusqu'ici avait comme *set-up* de mesure le cas de la simple plaque. En réalité dès le début de la thèse (DJEDIDI, MONSEF et al. 2014) l'idée était d'utiliser plusieurs échos. Dans ce qui suit nous allons présenter une synthèse des configurations étudiées.

## IV Configurations multi-échos

Les structures considérées permettent de générer plusieurs échos. Durant la thèse, deux types de configurations ont été étudiées : le dièdre et le cas de plaques parallèles.

## IV.1 Structures Diédrales

L'idée est ici de créer des sources images en nombre fini, afin de bénéficier de l'information portée par chacun des échos associé aux images. La structure diédrale consiste à prendre deux plaques formant un angle donné comme montré Fig. 4.14a. On s'est limité au cas d'un angle de  $90^\circ$  comme montré Fig. 4.14b où la source réelle est placée respectivement à une distance  $d_h$  et  $d_v$  des parois horizontale et verticale.

Comme dans les cas précédents, les études ont porté sur les cas TM et TE. Pour le cas TM, l'équilibre du système algébrique nécessite le recours à quatre fréquences de par la présence de quatre sources (1 réelle+3 images) ; le cas TE permet lui de n'utiliser que deux fréquences pour quatre sources.

L'analyse a porté sur l'étude des zones optimales au sens du conditionnement des matrices, dans le cas d'inversion directe. Il en est ressorti que la configuration diédrale à angle droit offre la possibilité d'atteindre des systèmes bien conditionnés utilisant des dimensions d'environnement de mesure de l'ordre de  $30\lambda_0$  et des bandes de fréquences de l'ordre de 6%. L'obtention de systèmes bien conditionnés est plus aisée dans le cas TE et met en jeu des bandes de fréquences plus étroites de par la sur-détermination permise par l'utilisation de deux coordonnées cartésiennes. Dans l'étude menée, on a envisagé d'avoir recours à un système de rotation qui permettrait de réduire d'un facteur 4 les temps de mesures classiques. Comme dans les cas précédents, la régression s'est montrée efficace dans sa capacité à réduire les erreurs sur le diagramme de rayonnement dans une fourchette de +/- 1 dB. Les erreurs sont essentiellement dues à l'hypothèse de champ lointain ainsi qu'à la diffraction sur l'antenne sous test.

## IV.2 Cas des plaques parallèles

Le cas des plaques parallèles est original car il introduit un nombre infini d'images. Afin de formaliser le problème, une troncature du nombre d'images est indispensable. Le problème dans ce genre de procédure est de définir un critère suffisamment pertinent pour ne pas perdre de l'information.

Ce cas est finalement le plus compliqué et paradoxalement, il a éveillé notre intérêt dès le démarrage de la thèse (DJEDIDI, MONSEF et al. 2014). Il ressort de cette étude que plus le nombre d'images est important, plus le nombre d'angles accessibles l'est aussi. Toutefois plus une image est lointaine, plus l'intensité de son champ rayonné devient faible devant les autres contributions ; les contributions seront donc d'autant plus faibles qu'une image est loin de la sonde de mesure, d'où l'intérêt de la troncature.

Au niveau mathématique, il ressort que plus le nombre d'images est important plus le conditionnement se dégrade et nécessite, d'une part, de plus grandes dimensions d'environnement de mesure, et d'autre part, de plus grandes bandes de fréquences utiles à la diversité fréquentielle. En outre, bien qu'il soit difficile de mettre en équation la capacité à réduire l'effort mécanique de mesure par rapport aux méthodes classiques, certains scénarios de test ont mis en évidence une capacité de scan azimuthal complet avec un pas angulaire de  $8^\circ$ , et ce, avec huit points de mesures.

Le grand nombre d'images implique un nombre important d'angles balayés. Cela est propice à l'utilisation de la régression. L'utilisation de cette technique a ainsi permis de passer à des erreurs de  $\pm 30$  dB par inversion directe à des niveaux d'erreur de l'ordre de  $\pm 1$  dB.

On renvoie au manuscrit de thèse<sup>7</sup> pour les détails des résultats qui ont essentiellement portés

---

7. Sec. 5.4 de la thèse de Mouad Djedidi

#### *4 Mesure d'antenne en milieu échogène*

sur l'étude du conditionnement des matrices de Green.

## **V Conclusion et perspectives**

Le travail de Mouad a permis de mettre un cadre théorique sur la faisabilité de la technique envisagée. Les simulations ont permis d'accéder à des aspects plus quantitatifs.

Les perspectives portent clairement sur la mise en place d'un prototype expérimental. Sur la fin de la thèse Mouad a procédé à des mesures afin d'obtenir un premier retour d'expérience sur la mise en place expérimentale du dispositif.

La perspective dans ce cadre est de proposer la mise en place expérimentale dans le cadre d'une thèse. Celle-ci portera sur l'exploitation d'une plaque réfléchissante pour accélérer les mesures. Une attention particulière doit être portée aux conditions expérimentales qui permettent d'observer un effet miroir "idéal". Les quelques essais réalisés par Mouad ont mis en lumière que cette partie nécessite d'y investir une minutie particulière et du temps.

## Références

- DJEDIDI, M. (2016). « Design of a Fast Antenna Characterization Method Exploiting Echoes ». Thèse de doct. Université Paris-Sud, CentraleSupelec (cf. p. 119).
- DJEDIDI, M., F. MONSEF et A. COZZA (2014). « Antenna Measurement Concept Exploiting Echoes Based on Frequency Diversity ». *Antenna Measurement Techniques Association, Tucson (USA), october 2014*. IEEE, p. 261-264 (cf. p. 124, 125).
- LAWSON, C. L. et R. J. HANSON (1995). *Solving least squares problems*. T. 15. Siam (cf. p. 119).
- SELVAN, K. T. et R. JANASWAMY (2017). « Fraunhofer and Fresnel Distances : Unified derivation for aperture antennas. » *IEEE Antennas Propagat. Mag.* 59.4, p. 12-15 (cf. p. 112).
- TORN, A. et A. ZILINSKAS (1989). *Global optimization*. Springer-Verlag New York, Inc. (cf. p. 124).

# CHAPITRE 5

## Liste de mes publications

### I Articles dans des revues internationales à comité de lecture

- COZZA, A., F. MASCIOVECCHIO, C. DORGAN, M. SERHIR, F. MONSEF et D. LECOINTE (2017). « A Dielectric Low-Perturbation Field Scanner for Multi-Path Environments ». *IEEE Trans. Antennas Propagat.* 65.4, p. 1978-1987.
- MONSEF, F. et A. COZZA (2014a). « Variability and Confidence Intervals of the Power Measured in a Reverberation Chamber ». *IEEE Trans. Electromagn. Compat.* 56 (5), p. 1238-1241.
- MONSEF, F. et A. COZZA (2014b). « Average number of significant modes excited in a mode-stirred reverberation chamber ». *IEEE Trans. Electromagn. Compat.* 56.2, p. 259-265.
- COZZA, A. et F. MONSEF (2017a). « Time Reversal in Diffusive Media ». *Electromagnetic Time Reversal : Application to EMC and Power Systems*, p. 29.
- COZZA, A. et F. MONSEF (2014). « Multiple-source Time-Reversal transmissions in random media ». *IEEE Trans. Antennas Propagat.* 62.8, p. 4269-4281.
- COZZA, A. et F. MONSEF (2017b). « Steering Focusing Waves in a Reverberation Chamber with Generalized Time Reversal ». *IEEE Trans. Antennas Propagat.* 65.3, p. 1349-1356.
- MONSEF, F., R. SERRA et A. COZZA (2015). « Goodness-of-Fit Tests in Reverberation Chambers : Is Sample Independence Necessary ? » *IEEE Trans. Electromagn. Compat.* 57.6, p. 1748-1751.
- DOLLFUS, P., S. GALDIN RETAILLEAU, A. BOURNEL, F. MONSEF, S. BARRAUD et P. HESTO (2004a). « Influence of discrete impurity position in the channel of an ultra-small MOSFET ». *Semicond. Sci. Technol.* 19.4, S152.
- SAINT-MARTIN, J., A. BOURNEL, V. AUBRY-FORTUNA, F. MONSEF, C. CHASSAT et P. DOLLFUS (2006a). « Monte Carlo simulation of double gate MOSFET including multi sub-band description ». *J. Comput. Electron.* 5.4, p. 439-442.
- MONSEF, F. et A. COZZA (2014c). « Variability and confidence intervals of the power measured in a reverberation chamber ». *IEEE Trans. Electromagn. Compat.* 56.5, p. 1238-1241.
- COZZA, A. et F. MONSEF (2015). « Transmission-Based Imaging of an Electrically Small Aperture in a Shielded System ». *IEEE Antennas Wireless Propagat. Lett.* 14, p. 591-594.
- DOLLFUS, P., S. GALDIN RETAILLEAU, A. BOURNEL, F. MONSEF, S. BARRAUD et P. HESTO (2004b). « Influence of discrete impurity position in the channel of an ultra-small MOSFET ». *Semicond. Sci. Technol.* 19.4, S152.

## 5 Liste de mes publications

- VALLON, H., F. MONSEF, A. COZZA et A.-S. CHAUCHAT (2016). « Increasing Peak-Power Field Generation Efficiency in Reverberation Chambers ». *IEEE Trans. Electromagn. Compat.* 58, p. 364-370.
- MONSEF, F. et A. COZZA (2015a). « A Possible Minimum Relevance Requirement for a Statistical Approach in a Reverberation Chamber ». *IEEE Trans. Electromagn. Compat.* 57.6, p. 1728-1731.
- COZZA, A. et F. MONSEF (2016a). « Layered electric-current approximations of cylindrical sources ». *Wave Motion* 64, p. 34-51.
- COZZA, A. et F. MONSEF (2016b). « On the Influence of a Medium Statistics on the Robustness of Time-Reversal Transmissions ». *IEEE Antennas Wireless Propagat. Lett.* 16, p. 38-41.
- MONSEF, F. (2012). « Why a Reverberation Chamber Works at Low Modal Overlap ». *IEEE Trans. Electromagn. Compat.* 54.6, p. 1314-1317.
- MONSEF, F., A. COZZA, D. RODRIGUES, P. CELLARD et J.-N. DUROCHER (2014). « Relative variance of the mean-squared pressure in multimode media : Rehabilitating former approaches ». *J. Acoust. Soc. Am.* 136.5, p. 2621-2629.
- MONSEF, F., A. COZZA, F. MONSEF et A. COZZA (2014). « Average number of significant modes excited in a mode-stirred reverberation chamber ». *IEEE Trans. Electromagn. Compat.* 56.2, p. 259-265.
- MONSEF, F. et A. COZZA (2011b). « Limitations of the equivalence between spatial and ensemble estimators in the case of a single-tone excitation ». *J. Acoust. Soc. Am.* 130, p. 1943.
- MONSEF, F., P. DOLLFUS, S. GALDIN et A. BOURNEL (2003). « Erratum : First-order intervalley scattering in low-dimensional systems ». *Phys. Rev. B* 67, p. 059903.
- MONSEF, F., P. DOLLFUS, S. GALDIN et A. BOURNEL (2002). « First-order intervalley scattering in low-dimensional systems ». *Phys. Rev. B* 65.21, p. 212304.
- MONSEF, F., P. DOLLFUS, S. GALDIN-RETAILLEAU, H.-J. HERZOG et T. HACKBARTH (2004). « Electron transport in Si/SiGe modulation-doped heterostructures using Monte Carlo simulation ». *J. Appl. Phys.* 95.7, p. 3587-3593.
- SAINT-MARTIN, J., A. BOURNEL, V. AUBRY-FORTUNA, F. MONSEF, C. CHASSAT et P. DOLLFUS (2006b). « Monte Carlo simulation of double gate MOSFET including multi sub-band description ». *J. Comput. Electron.* 5.4, p. 439-442.
- SAINT-MARTIN, J., A. BOURNEL, F. MONSEF, C. CHASSAT et P. DOLLFUS (2006). « Multi sub-band Monte Carlo simulation of an ultra-thin double gate MOSFET with 2D electron gas ». *Semicond. Sci. Technol.* 21.4, p. L29.

## II Articles dans des conférences internationales à comité de lecture avec actes

- DJEDIDI, M., F. MONSEF et A. COZZA (2015). « Preliminary study on the use of complex media for antenna characterization ». *Antennas and Propagation & USNC/URSI National Radio Science Meeting, 2015 IEEE International Symposium on*. IEEE, p. 278-279.
- DJEDIDI, M., F. MONSEF et A. COZZA (2014). « Antenna Measurement Concept Exploiting Echoes Based on Frequency Diversity ». *Antenna Measurement Techniques Association, Tucson (USA), october 2014*. IEEE, p. 261-264.
- COZZA, A. et F. MONSEF (2011). « How a physical definition of overmodedness can explain local statistical non-compliance ». *EMC Europe 2011 York*. IEEE, p. 137-142.

- DOLLFUS, P., S. BARRAUD, E. CASSAN, F. MONSEF et S. GALDIN (2002a). « Quantum and random impurity effects in ultra-short MOSFET ». *Materials science forum*. T. 384. Trans Tech Publ, p. 51-58.
- METON, P., A. COZZA, F. MONSEF, M. LAMBERT, J.-C. JOLY, P. BRUGUIÈRE et al. (2012). « Numerical analysis of pulsed local plane-wave generation in a TREC ». *Proceedings of EUROEM 2012 European Electromagnetics*.
- METON, P., F. MONSEF, A. COZZA, M. LAMBERT, J. JOLY et al. (2013). « Analysis of Wave-front Generation in A Reverberation Chamber for Antenna Measurements ». *Proceedings of the 7th European COnference on Antennas and Propagation*.
- MONSEF, F. et A. COZZA (2012). « Goodness-of-fit tests in radiated susceptibility tests ». *Workshop on Aerospace EMC, 2012 Proceedings ESA*. IEEE, p. 1-5.
- MONSEF, F. et A. COZZA (2011a). « Analysis of Time-Reversal-based propagation for spatial focusing and multiplexing ». *Antennas and Propagation in Wireless Communications (APWC), 2011 IEEE-APS Topical Conference on*. IEEE, p. 827-830.
- MONSEF, F., A. COZZA et L. ABOUD (2010). « Effectiveness of Time-Reversal technique for UWB wireless communications in standard indoor environments ». *ICECom, 2010 Conference Proceedings*. IEEE, p. 1-4.
- MONSEF, F. et A. COZZA (2015b). « Predicting Power Distribution Inside a Reverberation Chamber ». *URSI-RASC Conference Proceedings*. IEEE.
- DOLLFUS, P., S. BARRAUD, E. CASSAN, F. MONSEF et S. GALDIN (2002b). « Quantum and random impurity effects in ultra-short MOSFET ». *Materials science forum*. T. 384. Trans Tech Publ, p. 51-58.

### **III Brevets**

- COZZA, A., M. DJEDIDI et F. MONSEF (2017). « Method and device for measuring the radiation pattern of a radiative source in a echogenic medium ». WO2015FR52704 20151008.
- MONSEF, F. (2013). « Chambre réverbérante à uniformité de champ électromagnétique améliorée ». 1H170260 0310 FR /JBT/PAS.